Washington University in St. Louis

Department of Physics

Dissertation Examination Committee:
Jason C Woods, Chair
Mark S Conradi
Sophia E Hayes
Erik Henriksen
James G Miller
Ralf Wessel

Investigation of Lung Structure-Function Relationships Using Hyperpolarized Noble Gases

by

Robert P Thomen

A dissertation presented to the Graduate School of Arts and Sciences of Washington University in partial fulfillment of the requirements for the degree Doctor of Philosophy

May 2016
St Louis, Missouri

Contents

List of Figures

List of Tables

List of Physical Constants

Avogadro's Number	N_A	=	6.022×10^{-23}
Bohr Magneton	μ_B	=	9.274×10^{-24} J T^{-1}
Boltzmann's Constant	k	=	1.381×10^{-23} J K^{-1}
Electron Rest Mass	m_e	=	9.109×10^{-31} kg
Elementary (e$^-$) Charge	e	=	1.602×10^{-19} C
Nuclear Magneton	μ_N	=	5.051×10^{-27} J T^{-1}
Plank's Constant	h	=	6.626×10^{-34} J s
Proton Rest Mass	m_p	=	1.673×10^{-27} kg
Speed of Light	c	=	$2.997\ 924\ 58 \times 10^{8}$ m s^{-2} (exact)
Vacuum Permittivity	ϵ_0	=	8.854×10^{-12} F m^{-1}
Vacuum Permeability	μ_0	=	$4\pi \times 10^{-7}$ H m^{-1}

List of Abbreviations

ADC	Apparent Diffusion Coefficient
AM	Alkali Metal
BT	Bronchial Thermoplasty
BW	Bandwidth
CF	Cystic Fibrosis
COPD	Chronic Obstructive Pulmonary Disease
FA	Flip Angle
FEV_1	Forced Expiratory Volume in 1 second
FFT	Fast Fourier Transform
FLASH	Fast Low Angle Shot Sequence
FRC	Functional Residual Capacity
FVC	Forced Vital Capacity
GRE	Gradient Recalled Echo sequence
HP	Hyperpolarized
IPF	Idiopathic Pulmonary Fibrosis
IQR	Interquartile Range
MRI	Magnetic Resonance Imaging
NMR	Nuclear Magnetic Resonance
OP	Optical Pumping
PFT	Pulmonary Function Test
rf	Radiofrequency
SD	Spin Destruction
SDP	Segmental Defect Percentage

SE	Spin Exchange
SEOP	Spin Exchange Optical Pumping
SNR	Signal to Noise Ratio
SVP	Segmental Ventilation Percentage
TE	Echo Time
TLC	Total Lung Capacity
TR	Repetition Time
T/R	Transmit/Receive
UHP	Ultra High Purity
UTE	Ultra Short Echo Time
VDP	Ventilation Defect Percentage

Acknowledgements

"Sometimes people care too much. I think it's called love."

— Winnie the Pooh

It is my honor to recognize and thank my advisor Jason Clay Woods PhD for his immense contribution to this work, his continued scientific, financial, and personal support, his willingness to listen, provide feedback, and maintain a respectful and inviting atmosphere in and out of the workplace, and his often unmerited faith in my efforts. Because these qualities are so rarely found in a PhD advisor, I consider myself uniquely blessed to have actually *enjoyed* my graduate tenure, and for this I wish to convey utmost gratitude. It's been a pleasure working with you sir! (...see you Monday)

The Center for Pulmonary Imaging Research (CPIR) is a wonderland of brilliant, dedicated, hard-working individuals who have made my graduate tenure an immensely enjoyable experience. Thank you all for your friendship, support, and tolerance of my overwhelmingly hilarious puns.

If you are related to me, please be informed that you are among my favorite people who exist on the planet, and I look to you with great admiration. In particular, my parents are my models of personhood, and becoming like them is one of my supreme life goals (indeed much loftier than a doctorate in physics). Thank you all for your love and support.

Many very sick people, adults and children, volunteered for these studies because they believed that by their participation, we as scientists could in some small way alleviate the suffering of others.

This work is dedicated to them.

Abstract of the Dissertation

by
Robert P Thomen
Doctor of Philosophy in Physics
Washington University in St Louis, 2016
Professor Jason C Woods, Chair

Magnetic Resonance Imaging (MRI) is an application of the nuclear magnetic resonance (NMR) phenomenon to non-invasively generate 3D tomographic images. MRI is an emerging modality for the lung, but it suffers from low sensitivity due to inherent low tissue density and short T_2^*. Hyperpolarization is a process by which the nuclear contribution to NMR signal is greatly enhanced to more than 100,000 times that of samples in thermal equilibrium. The noble gases ^{3}He and ^{129}Xe are most often hyperpolarized by transfer of light angular momentum through the electron of a vaporized alkali metal to the noble gas nucleus (called Spin Exchange Optical Pumping). The enhancement in NMR signal is so great that the gas itself can be imaged via MRI, and because noble gases are chemically inert, they can be safely inhaled by a subject, and the gas distribution within the interior of the lung can be imaged.

The mechanics of respiration is an elegant physical process by which air is is brought into the distal airspaces of the lungs for oxygen/carbon dioxide gas exchange with blood. Therefore proper description of lung *function* is intricately related to its physical *structure*, and the basic mechanical operation of healthy lungs – from pressure driven airflow, to alveolar airspace gas kinetics, to gas exchange by blood/gas concentration gradients, to elastic contraction of parenchymal tissue – is a process decidedly governed by the laws of physics.

This dissertation will describe experiments investigating the relationship of lung structure and function using hyperpolarized (HP) noble gas MRI. In partic-

ular HP gases will be applied to the study of several pulmonary diseases each of which demonstrates unique structure-function abnormalities: asthma, cystic fibrosis, and chronic obstructive pulmonary disease. Successful implementation of an HP gas acquisition protocol for pulmonary studies is an involved and stratified undertaking which requires a solid theoretical foundation in NMR and hyperpolarization theory, construction of dedicated hardware, development of dedicated software, and appropriate image analysis techniques for all acquired data. The author has been actively involved in each of these and has dedicated specific chapters of this dissertation to their description.

First, a brief description of lung structure-function investigations and pulmonary imaging will be given (chapter 1). Brief discussions of basic NMR, MRI, and hyperpolarization theory will be given (chapters 2 and 3) followed by their particular methods of implementation in this work (chapters 4 and 5). Analysis of acquired HP gas images will be discussed (chapter 6), and the investigational procedures and results for each lung disease examined will be detailed (chapter 7). Finally, a quick digression on the strengths and limitations of HP gas MRI will be provided (chapter 8).

Preface

"Everyone knows ugly men make the best doctors."

— Richard Gilmore, *Gilmore Girls*

This dissertation is written in pursuit of a doctorate in physics, but discussed topics will also extend across the fields of chemistry, biology, physiology, statistics, signal processing, and medicine. As such its purpose is threefold: First, it is meant to convey to a select collection of experts in physics and related fields an appropriate level of academic achievement and original thought deserving of an advanced degree. Second, it must give an appropriate review of the fundamentals inherent in the discipline such that the uninitiated are adequately prepared to understand and appreciate the novelty of the work. Finally, it is to be a resource for those intending to continue or expand the work - an effective birds-eye view of a research notebook. The reader is assumed to have a basic understanding of the four fundamental branches of physics in order to fully understand the presented material: Classical Mechanics [1], Electrodynamics [2], Quantum Mechanics [3], and Statistical Mechanics [4].

Organization of the following chapters is highly unoriginal and follows a standard scientific outline: motivation (Ch1), background (Ch2), theory (Ch3), methods (Ch4-5), analysis (Ch6), results (Ch7), discussion and conclusions (Ch8). The work presented here has culminated into several peer-reviewed journal publications which will be cited *ad nauseum* throughout the text. While the content and results of this work have important implications for the field of pulmonary medicine, the author is not a medical professional and no part of this dissertation is to be considered as medical advice or opinion.

Please enjoy this work to the best of your ability.

Chapter 1

On the Respiratory System and the Physics of Medical Imaging

"ᚾᛈᛟ ᚷᚹᛈ ᛈᛖᛗᛗ ᚻᛟᚻᚾᛈᛒ"

— Frodo Baggins, *The Lord of the Rings*

Lungs stand out among other organs of the body as those which are most exposed to the harsh conditions of the outside world. This is because the surface area contained within the numerous airways and alveolar spaces of the lungs is estimated between 50 and 100 square meters [5], roughly the size of a tennis court. Even our external layer of human skin only protects a surface area of approximately 2 square meters[1] – thus, for an internal organ the lungs are uniquely vulnerable. At any given moment, adult lungs contain approximately 3 liters of atmospheric gases which are being continually cycled in and out at a rate of about 10,000 liters per day. For many, comfortable breathing is an involuntary, unrecognized activity often taken for granted; for others every successful breath is a precious commodity. In fact, respiratory disease is only superseded by heart disease and cancer as the most common cause of death in America [6]. Lungs are unique among biological viscera in that they are very mechanically active without themselves containing active muscle tissue. As we shall soon see, the process of respiration is decidedly governed by the laws of physics.

This work details research investigating the relationships between lung structure and

[1]Special thanks to Hannibal Lecter for providing this figure.

function using novel imaging techniques – in particular, hyperpolarized gas MRI. The precise structure of the respiratory system, from airway caliber to alveolar morphometry to epithelial wall thickness to alveolar duct architecture to chest cavity dimension, is integral to its ability to function effectively and efficiently. Before presenting the novelty and utility of hyperpolarized gases as a modality for studying lungs, the current tools for investigating lung structure and function, both in research and in clinic, must be discussed. This first chapter will present a basic overview of the physics of respiration, medical imaging, and, more generally, current standards of practice for imaging lungs. In particular, the need for less invasive diagnostic methods for pediatric imaging is a major factor driving the research at hand so these considerations will also be addressed.

1.1 Physiology and Mechanics of the Respiratory System

The process of respiration is twofold: fresh gas must be brought into the distal airspaces of the lungs (called *ventilation*), and oxygen must be exchanged with carbon dioxide in the blood by diffusing through alveolar cell walls into capillaries (called *perfusion*)[2]. All cells within the body derive energy from ATP (adenosine triphosphate) which they themselves produce from glucose and oxygen via cellular respiration. Red blood cells (RBCs), or *erythrocytes*, are carried in blood throughout the body to collect and distribute oxygen. The respiratory system begins with the trachea which branches just above the heart into two bronchi which respectively supply each lung with air (Figure 1.1) - the first generation branch. The bronchi then branch into lobar bronchi which supply each lobe with air (the second generation); the third generation branches supply bronchopulmonary segments with air. After approximately 17 airway branches, the *conductive* airways (airways which conduct gas flow and do not participate in gas exchange) end and the *respiratory* zone begins. Res-

[2]The physical process of gas transfer across the blood-gas barrier is often referred to as 'diffusion', but in the experimental context maintained in this dissertation, the term diffusion will refer to Brownian motion of gas *within* the alveolar airspaces.

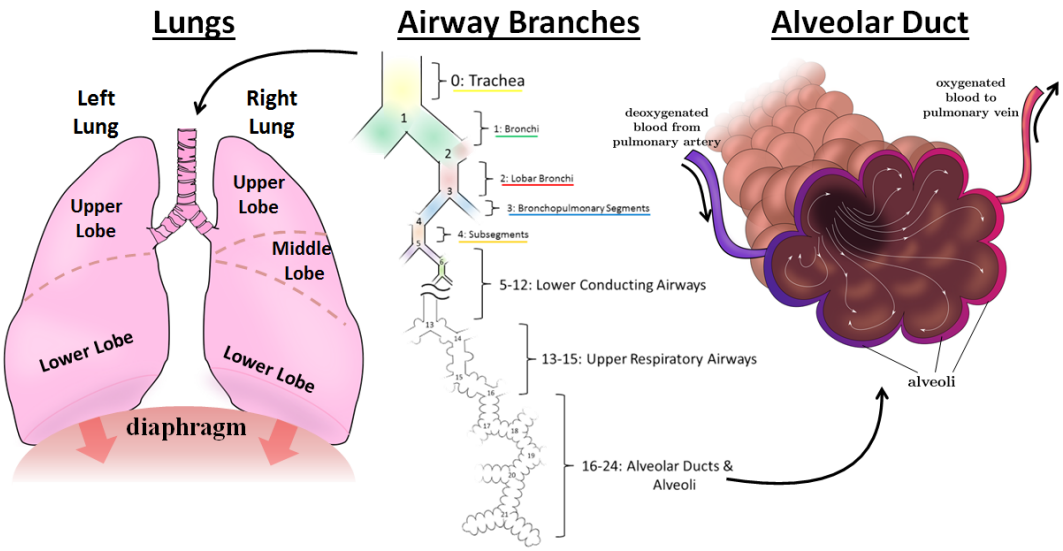

Figure 1.1: Cartoon diagrams of lungs (seen from posterior), airway branches and alveoli (capillaries of course surround all alveoli even though only a few are shown here).

piratory airways have budding alveoli which are the tiny sacs that facilitate gas exchange - the exchange of carbon dioxide for oxygen in the blood. The respiratory zone continues for approximately 6-7 more airway branches (for a total of about 23-24 branches between the trachea and individual alveolar ducts). The respiratory zone constitutes approximately 92% of the lung volume and is called the *parenchyma*. [5]

1.1.1 Ventilation

During inhalation the diaphragm contracts and the ribcage expands to increase the volume of the chest cavity. This creates negative intrapleural pressure which draws air into the lungs. Air is expelled from the lung during exhalation, a *passive* process which relies on the elastic nature of lung tissue to contract itself. Generally the chest cavity is at negative pressure during inhalation and zero pressure at end-exhalation. One can plot the volumetric expansion of the lung as a function of the negative pressure created by the chest cavity on a *Pressure-Volume* (PV) curve as shown in Figure 1.2. Note that there exists some hysteresis between inhalation and exhalation curves; during exhalation, lung volume at a given pressure

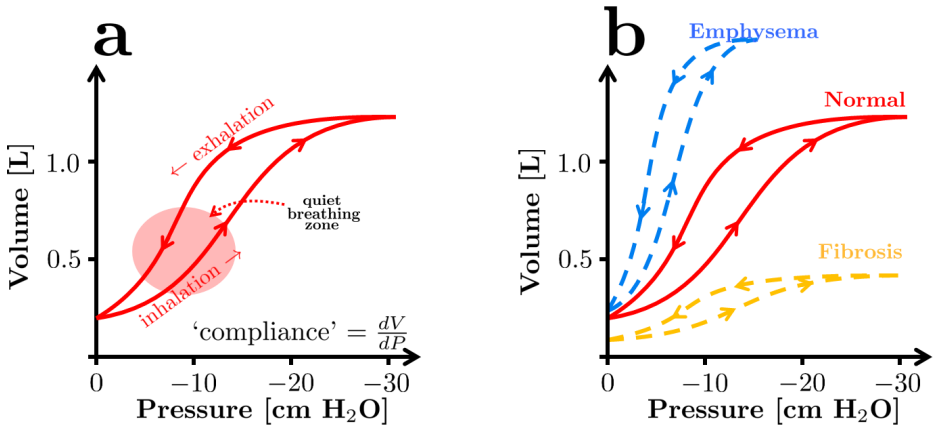

Figure 1.2: Pressure-Volume Curve: Lung Volume vs Chest Cavity Pressure. Panel (a) explicitly denotes the inspiratory and expiratory curves. Panel (b) compares PV curves for emphysematous (hypercompliant) and fibrotic (hypocompliant) lungs for comparison to normal. Curves are exaggerated here for illustration.

is always greater than for inhalation. The slope of the PV curve, $\frac{dV}{dP}$, is called *compliance* and is a useful measure of the mechanical integrity of the lung [7, 8]. Emphysema is characterized by deterioration of lung parenchyma and alveolar walls. Emphysematous lungs inflate very easily with low applied pressures (high compliance), but struggle to expel air due to poor parenchymal elasticity (greater flaccidity) which leads to air trapping and overinflation. Lungs with excess fibrotic tissue require more pressure to inflate (low compliance and greater rigidity), and often cannot be inflated to normal total lung capacity (TLC). These cases are illustrated alongside a normal case in Figure 1.2.b. [5]

The elastic quality of the lungs comes from the surface tension of the numerous air-tissue interfaces within the parenchyma. An aqueous coating of *surfactant* which is secreted by epithelial type II cells coat the interior of alveoli (Figure 1.3) which serve the purpose of *reducing* the elasticity of the lung and increasing compliance[3]. Indeed a deficiency of surfactant within the parenchyma leads to regions of atelectasis (collapsed alveoli) and reduced compliance. [9, 10]

As it so happens, the lungs demonstrate gravitational dependence in ventilation. When

[3]The surface tension of surfactant is less than that of water (approximately 10-30 dynes/cm), roughly the same as dish soap [5].

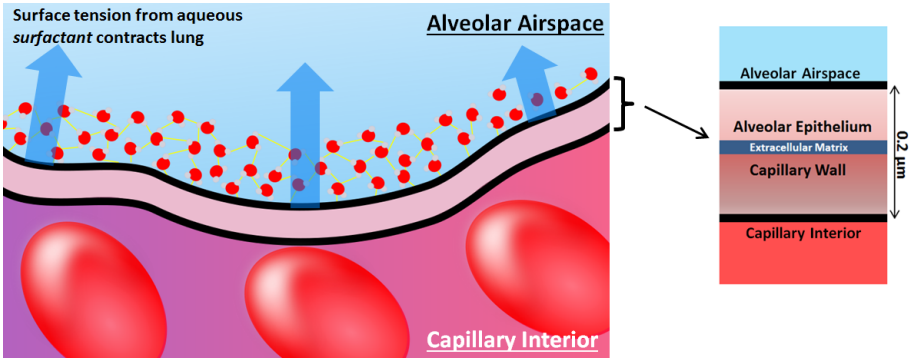

Figure 1.3: Illustration of the alveolus-capillary interface. The aqueous film of surfactant which coats the interior of alveolar airspace, represented by the water atoms and hydrogen bonds, reduces the force of contraction and increases lung compliance. A zoomed-in picture of the blood-gas interface in shown to the right. [9]

upright, the base of one's lungs experience a higher pressure (or, to be more precise, a less-negative pressure) than the apices due to the weight of the lungs' own tissue as well as that of the heart and blood. Thus, different regions of the lung ventilate according to their corresponding locations on the PV curve as illustrated in Figure 1.4. This means that the basal regions of the lung will draw a greater volume of air (greater ΔV) in a quiet tidal breath relative to the apical regions. [5]

Air moves within the lung parenchyma by laminar flow in high-caliber airways according

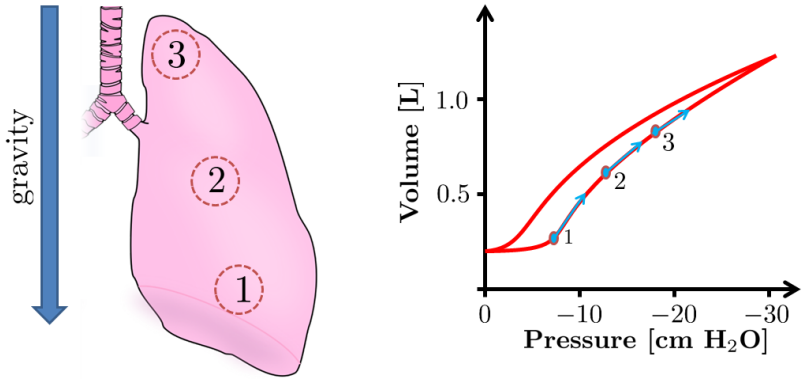

Figure 1.4: Gravitational Dependence of the Pressure-Volume Curve for three explicitly labeled regions. The base of the lungs are more compliant due to gravitational weighting and therefore demonstrate greater ventilation.

to the Poiseuille equation [11],

$$\frac{dV}{dt} = \frac{P\pi r^4}{8\eta l}, \tag{1.1}$$

where $\frac{dV}{dt}$ is fluid volume per unit time, P is the pressure differential at opposite ends of the airway, r is the airway radius, η is air viscosity, and l is airway length. The proportion of airflow to r^4 identifies airway caliber as the most critical parameter to proper ventilation. As airways split into smaller and smaller branches, gas flow eventually becomes driven by diffusion relying on Brownian motion to distribute gas atoms to/from airways to capillaries.

1.1.2 Perfusion

Once a fresh breath of air has been drawn into the distal airspaces of the lungs, oxygen (O_2) must be exchanged with carbon dioxide (CO_2) in the red blood cells (RBC's). This is a passive process which relies on *Fick's Law* of diffusion across a barrier for gas exchange:

$$\frac{dV}{dt} \propto \frac{A}{T} D(P_1 - P_2) \tag{1.2}$$

where A = Area, T = thickness, D = Diffusion Coefficient, and $(P_1 - P_2)$ indicate a partial pressure difference. Because lung parenchyma constitutes an approximately 50-100 square-meter gas-exchange surface area A, and the thickness of the blood-gas barrier is approximately $T = 0.2$ μm thick (Figure 1.3), the O_2 / CO_2 partial pressures between the alveolar airspace and the RBC's equilibrate in about 0.25 - 0.5 seconds. Blood spends about 3/4 second in an alveolar capillary during quiet breathing (about 1/4 second during exercise). [5, 9]

As stated above, a lung's structure is intimately related to its ability to function properly. Asthma is a common abnormality in which the airways supplying gas to the distal lung airspaces become constricted; this would be an impairment of ventilation. Pulmonary alveolar proteinosis is another disease in which a unusually grainy layer of surfactant is produced coating the interior walls of alveoli - an impairment of perfusion. Emphysema, characterized by deterioration of distal airways, demonstrates poor perfusion since alveolar surface area

is diminished, and poor ventilation since the lung is mechanically impaired and cannot adequately contract and exhale. The latter abnormality presents a particularly good example of how the lungs' ability to function well is directly related to their physical structure [12].

1.2 Quantifying Lung Structure and Function

While the physiology of the respiratory system and mechanics of breathing have been well understood for centuries [13], pulmonology has only been considered a medical specialty since the 1950's. Even today, relatively common pulmonary abnormalities (e.g., asthma, bronchitis, pneumonia, etc.) vary widely on an individual basis and in many cases require individualized treatment [14, 15]. The relationship between structure and function is not only imperative to understanding the nature of pulmonary abnormalities, but it is necessary to clinicians for making more informed diagnoses and more effectively treating maladies. Linking lung structure and function is a complicated task which has historically lagged behind advances in medical treatments for various lung diseases in terms of sensitivity and specificity. Structure and function are often measured separately: spirometric techniques are the clinical standard of evaluation of lung function, and medical imaging (mostly x-ray CT, section 1.2.5) is used to evaluate lung structure. This section will describe each of these techniques in detail along with their strengths and limitations. Then in the following section 1.3, a novel imaging technique will be presented which is emerging as the gold standard for investigation of *both* lung structure and function and is the modality highlighted in this dissertation: hyperpolarized gas MRI [16].

1.2.1 Quantifying Lung Function - Pulmonary Function Tests

Pulmonary function tests (PFTs) are currently the gold standard for evaluation of the functional state of the respiratory system in the clinic [10], and these methods include spirometry, gas diffusion techniques, inhalation challenge tests, plethysmography, and multiple breath washout. For the experiments described in this dissertation, spirometry was the re-

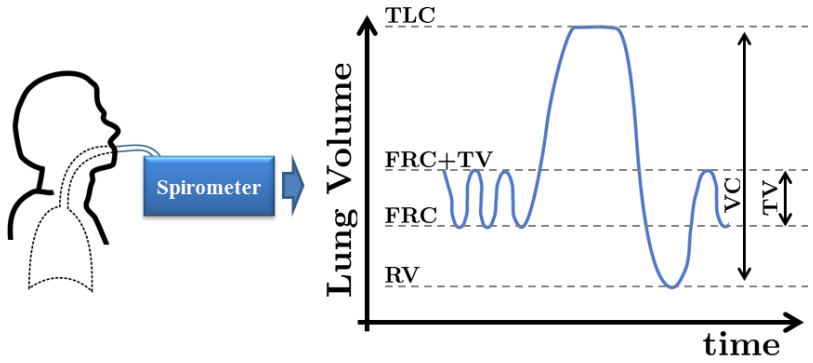

Figure 1.5: Illustration of Spirometry and Various Lung Volumes. This subject breathes normally then inhales maximally to total lung capacity (TLC). He then exhales to his minimum achievable lung volume (residual volume, RV), then resumes normal breathing. TLC = total lung capacity, FRC = functional residual capacity, TV = tidal volume, RV = residual volume, VC = vital capacity.

ported PFT since it is the most clinically relevant to the obstructive diseases [17]. Figure 1.5 illustrates the process of spirometric measurement. A spirometer measures airflow and can thus be used to evaluate the lungs' ability to inhale and exhale. The most informative spirometric technique for evaluation of lung disease is forced expiration in which the subject inhales to total lung capacity (TLC) then exhales as quickly and forcefully as possible to residual volume; the amount of gas exhaled within the first second is the subject's *forced expiratory volume in 1 second*, or FEV_1 (Figure 1.6). FEV_1 is measured in liters but is only clinically useful when reported as *percent of predicted* which takes into consideration subject differences due to age, race, sex, height, etc. For instance a 5'10" white male aged 29 years should be able to achieve an FEV_1 near 4.49 liters (according to the Hawkinson 1999 standard [18]); if such a subject were to actually achieve an FEV_1 of 4.3 liters his FEV_1 would be reported as $4.3/4.49 = 95.8\%$ of predicted. The total amount of gas exhaled is the subject's *forced vital capacity*, or FVC and the ratio FEV_1/FVC is another useful clinical marker of lung function.

Spirometric measures are useful for identifying the obstructive or restrictive nature of a disease as well as its severity. For instance, according to the Global Initiative for Chronic Obstructive Lung Disease (GOLD) and the American Thoracic Society (ATS), an FEV_1/FVC

GOLD Classification	Description	FEV_1
GOLD 1	mild	$FEV_1 \geq 80\%$
GOLD 2	moderate	$80\% \geq FEV_1 > 50\%$
GOLD 3	severe	$50\% \geq FEV_1 > 30\%$
GOLD 4	very severe	$FEV_1 < 30\%$

Table 1.1: GOLD Classification of COPD Severity [10].

ratio of < 0.7 is would indicate airflow obstruction, and FEV_1 would indicate the severity of disease (Table 1.1).

PFT's suffer from several limitations. First, they cannot diagnose specific diseases apart from clinical history and physiology. They cannot quantify lung function *regionally*, although multiple breath washout techniques can quantify the overall heterogeneity of disease within the lung. They do not always correlate with symptoms, especially in children [19]. However, PFT's are the current clinical standard for quantification of lung function. In this work, we shall see that hyperpolarized gas MRI is a novel method for quantifying lung function regionally which may improve our understanding of lung disease and provide insight for the efficacy of targeted treatments.

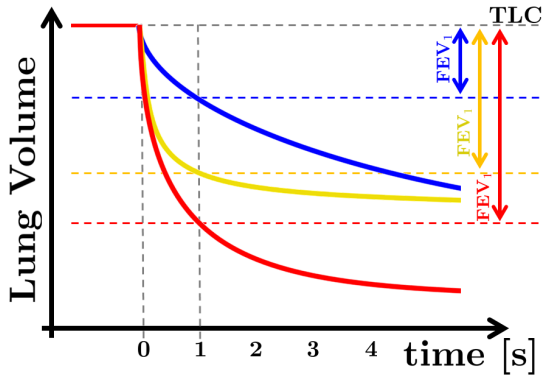

Figure 1.6: Forced Vital Capacity curves illustrating measurement of FEV_1. If the red plot indicates a normal FVC curve, the reduced FEV_1 of the yellow plot might indicate obstructive lung disease. The blue plot might be more indicative of restrictive lung disease since the FEV_1/FVC ratio is reduced as well. Note that these plots are referenced to TLC which can be dramatically different for various diseases as well.

1.2.2 Quantifying Lung Structure - Imaging

Generally, methods of medical imaging are best suited to provide a clear picture of how lung structure and function are related[4]. What are the predominant clinical imaging methods and how do they work? What pulmonary information can each reveal, and what pulmonary information can each *not* reveal? This section will detail a few common imaging modalities used in pulmonary medicine for clinical diagnoses and research. Of critical importance, some imaging methods can pose 'greater than minimal risk' to subjects from ionizing radiation (e.g., x-ray imaging or radiopharmaceuticals in nuclear imaging). Before discussing the intricacies of various medical imaging modalities, the issue of radiation exposure requires a brief digression as it presents the dominant restriction on their use for research especially in pediatric patients.

1.2.3 The Risks of Ionizing Radiation

Ionizing radiation is generally harmful to living beings. At the relatively mild and controlled dosages used in medical imaging (a few millisieverts, mSv) the major concern is potential induction of cancer, especially over continued lifetime exposure. This occurs almost exclusively from irreparable damage to DNA either by direct damage from the incoming photon(s), or indirectly from the creation of free radicals which react unfavorably with DNA. While any biological molecule is susceptible to damage from ionization, cellular function is rarely lost from inhibition of individual biomolecules; however, cellular function can be severely altered from loss of vital genetic information contained within DNA [20]. Clinicians and researchers must be able to justify any necessary human imaging with appropriate risk/benefit analysis, and appropriate assent/consent must be obtained from any and all subjects or their guardians. As per FDA regulation, any drug 'dose' required for imaging, whether pharmaceutical or radiation, must be **a**s **l**ow **a**s **r**easonably **a**chievable (ALARA)[5].

[4]Pun intended

[5]For an impressive and well-cited chart of comparative radiation exposure levels, see the 'Radiation Exposure Chart' [21] by Randall Munroe, creator of the webcomic *xkcd*.

There is a consensus that the risks associated with radiation exposure are greater in pediatric subjects [22], although available data are sparse and variable. Even in the case of equal radiosensitivity in children and adults, many cancerous metastases can remain dormant for years, even decades. Obviously, the window of opportunity for tumor development is greater for a 10-year-old compared to a 60-year-old. Pediatric protocols for radiographic imaging have been developed to reduce exposure without compromising diagnostic information, and the Alliance for Radiation in Pediatric Imaging has heightened awareness in the imaging community by suggesting medical practice changes. Currently the diagnostic quality of radiographic images (CT in particular) is unmatched in resolution and contrast, but development of minimal-risk imaging strategies in MRI and ultrasound have made these modalities increasingly attractive to health-care providers. The following are a few of the more common clinically-ordered imaging modalities and their utility in pulmonary diagnoses in particular. As magnetic resonance imaging (MRI), and to a lesser extent computed tomography (CT) are of particular interest in this work, they will be given fuller treatment here.

1.2.4 Projection X-ray

The most commonly ordered thoracic images are projection chest x-rays (CXR) [10, 23]. A projection x-ray image involves directing x-ray photons through the body and onto either a photographic or digital film where a 2D image of x-ray attenuation is formed. X-rays are in the energy range 5-150 keV [24], are attenuated as they pass through the body by Compton and Rayleigh scattering; thus, x-ray attenuation is effectively a measure of tissue density (or, to be more precise, electron density). A chest x-ray is often performed at total lung capacity (TLC) (unless investigating potential air trapping or pneumothorax), and approximately 0.1 mSv of dose is administered (slightly more if the mediastinum must be resolved). Projection x-ray is available in nearly every medical establishment and overhead cost is low. Fluoroscopy is to projection x-ray what video is to photography – it is an x-ray movie. It is rarely ordered for pulmonary applications except perhaps in guiding biopsies for

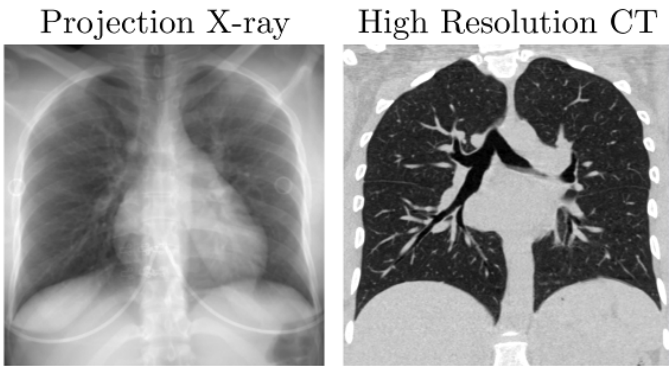

Figure 1.7: Comparison of Projection X-ray and CT a healthy volunteer. The projection x-ray is effectively a photon attenuation sum through the entire chest. The CT is a reconstructed 0.3-mm-thick coronal slice.

tumor diagnosis [25].

1.2.5 Computed Tomography (CT)

Computed tomography is an imaging modality in which 3D reconstructions of anatomic density are computationally performed using a series of x-ray projections through the sample at different imaging angles. A high-resolution CT scan (HRCT) yields images of rather stunning detail and resolution. Figure 1.7 shows a side-by-side comparison of a chest x-ray and HRCT; CT can quantify parenchymal density (compare the signal intensity of the lung to that of the major bronchi), and visualize lobar fissures, peripheral vessels, and high generation airway branches. In terms of diagnostic image quality for lung structure CT is the 'gold standard'. However, it involves a relatively high dose of ionizing radiation (Table 1.2) and is rarely ordered for children [21] except in cases where chest x-ray fails to provide conclusive diagnoses.

1.2.6 Ultrasound

Ultrasound produces profile images of biological tissue called sonograms by noting time difference between a pulse of high-frequency sound wave and its resultant echo on tissue.

The now-common 3D ultrasound can provide rather exquisite detail and tissue contrast. It is completely non-invasive, and hospital overhead is very low compared to other modalities (less than $50,000 for a high-end machine); therefore it is an attractive modality in research and clinical settings [26]. Ultrasound of lung in the clinic is currently limited to evaluation of pulmonary edema, emboli, pneumothorax, and undesired fluid accumulations, guiding biopsies, and evaluating atelectasis (alveolar collapse) and fibrosis. Because lung volume is mostly air its use in pulmonary structural imaging has historically been limited, but research in the field is thriving with novel applications of lung ultrasound (LUS) emerging regularly [27, 28].

1.2.7 Nuclear Imaging

Nuclear imaging by single photon emission computed tomography (SPECT) or positron emission tomography (PET) are highly sensitive measures of tissue function, and thus provides unique information relative to other modalities which largely measure structure. Although ionizing radiation is involved, the detection methods are sensitive enough that administered radiopharmaceutical volumes are quite small and radiation doses are similar to that of a chest x-ray (fractions of mSv). Mechanisms by which radiopharmaceuticals concentrate in tissue depend on cellular and biochemical processes [29], thus nuclear imaging is most commonly used in oncology, but ventilation / perfusion scans (abbreviated as $\dot{V}/\dot{Q}$) are a sensitive measure of lung function commonly ordered for evaluation of pulmonary emboli [15, 17]. A simple gamma camera and access to radiopharmaceuticals are baseline necessities with the option of producing radiopharmaceuticals in-house with the addition of a cyclotron (very expensive).

1.2.8 MRI

When placed in a magnetic field certain atomic nuclei demonstrate the ability to absorb and re-emit radiofrequency (rf) energy; the precise frequency of the rf signal is proportional to the magnetic field strength. Magnetic Resonance Imaging (MRI) involves transmission/re-

Modality	Dose [mSv]
MRI	0
Dental X-ray	0.005
Chest X-ray	0.02
Chest X-ray	1
Lung Ventilation/Perfusion by PET	2
Normal Yearly Background	4
Chest CT	7
Chest CT (for pulmonary embolism)	10

Table 1.2: Comparison of Dosage for Various Imaging Modalities. Data from [21, 30, 31]

ception of *rf* signals from nuclei in the body (almost exclusively hydrogen nuclei) during a concert of magnetic field gradients which are used to localize the signal origins in 3 dimensions. Among medical imaging modalities the elegance of MRI is exceptional with numerous methods of contrasting tissue available to the technician and physician (to be discussed in section 2.1.4). In particular, its ability to contrast adjacent soft tissues is unmatched, but it can also reveal quantitative information relating to fluid flow, cellular metabolism, and spectroscopic chemistry.[6]

In terms of pulmonary imaging, MRI is considered the most limited and is rarely ordered for investigation of lung pathology except in the cases of suspected nodules or cancers [17]. For reasons to be discussed later (section 5.6), the lung's parenchymal signal is artificially low in standard MRI sequences leading to inaccurate representation of tissue density. Figure 1.8 presents side-by-side comparison of a coronal MRI and coronal high-resolution CT (HRCT) alongside quantitative ROI results. The lungs are approximately 20-30% the density of other soft tissues within the lung (within a typical tidal volume), but MRI measures signals only slightly above noise within the parenchyma. CT clearly presents more accurate tissue density measures, and rather impressive signal-to-noise (SNR), contrast-to-noise (CNR), and resolution. A major goal of current MRI research is to achieve diagnostic image quality similar to that of CT thereby providing the same service with no ionizing radiation. MRI of lung is a rapidly developing field which has consistently seen emergence of new methods in

[6]The description of MRI here is cursory since the purpose of chapter 2 is to detail the basic physics of NMR and MRI.

the last 20 years; discussion here is limited to the work at hand, but those interested in the clinical side of MRI would do well to examine Kauczor and Baert's review text [32].

There are a few important limitations to note when considering MRI as a research tool, not least of which is cost. Hospital overhead for MRI is rather high since it requires constant cryogenic cooling to maintain high magnetic field strength (approximately 100,000 times greater than earth's field) by superconducting coils. Aside from the approximately $1-2 million cost of a new scanner, a year of upkeep and maintenance is roughly $100,000, and a single hour-long scan session can cost several thousand dollars [31, 33, 34]. Further, MRI is a notoriously insensitive technique requiring the subject to remain still for extended periods of time (a challenge for children, and simply not feasible for lungs) to acquire enough signal to produce a useful image.

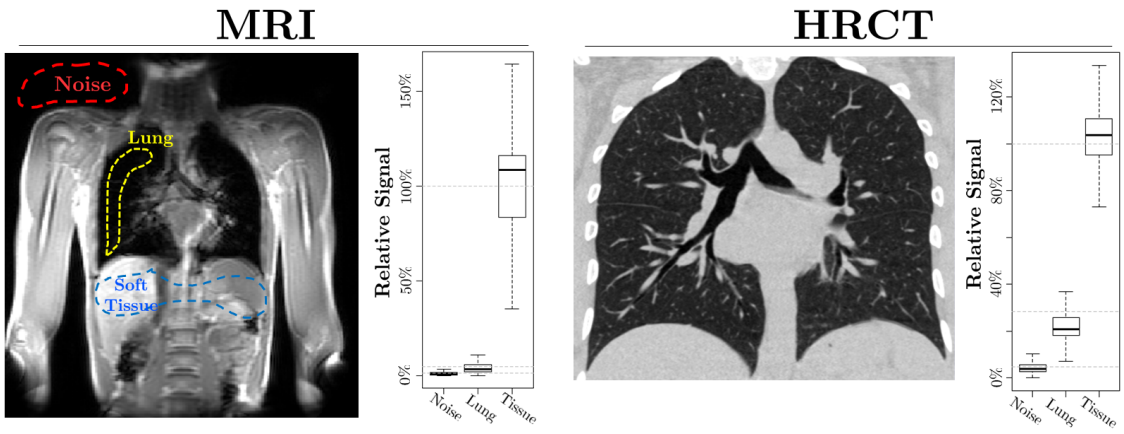

Figure 1.8: Measures of MRI and CT signal for Various Regions of Interest. The left image in a coronal MRI acquired at approximately FRC (voxel size = with a box plot showing the relative signal values for the indicated regions of interest (ROI's). To the right is a zoomed-in coronal high-resolution CT acquired at TLC and respective ROI box plot (voxel size = 0.3 x 0.3 x 0.75 mm^3, ROI's for CT not shown, but are similar to MRI). Signal measurements in each box plot are normalized to soft tissue. Both subjects in these images are healthy volunteers.

1.3 Introduction to Hyperpolarized Gas MRI and Dissertation Overview

Current research in pulmonary MRI is progressing quickly with the emergence of new methods for providing contrast, collecting data and reducing imaging time. In the early 1990's researchers at Princeton and Stony Brook recognized and adopted a unique imaging agent from the field of atomic physics which has become a revolutionary method of obtaining functional lung images using MRI – *hyperpolarized noble gases* [35].

1.3.1 Hyperpolarized Gas MRI

In standard proton MRI the magnitude of the detected signal comes from nuclear spin-alignment of a sample in the presence of a magnetic field. For field strengths used in medical imaging, the mismatch in number of nuclear spins aligned *with* versus *against* a magnetic field (and thus contribute to detectable signal) is on order of parts per million (ppm) according to Boltzmann statistics; hence the insensitivity of MRI. Hyperpolarization involves spin-polarizing a noble gas, either ^{3}He or ^{129}Xe in the case of this work[7], to have a much higher nuclear magnetic moment than is achieved in Boltzmann equilibrium, thus providing a greatly enhanced magnetic resonance signal. The prepared nuclear magnetization of these gases is so high (often 100,000 times greater than at Boltzmann equilibrium), that the *gas itself* can be imaged via the relatively insensitive modality of MRI. Because these noble gases are chemically inert, they can be safely inhaled by a subject, and the gas as it is distributed throughout the interior of the lung can be imaged. A comparison of standard proton MRI and HP gas MRI (^{129}Xe in this example) is given in Figure 1.9; the proton MRI shows body tissue whereas HP gas MRI shows the gas distribution within the lung interior. Notice that the gas distribution within the lung interior is relatively homogeneous, indicating uniform ventilation indicative of healthy lungs. Figure 1.10 shows similar images in a cystic fibrosis

[7]Hyperpolarized Krypton-83 is also emerging as a potential imaging agent of lung surface chemistry [36] though it is not addressed in this work.

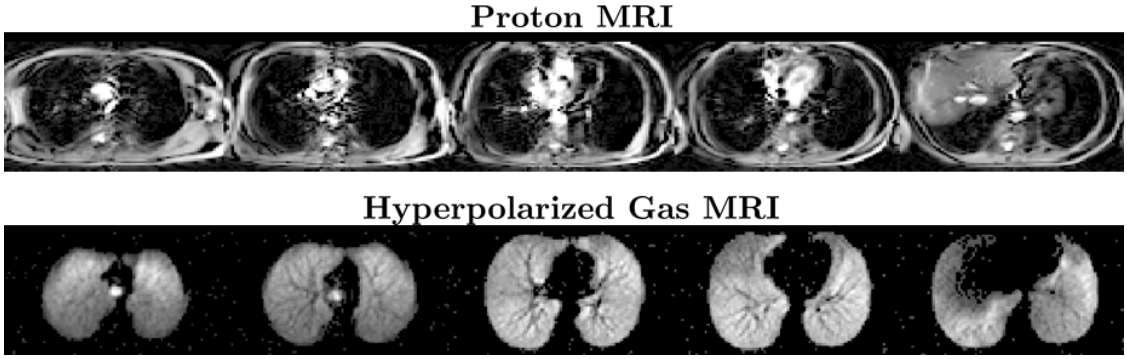

Figure 1.9: Comparison of Proton MRI with Hyperpolarized Gas MRI in a Healthy Volunteer. Five axial images (perpendicular to the head-to-foot axis) are given for a healthy volunteer imaged by proton MRI (top) and HP ^{129}Xe MR (bottom).

patient. Notice here that, unlike in the healthy volunteer, gas distribution is much more heterogeneous throughout the lung volume; the regions of poor ventilation are called *ventilation defects* and are a hallmark of HP gas MRI in diseased lungs [37, 38].

Hyperpolarized gas MRI provides exceptional, background-free contrast, can be imaged within tens of seconds (typical time of a breathold), and is a sensitive and quantitative measure of *both* lung structure and function which can non-invasively reveal unique information regarding these structure-function relationships *in vivo* [39]. This dissertation details a collection of adventures involving implementation of hyperpolarized gas MRI for investigation

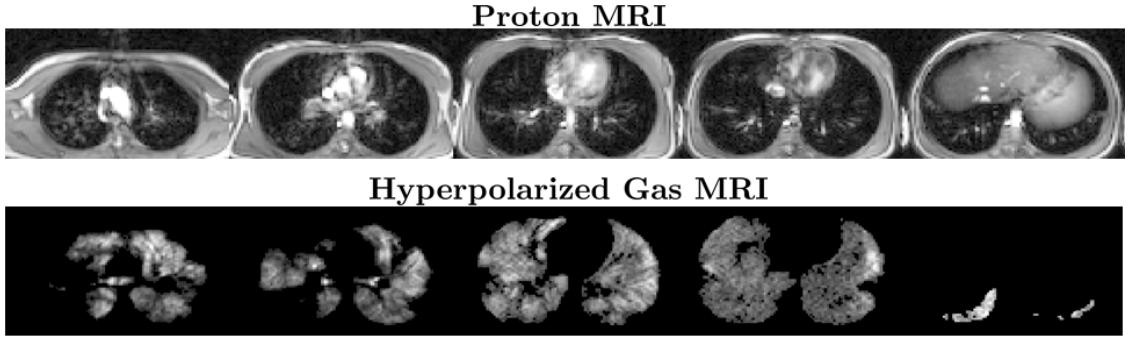

Figure 1.10: Comparison of Proton MRI with Hyperpolarized Gas MRI in a Patient with Cystic Fibrosis. Five axial images (perpendicular to the head-to-foot axis) are given for a healthy volunteer imaged by proton MRI (top) and HP ^{129}Xe MR (bottom).

of regional structure-function relationships in various lung pathologies.

1.3.2 Dissertation Overview

The author has been intricately involved with installation, implementation, optimization, and maintenance of hardware, software, and experimental protocols involved in hyperpolarized (HP) gas MRI. While this dissertation is meant to provide a detailed overview of the theory and methods of HP gas production, particular contributions of the author will be highlighted throughout. These include increasing achievable polarization in a dedicated ^{3}He hyperpolarizer by unique hardware upgrades, involvement in the construction of a ^{129}Xe hyperpolarizer, development of hardware/software necessary for HP gas imaging on a dedicated research MR scanner, development and implementation of a protocol for imaging HP gas *in vivo*, unique methods of HP gas image analysis, and novel imaging results which have advanced knowledge of lung structure-function relationships in several pulmonary abnormalities. Although the work presented here is categorically basic-physics research with motivation and application branching into biology and medicine, a major goal in developing these techniques is translation into the clinic [40].

The methods described in this work are motivated by a need for deeper understanding of lung structure-function relationships in general; to this end, a few specific pulmonary diseases have been investigated: asthma, chronic obstructive pulmonary disease (COPD), and cystic fibrosis (CF) in pediatric subjects. In this work I hypothesized that:

- **The ventilation defects revealed by hyperpolarized ^{3}He MRI in severe asthma can be identified on the level of bronchopulmonary segments (third-generation airway branches) and quantified to evaluate the efficacy of treatment by bronchial thermoplasty.** [41]

- **Hyperpolarized ^{129}Xe is a sensitive biomarker for alveolar airspace size in COPD.** [42]

- **Hyperpolarized ^{129}Xe is a sensitive measure of lung function in children**

with CF.

Now that motivation for the work at hand and major hypotheses have been presented (chapter 1), the fundamental, foundational NMR physics (chapter 2) and hyperpolarization theory (chapter 3) must be detailed. Methods of hyperpolarization *in situ* (chapter 4) and imaging techniques (chapter 5) and will be discussed followed by a brief prose on analysis of image data (chapter 6). Experiments have been carried out addressing the three major hypotheses, and their results are given in chapter 7. Finally, a concluding summary of the feasibility, efficacy, advantages, limitations, and future of hyperpolarized gas MRI of lung will be discussed in chapter 8.

Chapter 2

On the Phenomena of Nuclear Magnetic Resonance and Magnetic Resonance Imaging

> "These should give you the grounding you'll need in thermodynamics, hypermathematics, and of course microcalifragilistics."
>
> — Professor Frink, *The Simpsons*

This chapter is meant to provide the reader who may not be an NMR expert with an overview of the necessary physical principles on which the rest of the dissertation will be constructed: nuclear magnetic resonance (NMR) and magnetic resonance imaging (MRI). Although a necessary part of an otherwise incomplete thesis, it is understood that the material in this chapter has been intricately covered in standard texts by Abragam [43], Slichter [44], Ernst [45], Levitt [46], Gottfried and Yan [3], Fukishima and Roeder [47], Farrar [48], Haacke *et al.* [49], Bushberg *et al.*, [29], and others [50, 51, 52, 53, 54]. Any attempt to present the fundamental concepts of these texts with the clarity, completeness, and lasting impact achieved by their authors is a futile labor doomed to eternal failure and disgrace. Nonetheless, I shall make such an attempt in this chapter.

We shall see that nuclei of non-zero spin behave like tiny bar magnets which, under the

influence of an external magnetic field, tend to align with the field much like a compass needle aligns with the earth's magnetic field. However, spin as its name implies is a measure of angular momentum which, under the influence of an external field's torque, causes the spins to precess. This precession is detectable, and can be initiated by supplying 'tipping' pulses which torque spins out of alignment with the field. These spins can be spatially labeled using a precisely timed radiofrequency pulses and magnetic field gradients, and can be used to produce 3D maps of a sample's spin density.

2.1 Nuclear Magnetic Resonance

When placed in a magnetic field, certain atomic nuclei demonstrate the ability to absorb and re-emit electromagnetic energy whose frequency ω is proportional to the magnetic field strength B_0:

$$\omega = \gamma B_0 \tag{2.1}$$

Equation 2.1 is called the Larmor equation; the constant γ, called the gyromagnetic ratio, is a quantity inherent to a given atomic nucleus which dictates its nutation frequency at a given magnetic field strength – this phenomenon is called *nuclear magnetic resonance* (NMR). NMR is a consequence of an atom's nuclear spin $\mathbf{I}$ discovered by Stern and Gerlach [55] and described by Goudsmit and Uhlenbeck [56]. The first NMR experiment was performed by Isidor Rabi in 1938 [57, 58], Bloch and Purcell continued to expand the field in 1946 [59, 60], and today NMR is a staple of basic atomic and chemical structure exploration. Spin is an inherently quantum mechanical phenomenon, but it is most often introduced in a more intuitive fashion by treating an ensemble of nuclei as a rotating ball of charge. We will begin our discussion in the quantum regime to describe the behavior of a single spin after which the classical model of nuclear magnetic resonance will be described[1]

[1]Haacke's text [49] takes the top-down approach of beginning with the classical model then delving into the quantum theory.

Nucleus	Nuclear spin **I**	γ [MHz T^{-1}]	Natural Abundance [%]
^{1}H†	1/2	42.6	99.9
^{2}H	1	6.54	0.02
^{3}He†	1/2	32.4	0
^{13}C	1/2	10.7	1.1
^{17}O	5/2	5.77	0.04
^{21}Ne	3/2	-3.36	0.27
^{23}Na	3/2	11.3	100
^{31}P	1/2	17.3	100
^{83}Kr	9/2	1.63	11.5
^{129}Xe†	1/2	11.8	26.4
^{131}Xe	3/2	3.49	21.2

Table 2.1: List of commonly-studied nuclei in NMR [61, 62, 63, 64, 65]. Nuclei of interest for this work are indicated with a †. The gyromagnetic ratio is often expressed in Hz T^{-1} rather than rad T^{-1}, $\gamma = \frac{\gamma}{2\pi}$

2.1.1 The Quantum Model of NMR

The Hamiltonian of a nuclear magnetic moment $\boldsymbol{\mu} = \gamma\hbar\mathbf{I}$ in a magnetic field $\mathbf{B_0}$ is

$$\hat{H} = \boldsymbol{\mu} \cdot \mathbf{B_0} = \gamma\hbar\mathbf{I} \cdot \mathbf{B_0}, \tag{2.2}$$

and, for a magnetic field $\mathbf{B_0} = B_0\hat{z}$ has eigenvalues

$$E = -\gamma\hbar B_0 m_I. \tag{2.3}$$

Thus, for a spin-$\frac{1}{2}$ system, two energy states emerge – one for $m_I = -\frac{1}{2}$ spins aligned with the magnetic field ($\downarrow$) and one for $m_s = +\frac{1}{2}$ aligned against the magnetic field ($\uparrow$) :

$$E_{\downarrow} = -\frac{1}{2}\gamma\hbar B_0 \qquad E_{\uparrow} = \frac{1}{2}\gamma\hbar B_0 \tag{2.4}$$

The energy difference between these two states is therefore $\Delta E = \gamma\hbar B_0$, and by the Plank Relation $\Delta E = \hbar\omega$ we recognize that a transition between $\uparrow$ and $\downarrow$ energy states requires

$$\omega = \gamma B_0 \tag{2.5}$$

Note the absence of $\hbar$ here; according to the Correspondence Principle, this hints that we may adopt a classical interpretation of the resonance phenomenon without compromising potentially hidden quantum-mechanical behavior (section 2.1.2) [44, 54]. In the Heisenberg picture of quantum mechanics, [3] an observable $\hat{A}$ is related to its commutation with the system Hamiltonian $\hat{H}$ according to

$$\frac{d}{dt}\hat{A}(t) = \frac{i}{\hbar}[\hat{H}, \hat{A}(t)] \tag{2.6}$$

and can be used to calculate expectation values of the observables I_x, I_y and I_z using the canonical commutation relation for spin:

$$[\hat{I}_i, \hat{I}_j] = i\epsilon_{ijk}\hat{I}_k. \tag{2.7}$$

They follow

$$\frac{d\langle I_x\rangle}{dt} = \frac{i}{\hbar}[H, I_x] = \frac{i}{\hbar}\gamma\hbar B_0[I_z, I_x] = -\gamma B_0\langle I_y\rangle \tag{2.8a}$$
$$\frac{d\langle I_y\rangle}{dt} = \frac{i}{\hbar}[H, I_y] = \frac{i}{\hbar}\gamma\hbar B_0[I_z, I_y] = \gamma B_0\langle I_x\rangle \tag{2.8b}$$
$$\frac{d\langle I_z\rangle}{dt} = \frac{i}{\hbar}[H, I_z] = \frac{i}{\hbar}\gamma\hbar B_0[I_z, I_z] = 0 \tag{2.8c}$$

and can be more compactly written

$$\frac{d\mathbf{I}}{dt} = \mathbf{I} \times \gamma\mathbf{B}. \tag{2.9}$$

Equation 2.8c reveals that $\langle I_z\rangle$ is constant in time, but equations 2.8a and 2.8b are a pair of simultaneous differential equations of motion

$$\frac{d^2\langle I_x\rangle}{dt^2} = \omega^2\langle I_x\rangle \qquad \frac{d^2\langle I_y\rangle}{dt^2} = \omega^2\langle I_y\rangle. \tag{2.10}$$

Their solutions are [66]

$$\langle I_x \rangle = I_{x_0} \cos \omega t - S_{y_0} \sin \omega t \tag{2.11a}$$

$$\langle I_y \rangle = I_{y_0} \cos \omega t + S_{x_0} \sin \omega t \tag{2.11b}$$

$$\langle I_z \rangle = I_{z_0} \tag{2.11c}$$

From $\langle I_x \rangle$ and $\langle I_y \rangle$ we see that the magnetic moment vector $\boldsymbol{\mu}$ demonstrates rotational motion about the $\hat{z}$ axis. From Maxwell's equations (namely Faraday's equation, $\boldsymbol{\nabla} \times \mathbf{E} = -\frac{\partial \mathbf{B}}{\partial t}$), we infer that the presence of this changing magnetic field will produce an electromagnetic signal - not unlike a rotating bar magnet. Thus to perform NMR a detector must be positioned perpendicular to $\mathbf{B}$.

2.1.2 Classical Model of Spin Precession

The macroscopic behavior of an ensemble of quantum mechanical spins in a magnetic field can be intuitively described by modeling a spin sample as a single magnetic moment. Figure 2.1 illustrates the classical model of NMR beginning with foundational quantum-mechanical principles: an individual particle of non-zero spin obeys the canonical commutation relation for angular momentum – $[\hat{\mu}_i, \hat{\mu}_j] = i\hbar\gamma\epsilon_{ijk}\hat{\mu}_k$ – and thus behaves as a point mass rotating about its spin axis[2]. In the presence of a magnetic field, the magnetic moment $\vec{\mu}$ of a charged massive particle with non-zero spin will experience a torque according to $\vec{\tau} = \vec{\mu} \times \vec{B}$, much like a compass needle in the presence of earth's magnetic field. Like a spinning top under the influence of gravity [1], the magnetic moment will experience precession at frequency $\omega = \gamma B_0$ as shown in section 2.1.1.

Mathematically, this behavior is modeled using a single differential equation developed by Bloch [60]. In its simplest form, the *Bloch equation* describes spin precession as follows:

$$\frac{d\boldsymbol{M}(t)}{dt} = \gamma \boldsymbol{M}(t) \times \boldsymbol{B}(t) \tag{2.12}$$

[2]It is common practice in physics classrooms to use this analogy to describe quantum angular momentum for an *ensemble* of spins while noting it is an outright physical impossibility for an *individual* spin [67].

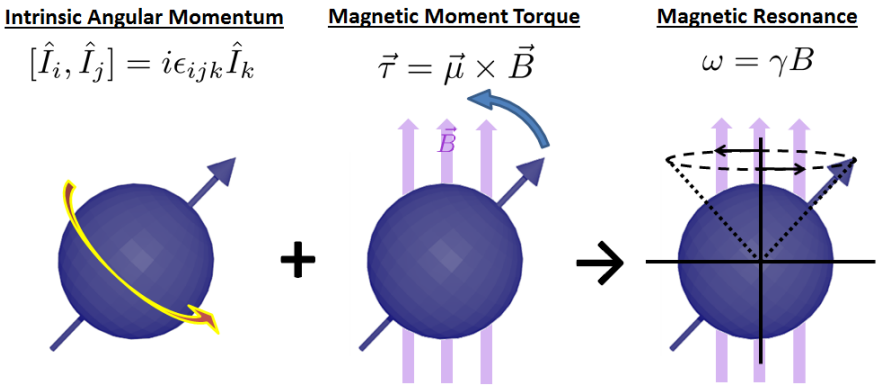

Figure 2.1: The classical model of nuclear magnetic resonance: a particle with intrinsic angular momentum under the influence of a torque will experience precession.

which, for $\boldsymbol{B}(t) = B_0\hat{z}$ simplifies to

$$\frac{d\boldsymbol{M}(t)}{dt} = \gamma\Big[(M_y B_0)_{\hat{x}} + (-M_x B_0)_{\hat{y}}\Big]. \tag{2.13}$$

This expression is identical to the Heisenberg equation 2.9.

From Lenz's Law ($\mathcal{E} = -\frac{\partial\Phi}{\partial t}$), if one were to place a coil of wire near a precessing magnetic moment (Figure 2.2), the changing magnetic flux would induce a voltage across the ends of the wire. According to the equations of motion in 2.8, this motion is sinusoidal with a frequency $\omega = \gamma B_0$. The relative amplitude of the measured signal depends on the angle θ between the magnetic moment $\boldsymbol{\mu}$ and the magnetic field $\boldsymbol{B}$ and the precession frequency ω:

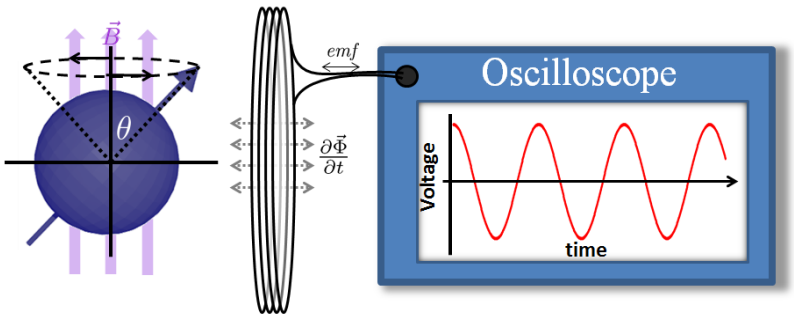

Figure 2.2: Precession of the magnetic moment presents changing magnetic flux within the coil. The voltage as displayed on an oscilloscope would oscillate sinusoidally.

$V_0 \propto \omega \sin(\theta)$, and due to the interaction of spins with each other, this angle θ quickly falls to 0 in time (discussed in section 2.1.4). The most conventional approach to NMR today involves using radiofrequency pulses, called B_1 pulses, to 'tip' the spins out of alignment with the B_0 field by a certain angle θ called the *flip angle* such that a detectable signal can be measured (detailed in section 2.1.5). The signal $S(t)$ detected by a spectrometer can be calculated using Faraday's law and follows

$$S = K\omega \sin\theta M_0 V_s \tag{2.14}$$

where K is an inhomogeneity factor (hereafter we let $K = 1$), M_0 is the Boltzmann magnetization of the sample, V_s is the volume of the sample, θ is the flip angle, and ω is the nutation frequency [68]. Signal is inherently stronger for nuclei with higher γ and/or Boltzmann magnetization M_0.

2.1.3 Net Magnetization of a Spin Ensemble

As discovered by Stern and Gerlach [55], spin angular momentum is quantized, and a spin-$\frac{1}{2}$ magnetic moment in a magnetic field can only be observationally aligned parallel to the magnetic field (low energy state) or anti-parallel to the magnetic field (high energy state). Spins will of course demonstrate preference for the low energy state giving rise to a slight mismatch in the eigenstate populations according to the Boltzmann factor:

$$P(E_i) = \frac{e^{-\frac{E_i}{kT}}}{\sum_i e^{-\frac{E_i}{kT}}} \tag{2.15}$$

which is used to evaluate the probability of finding a spin in either the high or low energy state in thermal equilibrium. Two spins aligned anti parallel to each other will necessarily result in a net cancellation of magnetization. The number of mismatched spins in a sample (the difference between the number of 'spin-up' nuclei $N_\uparrow$ and 'spin-down' $N_\downarrow$ nuclei) will therefore dictate its net magnetization. We define a quantity to express the fraction of spins

preferentially aligned with the field:

$$P \equiv \frac{N_\downarrow - N_\uparrow}{N_\downarrow + N_\uparrow} \tag{2.16}$$

called the *polarization* of the sample. Using equation 2.14 and the fact that $M_0 = PN\gamma\hbar/2$, we can express detected signal in terms of polarization[3]:

$$S = \frac{1}{2} N\gamma\hbar\omega P \tag{2.17}$$

Of critical importance here is the *linear dependence* of signal on ω and γ. Equation 2.15 can be used to calculate the polarization created in a spin-$\frac{1}{2}$ sample in thermal equilibrium due to the presence of a magnetic field:

$$P = \frac{e^{-\frac{\mu B_0}{kT}} - e^{\frac{\mu B_0}{kT}}}{e^{-\frac{\mu B_0}{kT}} + e^{\frac{\mu B_0}{kT}}} = \tanh(\frac{\mu B_0}{kT}) \approx \frac{\mu B_0}{kT} = \frac{hf}{2kT} \tag{2.18}$$

The approximation of $\tanh x \approx x$ is valid for $x \ll 1$ and is called the Curie regime in the context of spin polarization[4]. If we evaluate the polarization of an ensemble of hydrogen ^{1}H nuclei ($\gamma = 42.6$ MHz T^{-1}) at room temperature (T = 300 K) in the earth's magnetic field ($B_0 = 5{\times}10^{-5}$ T), the polarization is about $2{\times}10^{-10}$. That is, about 2 spins out of every ten billion are mismatched in the sample and contribute to a macroscopic magnetization M_0. In a sample of density ρ = N/V (number of spins per unit volume) we expect a net magnetization of

$$M_0 = \rho \sum_{m_s} P(E_i)\boldsymbol{\mu} = \frac{N\gamma\hbar}{V} \frac{\sum m_s e^{m_s\mu}}{\sum e^{m_s\mu}} = \frac{\rho\gamma^2\hbar^2 s(s+1)}{3kT} B_0. \tag{2.19}$$

This is called the Curie Law, and for a spin-$\frac{1}{2}$ system it simplifies to

$$M_0 = \frac{\rho\gamma^2\hbar^2}{4kT} B_0. \tag{2.20}$$

[3]We have allowed $K = \sin\theta = 1$ here.

[4]After Pierre Curie, not Marie Curie.

The detectable signal from a precessing volume of spins was given in equation 2.17; now using the Curie Law we find that the signal follows

$$S = \frac{\omega^2 N \gamma \hbar^2}{4kT} \tag{2.21}$$

Of critical importance here is the *quadratic dependence* of signal on ω (compare with equations 2.14 and 2.17) and the *linear dependence* on γ [69]. We are thus left with the following options for increasing the detectable magnetization of a sample in thermal equilibrium: increase the sample density ρ (not feasible in human tissue), decrease the temperature T (not feasible in human tissue), or increase the external magnetic field B_0 (feasible but expensive!)[5]. By increasing B_0 to a strength of 1.5 Tesla (a common field strength in commercial clinical MRI scanners) polarizations of 5×10^{-6} can be achieved – a factor of 10,000 above that of the earth's magnetic field. However, increasing the field strength can increase the prevalence of some undesirable behaviors of spins and their emitted signals; these effects are discussed in upcoming sections.

As an aside, the *noise* detected by a spectrometer is at least of order $N = \sqrt{4kT\Delta f R}$ where R is the circuit resistance (which is proportional to $\omega^{1/2}$), Δf is the bandwidth of the spectrometer, k is Boltzmann's constant, and T is the circuit temperature [70]. Thus we often refer to the *signal to noise ratio* (SNR) as an indicator of signal quality which is actually proportional to $\omega^{\frac{3}{4}}$ (or to $\omega^{\frac{7}{4}}$ in the case of samples in thermal equilibrium) [68], however, noise from the body itself should always surpass the intrinsic noise of a well-designed coil.

2.1.4 Relaxation Mechanisms

Spins in a magnetic field take time to achieve their Boltzmann magnetization M_0 described in section 2.1.3. This is called *spin-lattice* relaxation and is characterized by time

[5]Chapter 3 will discuss other methods of further increasing spin polarization, but these are non-equilibrium methods where Boltzmann statistics and the Curie Law do not apply.

constant T_1 in the following equation:

$$M_{\parallel}(t) = M_0(1 - e^{-t/T_1}). \tag{2.22}$$

$M_{\parallel}$ here denotes the magnetization of the sample parallel to the external field B_0. Figure 2.3 plots the magnetization of a spin sample as a function of time. This rate of recovery T_1 is unique to a sample's physical, chemical, and volumetric structures and can therefore be used to contrast materials. For instance, the T_1 of protons in cerebrospinal fluid is approximately 2400ms whereas the T_1 of those in fat is approximately 260ms in a magnetic field $B_0 = 1.5$T [29]. Thus, if an rf excitation is performed on a sample containing both CSF and fat a time $t = 500$ ms following the application of the B_0 field, the nuclear magnetization of protons in fat would be near Boltzmann equilibrium ($M \approx 0.85M_0$) whereas those in CSF would only be about 18% recovered. The signal emitted from fat would therefore be about 5 times greater than CSF. This is called T_1 weighting and is a common method of contrasting tissue in MRI.

When a sample's magnetic moment is excited by rf such that all spins begin nutation at the same phase in the transverse plane, it will precess according to the Larmor equation 2.1. Because of the constant interaction of spins with themselves in a sample, their relative phases will disperse, and the sinusoidal signal will decay in magnitude over time. This is called

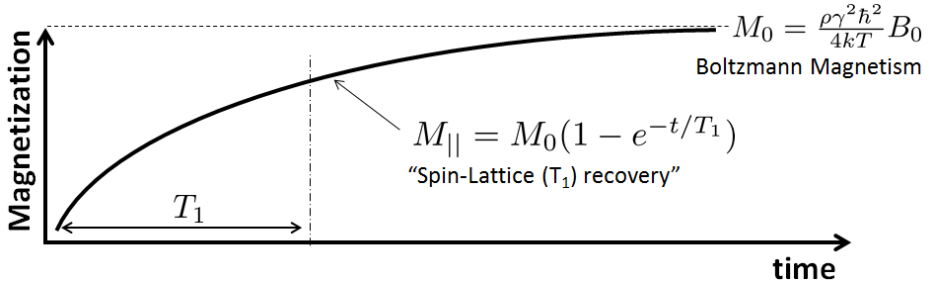

Figure 2.3: Plot of Spin-Lattice (T_1) Recovery. The magnetization of a sample $M_{\parallel}(t)$ approaches Boltzmann magnetism like a charging capacitor.

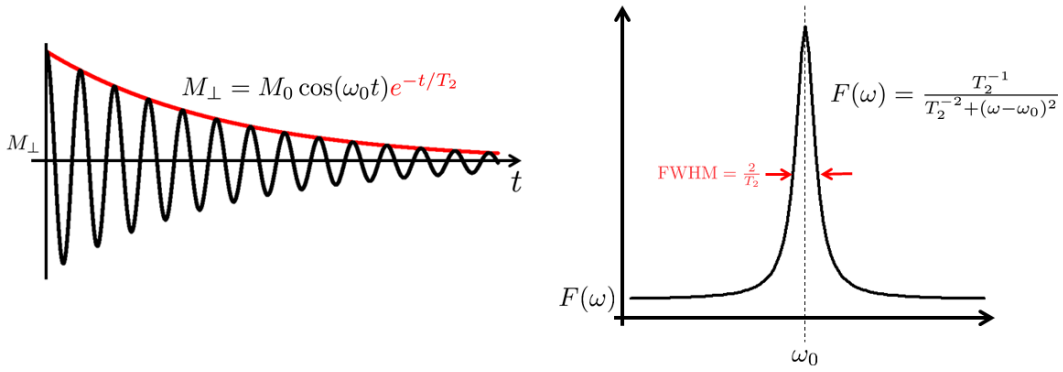

Figure 2.4: Plot of Spin-Spin (T_2) Decay. The magnetization of an excited sample $M_\perp(t)$ approaches zero like a discharging capacitor. Its Fourier Transform, given to the right, illustrates that linewidth increases with decreasing T_2.

spin-spin relaxation and is characterized by a time constant T_2 in the following equation:

$$M_\perp(t) = e^{-t/T_2}. \tag{2.23}$$

Figure 2.4 shows the decaying sinusoid seen following spin excitation: the Free Induction Decay (FID)[6]. Like spin-lattice recovery, the spin-spin decay rate T_2 is also unique to various samples and can also be used as a contrast mechanism in NMR and MRI. The frequency content of a decaying exponential follows a form of the Cauchy distribution called the the Lorentzian which is easily calculated from the FID using the Fourier Transform [46]:

$$f(t) = M_0 \cos(\omega_0 t) e^{-t/T_2} \quad \overset{FFT}{\Longrightarrow} \quad F(\omega) = \frac{T_2^{-1}}{T_2^{-2} + (\omega - \omega_0)^2}. \tag{2.24}$$

The Lorentzian distribution is effectively an answer to the question: How many spins are precessing at a given frequency? Note that a quicker decay (shorter T_2) will yield a broader lineshape (larger full width at half maximum, FWHM). Fourier Transforms and their utility in MRI will be given a fuller treatment in section 2.2.1. The magnitude of T_1 and T_2, depend

[6]The the signal decay of an FID is actually characterized by time constant T_2^* which is *not* characteristic of the sample but rather of magnetic field homogeneity and follows $\frac{1}{T_2^*} = \frac{1}{T_2} + \gamma \Delta B$. For simplicity here we assume perfect field homogeneity $\Delta B = 0$ and thus $T_2^* = T_2$. Effects from diffusion and susceptibility are also ignored in this prose.

on myriad properties of the sample and environment and are the chief mechanisms by which tissue contrast is created in MRI images.

2.1.5 Pulse NMR

In the early days of NMR, experiments would utilize a constant frequency B_1 field and a swept B_0 field to induce resonance within a sample [71, 72]. According to the Larmor equation $\omega = \gamma B_0$, sweeping B_0 necessarily sweeps the sample resonance frequency ω until it matches that of the B_1 field. At resonance, B_1 photons would be absorbed by the sample and a drop in B_1 transmission would be detected [59, 60]. This is called *cw* (continuous wave) NMR. In the late 1940's *pulse* NMR was developed in which a constant B_0 field (and thus a constant resonance frequency ω) is maintained, and a B_1 field oscillating at ω_0 is applied for a brief time period [73, 74]. This B_1 pulse induces transitions between upper and lower states 'tipping' the sample magnetization out of alignment with B_0 and into the transverse plane where the Bloch equation 2.12 can unfold and free precession can be detected.

Consider a spin in a static magnetic field B_0 as presented at t_1 in Figure 2.5. A second B_1 field is applied perpendicular to B_0 at time t_2 which oscillates at frequency ω. The B_1 frequency matches ω, therefore a component of the B_1 field is always perpendicular to $\vec{\mu}$. Because the moment $\vec{\mu}$ nutates about B_1 according to $\omega = \gamma B_1$, a B_1 experienced for time τ will 'flip' $\vec{\mu}$ by $\theta = \gamma B_1 \tau$. The perpendicular magnetization $M_\perp$ will then decay by T_2 relaxation and $M_\parallel$ by T_1 relaxation (acquired signal is of course proportional to $M_\perp$). This is the pulse-NMR experiment, often called a *ping* or a *pulse/acquire* experiment.

2.2 Magnetic Resonance Imaging

The foundations of NMR developed by Bloch, Purcell, Torrey, Hahn, and others evolved into one of the most powerful investigational tools of the 50's and 60's in materials science and physical chemistry. In 1973, Paul Lauterbur demonstrated spatial localization of spin densities by reconstructing a 2D image of two tubes of water in the presence of a magnetic

field *gradient* [75] – the first magnetic resonance image (MRI). MRI was rapidly developed in the mid-70's through investigations of unique pulse sequences [76, 77], emergence of faster computer processing techniques and the Fast Fourier Transform (FFT) [78], and application to clinical diagnoses [79]. Today, there are over 12,000 MRI scanners currently in operation in the United States [80].

Magnetic Resonance Imaging (MRI) is an applied field of NMR in which the measurements of various properties of spin ensembles can be spatially localized. On the surface, MRI involves little more than applying spatial magnetic field gradients instead of uniform fields following delivery of *rf* pulses: $\omega = \gamma B_0 \Rightarrow \omega(x) = \gamma B(x)$. If the magnetic B field can be mapped in space, $B \rightarrow B_z(x, y, z)$, then detected frequencies of an NMR sample can be spatially localized, $\omega(x, y, z) = \gamma B_z(x, y, z)$[7]. Delineating these frequencies mathematically

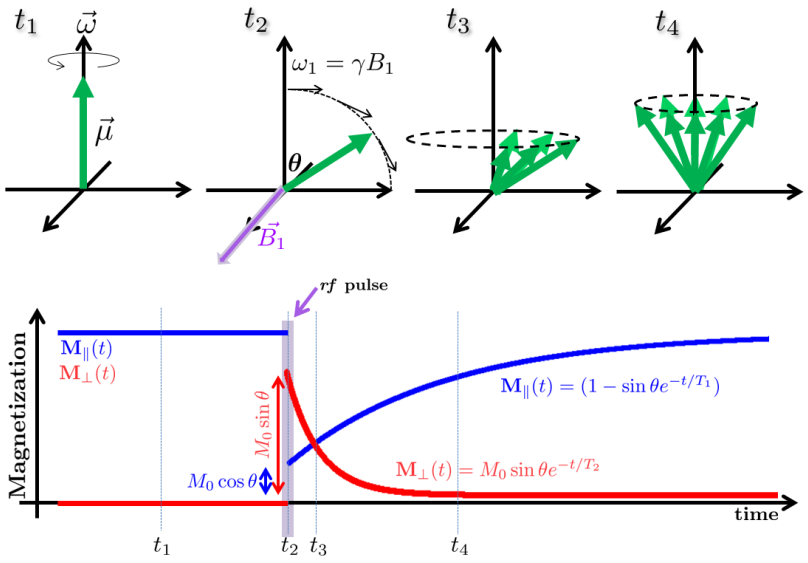

Figure 2.5: The Pulse-NMR Experiment (in the rotating frame) and Plots of Magnetization Parallel to B_0 ($M_\parallel$) and Perpendicular to B_0 ($M_\perp$) vs time. A magnetic moment at thermal equilibrium (t_1) experiences a 'tipping' B_1 pulse at time t_2. As individual spins dephase, $M_\perp$ decreases at a rate $1/T_2$. As individual spins realign with B_0, $M_\parallel$ increases at a rate $1/T_1$. Notice that even if perfect spin coherence could be maintained indefinitely, T_2 can never be observed to be longer than T_1.

[7]Here $B \rightarrow B_z$ is written explicitly to indicate that $B_y = B_x = 0$. It is the strength of B_z that must vary in space, not the direction of $\mathbf{B}$.

is precisely the function of the *Fourier transform*, and indeed no one can understand MRI without first understanding Fourier theory and *k-space*. As such, this is where our discussion will begin.

2.2.1 The Fourier Transform

The continuous Fourier Transform and inverse Fourier transform for a function $f(x)$ are defined

$$F(k) = \int_{-\infty}^{\infty} f(x)e^{-i2\pi xk}dx \qquad f(x) = \int_{-\infty}^{\infty} F(k)e^{i2\pi xk}dk. \tag{2.25}$$

Briefly, the Fourier transform is a mathemagical operation in which a function $f(x)$ is represented in terms of the various sinusoidal frequencies k of which it is composed, $F(k)$ (the variable k is generally reserved for *spatial frequencies* as appropriate here; *temporal frequencies* would be denoted by ω). Experimental NMR and MRI require transformation of discrete data $\{d_n\} = \{d_0, d_1, ..., d_{N-1}\}$; we thus define the discrete Fourier transform pair as

$$D_\nu = \sum_{n}^{N-1} d_n e^{-i2\pi n\nu/N} \qquad d_n = \frac{1}{N}\sum_{\nu}^{N-1} D_\nu e^{i2\pi\nu n/N}. \tag{2.26}$$

These discrete sums can be quickly calculated computationally using a Fast Fourier Transform (FFT) algorithm[8]. Note that while $\{d_n\}$ can be entirely real, its FFT $\{D_\nu\}$ will necessarily contain both real and imaginary components.

Figure 2.6 presents several different FIDs and their respective Lorentzian lineshapes showing real, imaginary, and modulus signals. Panel 2.6:A shows a typical FID and FFT. Panel 2.6:B shows the same FID as A but with a greater difference in frequency $\Delta\omega$; the Lorentzian is thus shifted further from ω_0 (the dotted line). Panel 2.6:C shows A with a decreased T_2; its Lorentzian is wider than A. Panel 2.6 is phase shifted relative to A; the Lorentzian modulus is unchanged, but the real and imaginary parts have shifted to reflect the different amounts of absorption and dispersion between them.

Panel 2.6:E contains only real information (thus the modulus equals the real component).

[8]The acronym FFT will denote any Fourier transform applied to discrete data in this dissertation.

This results in ambiguity in the 'progression' of phase in time, and two peaks of equal size and distance from ω_0 appear in the Lorentzian. This is perhaps most easily understood by recognizing that there exist 2 frequency components in the analytic-signal representation of the cosine: $\cos\theta = [e^{i\theta} + e^{-i\theta}]/2\pi$. Bernstein, King, and Zhou's text on MRI pulse sequences [81] provides an excellent discourse on the Fourier transform and its utility in MRI.

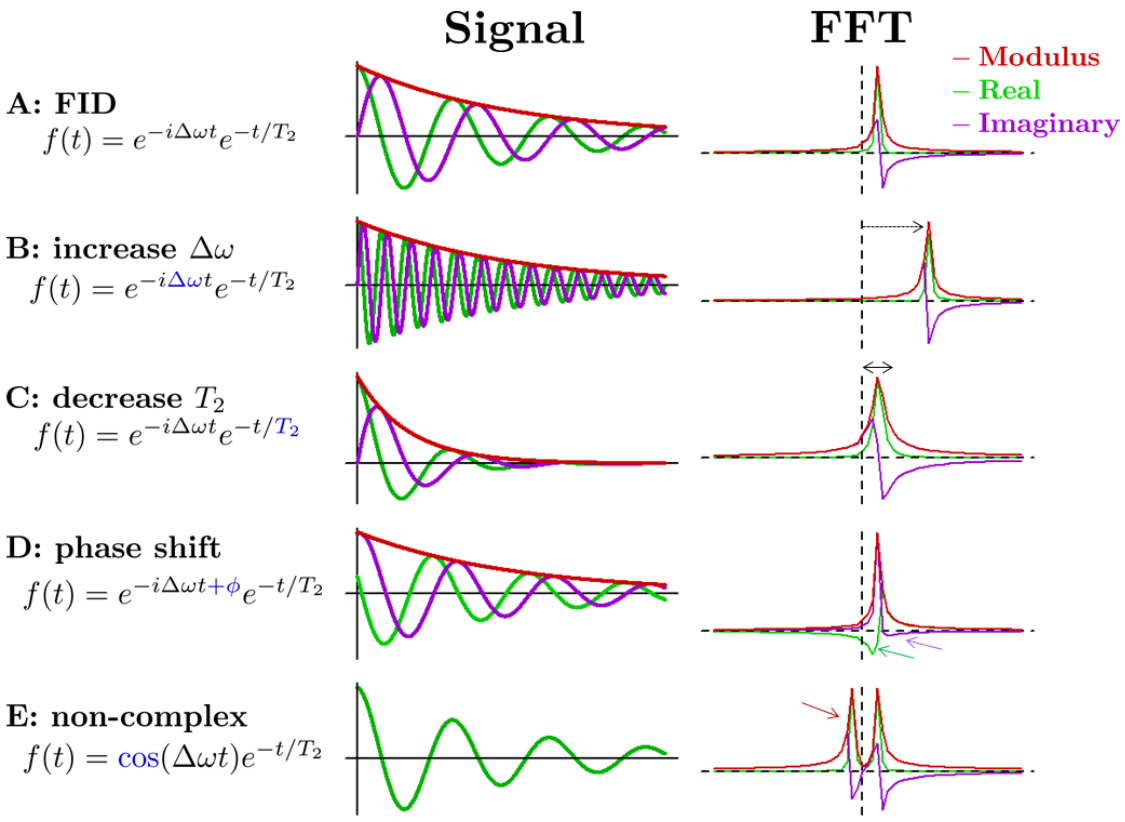

Figure 2.6: Examples of Various FID's and Respective Spectra. Red curves show function moduli; green and purple curves show real and imaginary parts respectively. **A:** A typical FID. **B:** The FID in **A** with a higher frequency $\Delta\omega$. **C:** The FID in **A** with a shorter T_2. **D:** The FID in **A** phase shifted by ϕ. **E:** The real part of **A** showing positive/negative frequency ambiguity. The vertical dotted line indicates ω_0.

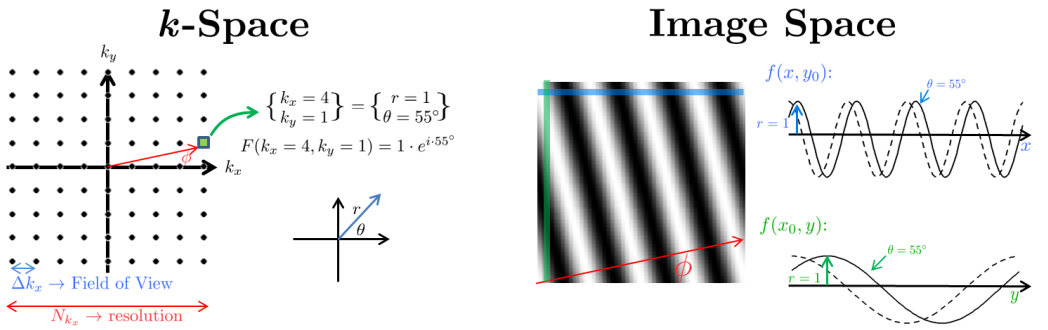

Figure 2.7: Illustration of K-space. A signal point in k-space is identified for this illustration, $F(k_x = 1, k_y = 4) = 1 \cdot e^{-i \cdot 55°}$. Considering only this point, the inverse Fourier transform of k-space is shown to the right – the Image Space. The image space is a 2D sinusoid whose frequency (number of cycles within the image space) is proportional to the distance from $k_x = k_y = 0$ and with phase-progression oriented at angle $\phi = \arctan \frac{k_y}{k_x}$. Plots of a single row ($f(x, y_0)$) and column ($f(x_0, y)$) are given to the right of the image; the dashed line indicates $\theta = 0$ reference.

2.2.2 *k*-space

The 2-dimensional Fourier Transform of a spatially varying function $f(x, y)$ yields a spatial-frequency varying function $F(k_x, k_y)$:

$$F(k_x, k_y) = \iint f(x) e^{-i2\pi(xk_x + yk_y)} dxdy \tag{2.27}$$

or, in discrete space

$$D_{\mu,\nu} = \sum_{n}^{N-1} \sum_{m}^{M-1} d_{m,n} e^{-i2\pi(n\nu/N + m\mu/M)}. \tag{2.28}$$

The coordinate system which defines an image $(\{x_1, x_2, ..., x_N\}, \{y_1, y_2, ..., y_N\})$ is called *image space*; analogously, the Fourier transform of an image defines a collection of frequency coordinates $(\{k_{x_1}, k_{x_2}, ..., k_{x_N}\}, \{k_{y_1}, k_{y_2}, ..., k_{y_N}\})$ called *k-space*. Figure 2.7 gives an illustration of how a single point in k-space translates to image space. The distance from $k_x = k_y = 0$ dictates a specific spatial frequency image; the complex phasor stored at the location (k_x, k_y) dictates the magnitude and phase of a 2D spatial frequency at that point. The image, as the inverse Fourier Transform, is the vector sum of spatial frequencies in k-space (Figure 2.8).

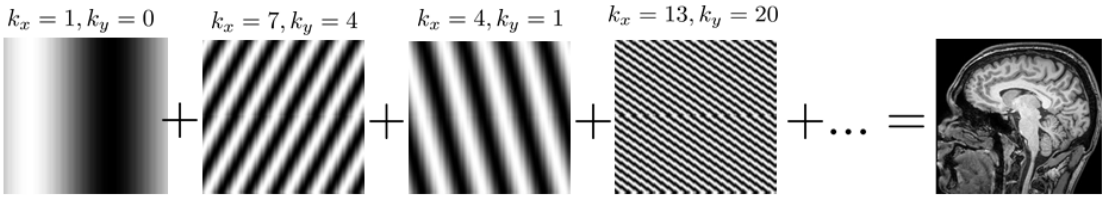

Figure 2.8: Illustration of Inverse Fourier Transform by Spatial Frequency Addition. The magnitude and phase of each point in k-space equates to a magnitude and phase of the spatial frequency image in image space. The inverse Fourier Transform is the vector sum of each frequency image.

Note that while an image $f(x, y)$ is real, its Fourier Transform $F(k_x, k_y)$ is necessarily complex; thus while an image contains $N_x \cdot N_y$ pieces of information its Fourier Transform contains $2 \cdot N_x \cdot N_y$. This redundant information arises from the fact that the Fourier Transform is an integral from *negative* k to *positive* k. The difference between frequency k and $-k$ is undefined in real image space. K-space is in fact Hermitian – half of the information is redundant. Importantly note that the spacing between discrete frequencies is equal to the inverse of the image field of view: $\Delta k = \frac{1}{\text{FOV}}$.

2.2.3 Spatial Encoding Gradients and the Gradient Echo Sequence

Consider a spin in a magnetic field during the application of a linear field gradient[9] $B(x) = G_x x$. If the gradient is applied for a time T, the spin will acquire phase according to

$$\phi = \int_0^T \omega dt = \gamma \int_0^T G_x(t) x dt = 2\pi x k_x \tag{2.29}$$

where we have defined a value

$$k_x(T, G_x) = \frac{\gamma}{2\pi} \int_0^T G_x(t) dt \tag{2.30}$$

[9]This discussion will take place in the rotating frame. Thus we ignore the B_0 component of the true field $B(x) = B_0 + G_x x$.

called the *k-space coordinate* (T is the gradient duration). In this example, we have defined our gradient in the $\hat{x}$ direction, but we note that the gradient direction determines the k-space coordinate location. If our spins are distributed with density $\rho(x)$ in the $\hat{x}$ dimension, the detected signal would follow

$$S = \int \rho(x) e^{-i\phi(x)} dx = \int \rho(x) e^{-i2\pi x k_x} dx \tag{2.31}$$

which is the Fourier transform of the spin density function. We now recognize k as a *spatial frequency* in the context of Fourier theory. These magnetic field gradients can be used to encode the received signals in k-space, and an inverse Fourier transform will then reveal the sample density distribution.

Consider a spin sample with spatial spin-density function $\rho(x, y, z)$. Imagine that we wish to excite *only* spins at a location z_0 within a certain thickness Δz. By application of a magnetic field gradient $G_z z$, the spins are spatially identifiable by frequency $\omega = \gamma B_z z$ and an *rf* pulse which follows $B_1(t) \propto \text{sinc}(\Delta\omega t)$ will only excite spins within the $\Delta\omega$ bandwidth. This is called *slice selection* and any signal obtained thereafter is known to come from within $z_0 \pm \Delta z$ (or from $\rho(x, y, z_0)$ for simplicity).

Consider that following slice excitation a linear gradient $B_z(y) = G_y y$ perpendicular to the slice axis is applied for a time τ. This is considered a *phase encoding* gradient, and from equation 2.30 we see $k_y = \gamma G_y \tau$. Consider then that we acquire signal during the application of yet another gradient orthogonal to both the phase encoding gradient and slice selection gradient $B_z(x) = G_x x$ (called a *readout* gradient); then $k_x = \gamma G_x t$. According to equation 2.31, the obtained signal would follow

$$s(G_y, t) = \iint \rho(x, y, z_0) e^{-i(\gamma y G_y \tau + \gamma x G_x t)} dx dy \tag{2.32}$$

or, substituting our definition of k from equation 2.30

$$s(k_x, k_y) = \iint \rho(x, y, z_0) e^{-i(k_x x + k_y y)} dx dy \tag{2.33}$$

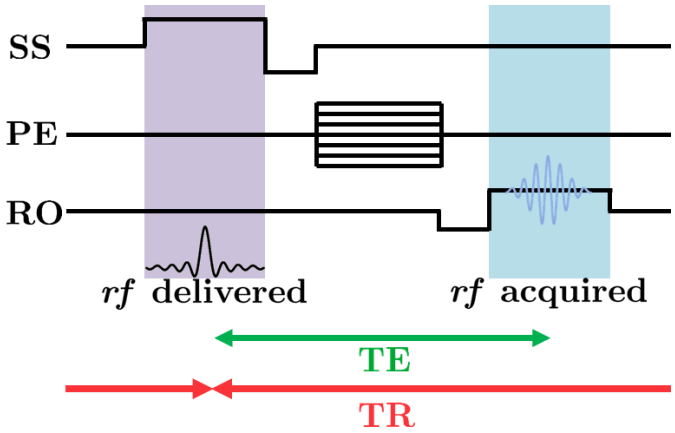

Figure 2.9: The Gradient Echo (GRE) Sequence timing. During application of the slice selection gradient an *rf* pulse excites spins within a specified bandwidth at a specified location. The phase encode gradient is applied to select a specified k_{PE} coordinate, and signal is acquired during the readout gradient which selects k_{RO} coordinates. The echo time TE is the time between *rf* excitation and acquisition; the repetition time TR is the time between *rf* excitations. One loop of a GRE sequence will return one line of k-space and must be repeated for each phase-encode dimension (dictated by desired field of view and resolution.

This is called the *imaging equation* and we immediately recognize that it is a Fourier transform of spin density ρ. This sequence of events – slice selection, phase encoding, and signal acquisition during a readout gradient – is known as the *gradient recalled echo* sequence (GRE). The creation of an image involves application of *rf* and magnetic field gradients so to adequately acquire the encoded signals in k-space which is then inverse-Fourier transformed. A generalized timing diagram for the GRE is given in Figure 2.9. [49]

2.2.4 Diffusion MRI

We noted in section 2.2.3 that a spin in the presence of a linear magnetic field gradient would acquire phase according to equation 2.29 wherein we assumed the spins to be stationary. Consider now that the spin is now allowed to diffuse by Brownian motion. The distribution of spins in space will give rise to a distribution of spin-phase such that the

probability of a spin having a certain phase ϕ follows a zero-centered Gaussian:

$$P(\phi) = \frac{e^{-\phi^2/2\langle\phi^2\rangle}}{\sqrt{2\pi\langle\phi^2\rangle}} \tag{2.34}$$

where $\langle\phi^2\rangle$ is the mean-square of all individual phase components [49]. This expression can be plugged into equation 2.31 to reveal the effect of spin diffusion on magnetization:

$$S = \frac{M_0}{\sqrt{2\pi\langle\phi^2\rangle}} \int e^{i\phi - \phi^2/2\langle\phi^2\rangle} d\phi = M_0 e^{-\langle\phi^2\rangle/2} \tag{2.35}$$

The mean square of ϕ follows $\langle\phi^2\rangle = \frac{1}{T}\int_0^T \phi^2 dt$, into which we substitute equation 2.29

$$\begin{aligned} \langle\phi^2\rangle &= \frac{\gamma^2 x^2}{T} \int_0^T \Big[\int_0^t G(t')dt' \Big]^2 dt \\ &= \gamma^2 2D \int_0^T \Big[\int_0^t G(t')dt' \Big]^2 dt = 2bD \end{aligned} \tag{2.36}$$

where we have substituted the Einstein-Smoluchowsky equation $x^2 = 2nDt$ ($n = 1$ for 1D diffusion) for the second line of equation 2.36, and we have defined a value b as

$$b = \gamma^2 \int_0^T \Big[\int_0^t G_x(t')dt' \Big]^2 dt \tag{2.37}$$

which is dependent only on the gradient waveform $G_x(t)$ [81]. From equation 2.36 we recognize that application of a gradient will effectively multiply the acquired signal magnitude by a weighting factor:

$$S = S_0 e^{-bD} \tag{2.38}$$

where S_0 is the signal of an image with no diffusion sensitizing gradient applied ($b = 0$)[10].

Figure 2.10.a shows the diffusion-weighted GRE timing diagram which we have adopted for diffusion experiments on hyperpolarized gases. Figure 2.10.b presents a detailed plot of

[10]Perhaps a more common approach to evaluating the effect of diffusion weighting is to solve the Bloch-Torrey equation [82] (the Bloch equation with an added diffusion term): $\frac{d\mathbf{M}}{dt} = (\text{Bloch terms}) + \nabla \cdot D\nabla\mathbf{M}$. The solution is identical to that of equation 2.38

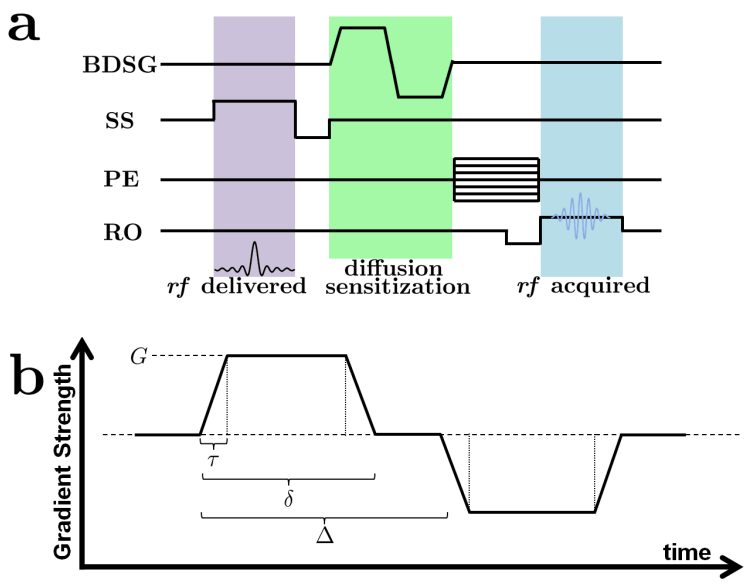

Figure 2.10: The Diffusion-Weighted Gradient Echo (GRE) Sequence timing diagram (a). Similar to Figure 2.9, this sequence includes a bipolar diffusion-sensitizing gradient (BDSG) which will reduce detected signal magnitude by e^{-bD}. Panel (b) shows the gradient waveform adopted for our experiments with HP gases.

the diffusion sensitizing gradient employed in HP gas diffusion experiments described in this work [83, 84, 85]. This waveform can be used to evaluate the magnitude of b which follows

$$b = \gamma^2 G^2 \Big[\delta^2 \Big(\Delta - \frac{\delta}{3}\Big) + \tau\Big(\delta^2 - 2\Delta\delta + \Delta\tau - \frac{7}{6}\delta\tau + \frac{8}{15}\tau^2\Big)\Big] \tag{2.39}$$

Generally, the timing parameters Δ, δ, and τ are left constant and G is varied to select appropriate b-values. The novelty of diffusion-weighted imaging lies in its ability to measure the diffusion coefficient of atomic nuclei *regionally* by solving equation 2.38 for D. Figure 2.11 illustrates creation of an *apparent diffusion coefficient (ADC) map* using a set of 9 diffusion-weighted images[11]. Because the gas is restricted by alveolar walls within the lung, the measured diffusion coefficient is 'apparent' indicating that the diffusion values measured are more representative of the parenchymal architecture rather than the intrinsic gas

[11]Since, according to $S = S_0 e^{-bD}$, only 2 b-values are truly required to calculate D, multiple b-values may seem unnecessary. In fact multiple b-values can reveal unique information related to alveolar micro-geometry (discussed in sections 5.5, 6.3.1).

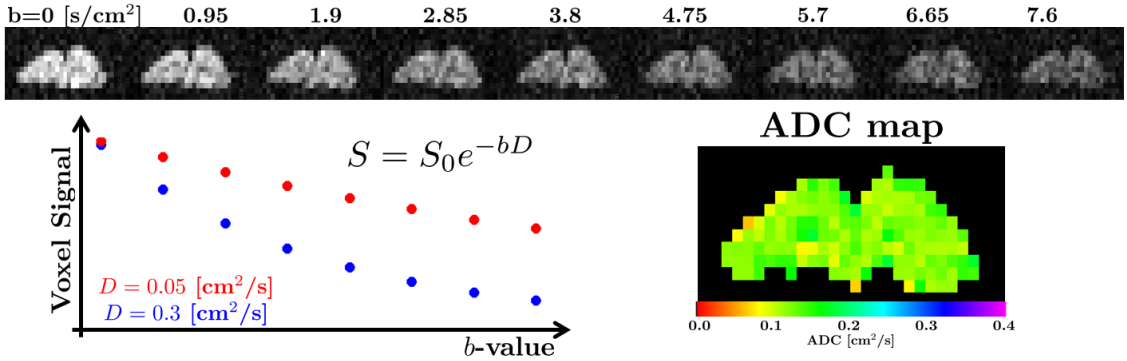

Figure 2.11: Example Data from a Diffusion-Weighted Sequence. At top are 9 images of hyperpolarized ^{3}He within an excised rabbit lung, each image acquired with a different b-value as noted above. Examples of individual voxel signal as a function of b-value are given in the plot highlighting relative signal decay for two different apparent diffusion coefficients (ADC). ADC's can be calculated for each voxel in the top images to produce an *ADC maps* as shown on the right.

diffusion length. This will be given a fuller treatment in sections 5.5, 6.3.1 and 7.3.

2.3 Summary

In this chapter a very cursory examination of the physical principles of NMR required to fully understand the novelty of the work has been presented. The next chapter will focus exclusively on the theory of hyperpolarization and preparation of noble gases for imaging. In turn Chapter 4 will detail the physical hardware and methods used to prepare hyperpolarized gases. Rest assured: while the preceding chapter contained substantial background perhaps considered unnecessarily remedial for an advanced dissertation, the discussed topics are critically necessary for the following chapters and will be referenced throughout.

Chapter 3

Theory of Hyperpolarization

> "I think we can put our differences behind us. For science. You monster."
>
> — GLaDOS, *Portal 2*

As discussed in section 2.1.3, the signal detected from a sample of precessing spin-$\frac{1}{2}$ nuclei is proportional to its nuclear-spin polarization: $S = \frac{1}{2}N\gamma\hbar\omega P$. For spins in thermal equilibrium polarization is in turn proportional to magnetic field strength B_0 as $P = \gamma\hbar B_0/2kT$. Thermal equilibrium polarizations are notoriously small (few parts per million, section 2.1.3), and MRI has been long known as a particularly insensitive imaging technique due to the inherent low signal from nuclear magnetic resonance. In this chapter, we will examine the theoretical foundations of 'hyperpolarization': preparing spin samples with *non-equilibrium* polarizations of more than 100,000 times Boltzmann polarization[1].

Hyperpolarized gases have been used for myriad applications including determination of neutron spin structure [86], measurement of various nuclear magnetic moments [87] and searches for permanent electric dipole moments [88], investigations of parity violations [89], and even quantum computing [90]. The most novel application of hyperpolarized gas production was realized by the Princeton / Stony Brook collaboration in 1994 with the first *in vivo* acquisition of an MR image of the lungs using hyperpolarized ^{129}Xe [35]. Hyperpolar-

[1] I will use the word 'polarization' to refer to an excess of angular momentum according to equation 2.16 and will explicitly state when other meanings are intended (e.g. light polarization).

ized gas MRI of the lung has led to great new understanding of lung structure and function by allowing for *regional* characterization of ventilation and perfusion [91].

There exist several methods for hyperpolarizing noble gas nuclei, and we have adopted the well-characterized method of *spin exchange optical pumping* (SEOP) [52] described in the following section. In short, SEOP involves spin-polarizing the single valence electron of alkali metal (AM) atoms using circularly polarized laser light; the electronic spin polarization is then imparted to the nuclei of a noble gas by collisional exchange mechanisms. SEOP has been studied extensively since the 1950's [92] culminating is several *de facto* resources addressing nearly every aspect of the process [50, 51, 52, 69, 93, 94, 95, 96, 97], and the interested reader would do well to examine these texts. An abridged discussion of optical pumping is given here with particular emphasis on more practical aspects of hyperpolarized gas production *in vitro*. This discussion will give particular attention to optical pumping of rubidium for spin exchange with ^{3}He or ^{129}Xe since they comprise all experiments performed in this work. A brief discussion contrasting hyperpolarization of ^{3}He and ^{129}Xe will be given, and chapter 4 will discuss the implementation of hyperpolarization on an experimental level.

3.1 Spin Exchange Optical Pumping

Spin-exchange Optical Pumping (SEOP) is a two-step process whereby (1) the valence electrons of an alkali metal (rubidium in this work) are selectively excited by circularly polarized σ_+ laser light to have a non-zero net spin polarization (optical pumping), and (2) the spin-polarized electrons impart their angular momentum to the nuclei of a target noble gas (spin-exchange). There are several other methods of producing hyperpolarized gases which are discussed in later sections; SEOP was used to hyperpolarize the gases used in this work and will thus be given a fuller treatment.

Property	Li	Na	K	Rb	Cs
Atomic Number	3	11	19	37	55
Stable Isotopes	^{7}Li, ^{6}Li	^{23}Na	^{39}K, ^{41}K, ^{40}K	^{85}Rb, ^{87}Rb	^{133}Cs
D_1 Transition Wavelength [nm]	670.8	589.6	769.9	794.7	894.4
D_2 Transition Wavelength [nm]	670.8	589.0	766.5	780.0	852.1
Operating temperatures [°C]	25	45	85	150	100-170

Table 3.1: Comparison of Alkali Metals for Optical Pumping. Only those with stable isotopes are presented. Data from [50, 96].

3.1.1 Rubidium in a Magnetic Field

Alkali metals have completely filled electronic shells with a single valence electron (making them hydrogen-like) and are thus well suited for selective electronic excitation experiments such as optical pumping. Any alkali metal can be optically pumped but some are better suited for hyperpolarizing noble gases (Table 3.1 presents several useful properties of the alkali metals for consideration). Rubidium is the alkali metal used in all experiments described here and has become the alkali metal of choice for hyperpolarization labs around the world due to its well-resolved D_1 transition wavelength (and availability of high-power lasers tuned to $\lambda_1 = 794.7$ nm), its low melting point and high achievable vapor pressure at moderate temperatures, its relatively high spin-exchange cross section, and its relatively low spin destruction cross section. Choice of alkali metal is often dictated by intended experimental conditions (working temperature, pressure, D_1 transition, well-resolved D_1 and D_2 transitions, etc...), but practical considerations aside, lighter AMs are better suited for lighter noble gases and heavier AMs for heavier gases based on relative spin-exchange and spin-destruction cross sections between AM/NG pairs [52][2].

Rubidium occurs naturally in two stable isotopes – 72.2% natural abundance ^{85}Rb ($\vec{I} = \frac{5}{2}$) and 27.8% natural abundance ^{87}Rb ($\vec{I} = \frac{3}{2}$)[3]. In order of decreasing strength, the Hamilto-

[2]Some groups have used 'hybrid' mixtures of alkali metals to greatly increase spin-up times and polarization of noble gases [98] with promising results.

[3]Technically, ^{87}Rb is unstable with a half-life of $t_{1/2} = 5 \times 10^{10}$ years [99]. Because this is roughly 4 times the accepted age of the universe, this footnote is decidedly unnecessary.

nian for an alkali metal in a magnetic field $B_0\hat{z}$ is [52, 96, 100, 101]

$$
\begin{aligned}
H = H_0 + H_{so} + H_{hf} + H_B = & \\
&= \frac{\mathbf{p}^2}{2m} - \frac{Ze^2}{r} && \textbf{(Bohr Model)} \\
&+ \frac{g_e Z e^2}{4m^2c^2r^3}\mathbf{L}\cdot\mathbf{S} && \textbf{(Spin-Orbit Coupling)} \\
&+ A\mathbf{S}\cdot\mathbf{I} && \textbf{(Hyperfine Interaction)} \\
&+ g_s\mu_B S_z B_0 && (B_0 - \textbf{e}^- \textbf{ interaction}) \\
&- \frac{\mu_I}{I} I_z B_0 && (B_0 - \textbf{nucleus interaction})
\end{aligned}
\tag{3.1}
$$

Bohr model energy states are separated by order 1eV, spin-orbit splittings are on order 10^{-4}eV (approximately H_0/α^2 where α is the fine structure constant), and hyperfine splitting is on order 10^{-6}eV (approximately m_e/M_{nucleus} times the spin-orbit strength). The order of Zeeman splitting is on order 10^{-10}eV (rf range) and is magnetic field dependent (about 0.5 MHz/Gauss for ^{85}Rb and 0.7 MHz/Gauss for ^{87}Rb) [102]. Figure 3.1 shows the atomic energy levels of ^{85}Rb indicating energy level splitting as different quantum-mechanical phenomena are incorporated. The energy levels for ^{87}Rb are nearly identical to those in Figure 3.1 except values of $\vec{F} = \vec{J} + \vec{I}$ would be one unit lower and thus Zeeman splitting would produce 2 fewer m_F states per hyperfine level.

3.1.2 Depopulation Optical Pumping

In the presence of a magnetic field, the AM electrons experience Zeeman splitting and electronic excitation requires the following selection rule be satisfied $\Delta m_F = \pm 1$. If this system is exposed exclusively to *circularly polarized* σ_+ light of AM D_1 transition energy, then by conservation of angular momentum m_F must necessarily increase by one unit: $\Delta m_F = +1$. Thus the only allowed transition is from $5s_{1/2}, m_F \rightarrow 5s_{1/2}, m_F + 1$. The excited state carries a lifetime of 10^{-8} - 10^{-9} s and electrons decay with restriction $\Delta m_F = 0, \pm 1$; thus on average each σ_+ photon results in $\Delta m_s = +1$. If the rate of photon absorption exceeds the

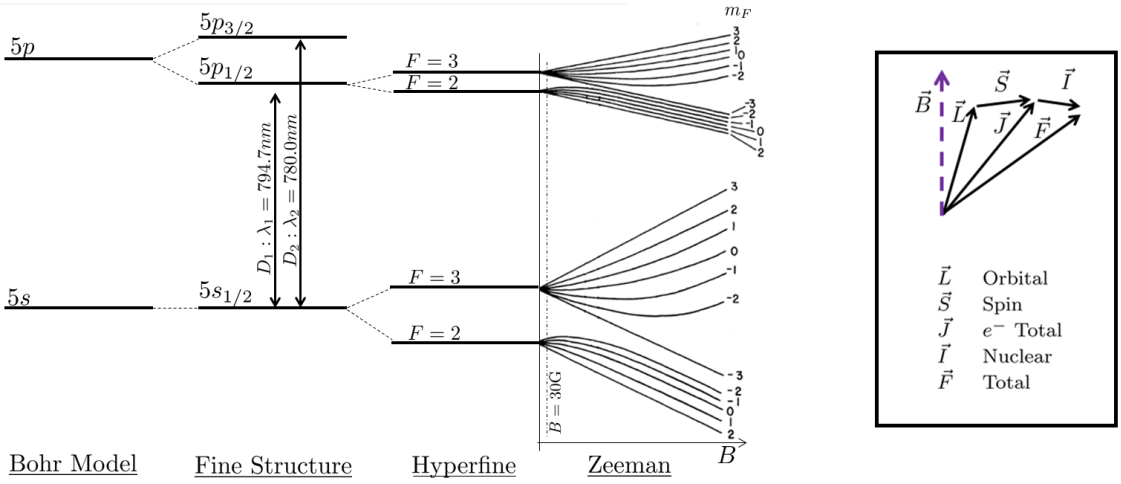

Figure 3.1: Low-Lying Energy Level Diagram of Rubidium-85 (not drawn to scale). Zeeman splitting is illustrated for increasing magnetic field B with $B = 30$G (a typical optical pumping field strength) shown explicitly (adapted from [50]). The box to the right provides a helpful reminder of angular momentum addition. [50, 94, 100]

rate of spin-state equilibration, then over time a non-equilibrium population of electrons will occupy the highest m_F spin state. Because electrons in this m_F can only *donate* angular momentum (desirable in context of spin exchange) it is considered the *polarized* electronic

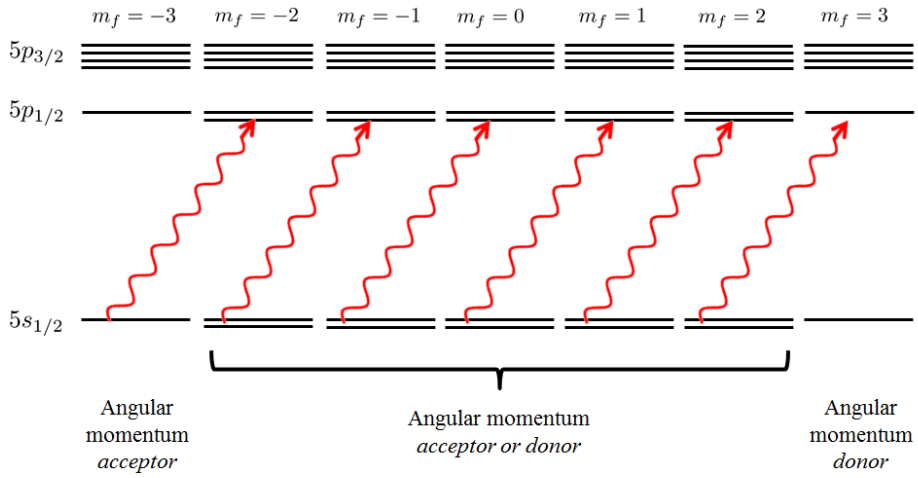

Figure 3.2: Optical Pumping Diagram for ^{85}Rb considering Hyperfine and Nuclear Zeeman Interactions. Note that for the purposes of spin exchange, the $m_F = -3$ state can only accept angular momentum from a noble gas nucleus whereas $m_F = 3$ can only donate angular momentum. ^{87}Rb would only have 5 m_F states: -2 - 2.

state (Figure 3.2). This is called *depopulation* optical pumping. [52, 96]

In our SEOP experiments rubidium in a pressurized glass cell is vaporized by external heating so an adequate vapor density is maintained for optical pumping may occur. The hyperfine structure of the Rb becomes unresolved due to both pressure broadening and Doppler broadening (order 10^{-5}eV) and may thus be ignored [52]. Optical pumping may be further simplified by ignoring the nucleus' contribution to Zeeman splitting (polarized state $m_F = F \rightarrow m_s = +\frac{1}{2}$, and unpolarized states $m_F < F \rightarrow m_s = -\frac{1}{2}$). This is considered acceptable since the OP polarization rate greatly exceeds the depolarization rate and thus achieves steady-state polarization quickly (10-20 ms) [95].

With these considerations we construct a simplified diagram of the low-lying electronic energy levels of the alkali metal involved in optical pumping: Figure 3.3. This two-state representation allows us to develop a simple mathematical description of optical pumping. The rate at which spins equilibrate between $m_s = -\frac{1}{2}$ ($m_\uparrow$) and $m_s = +\frac{1}{2}$ ($m_\downarrow$) states can be represented by Γ_{SD} (spin-destruction rate) and is considered equal for $m_\uparrow \rightarrow m_\downarrow$ and $m_\downarrow \rightarrow m_\uparrow$ transitions. The rate of σ_+ photon absorption is given by γ_{OP}. If the fractional

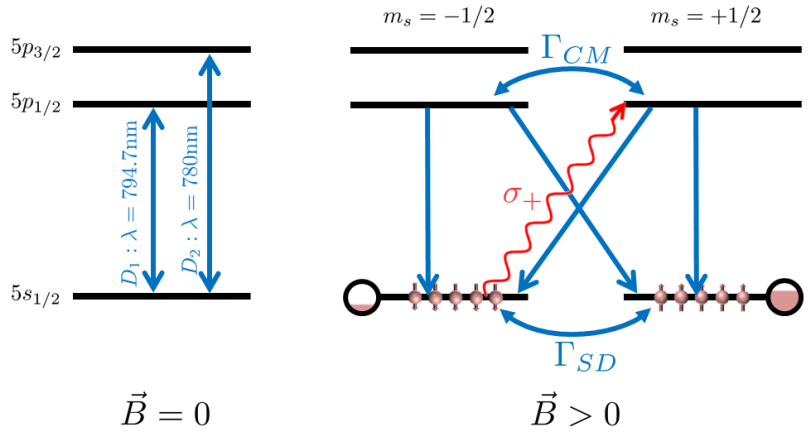

Figure 3.3: Optical Pumping Diagram ignoring hyperfine or nuclear Zeeman splitting. In the presence of a magnetic field $\vec{B}$ spin degeneracy is removed and circularly polarized σ_+ light can only excite electrons from spin-down $\downarrow$ to spin-up $\uparrow$ states. Collisional mixing between $5p_{1/2}$ spin states (Γ_{CM}) and spin destruction in the $5s_{1/2}$ states (Γ_{SD}) equilibrates the populations in the $\uparrow\downarrow$ states. As the $\downarrow$ state is depopulated, the electrons congregate in the $\uparrow$ state and polarization increases.

populations of $m_\uparrow$ and $m_\downarrow$ are ρ_+ and ρ_- respectively, then optical pumping may be described by a pair of simultaneous differential equations [95]:

$$\frac{d\rho_\pm}{dt} = \pm\Big(\gamma_{\rm OP} + \frac{\Gamma_{\rm SD}}{2}\Big)\rho_- \mp \frac{\Gamma_{\rm SD}}{2}\rho_+ \tag{3.2}$$

where $\rho_+ + \rho_- = 1$ necessarily. Using the definition of polarization (equation 2.16) the AM polarization is $P_{AM} = \rho_+ - \rho_-$ and has polarization rate

$$\frac{dP_{\rm AM}}{dt} = \gamma_{\rm OP}(1 - P_{\rm AM}) - \Gamma_{\rm SD}P_{\rm AM} \tag{3.3}$$

which has solution

$$P_{\rm AM}(t) = \frac{\gamma_{\rm OP}}{\gamma_{\rm OP} + \Gamma_{\rm SD}}(1 - e^{-[\gamma_{\rm OP}+\Gamma_{\rm SD}]t}). \tag{3.4}$$

Thus, maximum achievable alkali metal polarization occurs at $t \to \infty$ and is

$$P_{\rm AM} = \frac{\gamma_{\rm OP}}{\gamma_{\rm OP} + \Gamma_{\rm SD}}. \tag{3.5}$$

From this we recognize the need to *maximize* $\gamma_{\rm OP}$ and *minimize* $\Gamma_{\rm SD}$. Let us examine the optical pumping $\gamma_{\rm OP}$ and spin destruction $\Gamma_{\rm SD}$ mechanisms a little more closely.

First, the optical pumping rate $\gamma_{\rm OP}$ is defined

$$\gamma_{\rm OP}(\mathbf{r}) = \int \Phi(\mathbf{r}, \nu)\sigma(\nu)d\nu \tag{3.6}$$

where $\Phi(\mathbf{r}, \nu)$ is the photon flux and $\sigma(\nu)$ is the AM absorption cross section [103]. The natural electronic absorption cross section is a standard Lorentzian with linewidth Υ according to $\sigma(\nu) = \sigma_0(1+4(\nu-\nu_0)^2/\Upsilon^2)^{-1}$ [104]. In reality, the linewidth of $\sigma(\nu)$ is *pressure-broadened* by the noble gas within an optical pumping cell to nearly 1000× its natural linewidth (from $\Upsilon_{\rm nat} = 5.7$ MHz to $\Upsilon' = 18$ GHz/atm – hence the integration over all ν), and the peak absorption frequency is shifted by about 4.3 GHz/atm [105]. Photon flux (laser intensity per unit frequency) $\Phi(\mathbf{r}, \nu)$ must clearly be maximized, and the rapid development of diode laser

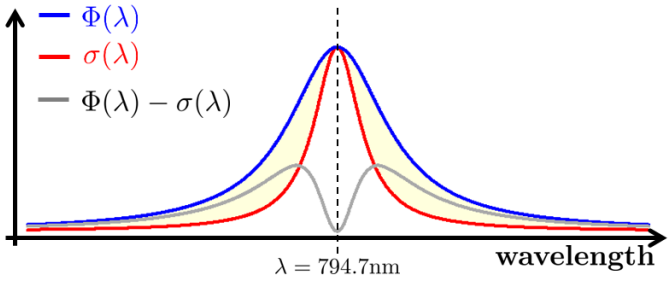

Figure 3.4: Photon flux Φ and AM absorption cross section σ vs wavelength λ. The difference between Φ and σ is given by the gray curve and indicates squandered photons which do not contribute to optical pumping.

technology in the 1990's has allowed for production of progressively higher hyperpolarized gas polarization and volume [106, 107, 108, 109]. Diode lasers have historically demonstrated very broad linewidths (often on order of a few nanometers or THz)[4], and this can be undesirable for efficient optical pumping. Figure 3.4 shows theoretical plots of laser photon flux $\Phi(\lambda)$ and rubidium absorption cross section $\sigma(\lambda)$. Broad laser linewidths lead to wasted laser power since off-resonance photons are not absorbed by rubidium, and linewidth-narrowing techniques such as Bragg diffraction feedback [110] can be used to achieve FWHM on order of a few tenths of nanometers.

Importantly, note that Φ is dependent on position, thus so is γ_{OP} and thus so is P_{AM}. As light is absorbed by the alkali metal, fewer and fewer photons are available to optically pump electrons which are a greater distance from the laser. In optically thick OP cells (high AM vapor density), photon flux follows [95]

$$\frac{\Phi(\nu, \mathbf{r})}{dz} = -\lambda^{-1}(\nu, \mathbf{r})\Phi(\nu, \mathbf{r}) \tag{3.7}$$

where[5]

$$\lambda^{-1}(\nu, \mathbf{r}) = 2[\mathrm{Rb}]\sigma(\nu)\rho_{\downarrow}(\mathbf{r}) = [\mathrm{Rb}]\sigma(\nu)[1 - P_{\mathrm{Rb}}] \tag{3.8}$$

[4]Recall the linewidth-bandwidth conversion formula $\Delta\nu = c\frac{\Delta\lambda}{\lambda^2}$. In the laboratory, it is more common to record laser flux vs wavelength λ rather than vs frequency ν.

[5]The factor $[1 - P_{\mathrm{Rb}}]$ is the *un-polarization* of rubidium – i.e. it is the fraction of spins in the unpolarized state.

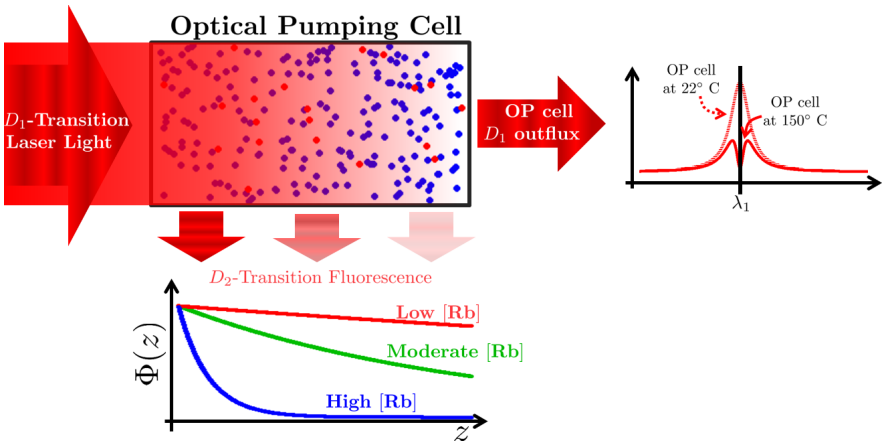

Figure 3.5: Illustration of Photon Flux Φ vs OP cell length z. As rubidium vapor density ρ_{Rb} increases photon flux decreases more quickly through the cell. Too low a vapor density leads to reduced γ_{OP} and inefficient optical pumping. Too high a vapor density leads to full light absorption near the front of the cell and leaves 'dark' regions near the back where γ_{OP} is near 0.

It is important to maintain a balance in alkali metal vapor density [Rb] such that optical pumping is optimized (Figure 3.5). Rubidium vapor density is of course temperature dependent and can be estimated by [111]

$$[\mathrm{Rb}] = \frac{10^{10.55-\frac{4132}{T}}}{1.38 \times 10^{-16} T} \tag{3.9}$$

From this discussion we've seen that some optimization of OP equipment will be necessary (methods of optimizing optical pumping efficiency will be discussed in section 4.1.6); generally speaking however, greater laser power and narrower emission linewidths will absolve many experimental sins when maximizing γ_{OP}.

Minimization of the spin destruction rate for the alkali metal electrons, Γ_{SD}, is also important in achieving maximum P_{AM}. Γ_{SD} is dependent on dozens of physical, chemical, and dynamic properties of the optical pumping process, but can be efficiently described as the sum of possible collisional interactions with an atomic species i (Rb - Rb, Rb - NG, Rb

- N_2, etc...):

$$\Gamma_{\mathrm{SD}} = \gamma_{\mathrm{SE}} + \gamma_{\mathrm{rt}} + \sum_i k_i N_i \tag{3.10}$$

where k_i is a binary collision coefficient and N_i is the species number density [112]. The rate of spin destruction due to spin exchange with the noble gas target is given by γ_{SE} (a desirable source of spin destruction), and γ_{rt} is the destruction rate due to *radiation trapping*.

One of the most critical methods of reducing the spin destruction rate Γ_{SD} is the introduction of *buffer gases* into the alkali-metal/noble-gas mixture to reduce γ_{rt}. When AM electrons decay from their excited state into the ground state they emit D_1 photons in random directions and with random polarization[6] which can rapidly depolarize other electrons and increase Γ_{SD}. A buffer gas can dramatically decrease Γ_{SD} by quenching the excited state electron fluorescence.

Buffer gases also mediate the collisional mixing of excited states thereby increasing OP efficiency γ_{OP}. Electrons in the $5p_{1/2}, m_\uparrow$ state can decay to $5s_{1/2}, m_\uparrow$ with probability $\frac{1}{3}$ or to $5s_{1/2}, m_\downarrow$ with probability $\frac{2}{3}$ resulting in a 33% photon efficiency for electron polarization. However, buffer gases facilitate equilibration of the AM electron excited states thereby equilibrating decay scheme probabilities and bringing photon efficiency up to 50% (denoted in Figure 3.3 by Γ_{CM}). Thus two photons are required on average to increase angular momentum by one unit according to this model[7]. Buffer gases also reduce the lifetime of the Rb excited states (from 28 ns to 1 ns) increasing γ_{OP} and facilitate pressure-broadening discussed earlier. The buffer gas used in the experiments described here is N_2 for its favorable properties and availability for OP [52].

[6] Light polarization here, not electronic spin ensemble polarization.

[7] When the rate of spin destruction is not negligible compared to the optical pumping rate (such as near cell walls where spin-destruction is accelerated), the nuclear contribution to Zeeman splitting cannot be ignored, and the 2 m_s simultaneous differential equations 3.2 blossom into 20 m_F equations. Wagshul and Chupp [95] have shown that this only slows the polarization time, but in fact the steady-state solution $P_{\mathrm{AM}}(t \to \infty)$ is unaltered.

3.1.3 Spin Exchange

Spin exchange is the process by which the alkali metal electronic polarization is physically transferred to noble gas (NG) nuclei (^{3}He or ^{129}Xe in this work): $e^-_\uparrow + \mathrm{NG}_\downarrow \rightarrow e^-_\downarrow + \mathrm{NG}_\uparrow$ [113, 114, 115]. In effect, there is a non-zero probability for angular momentum to be exchanged between the AM electron and the noble gas nucleus during collisions. If there exists an excess of Rb electrons in a polarized state then random collisions will statistically impart excess angular momentum to the noble gas nucleus. The rate at which polarization P builds in the NG nuclei follows

$$\frac{dP}{dt} = \gamma_{\mathrm{SE}}(P_{\mathrm{Rb}} - P) - T_1^{-1}P \tag{3.11}$$

and has solution [116]

$$P(t) = P_{\mathrm{Rb}}\frac{\gamma_{\mathrm{SE}}}{\gamma_{\mathrm{SE}} + T_1^{-1}}[1 - e^{-(\gamma_{\mathrm{SE}}+T_1^{-1})t}]. \tag{3.12}$$

Note the similarity of equations 3.11 and 3.12 to 3.3 and 3.4; of course this is expected since both AM polarization and NG polarization are modeled as two-state systems. Note also that maximum polarization $P(t \rightarrow \infty)$ is limited by P_{AM}; Figure 3.6 gives plots of maximum achievable polarization vs γ_{SE} for various T_1's. We have represented the noble gas spin-destruction rate by its respective time constant $T_1 = \frac{1}{\Gamma}$ which is a conglomerate of spin-destruction mechanisms characteristic of the OP environment within the glass OP cells. Similar to our discussion of P_{AM} optimization in section 3.1.2, we shall discuss the mechanisms of γ_{SE} and T_1^{-1} here for optimization of P.

Interaction of an AM atom with a noble gas nucleus is governed by the interaction

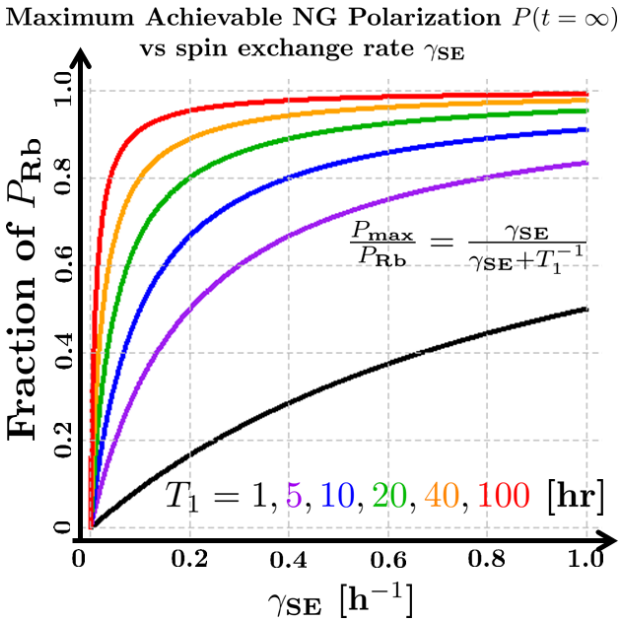

Figure 3.6: Plots of Maximum Achievable Polarization vs γ_{SE} for Various T_1's (expressed as a percentage of rubidium steady-state polarization P_{Rb}).

Hamiltonian[8]:

$$H_{SE} = \alpha \mathbf{K} \cdot \mathbf{S} \qquad \textbf{(magnetic-dipole interaction)} \tag{3.13a}$$

$$+ \varphi \mathbf{N} \cdot \mathbf{S} \qquad \textbf{(spin-rotation interaction)} \tag{3.13b}$$

where **S** is the electron spin, **K** is the nuclear spin of the noble gas, and **N** is the angular momentum of the alkali-metal-noble-gas pair [117] (Figure 3.7.a gives a cartoon representation of these angular momentum vectors). This Hamiltonian would be a perturbation added to the 'non-interacting' Hamiltonian of an AM atom given in equation 3.1. The magnetic dipole term is the mechanism by which spin exchange occurs [118] through Fermi contact interactions and is thus relevant in characterization of the spin exchange rate γ_{SE}. The spin-rotation term is the dominant source of intrinsic relaxation and thus shortens the T_1 of both

[8]There are actually several dozen interaction parameters we could consider, but these two are dominant for AM/NG spin exchange/destruction. A third term for Rb-Rb spin-exchange, $J(R)\mathbf{S}_i \cdot \mathbf{S}_j$, becomes necessary for hybrid AM mixtures and for describing regions near cell walls where rapid spin destruction occurs (not discussed here).

the alkali metal and the noble gas. The relative strength of each term is determined by α and φ, both of which are functions of AM electron/noble gas nucleus separation R. The strength of the magnetic dipole term 3.13.a follows from the Fermi contact interaction:

$$\alpha(R) = \frac{16\pi}{3}\frac{\mu_B\mu_I}{I}|\eta\phi(R)|^2 \tag{3.14}$$

The strength of the spin-rotation interaction leads to the formation of *van der Walls* molecules by which angular momentum is transferred between the AM and NG. It follows [119]

$$\varphi(R) = \frac{-mG}{\mu R}\frac{d|\phi(R)|^2}{dR} \tag{3.15}$$

where G is reflective of the strength of the spin-orbit interaction from the noble gas nucleus and the term $d|\phi(R)|^2/dR$ depends on the alkali metal atom. G has been reported by Walker and Happer [114] with the following values for helium and xenon: $G_{\mathrm{He}} = 0.00093$, $G_{\mathrm{Xe}} = 39$ [eVÅ]. The 4-order-of-magnitude difference between helium and xenon suggests that spin exchange by van der Walls molecule formation is much stronger in xenon than helium. Indeed it is the case that binary collision interactions are the dominant method of spin exchange for ^{3}He (spin exchange cross section $\sigma_{\mathrm{SE}} = 2.1 \times 10^{-8}$ [Å^2]) and formation of van der Wall molecules are dominant for ^{129}Xe ($\sigma_{\mathrm{SE}} = 1.6 \times 10^{-4}$ [Å^2]) [120, 121]; these mechanisms are illustrated in Figure 3.7, and a rigorous theoretical and experimental review of spin exchange and spin relaxation cross sections is given in Thad Walker's paper [117].

As can be inferred from the spin exchange cross sections given above, spin exchange by binary collisions is a notoriously slow process (interaction time τ on order of picoseconds) often taking several hours or sometimes days to achieve maximum noble gas polarization. The spin exchange rate for helium is proportional to AM concentration $\gamma_{^3\mathrm{He}} \propto \kappa_{\mathrm{RbHe}}[\mathrm{Rb}]$ where κ_{RbHe} is the spin exchange rate constant for Rb-He interactions. However this also means that spin destruction is a slow process as well and glass cells for optical pumping of helium can carry T_1's on order of tens of hours (hardware discussed in section 4.1.3). Van der Walls interaction times τ are on order of nanoseconds, so xenon can be polarized very

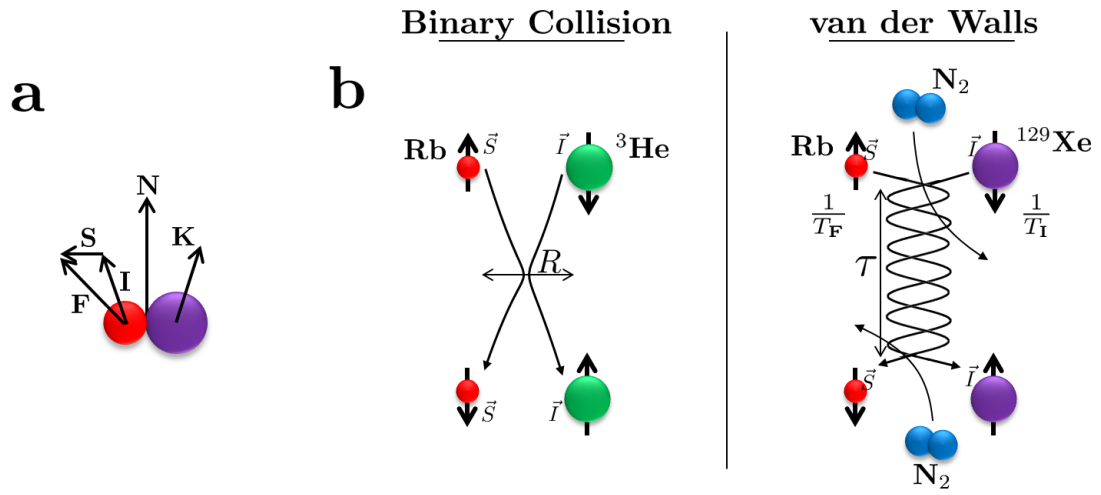

Figure 3.7: Panel (a) illustrates the various angular momentum vectors described by equation 3.13 [113]. Panel (b) gives an illustration of the two dominant spin exchange mechanisms for ^{3}He and ^{129}Xe. Fermi contact by *binary collisions* is dominant for ^{3}He and by creation of van der Waals molecules are dominant for ^{129}Xe. The molecule lifetime is given by τ and rubidium/xenon interaction rates are given by $\frac{1}{T_F}$ and $\frac{1}{T_I}$ respectively.

quickly (tens of minutes in 'batch mode' polarizers [122]; several seconds in 'flow-through' polarizers [106, 123]). Spin exchange for xenon is more complicated process than for helium for reasons discussed above and follows [112]

$$\gamma_{^{129}\text{Xe}-SE} = [AM]\left\{\frac{\gamma_{\text{AM-Xe}}}{[Xe]}\left(\frac{1}{1+0.275\frac{[N_2]}{[Xe]}}\right)+\langle\sigma\nu\rangle\right\} \tag{3.16}$$

where $\gamma_{\text{AM-Xe}}$ is the three-body interaction rate contribution, $\langle\sigma\nu\rangle$ is the binary collision cross section (velocity-averaged), and the value of 0.275 was calculated by Cates *et al.* [124]. Importantly, note that the polarization rate of xenon is inversely proportional to xenon concentration; thus a smaller [Xe]/[N_2] ratio will yield higher polarization. Of course this point is moot if a reduction in xenon concentration counterbalances the increase in xenon polarization (barring some method of xenon separation and extraction such as freezing [106]). Considering an 'apparent' xenon polarization defined as $P_{\text{app}} = \rho_{\text{Xe}}P_{\text{Xe}}$ where ρ_{Xe} is the fractional xenon concentration of a ^{129}Xe/N_2 gas mixture, the Nottingham group have shown

that a 50/50 xenon/nitrogen mixture provides optimum polarization per unit volume (23 W laser at 22 kPa) [125].

Sources of spin destruction for noble gas nuclei vary in strength between helium and xenon but can be summed into a few universal mechanisms[9]

$$\frac{1}{T_1} = \Gamma = \Gamma_{\text{intrinsic}} + \Gamma_{\text{wall collisions}} + \Gamma_{B_0\text{gradients}} + \Gamma_{\text{oxygen}} \tag{3.17}$$

The intrinsic relaxation of a gas is described by interactions of the gas with itself and is proportional to gas pressure; this has been well-characterized for both helium and xenon and places a fundamental upper limit on achievable T_1, $\Gamma_{^3\text{He}} = [^3\text{He}]/744$ hs^{-1}, $\Gamma_{^{129}\text{Xe}} = [^{129}\text{Xe}]/56$ amgt h^{-1}. Nuclei with quadrupolar moments demonstrate greatly accelerated spin-destruction rates; all noble gas isotopes except the spin-$\frac{1}{2}$ nuclei of ^{3}He and ^{129}Xe possess quadrupolar moments [65] and therefore have much shorter intrinsic T_1's. Collisions with the glass walls of the optical pumping cell depolarize nuclei at a rate $\Gamma = \frac{\beta \bar{v} S}{4V}$ where β is the probability of spin destruction for an individual collision, $\bar{v}$ is the rms nuclei velocity, S is the cell surface area, and V is the cell volume. OP cell wall collisions are the primary source of relaxation for monatomic gases such as helium. The strong contribution of cell wall collisions to noble gas relaxation has led many to develop coatings to protect the glass cell interior [127] and decrease the spin-destruction rate [128, 129], although to date, the precise mechanism governing wall relaxation is an unsolved problem. Nuclei experience spin destruction when traveling through inhomogeneous magnetic fields at a rate $\Gamma = D\frac{|\nabla \mathbf{B}|^2}{B_0^2}$ where D is the gas diffusion coefficient. Because ^{3}He has a higher diffusion coefficient than ^{129}Xe, it is intrinsically more susceptible to gradient relaxation, but our optical pumping cells are designed to confine the gas within the most homogeneous part of the B_0 field during SEOP. Hyperpolarized gas transport to the imaging suite for experiments generally results in a sizable loss of polarization because of this effect [130]. Finally, a gas mixture which has been contaminated with highly paramagnetic oxygen O_2 molecules will experience severe

[9] Thorough explanations of relaxation mechanisms are detailed in Newbury *et al.* [126] for ^{3}He and Brian Saam's chapter of [112] for ^{129}Xe.

relaxation: $\Gamma_{^3\mathrm{He}-\mathrm{O}_2} = 0.45[\mathrm{O}_2](299/T)^{0.42}\ \mathrm{s}^{-1}/\mathrm{amgt}$ [131], $\Gamma_{^{129}\mathrm{Xe}-\mathrm{O}_2,T=300\mathrm{K}} = 0.478[\mathrm{O}_2]$ amgt h^{-1} [112, 132]. As long as the plumbing used to fill OP cells are kept clean (often by nitrogen purging and rigorous leak testing) this is not a concern. However, hyperpolarized gases will necessarily encounter oxygen upon inhalation for *in vivo* experiments reducing T_1 to about 30 s [133].

All considerations described in this section have been taken into account in the design of dedicated hyperpolarizers for both ^{3}He and ^{129}Xe used for experiments described in this work. The following chapter will detail the design, construction, and operation of these hyperpolarizers for high-volume production of highly polarized helium and xenon. Spin exchange optical pumping is not the only method of noble gas hyperpolarization however, and it is prudent here to discuss the merits and limitations of other techniques.

3.2 Alternative Methods of Hyperpolarization

As stated above, spin exchange optical pumping is not the only method of achieving large non-equilibrium nuclear spin polarizations. Why then have we chosen to use SEOP and what alternatives may we consider? Generally, SEOP is the most cost effective method of hyperpolarizing the noble gases (in terms of signal per $), but alternative methods have demonstrated promise in hyperpolarizing other atomic nuclei as well. This section provides a very brief looks at some other methods of spin-polarizing nuclear for NMR studies.

3.2.1 Brute Force

One may postulate that directly pumping the ^{3}He or ^{129}Xe nucleus into a spin-polarized state would be the most straightforward method of hyperpolarization. Unfortunately, these transition energies exist in the energy-prohibitive UV range [91] and have not been attempted for large batch polarization. Perhaps it is possible to cool the noble gas to milliKelvin temperature in the presence of a large magnetic field B_0 so high polarization $P = \tanh \frac{\hbar\gamma B_0}{2kT}$ can be achieved. This is a very common technique for attaining high SNR in small volume

cryoprobes [134, 135]. Figure 3.8 shows a plot of ^{3}He polarization vs temperature for several different magnetic field strengths. Obviously, the dominant restriction for this method is

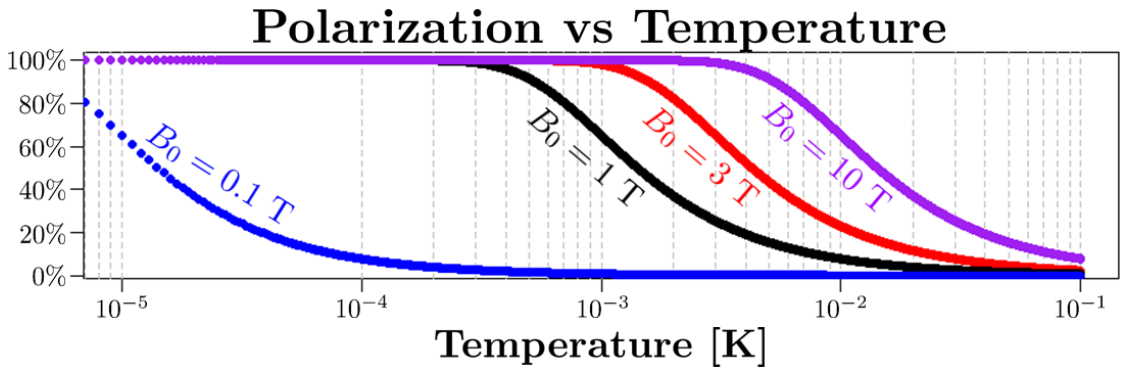

Figure 3.8: Plot of ^{3}He Polarization vs Temperature for Several Different Magnetic Field Strengths.

the extremely low target temperatures of milliKelvin, however it has been used to produce large quantities of HP ^{31}P and ^{129}Xe [135, 136] by first cooling the samples then heating to room temperature at a greater rate than the spin destruction rate [137]. This has not been demonstrated in ^{3}He.

3.2.2 Metastable Exchange Optical Pumping – (^{3}He only)

In 1963, research and development at Texas Instruments Incorporated (Dallas, TX) developed a method of polarizing ^{3}He nuclei by taking advantage of the metastable 2^3S_1 excited state of ^{3}He, a 3-step process called *metastable exchange optical pumping* (MEOP). First, electric discharge is used to excite/ionize electrons in a low pressure ^{3}He gas; a small fraction of these electrons (about 1 ppm) will subsequently decay into the 2^3S_1 metastable state. Radiative decay into the true ground state $2^3S_1 \rightarrow 1^1S_0$ is a forbidden transition, hence the extended lifetime[10]. Second, optical pumping is performed between the $2^3S_1 \rightarrow 2^3P_0$ states using 1083 nm σ_+ laser light to build spin polarization in the metastable

[10]This is true for the heavier noble gases as well, but extra relaxation mechanism from orbital angular momentum severely reduce the 2^3S_1 lifetime.

$2^3S_1(m_F = F = \frac{3}{2})$ hyperfine state. This polarization is quickly transferred to the corresponding *nuclear* metastable state due to efficient hyperfine coupling. Finally, spin exchange between the metastable nuclear state and the ground nuclear state yields excess ^{3}He angular momentum [138, 139], a process which is often expressed:

$$^3\mathrm{He}_\downarrow + ^3\mathrm{He}^*_\uparrow \rightarrow ^3\mathrm{He}_\uparrow + ^3\mathrm{He}^*_\downarrow \tag{3.18}$$

The major strength of MEOP is its quick polarization time [140]; however, it requires very low pressures of ^{3}He (often a few Torr) which must be subsequently compressed [141] so large quantities may be produced. Becker's group at University of Mainz has developed an impressive system which has been shown to produce 1 L/hr of ^{3}He at 50% polarization [142].

3.2.3 Dynamic Nuclear Polarization

Consider an electron-nucleus spin pair described by $|m_s, m_I\rangle$ in a high field at low temperature such that the 4 energy eigenstates (in decreasing-energy order $|\uparrow\uparrow\rangle$, $|\uparrow\downarrow\rangle$, $|\downarrow\uparrow\rangle$, $|\downarrow\downarrow\rangle$) are all well resolved. If microwave *rf* is applied to the system at the transition energy $\omega_{\downarrow\uparrow\rightarrow\uparrow\downarrow}$ (the *electron paramagnetic resonance* (EPR) transition) then a non-equilibrium polarization of $m_I = \uparrow$ will occur. *Dynamic Nuclear Polarization* (DNP) is a process by which microwave radiation is used to transfer angular momentum from electrons the nuclei of interest through cross relaxation, spin-state mixing, or thermal-mixing [143]. This is effectively a unique application of the Overhauser Effect [144] (electron-nuclear spin exchange)[11]; Abragam's report [145] gives an excellent and detailed description of the basic physics.

DNP is has been particularly successful at hyperpolarizing ^{13}C which can be used to enrich metabolic biomolecules such as pyruvate, glycine, aspartate, tryptophan, arginine, and others. These agents can be used as targets for studies of biosynthesis and metabolism in cells. DNP requires low temperatures (<4 K) and high field (several Tesla) both of which can be prohibitive challenges for the DIY hyperpolarizer community, but Oxford Instruments

[11] The Overhasuer effect was also Kaster and Bouchiat's inspiration for SEOP [92].

currently produces several commercial polarizers for DNP studies.

3.3 Summary

In this chapter we have examined the theoretical foundations of spin-exchange optical pumping and developed an experimental intuition for implementation *in situ*. It was shown that laser power must be maximized and linewidth minimized, Rb vapor pressure must be optimized for OP cell geometry, field gradients must be minimized, potential exposure to oxygen must be eliminated, OP mixtures must be optimized, etc. The next chapter will present methods we have developed to perform SEOP for MR imaging of lung. Knowledge of the theoretical framework of SEOP has allowed the author to make unique contributions to the hardware which increased achievable polarizations and have increased efficiency of the optical pumping process. These methods will be presented in the next chapter.

Chapter 4

Methods of Hyperpolarization

> "Ah, there's nothing more exciting than science! You get all the fun of sitting still, being quiet, writing down numbers, paying attention...science has it all."
> — Principal Skinner, *The Simpsons*

The theoretical foundation for hyperpolarization of noble gases presented in chapter 3 begs for a discussion of the more practical aspects of HP gas production. In this chapter, the hardware and methods used to produce hyperpolarized ^{3}He then for ^{129}Xe will be discussed. The author has been involved in design, construction and maintenance of polarizers for both noble gases each of which employ a standard 'batch mode' hyperpolarization design. The ^{3}He hyperpolarizer will be detailed first; because the polarizer designs are similar less attention will be given to the ^{129}Xe polarizer to avoid redundancy. A brief discussion of advantages and limitations of each setup will be given followed by a cursory examination of other common hyperpolarization techniques.

4.1 ^{3}He Polarizer Overview

The ^{3}He polarizer used for the experiments described in this work was originally constructed by Jason Woods, Brian Saam, Joe Dugas, and Mark Conradi [116]. The author

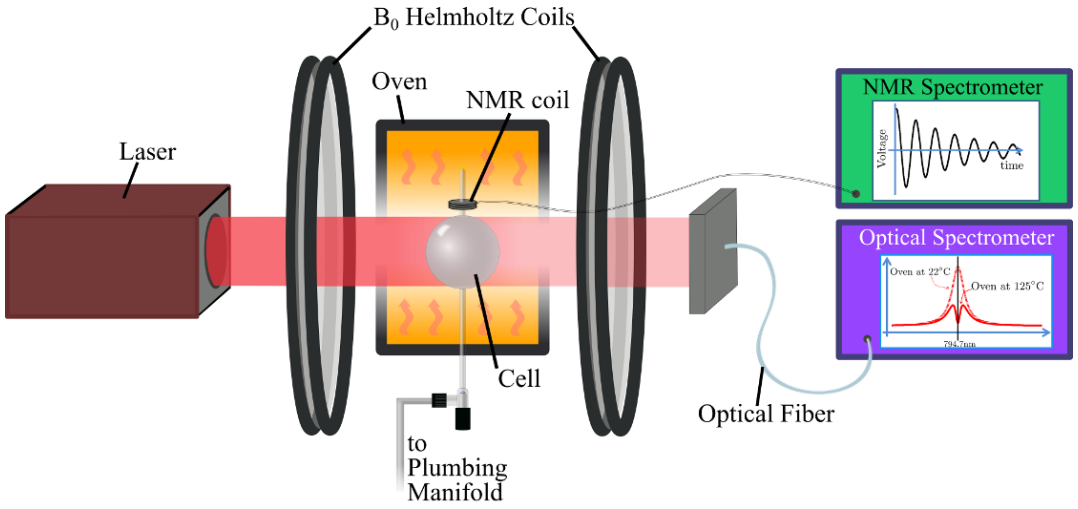

Figure 4.1: Diagram of a Hyperpolarizer (design here more representative of ^{3}He, but ^{129}Xe employs similar methods). High-power circularly-polarized σ_+ laser light tuned to λ_1 for rubidium illuminates the OP cell containing a small amount of rubidium and the pressurized noble gas / N_2 mixture. The cell is contained within a small oven for rubidium heating, and a small B_0 field is maintained by the helmholtz coils. Laser outflux (representative of Rb vapor density) is monitored with an optical spectrometer, and ^{3}He polarization is monitored by a homebuilt NMR spectrometer.

has refurbished this polarizer with upgraded laser and optical spectrometer, OP cell, dedicated plumbing manifold, and updated NMR monitoring. A diagram and a photograph of the polarizer are given in Figures 4.1 and 4.2 respectively. Production of HP ^{3}He begins with a steady supply of circularly polarized photons (Laser and Optics: section 4.1.1) which will spin-polarize the electrons of our alkali metal (Cell Oven and Rubidium Vapor Density: section 4.1.2) which is contained within a small magnetic field B_0. An optical spectrometer is used to measure the spectrum of the laser light following transmission through the optical pumping cell (Optical Pumping Cells: section 4.1.3), and a homebuilt NMR tuned to the noble gas frequency in the B_0 field is used to monitor the noble gas polarization over time (NMR spectrometer and SpinUp Monitoring: section 4.1.4).

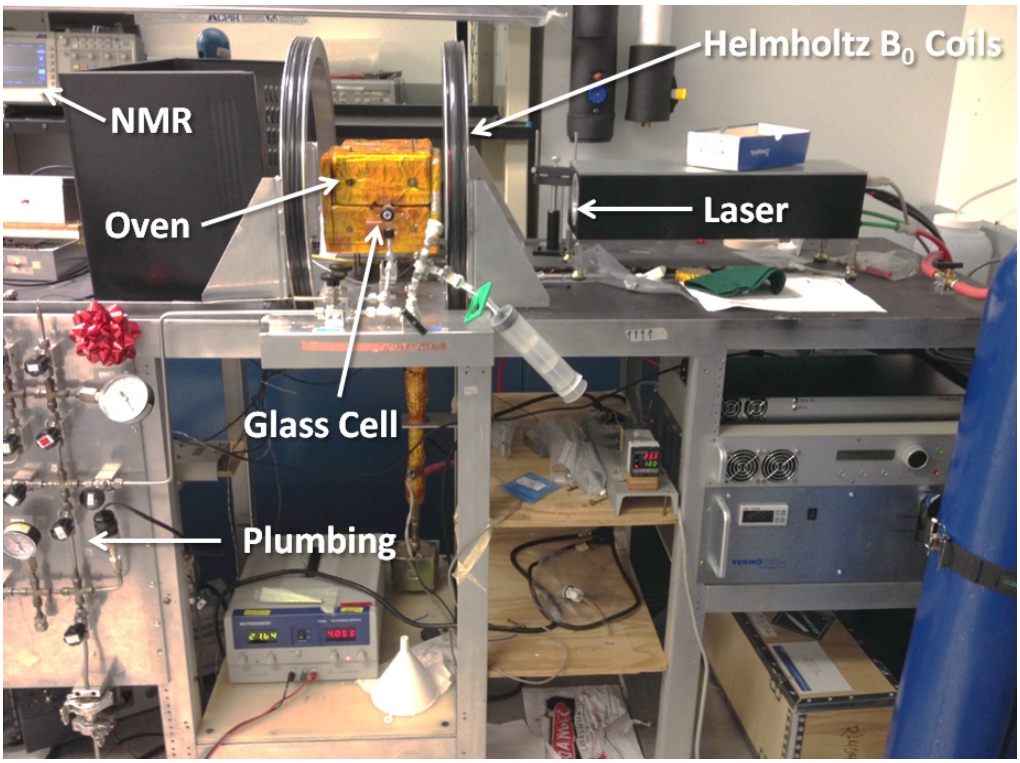

Figure 4.2: The ^{3}He Polarizer with Various Components Labeled. Note that the laser is on the opposite side to that shown in Figure 4.1.

4.1.1 Laser and Optics

The optical pumping laser must produce enough photons such that the rate of rubidium excitation exceeds the rate of rubidium relaxation and electron spin polarization is maintained for efficient spin-exchange. In general, greater D_1 resonant photon flux (more photons per second) through the OP cell is better: laser power must be maximized and linewidth must be minimized. Currently, the most powerful lasers available are diode array lasers which can lase many watts of power. The emission linewidths of diode lasers have historically been quite broad thus wasting a large percentage of emitted photons, but the rapid development of narrowing techniques such as Bragg diffraction crystals [110] have greatly improved efficiency. Diode lasers are electrically pumped by current flowing across a p-n junction which induces electronic transitions from the valence band to the conduction band of the gain medium [146].

Our ^{3}He pumping laser is a 100W DILAS (DILAS Diode Laser Inc, Tuscon, AZ) diode laser tuned to $\lambda = 794.7$ nm with an approximate FWHM = 0.8 nm = 380GHz (Figure 4.4.a). The Rb absorption linewidth is pressure broadened at 10 atm giving a bandwidth of approximately 180 GHz (0.38 nm at $\lambda = 794.7$ nm) indicating a 50% photon absorption efficiency for our experiments[1]. The efficiency is only an estimate however since it assumes Lorentzian profiles for both Φ and σ which, in reality, are slightly asymmetric. The laser must illuminate the entire cell volume so that no rubidium is unilluminated (or 'dark'). The laser emission axis must also be parallel to the B_0 field. The effects of off-axis laser emission relative to the OP field have been evaluated and characterized by Chann *et al.* [147] who found rubidium saturation polarization P_{AM} is reduced by a factor $\cos\theta$ where θ is the angle between B_0 and photon propagation direction.

4.1.2 Cell Oven and Rubidium Vapor Density

The rubidium within the cell must be vaporized so it can interact with ^{3}He for spin exchange; the optical pumping cell is therefore contained within an oven which can maintain a precise temperature during optical pumping. A balance must be maintained so that enough rubidium is vaporized to optimize the spin-exchange rate, but not so much that all laser photons are absorbed before traversing the entire cell leaving rubidium atoms unilluminated. The oven temperature is monitored using an RTD temperature sensor and Omega CN8592 temperature controller (Omega Engineering, Stamford, CN) which maintained temperature using the popular proportional-integral-derivative (PID) regulation algorithm [148]. However, the actual temperature inside the cell is substantially higher due to heating by the laser light. Figure 4.4 shows optical spectrometer measures of laser outflux following cell transmission immediately after turning the laser on (panel a) and approximately 3 minutes following (panel b). In this short time, the laser has substantially heated the cell and increased the rubidium vapor density leading to a greater number of absorbed photons and reduced laser

[1]The theoretical plots of $\Phi(\mathbf{x}, \nu)$ and $\sigma(\nu)$ presented in Figure 3.4 were created using these same bandwidths ($\Delta\lambda_{\mathbf{Rb}} = 0.38$ nm, $\Delta\lambda_{\mathbf{laser}} = 0.80$ nm).

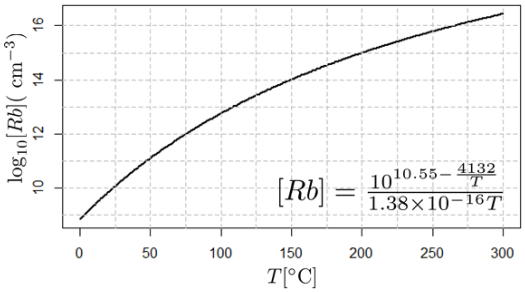

Figure 4.3: Logarithmic plot of Rubidium Vapor Density vs Temperature [111] (Temperature units in the equation are Kelvin; the horizontal axis has been converted to °C here.)

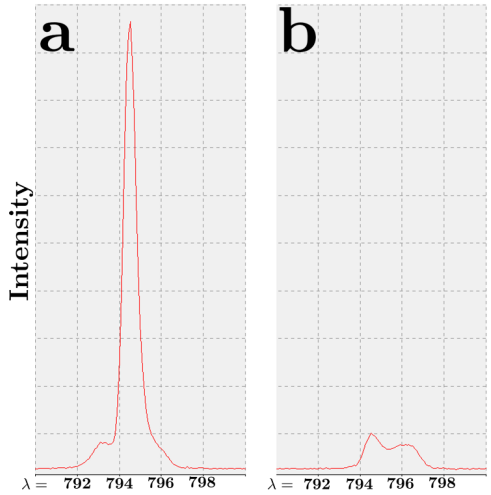

Figure 4.4: Laser Cell Outflux Intensity v Wavelength. Panel (a) shows laser outflux immediately after turning the laser on. Panel (b) shows laser outflux approximately 3 minutes following. If the pressure in the OP cell is reduced to 1 atm, the time for laser outflux to go from (a) to (b) is reduced to tens of seconds.

outflux. The precise oven temperature must be calibrated to that which maximizes achievable polarization. Because of the relative uncertainty in actual OP cell temperature, this is done experimentally by varying temperature for a series of spin-up datasets in order to evaluate which achieves maximum polarization (described in detail in section 4.1.6).

Note also in Figure 4.4 that the laser emission profile has shifted slightly toward longer wavelengths. Diode lasers are particularly susceptible to frequency shift due to heating of the p-n gain medium [104].

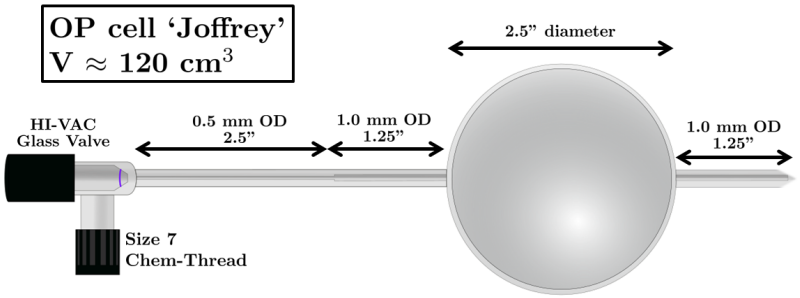

Figure 4.5: Diagram of Optical Pumping Cell Joffrey.

4.1.3 Optical Pumping Cells

Optical pumping cells for ^{3}He are designed according to several criteria: they must be able to withstand interior pressures of at least 10 atmospheres and temperatures of up to 200°C; surface-area-to-volume ratio must be minimized (as cell-wall interaction is a dominant relaxation mechanism), and the glass itself must not have paramagnetic properties. A cartoon diagram of the optical pumping cell ('Joffrey') used for our *in vivo* experiments is given in Figure 4.5. A spherical shape has been chosen to minimize surface area to volume thereby minimizing relaxation area within the glass. The cell is made of Pyrex® glass (Corning Incorporated, Corning, NY) – a borosilicate glass commonly used for optical pumping cells due to its strength and high tolerance to stark temperature changes [149]. As mentioned in section 3.1.3 depolarization due to gas collision with the glass cell walls are a principle source of relaxation, and it is currently speculated that ferromagnetic impurities within the glass are the culprit mechanism [150]. The fact that OP cell T_1 is dependent on cell orientation within the meager optical pumping field [151] and that T_1 can be significantly reduced by high-field exposure [152] is strong evidence for the ferromagnetic impurity theory. These relaxation effects can be reduced by *degaussing* a cell – a process of removing any potential glass magnetization by exposing the cell to a strong oscillating magnetic field. Joffrey has consistently demonstrated an acceptable T_1 (section 4.1.5) and thus has never been degaussed, but other OP cells used for hardware and sequence testing are always degaussed prior to polarization (Figure 4.6) since they are consistently exposed to the high magnetic

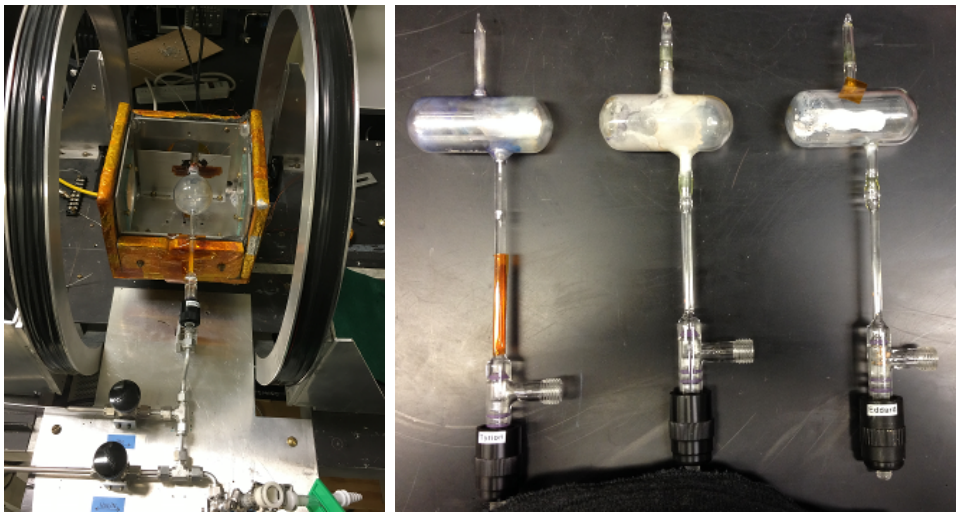

Figure 4.6: Photographs of OP cell Joffrey in the OP oven (left) and of other 'sausage'-shaped cells used for hardware and sequence testing in the 3T magnet (right).

field of the MRI scanner (3 Tesla). It has been found that degaussing consistently increases T_1 by a factor of 2-3.

4.1.4 NMR spectrometer and SpinUp Monitoring

The gyromagnetic ratio of ^{3}He is $\gamma = 3.24$ [kHz / Gauss], and the B_0 field is approximately 31 Gauss; thus the resonant NMR frequency of ^{3}He in an OP cell is very near $f = 100$kHz. Therefore the polarization of ^{3}He can be monitored *in situ* using simple DC electronics - no *rf* circuitry required![2] The NMR electronics used here were originally designed and built by Mark Conradi and Brian Saam [153], and have been updated by the author.

A basic diagram of an NMR spectrometer is shown in Figure 4.7 [153, 154]. A 100kHz clock signal is gated by the pulse generator to provide an approximately $50\mu s$ pulse amplified to $V_{pk-pk} = 5V$. The amplified pulse passes through the crossed diodes to the tuned circuit for excitation (coil inductance L = 900 μH). The received NMR signal is quite small and does not pass the crossed diodes [155]; it proceeds through the receiver amp to the phase

[2] I will however still refer to the 100kHz signal as *rf* in the context of transmitted/received **E** or **B** fields.

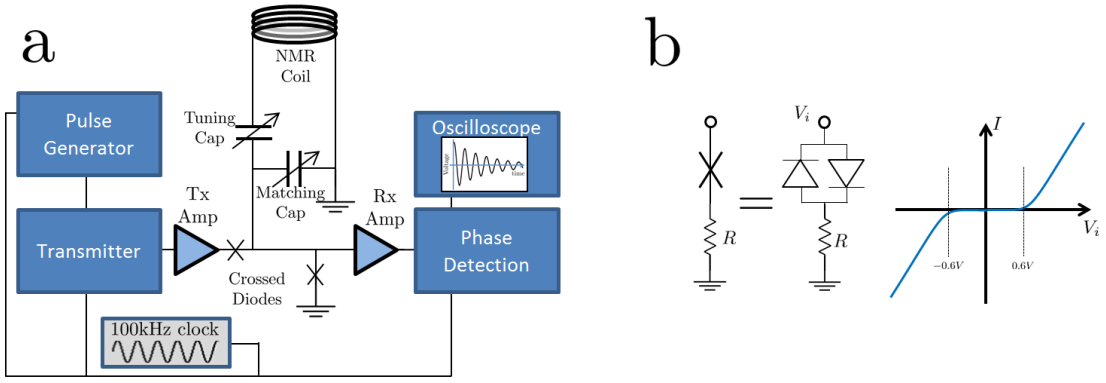

Figure 4.7: NMR spectrometer Diagram (a). Behavior of crossed diodes is shown in panel b. Note that this diagram is generalized; our system does not include a tuning capacitor as shown.

detector then to a monitoring unit such as an oscilloscope. Crossed silicon diodes are a passive component which ideally demonstrate zero impedance for $|V_i| > 1.2V$ (i.e., during transmit) and infinite impedance for $|V_i| < 1.2V$ (i.e., during receive); this voltage threshold can be increased by placing more crossed diodes in series (Figure 4.7.b).

Originally, the pulse generator was triggered by a push button mounted to the front panel of the chassis. Because ^{3}He polarization is a lengthy process often requiring overnight polarizer operation, automatic polarization monitoring is desirable. For this purpose an ATtiny85 (Atmel, San Jose, CA) microcontroller (μc) has been programmed with automatic pulse timing options and embedded into the NMR circuitry[3]. In the last decade, microcontroller technology and digital electronic prototyping have dramatically improved in capability, availability, and cost. Small programmable microchips have largely replaced the archetypal 7400- and 4000-series semiconductors in hobby electronics, and emphasis has shifted from circuit/hardware design to programming/software architecture [70, 157]. Figure 4.8 presents a photo and diagram of the circuit; the code programmed into the μc is given in Appendix A.1. The rotary switch is wired as a binary counter to select a preferred delay between pulses (5 sec, 3 min, 10 min, 30 min, 60 min, or ∞).

[3]The Author programmed the microcontroller using an Arduino Uno (Arduino, Torino, Italy) prototyping board [156].

Of course, automatic pulse generation does little good if the measured NMR signal cannot also be recorded. A universal serial bus (USB) controlled oscilloscope (Hantek® model DSO3064A, Qingdao City, Shandong Province, China) connected to a standard PC running Windows® (Microsoft, Redmond, Washington) has also been implemented for automatic recording of the HP gas FID's. Figure 4.9.a shows a typical FID of hyperpolarized ^{3}He as measured by the oscilloscope. The signal magnitude of a single FID can be calculated by taking the sum of the FID Fourier transform, $S = \int_\omega d\omega \int_t V(t)e^{-i\omega t}dt$, but historically, the peak-to-peak voltage of the FID has been used to monitor polarization and is a more intuitive measure than the arbitrary frequency units of FFT. We have kept the V_{pk-pk} convention for convenience (Figure 4.9) but note the FFT-sum method is frequency- and T_2^*-independent and is therefore less susceptible to B_0 drift. This is because V_{pk-pk} is measured using the first crest and trough of the FID; as ^{3}He resonance frequency moves away from the 100kHz spectrometer frequency the first crest/trough occur sooner and V_{pk-pk} increases[4].

The microcontroller timing circuit and USB oscilloscope has allowed for continuous remote monitoring of ^{3}He polarization. Figure 4.9.b presents a plot of ^{3}He polarization in an OP cell during SEOP which builds according to equation 3.12 as discussed in section 3.1.3. Figure 4.9.c shows a plots the polarization decay of ^{3}He as a function of time in a cold OP cell

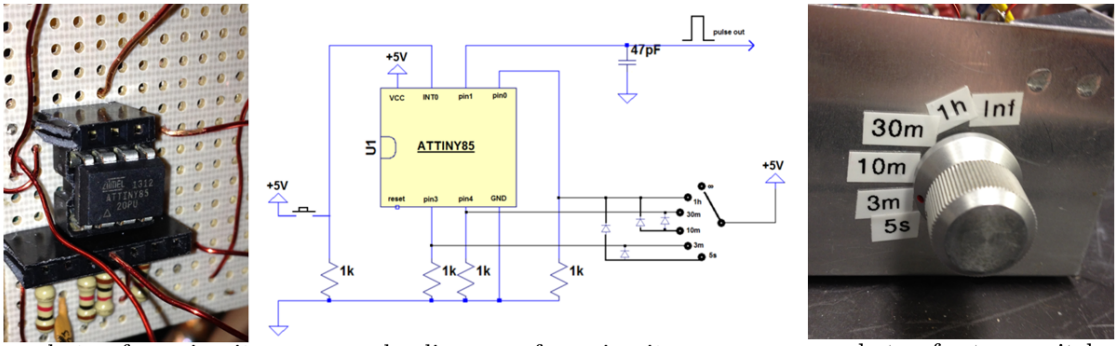

a: photo of **μc** circuit b: diagram of **μc** circuit c: photo of rotary switch

Figure 4.8: NMR Microcontroller Pulse Trigger, (a) photo, (b) circuit diagram, (c) timing control.

[4]This assumes modest B_0 shifts. More extreme shifts in ^{3}He resonance frequency relative to the NMR spectrometer frequency will of course result in lower delivered flip angles due to off-resonance excitation.

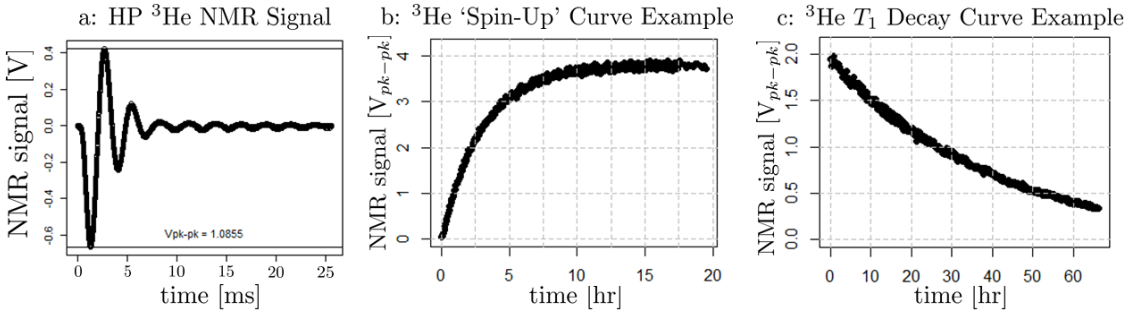

Figure 4.9: Example Plots of ^{3}He NMR FID, Spin-up Curve, and T_1 decay Curve. Panel a shows a typical NMR FID from hyperpolarized ^{3}He with the peak-to-peak voltage, V_{pk-pk}, explicitly stated. Panel b shows a typical ^{3}He 'Spin-up' curve; the peak-to-peak voltage of each measured FID becomes a datapoint on this curve as a function of time. Panel c shows a typical T_1 decay curve for ^{3}He; this data in particular is for OP cell 'Joffrey'.

with no laser illumination. These data allow for proper characterization of the OP cell T_1, spin exchange rate γ_{SE}, and rubidium polarization P_{Rb}, which is discussed in sections 4.1.5 and 4.1.6.

4.1.5 Calculation of Cell T_1 and NMR Flip Angle θ

When unilluminated, polarization of ^{3}He *in situ* will decay as $S = S_0 e^{-t/T_1}$ where T_1 is characteristic of the OP cell. Measuring a cell's T_1 *in situ* is a simple matter of performing pulse/acquire NMR no fewer than 2x in order to measure the signal decay in time by $ln(S) = -t/T_1 + ln(S_0)$. A greater number of NMR signal measurements will generally increase the precision of the T_1 measurement but will also artificially lower the signal S of subsequent NMR experiments according to

$$S_n = S_0 e^{-t/T_1} \cos^{n-1}\theta \tag{4.1}$$

It is often assumed that the flip angle θ is negligible – or, to be more precise, that the volume of ^{3}He excited by an NMR experiment is negligible compared to the total volume of ^{3}He in the cell. The integrity of this assumption can be evaluated by a few simple experiments.

Precise measures of the OP cell T_1 and NMR spectrometer flip angle θ can be delineated by measuring the decay in sample polarization from 2 sets of NMR experiments: one set of many *rf* excitations per unit time and one set of few *rf* excitations per unit time. Figure 4.10 shows plots of ^{3}He polarization as a function of time for the cases of no NMR monitoring, NMR monitoring with regular *rf* pulses at long time intervals (noted by subscripts s for *slow*), and NMR monitoring with *rf* pulses at regular short-time intervals (f for *fast*). The *slow* and *fast* experiments provide two equations with 2 unknowns which can be used to solve for θ and T_1:

$$P_s = e^{-t/T_1} \cos^{n_s} \theta \qquad P_f = e^{-t/T_1} \cos^{n_f} \theta \tag{4.2}$$

where n_f and n_s are the number of *rf* pulses delivered in the *fast* and *slow* experiments respectively for the time interval t (for simplicity we let initial Polarization $P_0 = 1$ for both cases). If the time between pulses for each experiment are Δt_s and Δt_f then $n_s = t/\Delta t_s$ and $n_f = t/\Delta t_f$ (the experiment time t does not need to be the same for both experiments, but may make calculations a bit simpler). Using P_f from equation 4.2 we can solve for $\cos\theta$

$$\cos\theta = P_f^{1/n_f} e^{\frac{\Delta t_f}{T_1}} \tag{4.3}$$

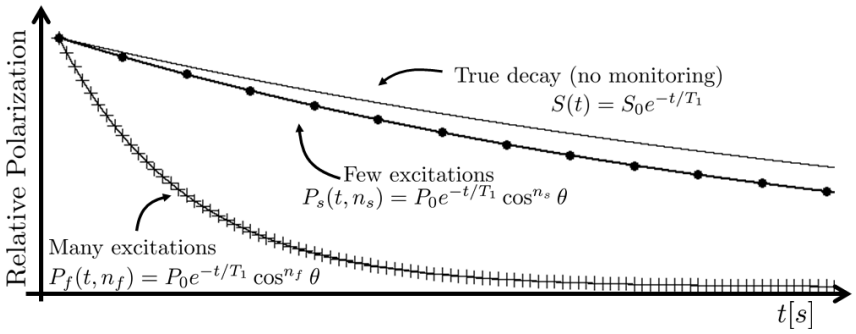

Figure 4.10: Plot of ^{3}He Polarization vs time with no *rf* excitation $S(t)$, few *rf* excitations $S(t, n_s)$, and many *rf* excitations $P_f(t, n_f)$. Subscripts s and f indicate *slow* and $fast$ excitation rates respectively.

which we then substitute into P_s from equation 4.2 to find both θ and T_1:

$$\begin{aligned} \frac{1}{T_1} &= \ln\left[\left(P_s P_f^{-n_s/n_f}\right)^{\frac{1}{\Delta t_f n_s - \Delta t_s n_s}}\right], \\ \cos\theta &= P_f^{1/n_f}\left[\left(P_s P_f^{-n_s/n_f}\right)^{\frac{\Delta t_f}{\Delta t_f n_s - \Delta t_s n_s}}\right]. \end{aligned} \tag{4.4}$$

This solution has been verified computationally, and respective code is presented in the Appendix section A.2. An example T_1 printout is given in Figure 4.11.

After performing *fast* and *slow* experiments on the ^{3}He polarizer with OP cell 'Joffrey', measured data were

$$\begin{aligned} \Delta t_f &= 5[\text{s}], \quad n_f = 2500, \quad P_f = 0.590 \\ \Delta t_s &= 600[\text{s}], \quad n_s = 84, \quad P_f = 0.696 \end{aligned} \tag{4.5}$$

leading to the following calculated NMR flip angle and T_1 for 'Joffrey'[5]:

$$\begin{aligned} T_{1,\text{Joffrey}} &= 40.2 \text{ [hr]} \\ \theta_{\text{eff}} &= 1.08^\circ \end{aligned} \tag{4.6}$$

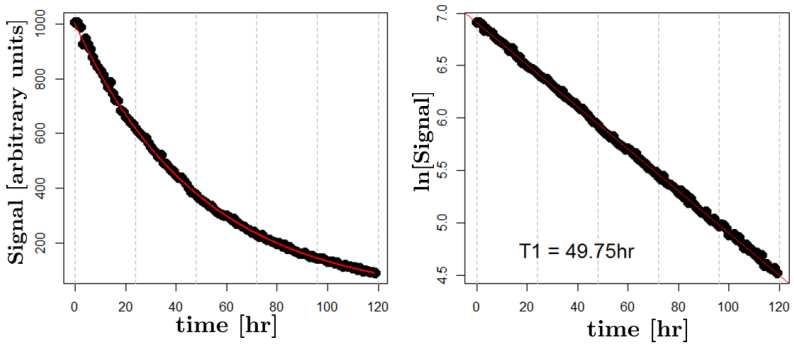

Figure 4.11: Example of T_1 Data Curves. The data on the left follows $S = S_0 e^{-t/T_1}$ and the data on the right is the natural log of the left plot $\ln(S) = \ln(S_0) - t/T_1$. These are early data are from OP cell Joffrey whose T_1 has since declined to $T_1 = 40.2$ [hr] (equation 4.6) over the course of approximately 20 fills.

[5]The *effective* flip angle, written as θ_{eff}, is given here, and is meant to indicate that $\cos(\theta_{\text{eff}})$ is the fraction of polarization remaining following an excitation. In reality, a much higher flip angle (near 90°) is delivered to a very small percentage of spins, but the model given here assumes that the entire cell volume experiences excitation.

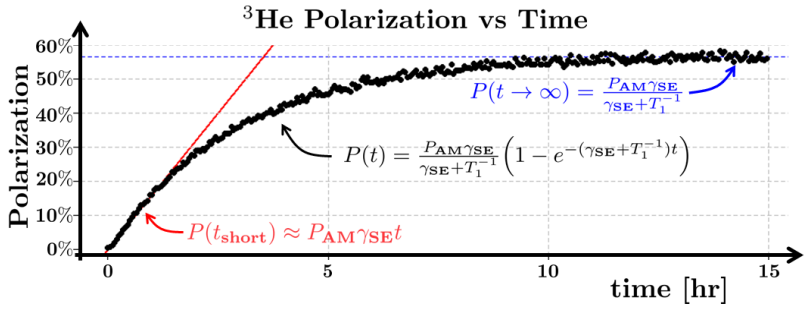

Figure 4.12: Example of a Polarization 'Spin-Up' Curve. Early time points follow a the linear relationship given in equation 4.8; late time points asymptotically approach the polarization given in equation 4.9. Data presented are from OP cell Joffrey.

The respective error for T_1 and θ_{eff} can be estimated by propagating the error of each measured value in equation 4.5; this is left to the reader as an exercise.

4.1.6 Characterization of γ_{SE} and P_{AM}

Recall from section 3.1.3 that noble gas polarization as a function of time follows

$$P(t) = \frac{P_{\text{AM}}\gamma_{\text{SE}}}{\gamma_{\text{SE}} + T_1^{-1}}\left(1 - e^{-(\gamma_{\text{SE}}+T_1^{-1})t}\right) \tag{4.7}$$

In the short-time limit $t(\gamma_{\text{SE}} + T_1^{-1}) \ll 1$, this simplifies to a linear relationship

$$P(t(\gamma_{\text{SE}} + T_1^{-1}) \ll 1) \approx P_{\text{AM}}\gamma_{\text{SE}}t \tag{4.8}$$

and, as we've already seen (section 3.1.3) the long time limit $t \to \infty$ yields

$$P(t \to \infty) = \frac{P_{\text{AM}}\gamma_{\text{SE}}}{\gamma_{\text{SE}} + T_1^{-1}} \tag{4.9}$$

Figure 4.12 shows 'spin-up' data from OP cell Joffrey. The slope of the curve during the first 30 minutes of spin-up time (first 10 time points) is $P_{\text{AM}}\gamma_{\text{SE}} = 19.3$; Joffrey's peak polarization was measured to be $\frac{P_{\text{AM}}\gamma_{\text{SE}}}{\gamma_{\text{SE}}+T_1^{-1}} = 60\%$ yielding a spin exchange rate and rubidium

polarization of[6]

$$\begin{aligned} \gamma_{\mathrm{SE}} &= 0.32\ [\mathrm{hr}^{-1}] \\ P_{\mathrm{Rb}} &= 60.8\%. \end{aligned} \tag{4.10}$$

Final polarization was measured on a Polarean® polarimetry station (Polarean, Inc., Durham, NC). Those that can afford higher-level programming platforms could also employ data-fitting techniques to enhance the accuracy of the γ_{SE} and P_{Rb} calculation.

The OP cell temperature, and thus the Rb vapor density, must be properly calibrated in order to optimize achievable polarization. Unfortunately, the RTD temperature sensor only reports the oven temperature, not the actual cell temperature. At this point, optimization of the PID set temperature requires experimental intervention. Figure 4.13 shows a collection of spin-up curves for OP cell Tyrion and several different oven temperatures indicating that this particular cell prefers lower temperatures for maximum polarization. These experiments have been performed on each OP cell with the result that the optimal oven temperature can vary widely among cells, but is consistent for an individual cell. It is worth noting that other

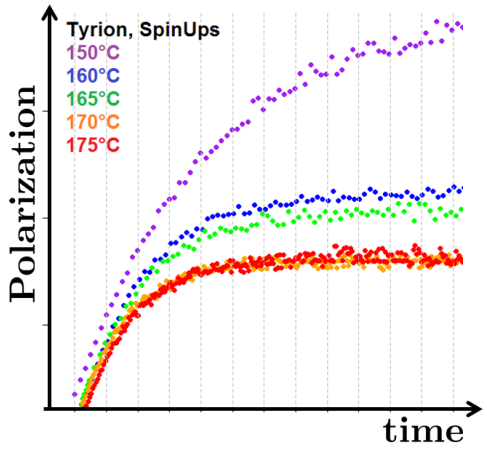

Figure 4.13: Plot of Relative Polarization vs Time for Several Oven Temperatures. These particular data are for OP cell Tyrion; both axes are arbitrary but consistent for each dataset.

[6]Upon calculation of the rubidium polarization, we begin to question the validity of the model in equation 4.7 since the rubidium polarization is expected to be much higher (near 100%) in this experimental setup [158].

groups have had success employing Raman scattering techniques for accurate OP cell gas temperatures [159].

4.1.7 Gas Handling and Plumbing

Transfer of ^{3}He to/from the OP cell requires rigid, leak-free plumbing to (1) keep paramagnetic impurities such as oxygen from contaminating the gas mixture and (2) avoid losing any amount of the costly ^{3}He gas. As discussed in section 3.1.3, contamination of the HP gas mixture with O_2 is a dominant source of relaxation of HP ^{3}He and must be strictly avoided. This is especially critical before gas transport to the OP cell which could be irreversibly contaminated by oxygen exposure. The design of the plumbing manifold for the ^{3}He polarizer is given in Figure 4.14. The flow of ^{3}He through the manifold follows valves V1-V2-V3-V4-V6-V16-cell; once a bottle has been attached, this path from V1-V16 is always at pressure (130 psi) and it is critical that valves V9 and V15 remain closed so no amount of ^{3}He is lost. Valve V13 separates the manifold from a mechanical vacuum pump, and valves V14 and V15 separate the manifold from an ultra-high purity (UHP, 99.999% atom purity) nitrogen supply line (maintained at ≈7 psi). The vacuum/N_2 lines are used to 'purge' the manifold of oxygen before ^{3}He is introduced. This process involves pressurizing the manifold with nitrogen, then evacuating to <10 mTorr no fewer than 3x for each OP cell fill/dispense. The manifold is made of 316 stainless steel except for plumbing between valves V16, V17 and V18 which is aluminum (V18 is also aluminum); steel contains iron which will depolarize the gas very quickly during dispense so aluminum is used here.

4.2 ^{129}Xe Polarizer Overview

The details above are specific to the ^{3}He polarizer, but the same concepts apply to our homebuilt ^{129}Xe polarizer 'Alix' (**A**pparatus for **L**ung **I**maging with **X**enon) designed by Laura L Walkup, Nara S Higano, and the author [160]. There are a few minor differences between the ^{129}Xe polarizer and ^{3}He polarizer to address. The xenon polarizer uses a 200

watt laser system (compared to 100 W for the helium polarizer); since the spin destruction rate is greater for xenon than helium it appropriately utilizes a greater number of photons[7]. Xenon OP cells are filled with 2 atm of a 50/50 xenon/nitrogen mixture in order to maximize

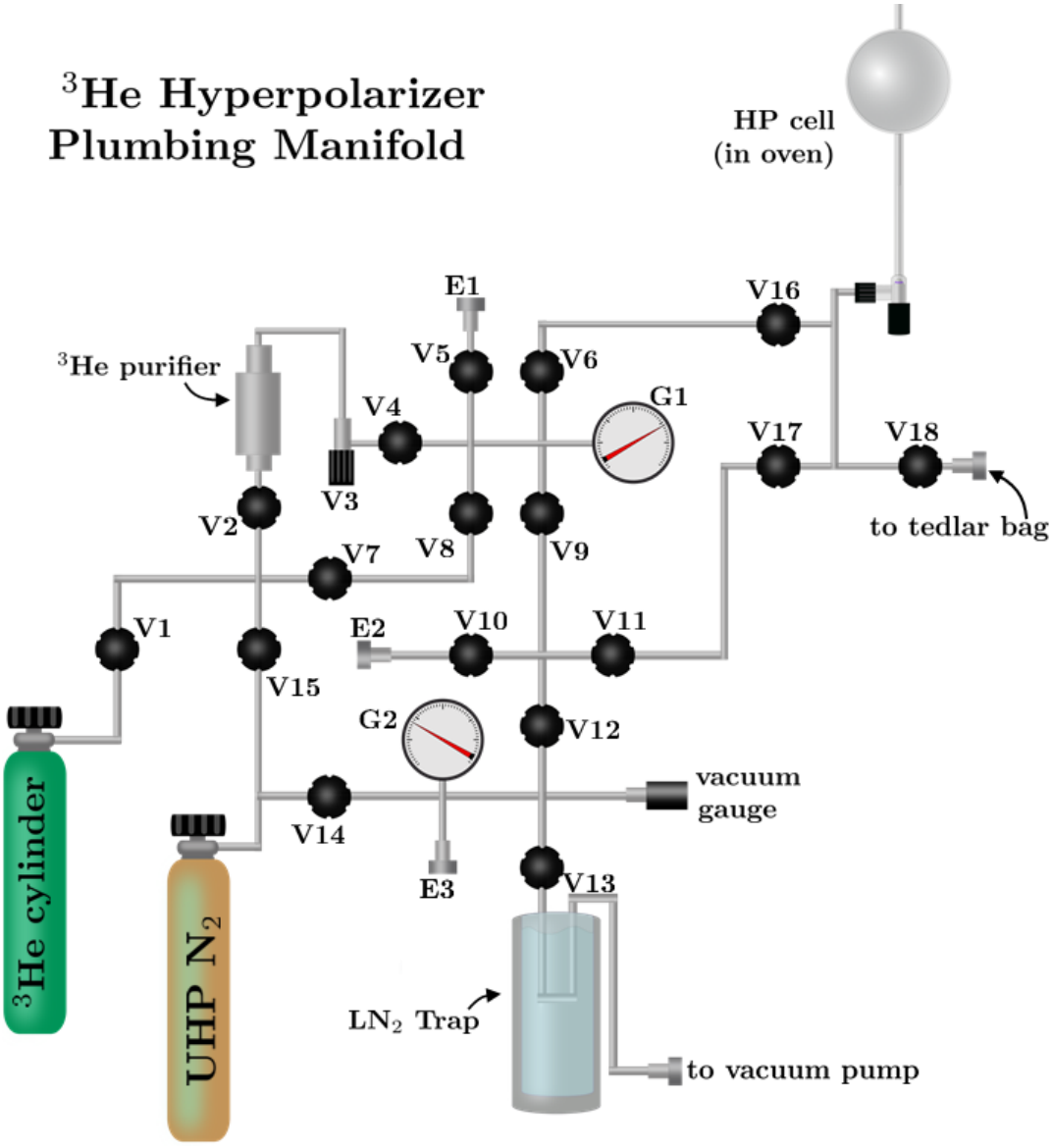

Figure 4.14: Diagram of the ^{3}He Plumbing Manifold. V-labels indicate valves; E-labels indicate expansion ports (always plugged if not in use); G-labels indicate gauges.

[7]Interestingly, the extra laser power obviates the need for external cell cooling. In fact, an external air cooling plumbing manifold has been installed to maintain appropriate xenon cell temperature.

Figure 4.15: Photograph of the ^{129}Xe Polarizer 'Alix' designed and built by Laura L Walkup, Nara S Higano, and the author.

the effective xenon polarization ($P_{\text{ef}} = P_{^{129}\text{Xe}}/[\text{Xe}]$) [112]. The cells are therefore larger in volume than ^{3}He cells (about 0.5-1 L). The OP cells for xenon possess two separate HI-VAC values, one for filling and one for dispensing. The plumbing was built to accommodate this design by anchoring the dispense line (since aluminum must be used) and allowing the fill line to be flexible with the use of stainless steel capillary tubing. Finally, the NMR spectrometer (built by Nara Higano) is tuned to 62.5kHz so the B_0 field is maintained at approximately 53 Gauss for Polarization monitoring.

4.2.1 Troubleshooting

It is possible however unthinkable that achievable NMR signal from the polarizer is anomalously sub-optimal. This can occur for dozens of reasons including decreased laser output power, shifted laser frequency, broadened laser linewidth, cell T_1 decrease due to oxygen contamination, improper buffer gas concentration, poor NMR calibration or malfunction, B_0 drift, many other reasons, or any combination of these. Some of these, such as improper NMR calibration or B_0 drift, do not actually result in decreased noble gas polarization but rather a handicap on proper polarization detection. What consequences are expected due to these anomalies and how can they be addressed?

Laser issues can be mitigated by proper initial characterization of laser output. A laser power meter makes easy work of identifying reduction in output power; poor power output is often a result of burnt diodes and require replacement. An optical spectrometer will showcase any shifts in output frequency or linewidth. Diode lasers are particularly sensitive to temperature fluctuations, and the center frequency of the laser emission tends to shift toward longer wavelengths as the diode bars heat. Our lasers are water-cooled, and the precise cooling temperature can be specified as desired for precise frequency tuning.

If laser emission is optimal but polarization still suffers potential problems with the cell may be considered. First the OP cell should be visually examined for any sign of golden-yellow tint which may indicate oxidation. If a cell appears oxidized it may need to be replaced, and the plumbing must be leak tested and repaired if necessary. If the cell does not show signs of oxidation, it could be that the gas mixture is incorrect. Figure 4.16 presents several spin-up curves for OP cell 'Joffrey' upon attaching a new ^{3}He bottle to the plumbing manifold. Typically, our ^{3}He bottles come pre-mixed with 99.25% ^{3}He and 0.75% N_2; as it so happens a mix-up had occurred in delivery of the ^{3}He gas, and our mixture contained no buffer gas. Each subsequent fill of Joffrey resulted in less and less buffer gas, and polarization decreased steadily. Upon realization of the issue, a new bottle with the proper mixture was ordered and installed, and the polarization recovered (Figure 4.16). Laser light outflux from the cell may indicate incorrect oven temperature if the laser emission is not substantially

different from the laser emission profile. Also, powering off the B_0 field can reveal the extent of Rb polarization since this collapses the polarized/unpolarized electronic states; laser outflux will decrease since the once polarized Rb electrons can now absorb photons[8].

If there are no problems with the laser emission profile and the OP cell shows no obvious problems, the B_0 field may need adjustment. If the noble gas resonance frequency drifts too far from the spectrometer, the delivered flip angle and received signal will be reduced. A Gaussmeter can be used to verify the field strength of the B_0 coils if necessary.

4.3 Summary

Here we have seen that spin exchange optical pumping requires unique dedicated hardware to achieve optimum noble gas polarization, and we have become familiar with important

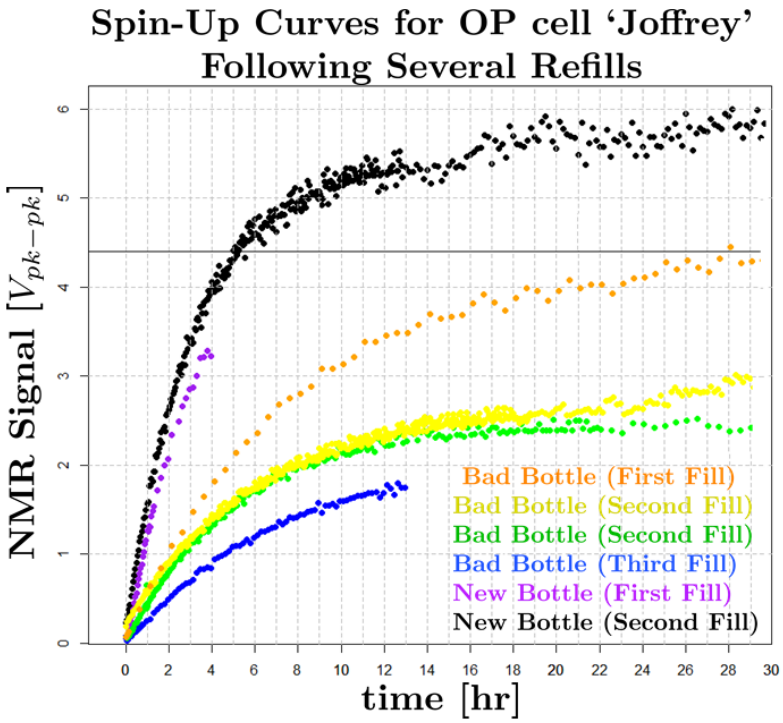

Figure 4.16: SpinUp Curves for OP cell 'Joffrey' Before and After N_2 Addition.

[8]This is only recommended if the B_0 power supply is protected, and the B_0 coils are equipped with fly-back diodes.

quality control protocols to ensure the equipment functions properly. Once hyperpolarized gas has been successfully produced, it is ready to be dispensed and delivered to the scanner suite for inhalation by the subject, and *in vivo* images may be acquired. An HP gas imaging session requires careful planning, and the ability to recognize and address potential difficulties in real-time is critical, and the next chapter will expound upon the protocol used to obtain high-quality MR images of inhaled HP gases.

Chapter 5

Hyperpolarized Gas Imaging Protocol

> "So you do have a plan! Yeah Mr. White! Yeah science!"
>
> — Jesse Pinkman, *Breaking Bad*

This chapter will guide the reader through a typical HP gas imaging session and detail the tools and techniques employed to achieve optimal images of human lungs *in vivo*. Understanding the reasoning behind each implemented step requires a solid MR imaging foundation (section 2.2 and Bushberg *et al.* [29]). Maximization of the ratio of signal to noise (SNR) in MR images is the supreme goal of an MRI experiment, and several methodological techniques have been developed as standardized practice to achieve optimal SNR. These methods have been implemented on a Philips® Achieva 3 Tesla MR scanner (Philips Healthcare, Best, Netherlands) for our purposes.

There are a few major considerations when performing HP gas MRI which are fundamentally different from standard proton imaging. Most importantly, the magnetization for HP gas is *non-renewable*; this is perhaps the biggest conceptual hurdle for those more familiar with proton scanning. As a consequence, HP gas imaging sequences must use small flip angles to preserve magnetization. Because return to Boltzmann equilibrium by T_1 relaxation is undesirable for HP gases[1], every effort must be made to maintain long HP gas T_1

[1]Fun Fact: HP gas researchers can be easily distinguished in a crowd because they will curiously refer to spin-lattice relaxation as T_1 *decay* rather than T_1 *recovery*.

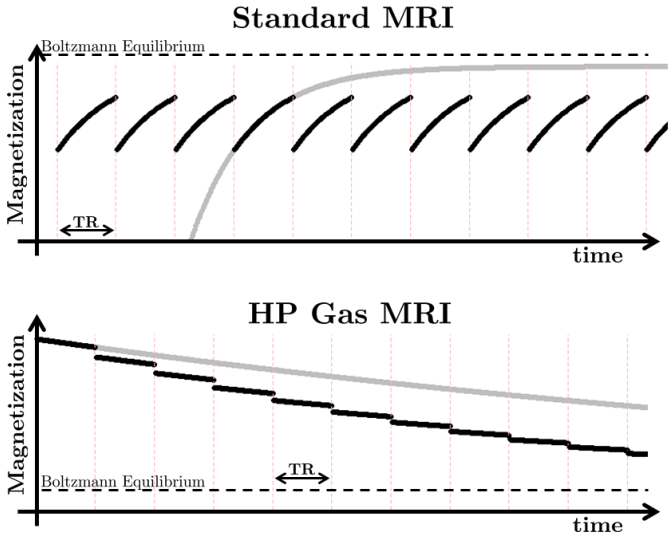

Figure 5.1: Comparison of Magnetization vs time for Standard MRI and HP gas MRI. Each *rf* excitation lowers the available magnetization of the sample which is constantly equilibrating toward Boltzmann equilibrium (importantly, note the difference in Boltzmann magnetization relative to signal). Undisturbed recovery curves (no *rf*) are given in gray for comparison.

and preserve the non-equilibrium magnetization. Generally this necessitates that images be acquired quickly (shortest possible TR); because a complete set of images must be acquired during a breathold anyway, this is not a concern. Figure 5.1 illustrates the fundamental difference between standard MRI and HP gas MRI; note that for conventional MRI, longer TR provides greater magnetization for each *rf* excitation, but reduced magnetization for HP gas imaging. The techniques detailed here are specific to our imaging hardware and scientific investigations; for a general review of techniques used in HP gas MRI, the reader should consult Harald Möller's 2002 article [69].

Development of the HP gas imaging protocol, implementation of unique hardware on the Philips platform, and realization of a successful image acquisition routine was an involved project in which the author played a major role and required extensive under-the-hood knowledge of the Philips hardware architecture and software environment[2]. This chapter

[2]Information specific to the Philips environment is considered proprietary and cannot be discussed in detail here.

will present the logistics of a typical HP gas imaging session. Greater detail will be given when considering the various imaging parameters chosen for our experiments and their effect on image quality. The means by which quantitative physiological information is derived from the acquired images will then be discused in Chapter 6.

5.1 MRI Scanner and Peripheral Hardware

Our studies utilize a Philips 3T Achieva with multinuclear capability for all of our HP gas imaging protocols. The question of field strength was curiously never asked of our group, but a few implications of field strength on NMR signal are presented alongside an MRI magnet diagram in Figure 5.2. Recall from section 2.1.3 that detected signal from HP gases compares to Boltzmann equilibrium (BE) signal as follows

$$S_{\mathrm{HP}} = \frac{1}{2}\gamma\omega\hbar NP \tag{5.1a}$$

$$S_{\mathrm{BE}} = \frac{\gamma\omega^2\hbar^2 N}{4kT} \tag{5.1b}$$

For samples in thermal equilibrium, signal magnitude increases as $S \propto B_0^2$, thus an increase in magnetic field can dramatically improve SNR, but it can also introduce new challenges related to relaxation rates, field susceptibility, and chemical shift (Figure 5.2). Hyperpolarized gas polarization is not dependent on B_0, thus detectable signal from HP gases only increases as $S \propto B_0$, . The trade-offs between signal and relaxation rates in HP gases due to different field strengths actually imply that lower fields are more desirable for HP gas imaging. In illustration of FID signals for HP gases at 1.5T and 3.0T are given in Figure 5.3. Nevertheless the only available multinuclear imaging system available for our studies is at field strength of 3 Tesla (3.0T).

Our multinuclear setup required construction of transmit/receive (T/R) coils tuned to the resonant frequencies of the noble gases at 3 Tesla (helium $f_{^3\mathrm{He}} = 97.3\mathrm{MHz}$, and xenon $f_{^{129}\mathrm{Xe}} = 35.3\mathrm{MHz}$). For each nucleus two coils have been constructed: a small loop coil for

sequence and scanner testing and a saddle shaped coil for *in vivo* imaging [165]. Two imaging phantoms, one for ^{3}He and one for ^{129}Xe, have been prepared for proper coil calibration in the magnet (Figure 5.4). This is necessary to adjust the scanner *rf* power so the delivered flip angle to the sample is reasonably close to the prescribed flip angle. Once an appropriate *rf* power level has been set, the coils can be *loaded* by surrounding the coil in the scanner with a conductive medium (such as saline) to emulate coil performance in the presence of tissue. Human tissue near the coil will alter its resistive impedance reducing the Q of the tuned circuit (recall $Q = f/\Delta f$ where f is the tuned circuit peak frequency and Δf is the its response bandwidth). These effects require tuning and matching adjustment in the B_0 field for precise flip angle calibration[3].

Also of import, an MRI coil must fall within certain FDA guidelines to be approved for research studies. The most important of these guidelines pertains to the amount of energy absorbed by the imaging sample due to the delivered *rf* called the *specific absorption rate* (SAR). SAR is defined as an amount of absorbed power per unit of tissue mass (given in units of W/kg) and is proportional to $B_1^2(t)$, the magnetic flux density of the delivered *rf* pulse. SAR generally manifests itself in the form of tissue heating; thus an important part of MR coil development involves measuring the temperature increase of a phantom while

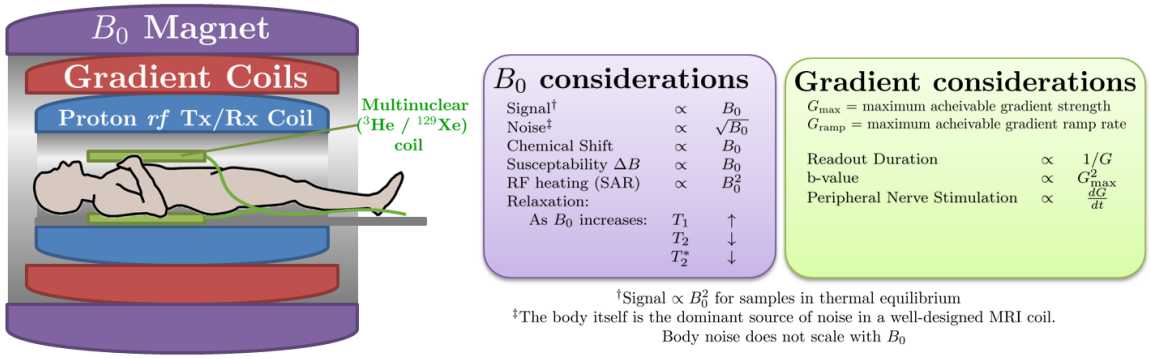

Figure 5.2: Illustration of an MRI magnet and Some Important Hardware Considerations for Imaging. [161, 162, 163]. The dedicated proton Tx/Rx *rf* coil is often a 'birdcage' design [164].

[3]For reasons discussed in section 5.3, precise flip angle calibration is more critical in HP gas imaging than in traditional proton imaging.

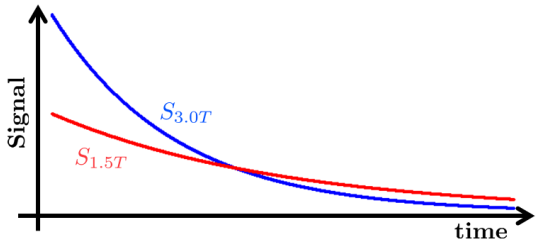

Figure 5.3: HP Gas Signal Magnitude of a Single FID as a Function of Time for Two Different Field Strengths. Initial signal $S(t = 0)$ is proportional to field strength B_0, but T_2^* decreases as field increases. At longer time scales lower fields will yield higher signal.

the coil runs continuously within the magnet. These safety tests were performed for all coils used in these experiments. HP gas scans performed in this work involve low flip angles (low *rf* power) for scan times on order of tens of seconds (within a single breathold) so SAR is not a major concern here [49].

5.2 Preparation and Proton Survey

When the subject is ready to be scanned, he or she enters the magnet with the dedicated helium or xenon coil folded like a clamshell on the thorax (Figure 5.5). Once in the magnet

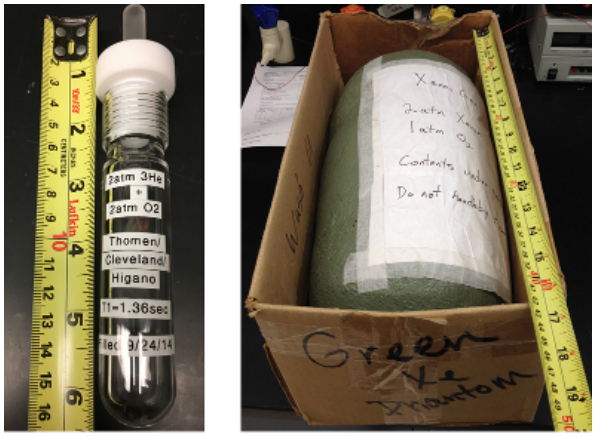

^{3}He Phantom ^{129}Xe Phantom

Figure 5.4: Photographs of the ^{3}He and ^{129}Xe Phantoms. To give a sense of scale, the tape measure in each image is approximately 1 inch wide.

Figure 5.5: Photographs of the Multinuclear Coil and a Subject in the Magnet. Panel a: The ^{129}Xe coil (uncovered). Panel b: The coil placed on a subject (censored to conceal Jason's identity). Panel c: Subject with coil about to be placed in scanner bore.

a ^{1}H 'survey' scan (body coil, GRE sequence, 3 slices in the 3 orthogonal planes, 9 images total) is performed for proper localization of the patient for scan planning. Hyperpolarized gas imaging requires step-by-step coaching of the subject while in the magnet, so before performing multinuclear imaging, a proton image is prepared for which the subject can 'practice' following instructions during the breathold with a bag of air. The subject is coached by a gas-delivery person who instructs them to inhale-exhale twice before giving them the gas bag mouthpiece for inhalation of the dose. They are coached to inhale the entire contents of the bag, hold their breath, and the scanner operator is signaled to begin the scan which lasts no more than 16 seconds (according to our FDA-approved protocol). Aside from allowing the subject to practice the imaging routine, this serves a second purpose of acquiring a proton scan of the exact imaging geometry (patient location, voxel size, FOV, etc.) to be used for the multinuclear scan. This can be used for co-registration of the proton and HP gas scans since the lungs of each image will exactly match voxelwise. This also simplifies the scan planning process by allowing the operator to simply copy the successful proton scan and change the target nucleus.

After a successful proton scan, the HP gas scans are acquired: a flip-angle calibration scan and an imaging scan – either 'ventilation' or 'diffusion' or both. Proper preparation of

the HP gas dose and choreography of the gas delivery are critical for a successful imaging session. As soon as the gas is dispensed into the Tedlar bag used for delivery, magnetization decays rapidly with T_1 in the bag on order of 0.5 - 2 hours depending on dose size and gas concentration [166] – every minute lost results in signal lost. Generally, the imaging session and HP gas preparation have been meticulously planned such that gas is dispensed the moment its respective scan is ready. As discussed in chapter 4, this is less of a concern with our homebuilt polarizers since gas can be directly dispensed from the OP cell as needed; the flow-through design of the commercial xenon polarizer requires proper foresight and planning.

5.3 Flip Angle Calibration

The transmit/receive (T/R) coil used for imaging hyperpolarized gas, either ^{3}He or ^{129}Xe, must be able to accommodate a wide range of chest sizes from children to adults. It is a concern that coil tuning may vary widely from subject to subject (or even from inspiration to expiration) rendering the delivered *rf* flip angle θ highly variable among scans. This is less of a concern in traditional proton imaging since the delivered flip angles are generally much higher than for HP gases, and therefore a difference between prescribed and delivered flip angle does not severely affect SNR which is proportional to $\sin\theta$ (the difference in signal between an 8° vs 9° flip angle is substantially greater than that between an 80° vs 90° flip angle). Thus, before a HP gas imaging scan is performed, the flip angle must be calibrated to the subject, and we have implemented a dedicated sequence and analysis protocol for this purpose.

The flip angle calibration sequence is simply a 64-*rf* excitation pulse/acquire scan to be performed following inhalation of a small volume (often about 250ml) of HP gas. The scan duration is approximately 2 seconds performed during breathold – a short enough amount of time that signal decay from T_1 relaxation is negligible (about 30 seconds *in vivo* [133]). The signal magnitude of each subsequent *rf* pulse will be reduced by a factor of $\cos\theta$, thus

for n pulses the signal magnitude will follow

$$S_n = S_0 cos^{n-1}\theta \tag{5.2}$$

where the $n-1$ exponent indicates that the magnitude of the first FID, $n = 1$, defines S_0. The delivered flip angle θ is then simply $\theta = \arccos^{\frac{1}{n-m-1}}(S_n/S_m)$. Once the actual flip angle delivered in the calibration sequence is determined, the prescribed flip angle can be adjusted accordingly. If for instance the scanner operator *prescribed* a flip angle of θ_p for the calibration sequence, and the analysis of the signal decay determined that an *actual* flip angle of θ_a was delivered, it is a simple matter of scaling the desired flip angle of future scans by a factor θ_p/θ_a.

Because the sequence records 64 FID's, there exist 2,016 solutions for θ, all with varying degrees of precision depending on $m-n$ and SNR. A cleaner approach would be to simply fit equation 5.2 to the data. The discrete difference equation which describes the signal decay can be expressed

$$\begin{aligned} S_{n+1} &= S_n \cos\theta \\ S_{n+1} - S_n &= S_n \cos\theta - S_n \\ DS_n &= (\cos\theta - 1)S_n \end{aligned} \tag{5.3}$$

and, because it contains no singular points, has an analogous continuous differential equation and solution:

$$\begin{aligned} \frac{dS(n)}{dn} &= (\cos\theta - 1)S(n) \\ S(n) &= S_0 e^{(\cos\theta - 1)n} \end{aligned} \tag{5.4}$$

The statistical programming language R is used to calculate flip angles by linearly fitting $\ln S = (\cos\theta - 1)n + \ln(S_0)$. The flip angle calibration code is given in Appendix A.4. Output for a signal flip angle calibration is given in Figure 5.6. The calculated flip angle is printed in the final panel alongside flip angles to prescribe for ventilation and multi-b-value diffusion images; the number of phase encodes is input by the user.

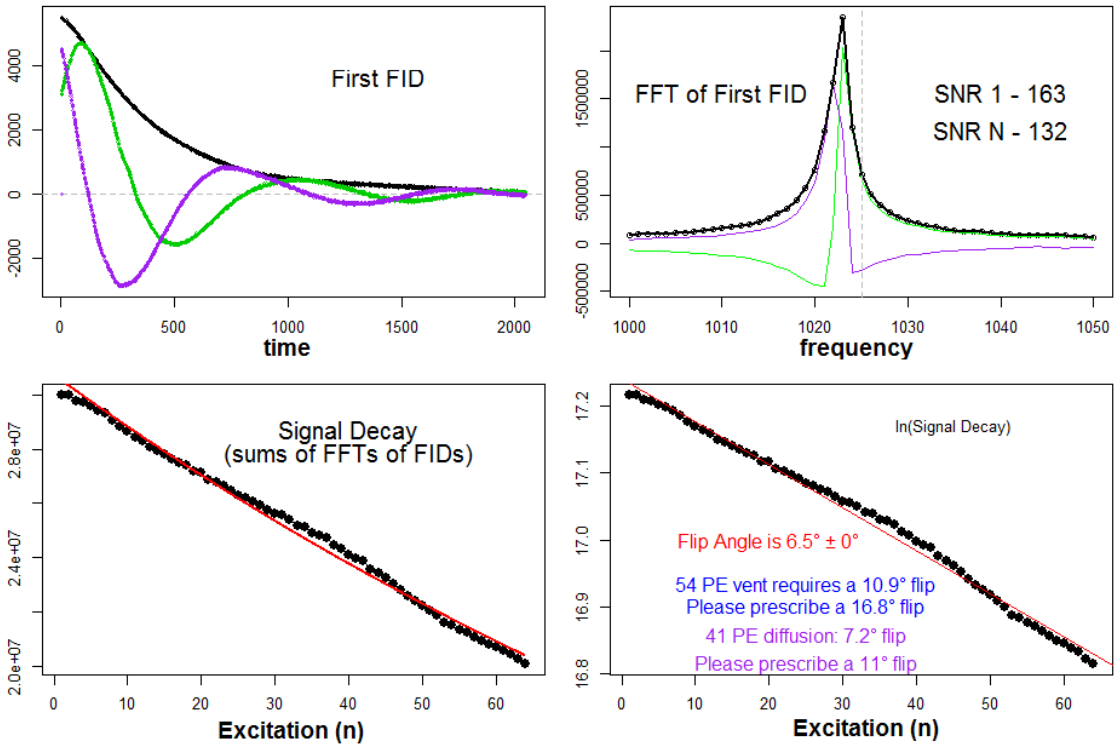

Figure 5.6: Example of Flip Angle Calibration Printout. All y-axis units are arbitrary. Panels are (a) plot of first FID, (b) FFT of first FID, (c) plot of FID FFT magnitude (S_n) vs excitation S_n, (d) plot of the natural log of FID FFT ($\ln S_n$) vs excitation number. For complex points, real values are green and imaginary values are purple.

5.4 Ventilation Imaging

Ventilation scans provide spin density images of the hyperpolarized gas during a breathold; that is, the signal intensity of a given voxel is proportional to the number of hyperpolarized nuclei contained therein. Dozens of parameters must be considered for each scan to produce optimal images in terms of SNR and resolution, but a few criterion must always be satisfied: the scan must not exceed 16 seconds (according to our FDA-approved protocol), the field of view must be as small as possible but contain the entirety of the lung volume, and voxel size must be 3 x 3 x 15 mm^3.

The ventilation scan is a 10-15 slice, linearly-encoded, small-flip-angle, gradient echo scan with the shortest possible TR and TE – often referred to as a FLASH sequence (**F**ast

Low **A**ngle **Sh**ot) [167]. The 3 x 3 mm^2 in-plane voxel size generally places the number of phase encodes between 45-65. Phase encoding is always performed along shortest matrix dimension (to minimize the number of *rf* excitations) which, so far, has always been in the anterior-posterior direction. The choice of flip angle is the first important parameter to consider. Higher flip angles will of course result in greater signal, but because the HP gas magnetization in non-renewable, each subsequent flip angle n will yield less signal according to $S \propto \cos^{n-1}\theta \sin\theta$. If theta is chosen too small, the HP gas signal remains largely underutilized and SNR suffers; if the flip angle is too big, the HP gas magnetization is fully consumed before all phase encodes have been acquired and SNR suffers. Figure 5.7 illustrates this phenomenon.

The HP gas magnetization M_n and detected signal S_n following a flip angle θ are

$$\begin{aligned} M_{n+1} &= M_n \cos\theta \\ S_n &= M_n \sin\theta = M_0 \cos^{n-1}\theta \sin\theta \end{aligned} \tag{5.5}$$

The total signal acquired during a scan with N phase encodes then follows

$$\sum_{n=1}^{N} S_n = \sum_{n=1}^{N} M_0 \cos^{n-1}\theta \sin\theta \tag{5.6}$$

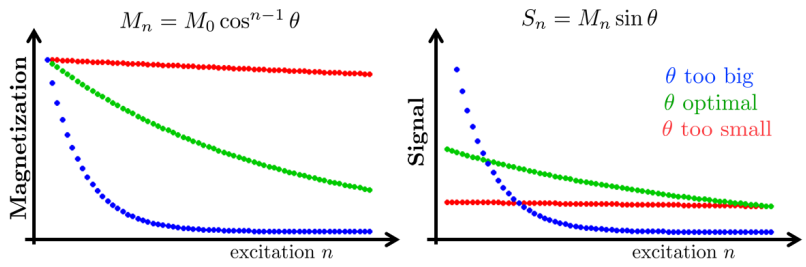

Figure 5.7: Optimization of Flip Angle for HP gas MRI. Plots of HP gas magnetization vs excitation number (left) and detected signal vs excitation number (right) are presented for the cases of θ too big (blue), θ too small (red), and optimal θ (green). The total detected signal (area under the curve) is maximized for optimal θ. Number of phase encodes $N = 64$ for these cases.

The author has computationally evaluated optimal values of θ as a function of the number of phase encodes N presented in Figure 5.8 (code is presented in Appendix A.5). Because SNR is largely defined by the signal acquired at $k = 0$, it may be more desirable to maximize signal specifically for this k-space line. If this k-space line occurs at the n_0 excitation, this condition effectively removes the summation from equation 5.6 yielding the following solution for $\frac{dS}{d\theta} = 0$:

$$\tan^2\theta = \frac{1}{n_0 - 1} \tag{5.7}$$

This solution has been adopted by several groups [168, 169] including ours. Because our experiments employ linear encoding, we choose flip angles which satisfy $\theta = \tan^{-1}\sqrt{2/N}$; this is presented in Figure 5.8 alongside the computational solution to equation 5.6. The solution to equation 5.6 is meant to maximize total acquired signal during a scan, whereas equation 5.7 seeks entirely to maximize the signal acquired from the $k = 0$ line; the striking similarity between the two results shown in Figure 5.8 indicates that, as expected, SNR of an image is largely contained within the low-frequency components of k-space. While the discussion here assumes a constant flip angle θ for all n, other groups have had success employing a variable flip angle designed to maintain constant detected signal across all k-space: $\theta(n) = \tan^{-1}(1/\sqrt{N-n})$, [170].

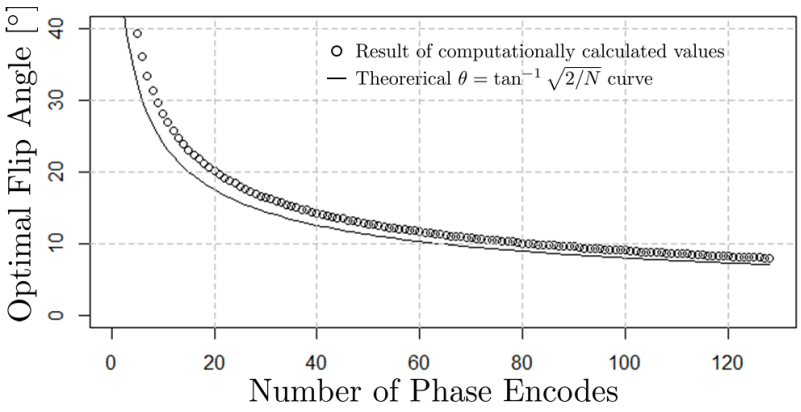

Figure 5.8: Plot of Optimal Flip Angle θ vs Number of Phase Encodes N. Circles are computationally evaluated data; line is the curve $\theta = \tan^{-1}\sqrt{2/N}$.

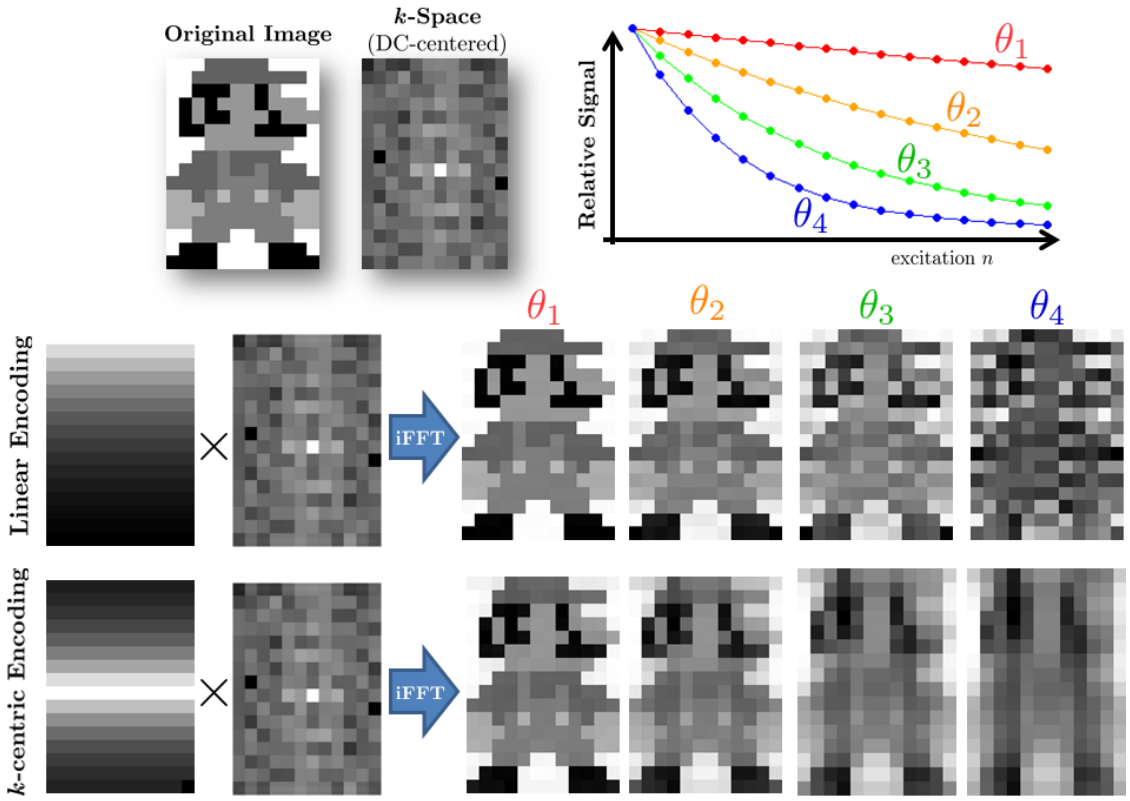

Figure 5.9: Illustration of Signal Decay on Phase Encoding Schemes. Signal decay from several flip angle θ's are plotted at top. These signal decays have been applied to the k-space of an image (given at top) in both linear-encoding order (middle row) and k-centric encoding order (bottom row). The effect of signal decay on the reconstructed images is shown for increasing flip angle θ's.

Although SNR can be optimized by judicious selection of constant θ, k-space will be necessarily modulated by the decaying signal inherent in HP gas imaging. The effects of k-space modulation on resultant images is given in Figure 5.9 for cases of linear and k-centric encoding schemes. Note that linear encoding preserves resolution over SNR and vice versa for k-centric encoding. We choose linear encoding schemes for our experiments because we are more interested in structural details of the lung; priority therefore goes to higher spatial frequencies in k-space.

Once the flip angle calibration scan has been performed, the data are exported, analyzed, and the flip angle to be used in the ventilation scan is prescribed. A ventilation scan 'dry run'

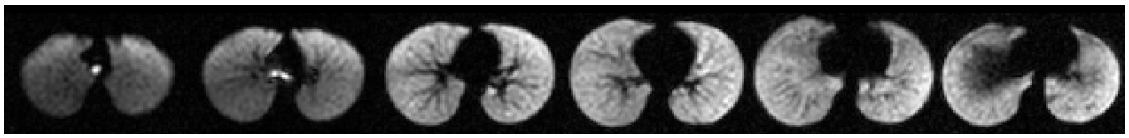

Figure 5.10: Example of *in vivo* HP ^{129}Xe Ventilation Images on a Healthy Volunteer. Images are axial slices of inhaled hyperpolarized ^{129}Xe in a 6 year old subject. Images proceed from apical to basal slices. Left lung is on the right side of each image; right lung is on the left.

(no HP gas) is executed to verify that the acquired noise profile is acceptable[4] and the HP gas may be fetched for the ventilation scan. When ready, the gas polarization is measured on a dedicated Polarean polarimetry station and very quickly carried to the imaging suite for delivery to the subject. As with the practice bag of air, the subject is coached to inhale-exhale twice, then given the HP gas to inhale for imaging during a <16 second breathold. Examples of ventilation images in a healthy volunteer are given in Figure 5.10. Imaging parameters can vary among scans but generally fall within ranges: flip angle =10°-12°, TR/TE = 8ms/4ms, voxel size = 3x3x15 mm3, 9-14 slices. Images are acquired axially (perpendicular to the B_0 field) since we often perform comparative analyses between HP gas MRI and CT. Discussions of ventilation image analysis and physiological significance are presented in section 6.2.

5.5 Diffusion Imaging

Diffusion imaging has been shown to provide sensitive measures of parenchymal architecture on the alveolar level and is often performed when a subject's pathology is expected to result in unique alveolar micro-geometry. In section 2.2.4 we realized that application of a bipolar diffusion-sensitizing gradient will lower the detected NMR signal by a factor of e^{-bD} where D is the diffusion coefficient of the sample and b is a parameter dependent on the exact timing of the diffusion-sensitizing gradient. Because every point in acquired k-space is multiplied by this factor, we know from Fourier linearity ($\mathrm{FFT}\left[a \cdot f(t)\right] = a \cdot F(\omega)$)

[4]This quality control measure was deemed necessary after several instances of poor data acquisition related to data discretization due to gain loss, incorrect gain adjustment in between excitations, non-Gaussian *rf* noise from misbehaving devices within the magnet room, and other reasons. See section 5.7.

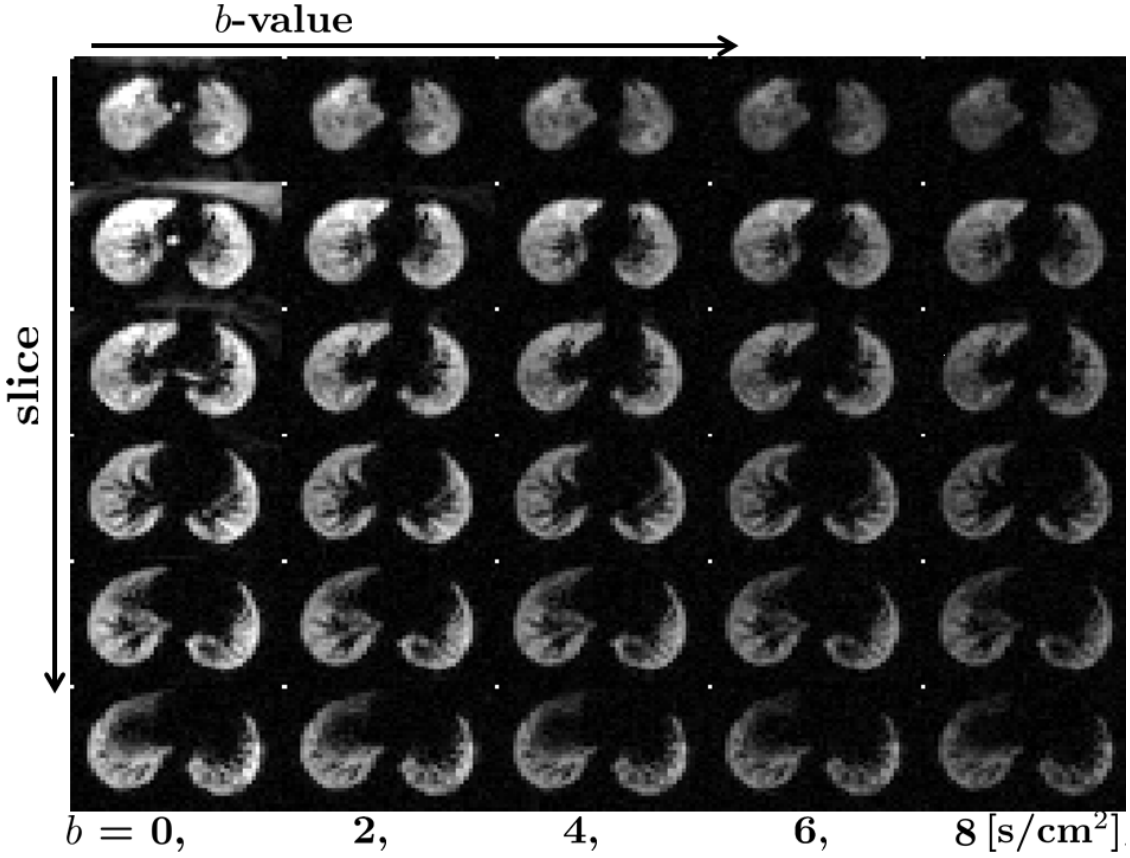

Figure 5.11: Example of *in vivo* HP ^{3}He Multi-b-Value Diffusion Images. As the b-value increases, the signal intensity is reduced. Regions of the image where gas diffusion is less obstructed (such as in the trachea) demonstrate greater signal attenuation with increasing b as per $S = S_0 e^{-bD}$.

that this factor is also applied to the signal intensity of the reconstructed image. Examples of multi-b-value diffusion images acquired with ^{3}He are given in Figure 5.11 showing the reduction in signal as b-value increases.

Note that the images with no diffusion weighting ($b = 0$) are, in essence, ventilation images. However, because the number of excitations involved in a diffusion image is increased by a factor of the number of b values used, image resolution is generally sacrificed so that SNR does not suffer. For our diffusion images a voxel size of 5 x 5 x 20 mm^3 is employed to preserve SNR while maintaining acceptable resolution (since SNR is proportional to voxel size V_{vox} [49]). This will in turn increase the precision of an individual voxel's calculated diffusion

coefficient (section 6.3.1) at the expense of resolution. The diffusion sequence acquires all b-values within a single k-space line sequentially. Thus k-space would be acquired according to the following pseudocode:

```
for (each slice){
     for(each phase encode){
          for(each b value){
               acquire 1 line of k-space
          }
     }
}
```

The number of b-values N_b used in the diffusion scan will also extend the scan time by a factor of N_b. Sacrificing phase encoding steps will decrease scan time as stated above, but often the number of slices must also be downgraded. The flip angle used in diffusion scans is chosen such that 20% of the initial HP gas magnetization remains upon completion of the scan: $\theta = \cos^{-1}\left[0.2^{\frac{1}{N_b * N_{\mathrm{PE}}}}\right]$. This was chosen as a compromise since each subsequent line of k-space is N_b excitations removed from its neighbor and any artifacts in the images can severely affect calculated ADC's.

Acquisition of both ventilation and diffusion images is rarely performed within the same imaging session since production of 2 separate imaging doses of HP gas is logistically difficult within the 15 minute window of HP gas imaging time. Ventilation imaging is typically chosen in lung diseases expected to demonstrate regional ventilation heterogeneity and more precise localization of pathology (and therefore, higher resolution) is desired. Such is the case in asthma which is characterized by airway inflammation but not by microstructural changes of alveoli. Conversely, diffusion images reveal the dynamics of the HP gas within the parenchyma and are therefore better suited to investigate diseases such as emphysema which is characterized by deterioration of alveolar walls. Discussions of diffusion image analysis and physiological significance are presented in sections 6.3.1 and 6.3.2.

5.6 Ultra-Short Echo (UTE) imaging

Clinical imaging is generally perceived as a method of providing *structural* information in the form of detailed anatomic maps of tissue but do not necessarily reveal information relating to how well said tissue performs its biological tasks. Investigations of lung structure-function typically involve retrospectively relating structural and functional measures which have been acquired separately. As the following chapter will reveal, hyperpolarized gas images provide unique and quantitative *functional* lung information regionally; combining regional information relating to airways, parenchyma, and vasculature with ventilation information from HP gas images will allow for structure-function relationships to be evaluated quantitatively. As discussed in section 1.2.8, MRI has historically been the most limited clinical imaging modality for investigation of lung structure. As such CT reigns supreme as the gold standard of pulmonary structural imaging, but its use of ionizing radiation keeps attention focused on MRI as an attractive alternative *if* it can be shown to provide similar diagnostic information. Recently a novel MRI acquisition protocol has been shown to provide such information and has been adopted by our group: *Ultra-short Echo* (UTE) MRI[5].

The reason for poor MRI performance within the lung space is the magnetic susceptibilities of the numerous air-tissue interfaces within the lung parenchyma which greatly increase B_0 heterogeneity ΔB. As a result, the T_2^* of the parenchyma is severely reduced (recall $\frac{1}{T_2^*} = \frac{1}{T_2} + \gamma \Delta B$ from section 2.1.4) to the order of 500 - 1000 microseconds. Recall the echo time (TE) of a typical GRE sequence is approximately 2-4 ms, at which point, the signal of lung parenchyma would be reduced to only a few percent of its true value. This is further confounded[6] by the inherently low tissue density of lung (about 30% that of other organs). Figure 5.12 shows FID signal magnitudes for most biological tissues (red) alongside that for lung parenchyma (blue). Images acquired at highlighted echo times are given below the plot. The ultra-short echo time of TE = 0.2 ms preserves the parenchymal signal before it is fully decayed and is thus the most accurate measure of spin-density; parenchymal signal

[5]Other protocols which show similar potential would include SWIFT (Sweep Imaging with Fourier Transform) [171], ZTE (Zero Echo-Time) [172], and Fourier Decomposition [173].

[6]or 'compounded'

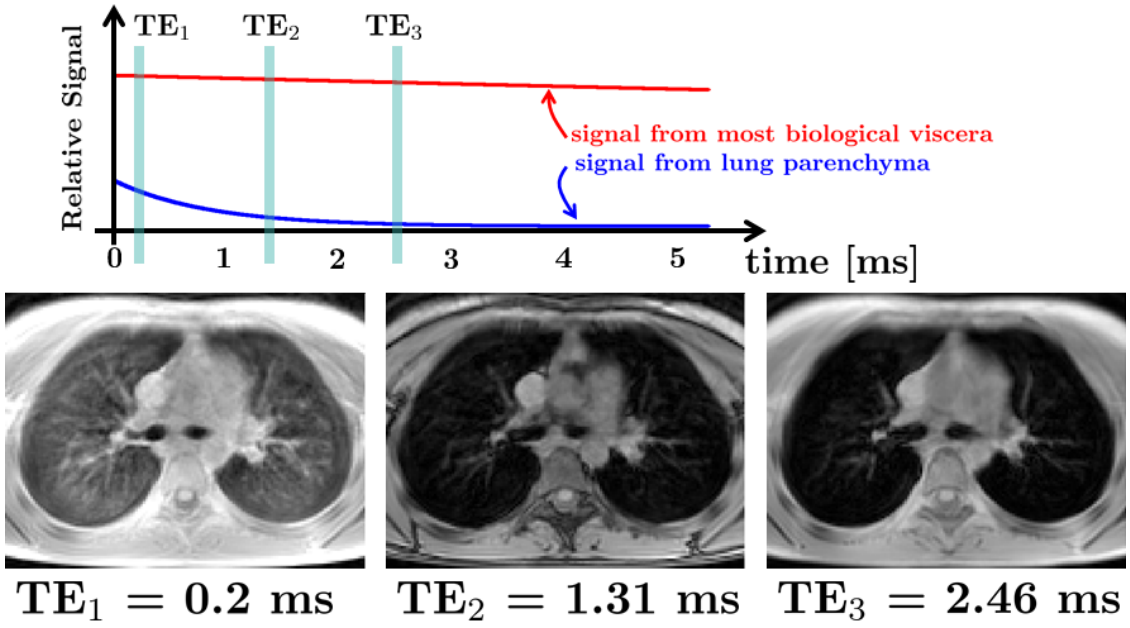

Figure 5.12: Ultra-Short Echo (UTE) Illustration Comparing FID Signal of Most Biological Tissues with Lung Parenchyma Signal. Three different echo times are highlighted with respective acquired images below (axial slices, TR = 5.78 ms, Flip Angle = 5, Voxel Size = 1.39 × 1.39 × 4 mm^3). The signal for TE_1 = 0.2 ms is considered an Ultra-Short echo time.

of the other 2 images is artificially low due to the rapid T_2^* decay. In order to achieve such short echo times, the k-space encoding scheme must be altered. For UTE MRI, k-space is acquired *radially* – that is, encoding begins at $k_x = k_y = 0$ and proceeds outward.

5.7 Troubleshooting

It is possible, however unthinkable, that image SNR is anomalously sub-optimal or that image artifacts present themselves at inopportune times. In the supreme goal of maximizing SNR, much of the discussions in this work has focused on optimization of signal, but it is equally important to identify and minimize all sources of noise. As discussed in section 2.1.3, there is an inherent level of noise in any electronic system with non-zero temperature called *Johnson noise* which follows $N = \sqrt{4kT\Delta f R}$. Minimizing spectrometer bandwidth Δf is a good first attempt to minimize noise within the scanner software; this noise must be properly

characterized to be considered baseline within the MRI spectrometer.

5.7.1 B_1 Inhomogeneity

Because the multinuclear coil hardware is constructed in-house, it is necessary to characterized the sensitivity profile of the delivered/received B_1. An early prototype of the ^{129}Xe saddle-shaped coil demonstrated a particularly stark *rf* sensitivity profile as shown in the left panel of Figure 5.13.a. The ventilation sequence was used to acquire these images which

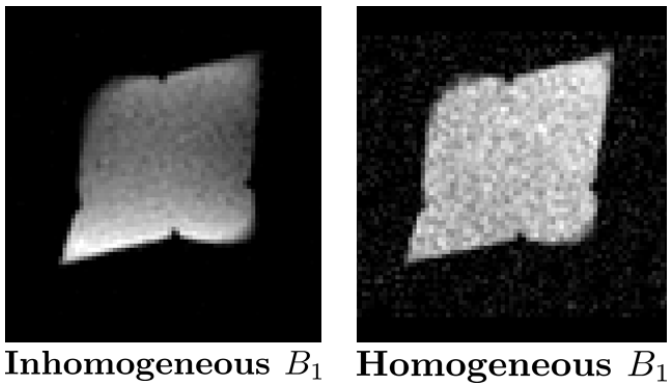

Figure 5.13: Images of HP ^{129}Xe in a Tedlar bag with Inhomogeneous vs Homogeneous *rf* sensitivity. Two different coils were used to create each image (coil elements at top and bottom of images); the coil with the homogeneous B_1 profile is currently used for all *in vivo* ^{129}Xe studies.

are known to provide spin-density maps of HP ^{129}Xe. The xenon gas is of course uniformly distributed throughout the bag volume, so we infer that spatial coil sensitivity is responsible for the signal increase near the coil elements. If this *rf* sensitivity profile is consistent for all subjects and can be precisely measured, the acquired images of *in vivo* scans can be corrected retrospectively; this was the approach taken in data collected for our asthma study detailed in section 7.1 (correction described in section 6.2). A second ^{129}Xe coil was constructed with larger conductive elements to achieve greater B_1 homogeneity (Figure 5.13 right panel); however this coil demonstrates about 70% the SNR of the first coil with the

same flip angle[7]. The author is convinced that this trade is more than fair as sensitivity correction has high potential for systematic error (this will be described in more detail in section 6.2), and mitigation of these issues at earlier points in the data processing chain is always preferred.

5.7.2 Minimizing Noise

One critical issue which became apparent soon following implementation of hardware for HP gas imaging was the emergence of atypical noise profiles in the data. Figure 5.14 presents several plots of acquired noise data at the ^{129}Xe frequency ($f_{^{129}\mathrm{Xe}} = 35.3$ MHz) both before and after a major noise source was rectified. Notice the apparent noise 'spikes' in the FID data (a). The histogram of (a) shown in panel (b), appears Gaussian, but the horizontal scale indicates that the tails of the distribution are anomalous. This is more apparent in panel (c) which is a Q-Q plot of the data in (a); the non-linear portion of the plot indicate problematic data[8]. By simply recording the noise within the magnet room using the ^{129}Xe coil as an antenna, the source of the anomalous noise can be identified. In the case of this particular noise hunt, the source of the spikes was found to be a misbehaving mechanical fan within the scanner bed. The fan has been replaced, and identical experiments reveal the appropriate Gaussian noise distribution (panels d,e,f).

5.7.3 Identifying Gain Issues

It is desirable to avoid any possible sources of HP gas relaxation in between dispense and administration to the subject. When an MRI sequence is executed, scanners generally employ various preparation phases prior to performing the desired imaging sequence. Some of these

[7]The images in Figure 5.13 show the same bag of HP ^{129}Xe imaged twice in succession – first with the inhomogeneous coil, then with the homogeneous coil. Of course, the polarization loss from the first scan was taken into account in the calculation of the SNR discrepancy of 70%.

[8]As a reminder, a Q-Q plot is a visualization of how well data match a given probability distribution. These Q-Q plots are generated by measuring the mean and standard deviation of the data and creating a Gaussian dataset with equal mean, standard deviation, and length. When the data of the two distributions are sorted least to greatest and plotted against one another, a linear relationship of slope = 1 indicates the Gaussian distribution appropriately models the data.

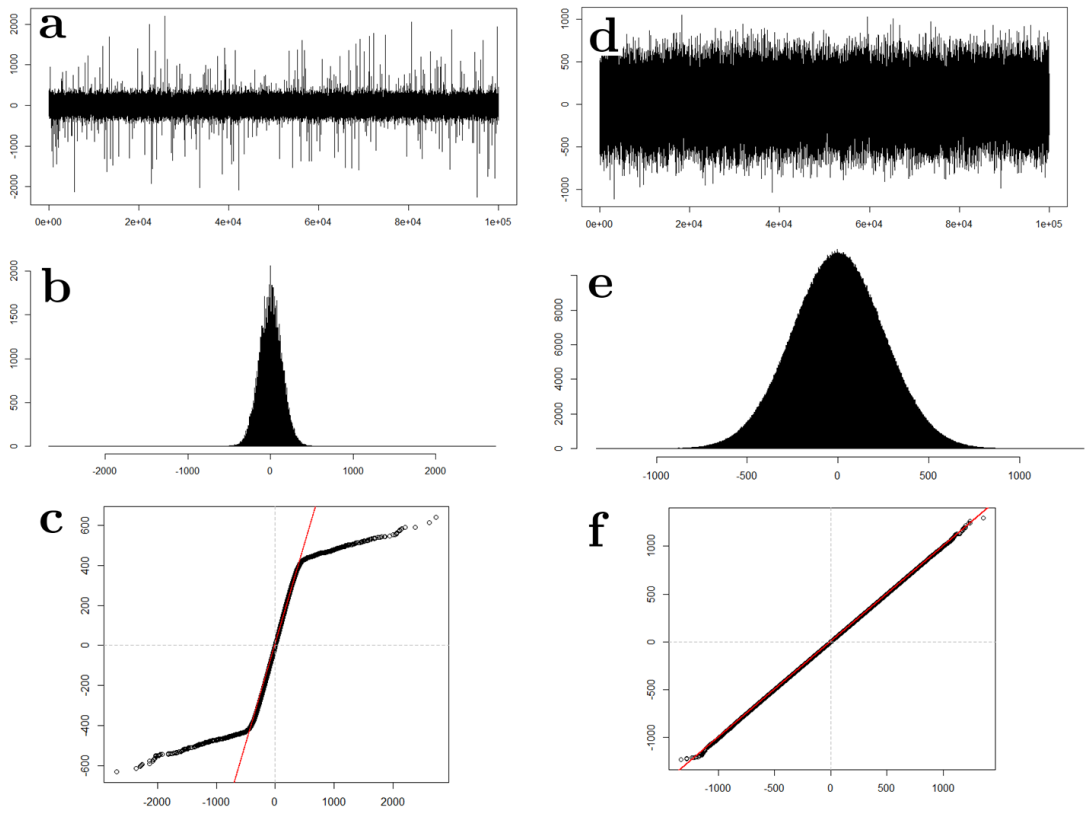

Figure 5.14: Plots of 'Bad' (a,b,c) and 'Good' (d,e,f) Noise Profiles. Panels **a** and **d** are single FID's – y axes are arbitrary but congruent, x axes are acquisition number. Panels **b** and **e** are histograms of the acquired FID data. Panels **c** and **f** are Q-Q plots of the FID data – x axes are acquired data, y axes are synthesized data (the red line indicates the line $y = x$).

include gain optimization, magnet shimming, automatic coil tuning/matching adjustments, etc. Because a number of these preparation phases involve delivery of *rf* to the sample, early experiments revealed that approximately 20% of HP gas polarization was lost during the preparation phases. Therefore it was originally decided that these 'prep phases' be disabled for HP gas scans. Unbeknownst to us at the time, this resulted in a sizable drop in pre-digitization gain within the signal receive chain which, unfortunately, went unnoticed for a number of *in vivo* scans. As a consequence, the dynamic range of the received signal was not appropriately scaled to that of the analog-digital converter resulting in loss of bit depth. The received signal was therefore inappropriately discretized as shown in Figure 5.15.

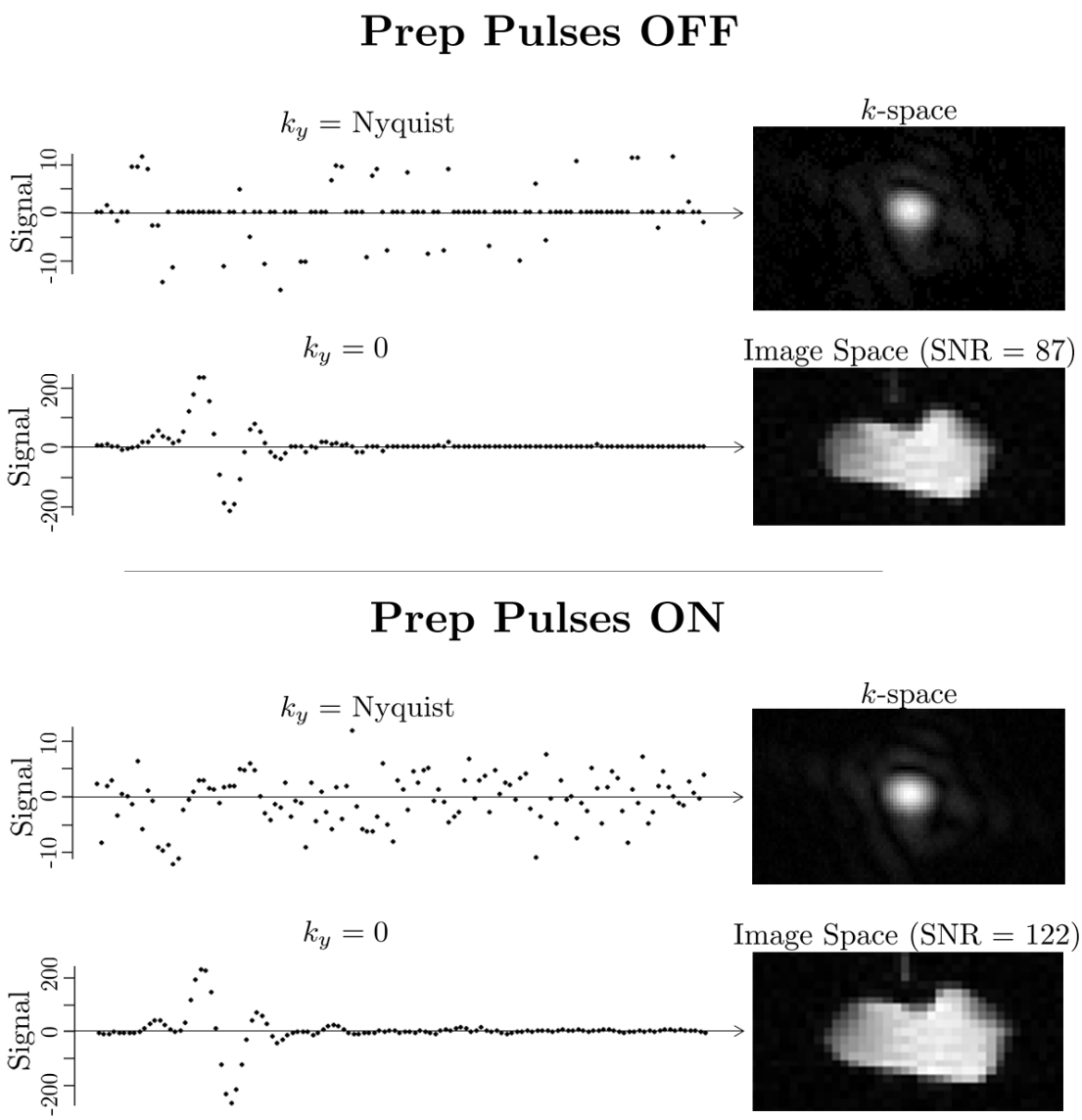

Figure 5.15: Illustration of the Effects of Low Bit-Depth on Acquired Images. When the prep pulses are off, the receiver gain is miscalibrated and the acquired signal is discretized resulting in a loss of SNR. When the prep pulses are on, the gain is appropriately scaled to the receiver analog-digital converter. Signal is given in arbitrary units but is consistent for all plots.

When preparation phases are off, receiver gain is not optimized and individual data points become 'binned' to the few digital levels across which the signal spans. This is perhaps more easily seen in readouts near the Nyquist frequency where NMR signal is low. As shown, this

results in a loss in SNR. Proper gain calibration scales the analog signal across all available digital levels of the analog-digital converter and the bit depth of k-space is preserved. Notice that this problem is only recognized by meticulous evaluation of the raw signal data since the issue does not prohibit production of a seemingly satisfactory image. As a standard part of our protocol, all preparation pulses are allowed to run, but no HP gas enters the magnet room until they have completed and the scanner operator is prompted to begin a breathold.

5.7.4 The Dangers of Real-Time Gain Optimization

Sometimes, MRI scanners perform undesirable operations under-the-hood which can unfavorably alter sequence parameters or acquired data. Automatic receiver optimization was one particular occurance where this behavior produced dazzling errors in our acquired data. In essence, receiver gain was being inconsistently adjusted for each individual readout acquisition. Figure 5.16 illustrates this error and the resulting k-space and image space artifacts. Clearly, the gain of several readouts was incorrectly applied resulting in 'VCR tracking' noise[9]. This issue can be manually disabled, but is generally not a problem as long as the sample is appropriately placed at the isocenter of the magnet (this is most often a problem with phantoms rather than human subjects).

5.7.5 Troubleshooting Summary

If not abundantly clear, the moral of this section is to *know your equipment*, a critical part of which is proper characterization and minimization of noise. If the noise is not Gaussian, there remain issues to be resolved. Although a pulse sequence diagram seemingly reveals all necessary information to understand image acquisition, an MRI scanner is a complicated machine with multitudes of standard operations performed to produce an image. Scanner issues tend to present themselves at the most unfortunate times, but a working knowledge of the underlying software architecture and procedures allows one to address and potentially

[9] A video cassette recorder (VCR) is an artifact from ancient cultures used to record and playback video information.

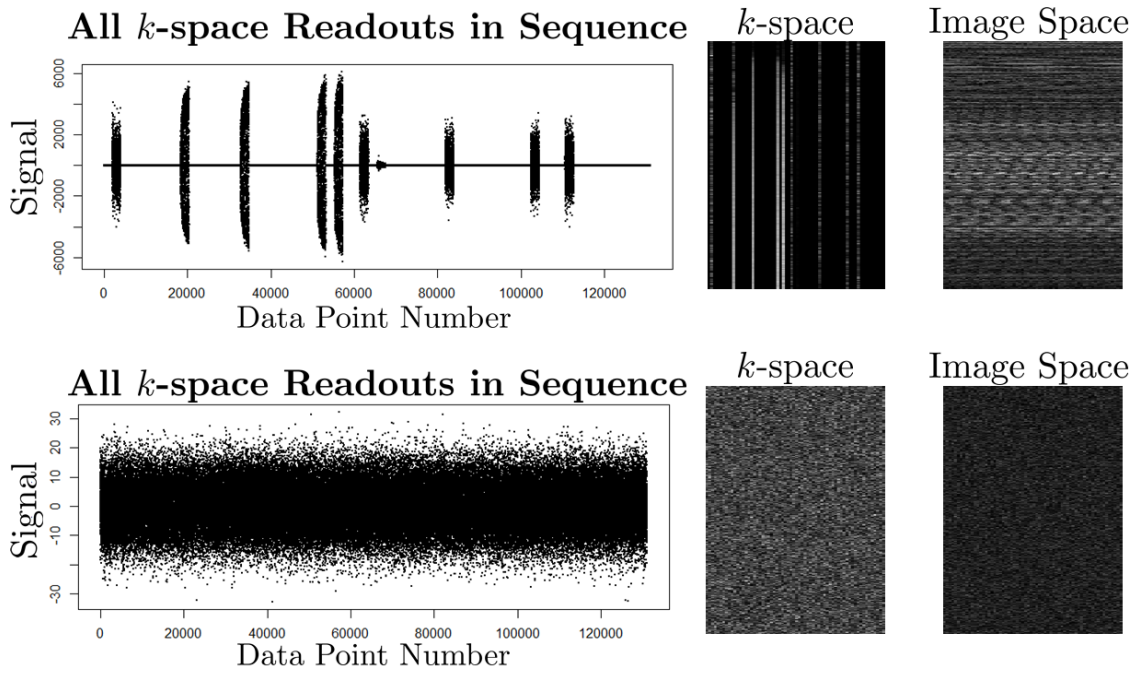

Figure 5.16: Illustration of the Effects of Variable Readout Calibration. Improper gain optimization was performed in the data at top; no correction is applied for data at bottom. Plots are of all acquired data in sequence (all readouts end-to-end).

mitigate costly problems in real-time.

5.8 Summary

We have now been introduced to the HP gas acquisition protocol as it is performed *in vivo* for our experiments along with some anecdotes regarding scanner issues and solutions. The next chapter will detail the various methods of analysis of the acquired data which in effect will identify connection between imaging information and lung function. The reader will then be fully equipped to understand the novelty and uniqueness of the results presented in chapter 7.

Chapter 6

Image Analysis for Quantitification of Lung Structure and Function

> "The right man in the wrong place can make all the difference in the world."
>
> — Gman, *Half-Life 2*

In the last chapter we examined the process by which images of lungs are acquired on a 3.0T MRI scanner. This chapter will detail the analysis by which these 2-dimensional, discrete functions of intensity are used to reveal *quantitative* information related to lung structure and lung function. First we will consider proton images (which generally reveal measures of anatomic structure), then hyperpolarized gas images (which can reveal measures of *both* structure and function).

As discussed in chapter 5, standard thoracic GRE images reveal little useful information concerning lung structure or function and are therefore not discussed in detail here. It is notable however, that dozens of researchers around the world have developed novel techniques of bringing lung structure-function to light (see ref [32]). In the context of proton imaging here, pulmonary information is exclusively evaluated from UTE MRI described in section 5.6. This chapter will begin by presenting UTE analysis and move into hyperpolarized gas image analysis following. A brief comparison of ^{3}He and ^{129}Xe in the context of HP gas imaging

will then be given.

6.1 Ultra-Short Echo Images

UTE images are produced so that structural pulmonary information may be deduced similar to that of a CT. Figure 6.1 presents UTE images of a healthy volunteer alongside ROI signal measures similar to those presented in Figure 1.8. This technique is still in

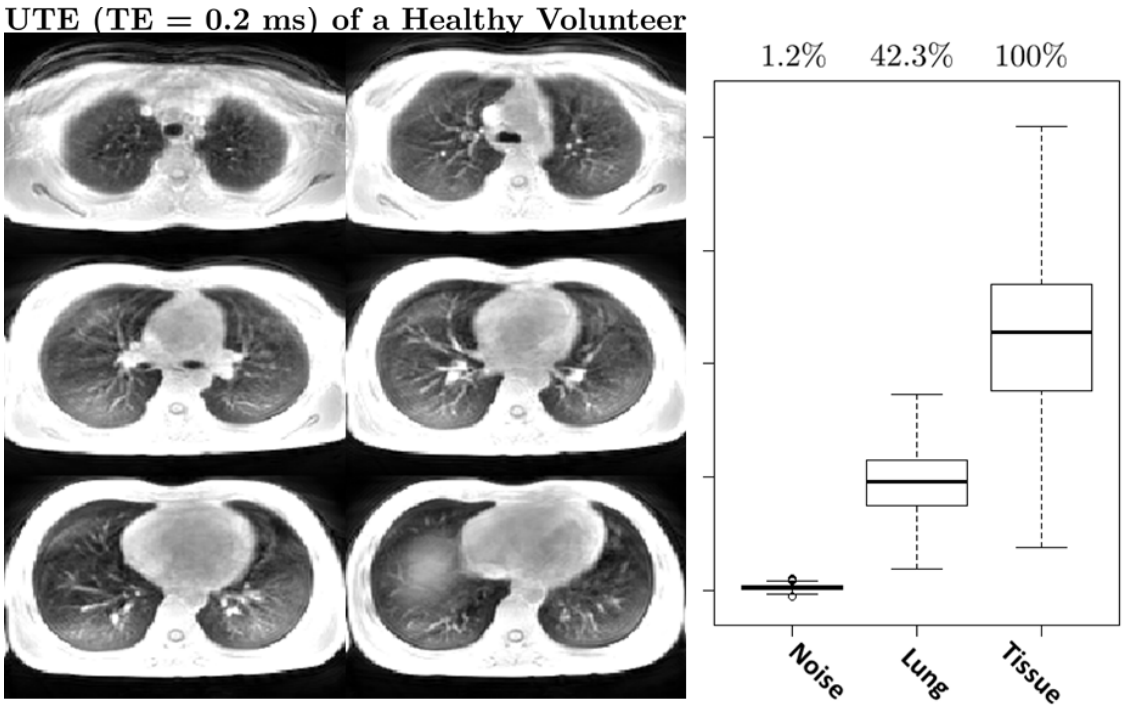

Figure 6.1: Example UTE Images of a Healthy Volunteer and Measures of MRI and CT signal for Various Regions of Interest. Compare with values from Figure 1.8.

its infancy, and the resolution and contrast of these images are approaching that of CT, but pulmonary MRI of this quality is truly a landmark accomplishment and has already been shown to reveal structural pathology in agreement with CT [174, 175]. For studies in this dissertation, methods of UTE analysis are limited to radiological interpretation (by a radiologist, not by the author) using various scoring methods. In particular, the 'Brody' scoring [176, 177] method of pathology identification has been used for study of cystic fibrosis

alongside HP gas imaging. This will be presented in more detail in section 7.2.

As an aside, because our UTE sequence produces 3 images at different echo times, we have the unique ability to produce T_2^* maps of lungs. Figure 6.2 presents an example image of a T_2^*map created from the Multi-Echo UTE. It is currently hypothesized that regional T_2^*

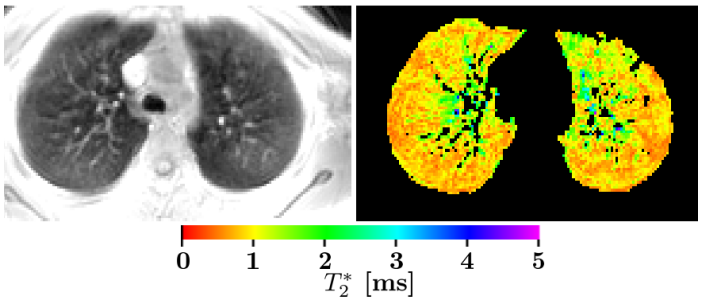

Figure 6.2: Example of a T_2^* Map Created from Multi-Echo UTE.

may be an indicator of alveolar structure since the multiple air-tissue interfaces create stark magnetic susceptibility differences in the parenchyma.

6.2 Ventilation Images

Ventilation images are meant to provide spin-density maps of the inhaled HP gas during a breathold. In effect this allows one to answer the question *Where does the gas go when inhaled?* For healthy lungs, one might expect that the inhaled HP gas would completely flood the interior of the lung. In fact, this is largely the case. Figure 6.3 presents example ventilation images of ^{3}He in a healthy adult volunteer. Notice that that the signal is homogeneously distributed throughout the lung volume indicating uniform ventilation within the parenchyma. Figure 6.4 presents similar images from a subject with severe asthma. In this case the signal is considerably more heterogeneous throughout the lung volume, and of particular importance, there appear to be regions in which no HP gas seems to be present. These regions of defective ventilation are called *ventilation defects*[1], and are a hallmark of disease in HP gas imaging [37, 178, 179, 180, 181]. Defects have been identified in these

[1]Etymology unknown

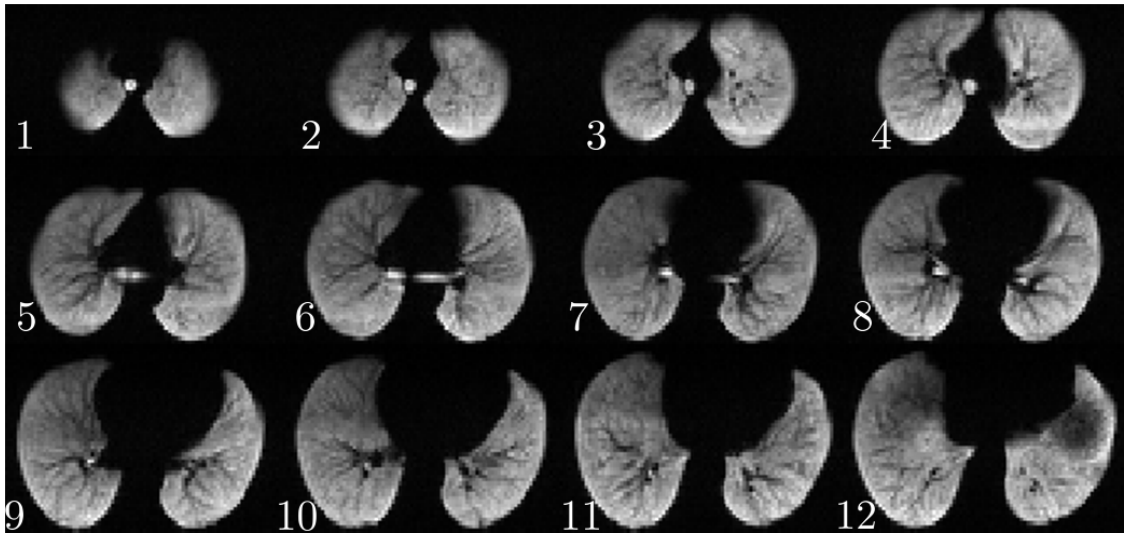

Figure 6.3: Example HP ^{3}He Ventilation Images of a Healthy Adult Volunteer. Images proceed in chronological order from apex to base. TE/TE = 140/3 ms. Matrix = 64 PE × 128 RO, FA = 5°, Voxel size = 3 × 3 × 10 mm^3.

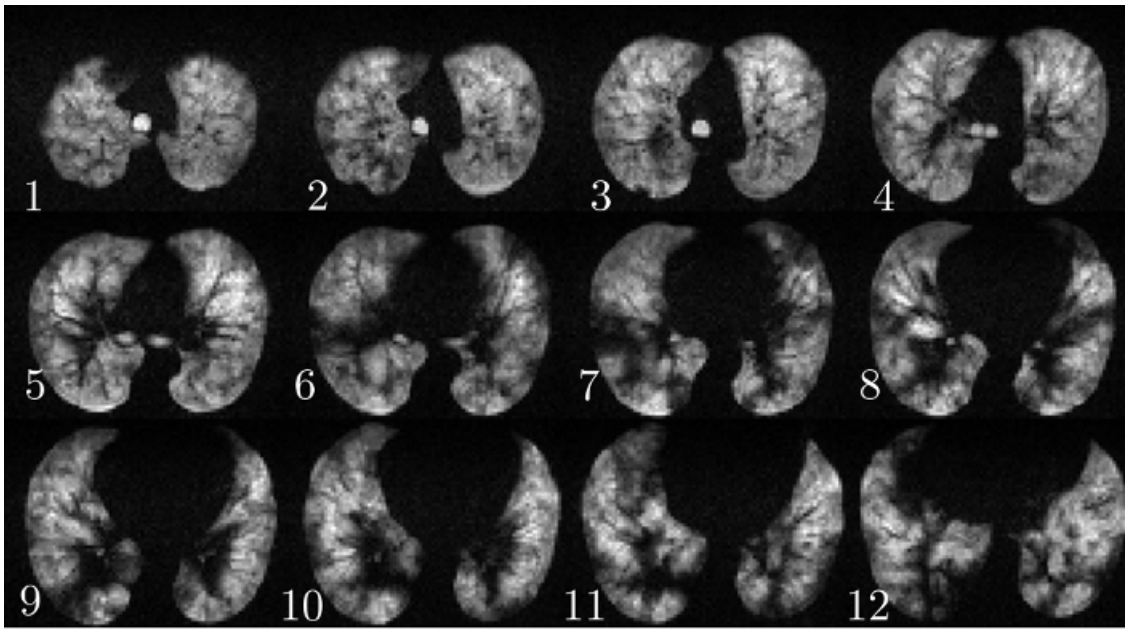

Figure 6.4: Example HP ^{3}He Ventilation Images of an Adult Volunteer with Severe Asthma. TE/TE = 140/3 ms. Matrix = 64 PE × 128 RO, FA = 5°, Voxel size = 3 × 3 × 10 mm^3.

images as voxels with signal less than 60% of the whole-lung signal mean since this provides the greatest contrast between healthy and pathologic lungs (Figure 6.5.a) [41]. Histograms of conglomerate voxel signal intensity for a collection of 6 healthy adults is compared that of 9 severe asthma patients in Figure 6.5.b. Importantly, note the greater percentage of voxels with signal intensities both above and below the mean for asthmatic data. This is expected since each subject inhales the same amount of HP gas – thus, if a region of the lung is hypoventilated there must exist regions which are hyperventilated in response.

A popular method of quantifying disease severity from ventilation images is to measure the percentage of lung volume in which ventilation is defective. As noted above, this has been adopted by our group in the form of a simple *defect threshold*: if the signal within a voxel is below this threshold it is marked as a defect voxel. The defects are then 'cleaned up' by applying a median filter to the defect array (3×3 voxel kernel size) which removes defects less than 5 voxels in size (considered inconsequential) and smooths defect contours. Obviously, only voxels which intersect the parenchymal volume are to be evaluated; a 'mask' array is used to identify such voxels. Figure 6.6 illustrates this process for ^{3}He ventilation images of a healthy volunteer. Figure 6.7 shows the same for a severe asthma patient. The mask arrays are generated semi-automatically by the user either by direct registration of pre-existing masks (as was done in the case of asthma, section 7.1) or by manual generation of masks based on visible anatomic markers (as was done in the case of cystic fibrosis,

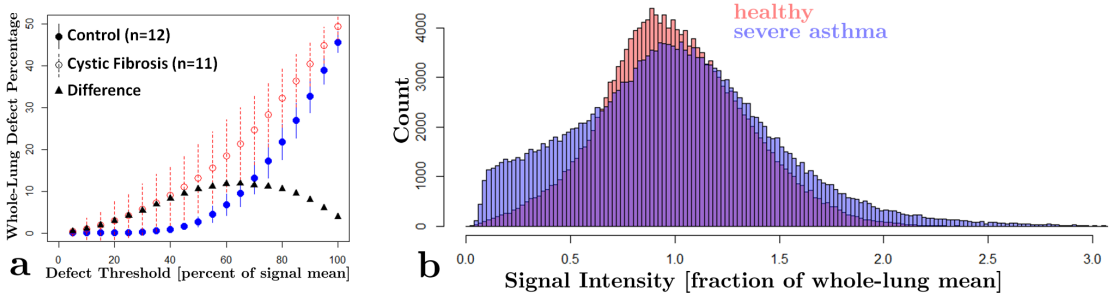

Figure 6.5: Plot of Defect Percentage vs Threshold (expressed as percentage of whole-lung signal mean) for healthy and systic fibrosis groups (a) and Overlapping Histograms of Signal Intensity for HP Gas Images of Healthy Volunteers and Severe Asthma Patients (b). Each image set is normalized to its own signal mean.

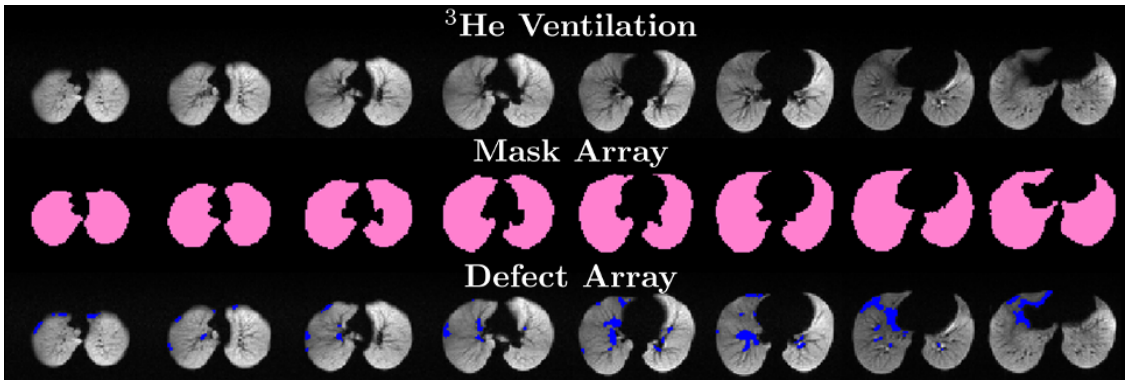

Figure 6.6: Ventilation Image Analysis of a Healthy Volunteer.

section 7.2). Other groups have had success employing more elaborate approaches to defect identification [16, 182, 183], but our simple binary identification method effectively emulates manual, visual defect identification by a radiologist.

Although ventilation defect percentage (VDP) is a useful and well-accepted metric for evaluation of lung function its functional specificity is lacking [37, 183, 184, 185]. The binary nature of the VDP may suppress the extent to which defects present themselves physiologically. A second measure of lung ventilation was developed by the author which quantifies *respective* ventilation within individual lung compartments. This has been useful for airway studies in which an upper airway constriction may adversely effect the ventilation

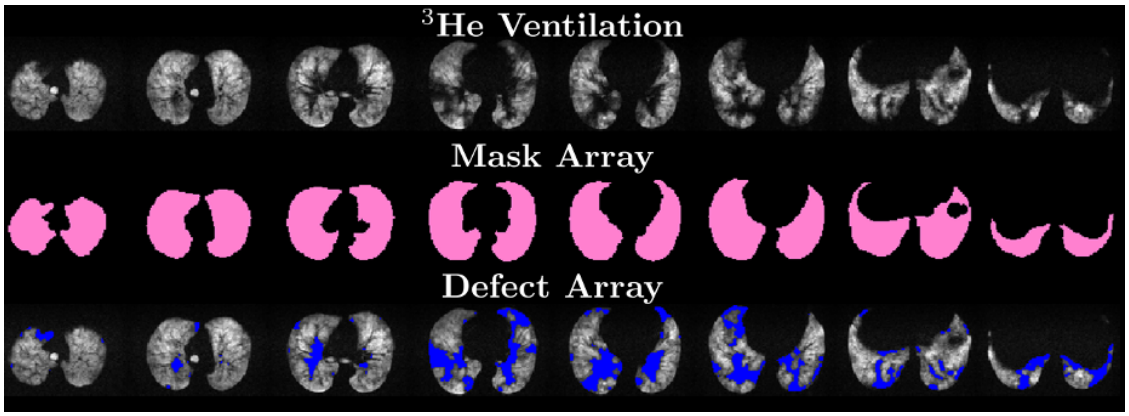

Figure 6.7: Ventilation Image Analysis of a Severe Asthma Patient.

of an entire lobe or bronchopulmonary segment. This measure has been deemed a *segmental ventilation percentage* (SVP) (so called because it is specific to a particular lung segment). Because this technique was developed in the context of severe asthma research it will be discussed in detail in section 7.1.

6.3 Diffusion Images

In section 2.2.4 we developed the theoretical framework for diffusion MRI, and in section 5.5 the methods of diffusion imaging were described. Here the methods of linking a collection of diffusion images to pulmonary physiology will be detailed. The methods described here are applicable to both noble gases of interest in this work, but because their respective diffusion coefficients are quite different ($D_{^3\mathrm{He}} = 0.88$ cm^2/s, $D_{^{129}\mathrm{Xe}} = 0.14$ cm^2/s dilute in air [69]), *in vivo* validation must be performed separately. Because the same analysis applies to both gases, the sensitivity of diffusion imaging can be appropriately adjusted to each noble gas by judicious selection of diffusion weighting b-values as per $S = S_0 e^{-bD}$. Section 6.4 will compare/contrast ^{3}He and ^{129}Xe in this regard; the analysis described here is relevant for both gases.

The following discussion is separated into two categories: 2-b-value diffusion imaging and multiple-b-value diffusion imaging. This has been chosen primarily to highlight the author's contribution to the field (xenon validation as a biomarker for airspace size [42]), but novel multi-b diffusion methods has been shown to reveal information relating even to acinar microgeometry and require discussion as well. Multi-b-value analysis will be given less attention however since only the 2-b-value techniques have been applied to investigations of the major hypotheses in this work[2]

[2]No doubt the reader is privately questioning the necessity of separate discussion since, according to section 2.2.4, any number of b-values describes diffusion by $S = S_0 e^{-bD}$. Well, prepare to be dazzled...

6.3.1 2-b-value Diffusion Images

Upon application of a bipolar diffusion sensitizing gradient, the signal of the acquired MR image will be weighted according to $S = S_0 e^{-bD}$ where b is the b-value defined by the imaging gradient waveform parameters, and D is the diffusion coefficient of the gas. Because b is a precise measure input by the scanner operator, the diffusion of the gas D can be measured using no fewer than 2 images: one unweighted ($b = 0$ s/cm^2) and one or more diffusion-weighted ($b > 0$ s/cm^2). For the case of 2 b-values, $b = [0, b_1]$ s/cm^2, diffusion can be measured by $D = \frac{1}{b_1}\big[\ln S_0 - \ln S\big]$.

Gas that has been inhaled and resides within the lung parenchyma is restricted in its diffusive motion due to collisions with the alveolar walls. As such the measured diffusion coefficient is *not* characteristic of the gas itself, rather it reflects *airspace size* and is thus called an *apparent diffusion coefficient* (ADC). Figure 6.8 illustrates a particular lung pathology in which gas diffusion is uniquely sensitive to alveolar structure: emphysema. Emphysema

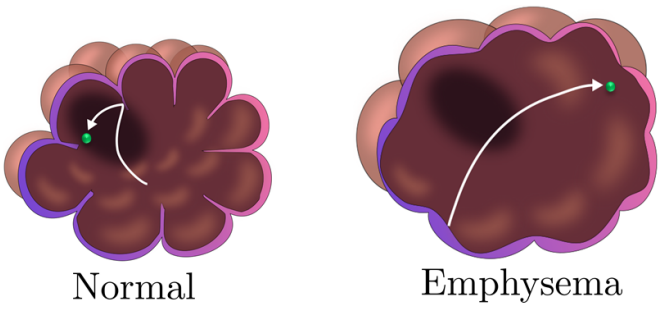

Figure 6.8: Illustration of Normal vs Emphysematous Alveolar Duct. Gas diffusion is more restricted in normal lung; measured ADC is therefore expected to be higher in lungs with emphysema.

is characterized by deterioration of alveolar walls, and hyperpolarized gas MRI has demonstrated unparalleled sensitivity in revealing the precise extent of parenchymal damage and tissue destruction [186, 187, 188, 189]. Figure 6.9 presents unweighted ($b = 0$ s/cm^2) and diffusion weighted ($b = 12.5$ s/cm^2) HP ^{129}Xe images of an explanted human lung alongside their respective calculated ADC map. These data were acquired on a Siemens Avanto 1.5T MRI scanner (Siemens Medical Solutions, Malvern, PA, USA).

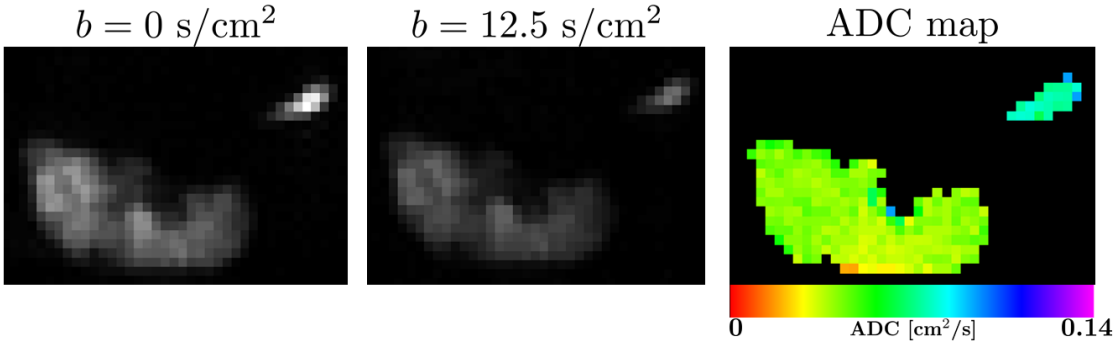

Figure 6.9: Illustration of 2-*b*-Value Images and ADC map. FA = 4-6°, TR/TE = 22/16 ms, 6 × 6 × 6 mm^3 voxel size, pixel BW = 130Hz, $\Delta = \delta = 5$ ms. Notice that the gas delivery tube in the top right corner of each image demonstrates greater HP gas diffusion than the lung interior.

Selection of an appropriate *b*-value for the anticipated gas diffusion coefficient is imperative to acquiring optimum data for precise ADC calculation. First, appropriate *timing* of the diffusion gradient must be chosen such that an individual gas atom appropriately 'samples' the alveolar environment[3]. If the diffusion time is too short, an HP gas atom does not have sufficient time to encounter an alveolar wall, and the measured ADC will reflect the intrinsic gas diffusion coefficient rather than the sample airspace size. If the diffusion time is too long, gas atoms are able to diffuse across several alveolar ducts and do not represent average duct size[4] (see Gierada *et al.*, for an experimental investigation of these sampling regimes [193]). This is illustrated in Figure 6.10. Using the Einstein-Smoluchowsky equation one can determine an appropriate gradient time $\Delta = \frac{L^2}{4D_0}$ for a given HP gas; for our experiments $\Delta_{^3\mathrm{He}} \approx 1.5$ ms and $\Delta_{^{129}\mathrm{Xe}} \approx 6.4$ ms.

Once gradient timing is fairly chosen for the HP gas of interest, the appropriate *b*-value magnitude (proportional to the square of the diffusion-weighting gradient strength G^2) can be chosen. Figure 6.11 illustrates relative signal attenuation for an individual voxel for 3 different *b*-values magnitudes. Too small of a *b*-value (shown in green) provides too little

[3]Recall from section 2.2.4 that $b = \gamma^2 G^2 \left[\delta^2\left(\Delta - \frac{\delta}{3}\right) + \tau\left(\delta^2 - 2\Delta\delta + \Delta\tau - \frac{7}{6}\delta\tau + \frac{8}{15}\tau^2\right)\right]$ where Δ is the time between bipolar gradient lobes and δ is the lobe duration.

[4]Some have taken advantage of this fact to examine the role of collateral pathways in diffusion imaging [190, 191, 192] (only in ^{3}He due to its much larger diffusion coefficient compared to xenon).

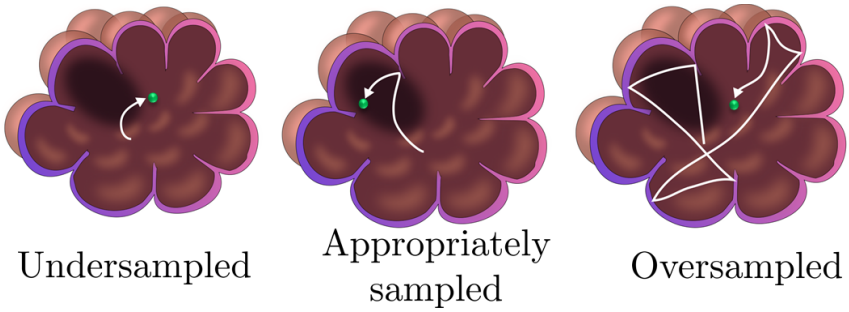

Figure 6.10: Illustration of Alveolar Sampling Regimes.

contrast between weighted and unweighted images. Too large of a b-value will attenuate the signal into the noise floor yielding no useful information. What b-value should be chosen such that the error on an individual voxel measurement is minimized[5]?

The error of an individual voxel can be calculated by applying simple error propagation [194] to the ADC solution $D = \frac{1}{b_1}\big[\ln S_0 - \ln S\big]$ which follows[6]

$$\begin{aligned}\sigma_D^2 &= \sigma_{S_0}^2\Big(\frac{\partial D}{\partial S_0}\Big)^2 + \sigma_S^2\Big(\frac{\partial D}{\partial S}\Big)^2 \\ &= \frac{1}{b^2}\Big[\frac{\sigma_{S_0}^2}{S_0^2} + \frac{\sigma_S^2}{S^2}\Big]\end{aligned} \tag{6.1}$$

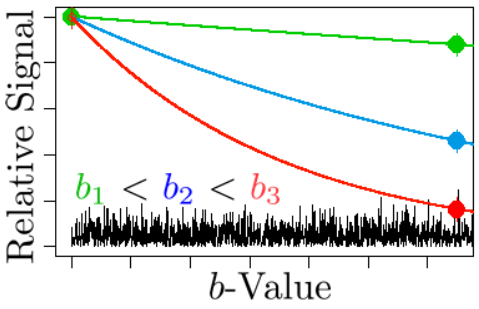

Figure 6.11: Illustration of 2-b-Value Diffusion Measurement Precision for the cases of too small a b-value (green) too large of a b-value (red) and an appropriate b-value (blue). The image noise floor is represented by the jagged black line.

[5]Since the error obviously depends on the diffusion coefficient which is unknown, a more appropriate question would be 'what b-value will minimize error for the greatest *range* of measurable diffusion coefficients?'

[6]For simplicity here, D is used in lieu of ADC.

Here we recognize that the expression S_i/σ_{S_i} is the SNR of the i^{th} image (SNR_0 for unweighted, SNR_1 for weighted). Also, the noise floor of two images which follow identical acquisition protocols are in fact equal $\sigma_{S_0} = \sigma_S$. Upon substitution of $S = S_0 e^{-bD}$ we find

$$\sigma_D^2 = \frac{1}{b^2}\left[\frac{1}{\mathrm{SNR}_0^2} + \frac{1}{\mathrm{SNR}_1^2}\right] = \frac{1}{b^2 \cdot \mathrm{SNR}_0^2}\left(1 + e^{2bD}\right). \tag{6.2}$$

Thus the percent error of an individual voxel follows

$$\frac{\sigma_D}{D} = \frac{1}{b \cdot D \cdot \mathrm{SNR}_0}\sqrt{1 + e^{2bD}}. \tag{6.3}$$

Importantly, the unweighted image SNR_0 is the dominant variable in the expression for increased precision (relative to b or ADC). Figure 6.12 shows plots of ADC percent error as a function of measured ADC for b-values ranging from 1 s/cm^2 to 25 s/cm^2 (assuming SNR_0 = 100). The ADC and b-value ranges depicted here are appropriate for ^{129}Xe imaging, but

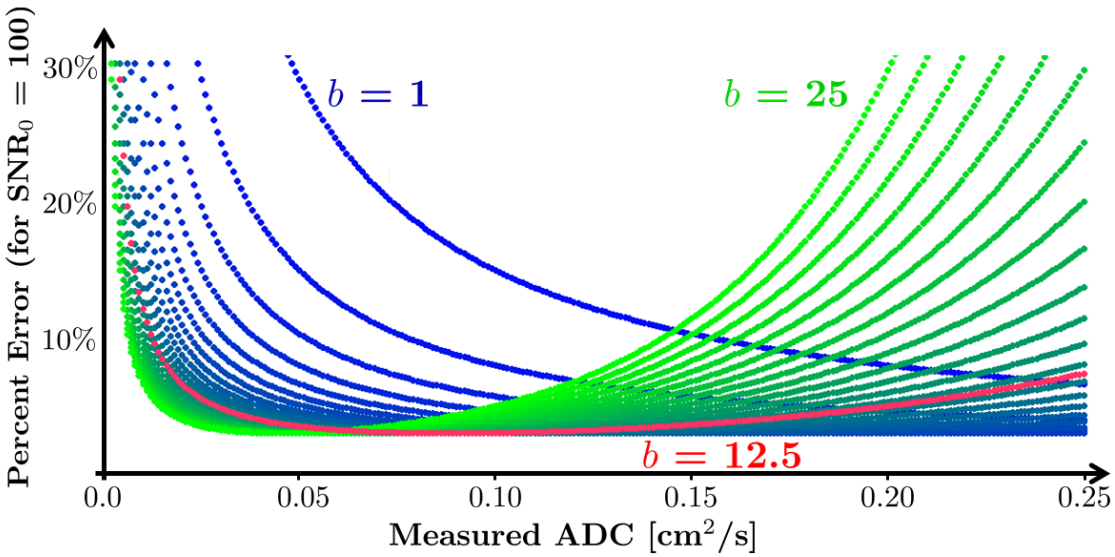

Figure 6.12: ADC Percent Error vs ADC for Several Different b-Values. The b-value $b = 12.5$s/cm^2 is highlighted red as this is the chosen b-value for HP ^{129}Xe experiments in explanted COPD lungs (section 7.3). Note that this plot presents ADC values much greater than that of dilute xenon in air (D_d = 0.14 cm^2/s) to better illustrate the behavior of 2-b diffusion error.

the error behavior would be similar for ^{3}He. Notice that, as expected, low b combined with low ADC does not provide satisfactory contrast for precise ADC measurement. Likewise a large b-value and large ADC will drop the diffusion-weighted signal into the noise degrading precision. For experiments with ^{129}Xe described in this work (section 7.3) a b-value of $b = 12.5$ s/cm^2 is used (highlighted red in the image).

6.3.2 Multi-b-value Diffusion Images

As one might imagine, a greater number of diffusion weighted images will generally increase the precision of an individual voxel ADC measurement. In general this is true, but in fact, the true merit of multiple-b-values is in its ability to reveal information related to actual alveolar micro-geometry; that is, even parameters such as alveolar duct morphometry and alveolar sac radius can be quantified [258, 259, 261].

We have recently implemented a 5-b-value diffusion sequence for our studies which can be used for these purposes, and the author verified the integrity of the results by a simple test experiment which is presented in Figure 6.13. Two bags of hyperpolarized ^{129}Xe were prepared with different xenon concentrations in the presence of nitrogen. Estimates of noble gas diffusion coefficient D can be expressed as a function of concentration in air using the following relationship [195]

$$\frac{1}{D} = [X]\frac{1}{D_0} + (1 - [X])\frac{1}{D_d} \tag{6.4}$$

where $[X]$ is the noble gas concentration in air (expressed in units of atom fraction), D_0 is the noble gas self-diffusion coefficient ($D_{0,^3\mathrm{He}} = 2.05$, $D_{0,^{129}\mathrm{Xe}} = 0.06$ [cm^2/s], at STP), and D_d is the noble gas diffusion coefficient dilute in air ($D_{d,^3\mathrm{He}} = 0.86$, $D_{d,^{129}\mathrm{Xe}} = 0.14$ [cm^2/s], at STP) [69]. Diffusion coefficients for xenon and helium in air are plotted in Figure 6.14. As Figure 6.13 illustrates, analysis of a control dataset (unrestricted diffusion xenon at a known concentration) reveals the expected result for diffusion coefficient; thus we conclude that the sequence is working properly and is ready for *in vivo* experiments.

6.4 ^{3}He vs ^{129}Xe

So far throughout this dissertation, hyperpolarized ^{3}He and ^{129}Xe have been treated as if they are interchangeable. Now that the theoretical, methodological, and analytical techniques of hyperpolarized gas MRI have been discussed in detail, it is prudent to thoroughly examine the strengths and weaknesses of each. Chapter 3 presented a very cursory glance at other noble gas nuclei and their utility (or lack thereof) in HP gas research so this section will focus exclusively on ^{3}He vs ^{129}Xe.

Table 6.1 presents comparisons of several important properties for helium and xenon to

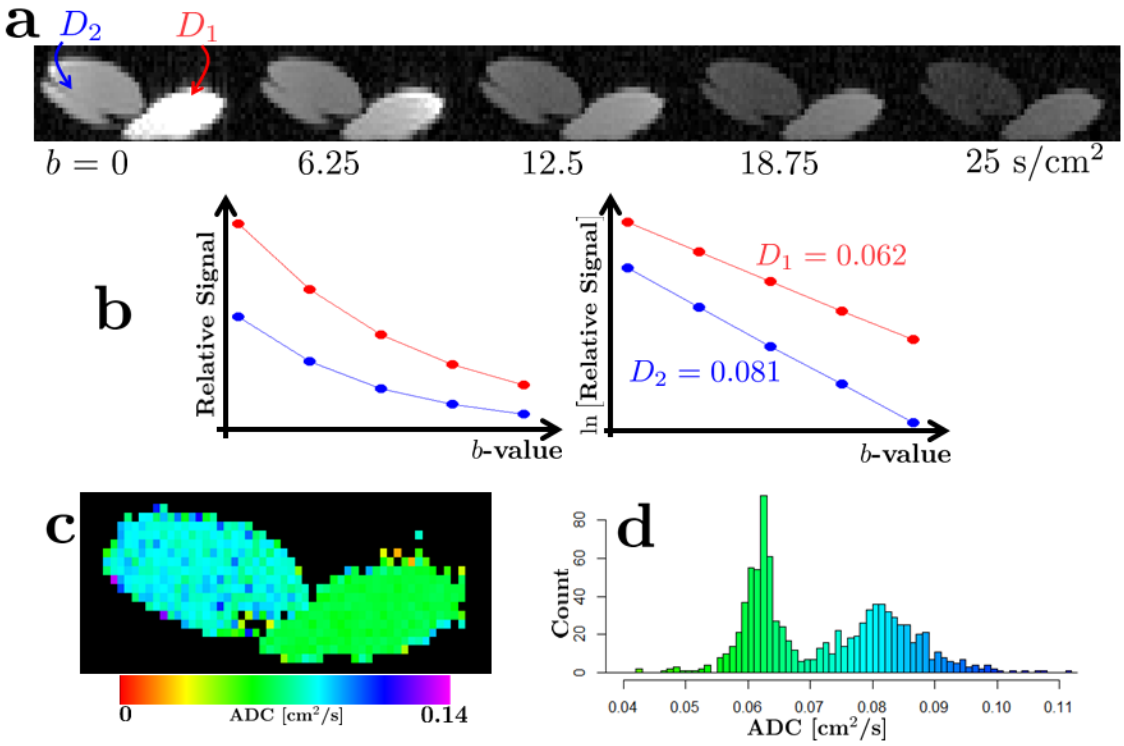

Figure 6.13: Diffusion Images of 2 Tedlar Bags with Different Concentrations of ^{129}Xe (a). One bag is 100% xenon the other is a mixture of 50% xenon, 50% N_2. The different xenon diffusion coefficients lead to different decay rates (b). An ADC map of the diffusion images is given in (c), and a histogram of the diffusion values in the ADC map (with matching color scale) is given in (d). Calculated diffusion coefficients were $D = 0.083 \pm 0.009$ for the 50/50 mixture and $D = 0.063 \pm 0.006$ for the 100% mixture. The uncertainty of each D measurement increases with reduced SNR, hence the 50/50 mixture demonstrates a broader histogram peak.

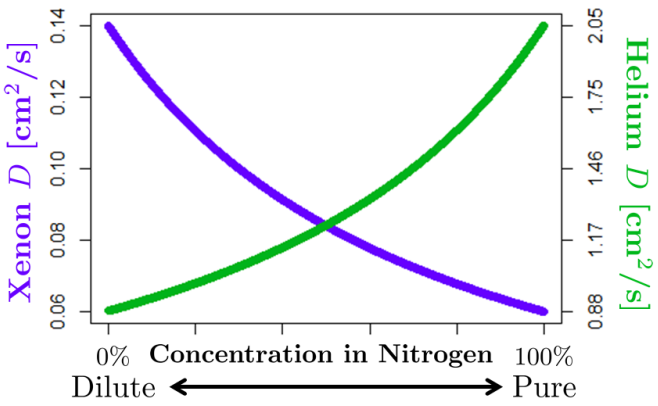

Figure 6.14: Plots of Xenon and Helium Self-Diffusion Coefficient as a Function of Concentration in Nitrogen (Air) – calculated from equation 6.4. Values for xenon are on the left axis, helium on the right. [195, 196]

be taken into account for HP gas imaging. First, the gyromagnetic ratio of ^{3}He is $\gamma_{^3\text{He}} = 32.4$ MHz/T and for ^{129}Xe is $\gamma_{^{129}\text{Xe}} = 11.8$ MHz/T yielding a γ which is 2.75 times higher for helium. We therefore expect nearly 8 times the signal from helium compared with xenon at equal concentration and polarization since $S_{\text{HP}} = \frac{1}{2}N\gamma^2\hbar B_0 P$ (section 2.1.3). Further, xenon has historically lagged behind helium in maximum achievable polarization (currently, the world record for helium polarization is 81% [197]); this has become less of a concern recently with rapid development of high-powered diode laser technology and unique hyperpolarizer

Property	^{3}He	^{129}Xe
gyromagnetic ratio γ [MHz/T]	32.4	11.8
T1 in situ† [hr]	50	20
T1 in vivo [s]	30	30
Spin-Up Time† [hr]	24	0.5
Achievable Polarization†	60%	25%
Self Diffusion D_0 [cm^2/s]	2.05	0.061
Dilute Diffusion D [cm^2/s]	0.86	0.14
Ostwald Solubility [L]	0.0085	0.17
Natural Abundance	0%	26%
Cost (enriched) [\$/L]	>1000	200

Table 6.1: Comparison of Various Properties of ^{3}He and ^{129}Xe. † indicates measured properties specific to our hyperpolarization setup.

design [106, 108].

The major disadvantage of ^{3}He is its scarcity (natural abundance of ^{3}He is 0.000137%). In fact, the only terrestrial source of ^{3}He is decay of tritium ^{3}H used in the manufacture of nuclear weapons during the Cold War[7] [201]. As such the cost of ^{3}He has dramatically increased in the last few decades (compare the 2002 cost of \$100/L cited in Harald Möller's paper [69] to today's estimated > \$1000/L). This has led researchers to 'make the most' of the much more readily available ^{129}Xe (26.4% natural abundance); as a result of this and the rapid development of laser technology, the gap in SNR between ^{3}He and ^{129}Xe has narrowed dramatically (the current world record for xenon polarization is 70% [108]).

Physiologically, pulmonary ventilation of ^{3}He and ^{129}Xe is similar with the notable caveat that xenon tends to demonstrate greater defect volume in the same lungs *in vivo* [183]. The two most important differences between the gases for *in vivo* studies is (1) their different diffusion coefficients, and (2) their different Ostwald solubilities. Diffusion imaging with ^{3}He has been rigorously validated [187] and its rapid diffusion rate allows it to sample the pulmonary airspaces quickly, requiring smaller b-values in a diffusion sequence. While xenon research has been accelerating recently, its utility in similar diffusion studies has shown similar but attenuated sensitivity compared to helium in studies of alveolar microstructure [181, 188]. In response to this a major hypothesis investigated in this work has been related to evaluation of xenon as a similar biomarker of airspace size (section 7.3). Generally, helium and xenon are interchangeable for diffusion experiments if appropriate b-values (and therefore gradient strengths/timings) can be achieved; however, studies of collateral pathways cannot be performed with xenon due to its much lower diffusion coefficient [190].

Helium is arguably the most inert substance in the universe and carries a negligible Ostwald solubility in tissue of 0.0085 L. Xenon however demonstrates the ability to perfuse into tissue, blood, and even red blood cells (Ostwald solubility of 0.17 L) when inhaled and has been used medically an anesthetic for this reason. This could potentially raise safety

[7]Interestingly, the moon's atmosphere contains an large abundance of ^{3}He believed to be the result of solar winds. The ^{3}He crisis has become such an inflated issue lately that in as little as 3 years, the initiative to mine the moon for ^{3}He has gone from 'unnecessary' [198] to 'likely' [199] to 'happening' [200].

concerns regarding its used as an imaging agent, but recently the safety of inhaled xenon for MRI has been shown to pose no health risk even in pediatric subjects [202]. As xenon perfuses from the alveolar airspaces into tissue and red blood cells, it experiences *chemical shift* to different degrees in each of these environments leading to 3 distinct frequency peaks *in vivo*. Thus xenon is uniquely suited for experiments quantifying gas perfusion [203, 204]. By tuning the MR spectrometer to the xenon frequency characteristic of its environment (i.e., gas phase, dissolved phase), images of xenon in lungs and in blood can be produced [205]. This is an active area of research within our group, and it is eagerly anticipated that upon successful realization of these techniques we will have a full quiver of lung structure/function imaging techniques at our disposal.

6.5 Summary

Here we have become familiar with the various methods by quantitative physiological information regarding lung structure and function can be revealed from HP gas MR images. A major part of the author's work in the research group has been implementation, calibration, and testing of these sequences and developing the image analysis techniques. Now that the reader is fully equipped to understand and appreciate the novelty of HP gas MRI of lungs, the next chapter will address the major hypotheses stated at the beginning of this dissertation and their respective investigations performed by the author.

Chapter 7

Specific Experiments Relating Lung Structure and Function

> "Every man has a weakness; mine was always cigarettes."
>
> — Cigarette Smoking Man, *The X-files*

By now the reader has been thoroughly exposed to the wonder and whimsy of hyperpolarized gas MRI of lung and is equipped to appreciate the novelty of the author's contribution to the field. This chapter will detail three particular applications of HP gas MRI in the interest of revealing novel structure-function relationships of various lung pathologies. These are asthma, cystic fibrosis, and chronic obstructive pulmonary disease (COPD). It is here that the investigations of the major hypotheses presented in chapter 1 will be restated and evaluated. Each section is dedicated to a particular study and is organized in a standard scientific outline. Studies which have been published in peer-reviewed journals are given an abridged prose here as per copyright regulation.

All studies were approved by their respective Institutional Review Boards (Washington University in St Louis for sections 7.1 and 7.3, and Cincinnati Children's Hospital Medical Center for section 7.2), and appropriate consent/assent was obtained from all subjects in compliance with HIPAA regulations. The FDA currently recognizes ^{3}He and ^{129} as Investi-

gational New Drugs (IND) and were approved in all studies. The author affirms the scientific integrity of all presented data, and will acknowledge fellow collaborators involved in their respective sections.

7.1 Hyperpolarized Gas in Asthma and the Efficacy of Bronchial Thermoplasty

The section describes experiments performed by the author, Ajay Sheshadri, James D Quirk, Jim Kozlowski, Henry D Ellison, Rhonda D Szczesniak, Mario Castro, and Jason C Woods. The results obtained in this work were published in *Radiology* **274**:1 January 2015 entitled 'Regional Ventilation Changes in Severe Asthma after Bronchial Thermoplasty with ^{3}He MR Imaging and CT.' [41]. This research was supported by the Severe Asthma Research Program, National Institutes of Health grant U10 HL109257.

7.1.1 Introduction

Asthma is the most common pulmonary disease currently treated in the clinic [17, 206] affecting 15.7 million adults and 6.7 million children (approximately 8% of the general population). It was the cause of approximately 3,780 deaths in 2004 and was estimated to have cost $11.5 billion in drugs and hospitalizations [207]. Asthma is characterized by chronic airway inflammation which restricts ventilatory function; it is thus placed in the category of *inflammatory* lung disease associated with high neutrophil count. Symptoms include coughing, wheezing, shortness of breath, and sensations of chest tightness. For mild to moderate cases of asthma, symptoms are reduced through use of inhaled corticosteroids and avoidance of allergens. For more severe refractory cases of asthma, short-acting beta-2 agonists may also be required. In 2010, a new therapy for severe asthma was approved by the FDA: *bronchial thermoplasty* [208].

Bronchial thermoplasty (BT) involves bronchoscopy of the sedated patient and delivery of *rf* heating of the airway interior walls in order to ablate the smooth muscle tissue believed to

be the cause of overconstriction[1] [210]. A cartoon illustration of the application of *rf* heating to an airway interior is shown in Figure 7.1. Three sessions of treatment are performed: one

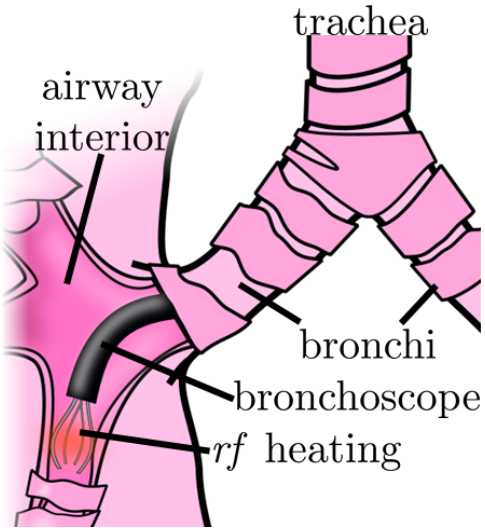

Figure 7.1: Illustration of Bronchial Thermoplasty. The metal fingers from the bronchoscope are pressing against and heating the airway interior. This cartoon illustrates BT for a lobar bronchus (2^{nd} generation airway), but in reality the 3^{rd} generation airways feeding individual bronchopulmonary segments can be treated as well.

targeting the airways in the upper lobes, one targeting the left lower lobe, and one targeting the right lower lobe (right middle lobe is not treated). Reasons for FDA approval of BT are largely clinical, not physiological. A collection of clinical trials showed that the procedure resulted in increased quality of life for the patient and a reduction in exacerbations following treatment[2] [211, 212, 213, 214, 215]. In this study, hyperpolarized ^{3}He MRI was performed on severe asthma patients both before and after undergoing treatment by BT and were compared with those of healthy volunteers. We hypothesized that quantification of ^{3}He ventilation at the level of bronchopulmonary segments is indeed feasible, and that airway treatment by BT would lead to improved ventilation as measured in HP ^{3}He images.

[1] In fact, the true physiologic relevance of airway smooth muscle tissue is unclear [209].

[2] A clinically relevant improvement was also seen in patients who received placebo treatment, but the effect was slightly less pronounced than for the true treatment group.

7.1.2 Methods

A total of 6 healthy volunteers (no history of pulmonary disease) and 10 patients with severe asthma ($FEV_1 < 78\%$) were imaged via hyperpolarized ^{3}He ($\approx 30\%$ polarization, mixture of 30% helium / 70% nitrogen) MRI on a 1.5T Siemens Avanto (Siemens, Munich, Germany) MRI scanner using an 8-channel Tx/Rx flexible phased array chest coil [154] (2D gradient echo, 10 - 15 mm slices, 3 - 4 mm in-plane resolution, 64 $\times$ 128 matrix, acquired at Functional Residual Capacity + 1 L (FRC+1)). Of the 10 severe asthma patients, 7 received treatment by bronchial thermoplasty and underwent a second HP ^{3}He MRI. All subjects were maximally bronchodilated [216] to avoid reversible airway obstruction. All subjects were also imaged via CT (0.4-0.7 mm in plane resolution, 512 $\times$ 512 matrix, 0.5 - 0.7 mm slice thickness, acquired at total lung capacity (TLC)).

Analysis of the CT involved segmentation labeling of the lung by bronchopulmonary segments using an airway tracking software Apollo (VIDA Diagnostics, Coralville, IA). Apollo returns a collection of 'masks' for each CT slice wherein individual voxels are labeled by bronchopulmonary segment. These mask images were registered to the ^{3}He images by a user-guided landmark-based registration algorithm based on Delaunay triangulation [217] written by the author in MATLAB (Mathworks, Natick, MA). Figure 7.2 illustrates the labeled mask and registration (registration code presented in Appendix A.7). Because the algorithm performs registration in 2D, care must be taken to ensure that the chosen slice exactly match the ^{3}He slice anatomically. The right and left lung of each slice are registered separately.

The images demonstrate clear *rf* sensitivity profiles – regions in the anterior/posterior appear brighter than the lung center as do slices inferior to the carina – and required correction before analysis is performed since the intention was to use a single threshold value to identify defects. Care must be taken here so not to suppress physiologically relevant ventilatory information (e.g. gravitational dependence of ventilation [218, 219]). This sensitivity was measured in the anterior-posterior and superior-inferior directions (right-left direction demonstrated no *rf* heterogeneity) of the 6 healthy volunteers only, and images for all sub-

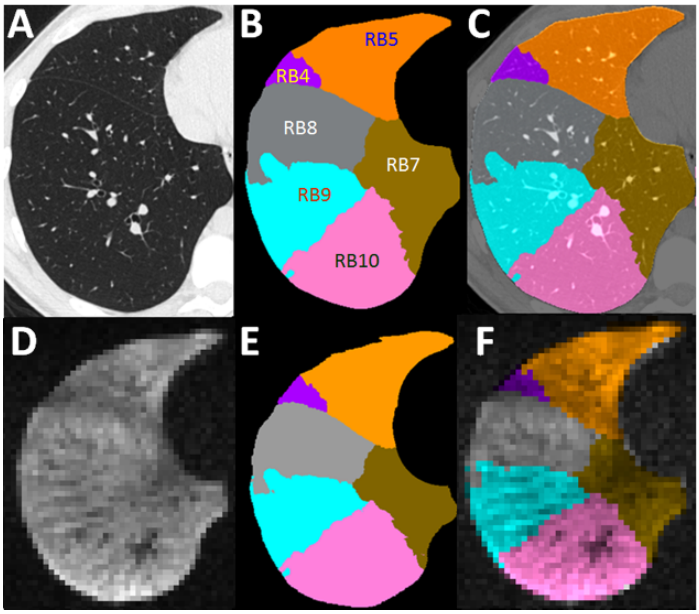

Figure 7.2: Illustration of the CT Mask Registration Process. A: CT of right lung. B: Respective mask with bronchopulmonary segments labeled (RB = 'Right Bronchiole'. C: CT/mask overlay. D: HP ^{3}He ventilation image corresponding to the CT section in A. E: mask in B registered to D. F: ^{3}He / mask overlay. Figure published in Thomen *et al. Radiology* 2015 [41].

jects were corrected accordingly.

Upon registration of the masks to the ^{3}He images, ventilation defects are calculated. Voxels within the lung parenchyma (as defined by the registered mask) are considered defects if their total HP gas signal falls below 60% of the whole-lung signal mean (section 6.2). A whole-lung defect percentage can be calculated along with a *segmental defect percentage* (SDP): the percentage of defect volume for an individual segment. This provides a useful *intra-segmental* measure of ventilation. Because bronchial thermoplasty targets airways supplying individual bronchopulmonary segments, it would be useful to quantify relative ventilation changes among segments (recall that regions of hypoventilation must necessarily result in regions of hyperventilation). The author has developed a measure called the *segmental ventilation percentage* to quantify *intra-segmental* ventilation. The SVP of segment

i would be calculated as follows:

$$\text{SVP}_i = \frac{\text{Signal Percentage of } i}{\text{Volume Percentage of } i} \tag{7.1}$$

For instance is a particular segment contains 5% of the whole-lung HP gas signal but only makes up 4% of the whole-lung volume, this segment would be assigned a value of 5%/4% = 125% indicating that this segment is relatively hyperventilated. We thus expect that for an individual HP gas image set, some segments will have greater than 100% ventilation and some less than 100% but indeed the average of all SVPs should be very near 100%. The intra-segmental nature of the SVP can be used to identify defective ventilation specific to the 3$^{\text{rd}}$ generation airway responsible for gas delivery; SDP is inherently less sensitive to airway-specific ventilation although it demonstrates strong sensitivity to sub-segmental defects. Bronchial thermoplasty currently targets all lobar bronchi, but the HP gas SVP's may allow a clinician to make a more informed diagnosis and avoid ablating airways unnecessarily.

7.1.3 Results

For the six healthy volunteers, SVP's averaged 100% ± 18% (mean ± standard deviation), and for the 10 asthma patients SVP = 97% ± 23% indicating greater ventilatory heterogeneity in the asthma group as expected. Figure 7.3 presents collections of right lung images with and without defects labeled according to bronchopulmonary segment. Segmental Ventilation Percentages for all measured segments are plotted against their respective Segmental Defect Percentages in Figure 7.4 The median (interquartile range [IQR]) of all segmental Defect Percentages (SDP's) were 6.0% (5.6% - 6.3%) for healthy volunteers and 13.5% (8.9% - 17.8%) for severe asthma patients ($P < 0.005$)[3]. A Spearman correlation of r = -0.82 was calculated between the number of days between final treatment and HP gas imaging and the change in whole-lung defect percentage (Figure 7.5). Numeric results for all segments in all subjects are given in [41].

[3]Median (IQR) is more appropriate here (compared to mean ± standard deviation) since SDP's cannot be negative and are thus distributed in Poisson-like fashion.

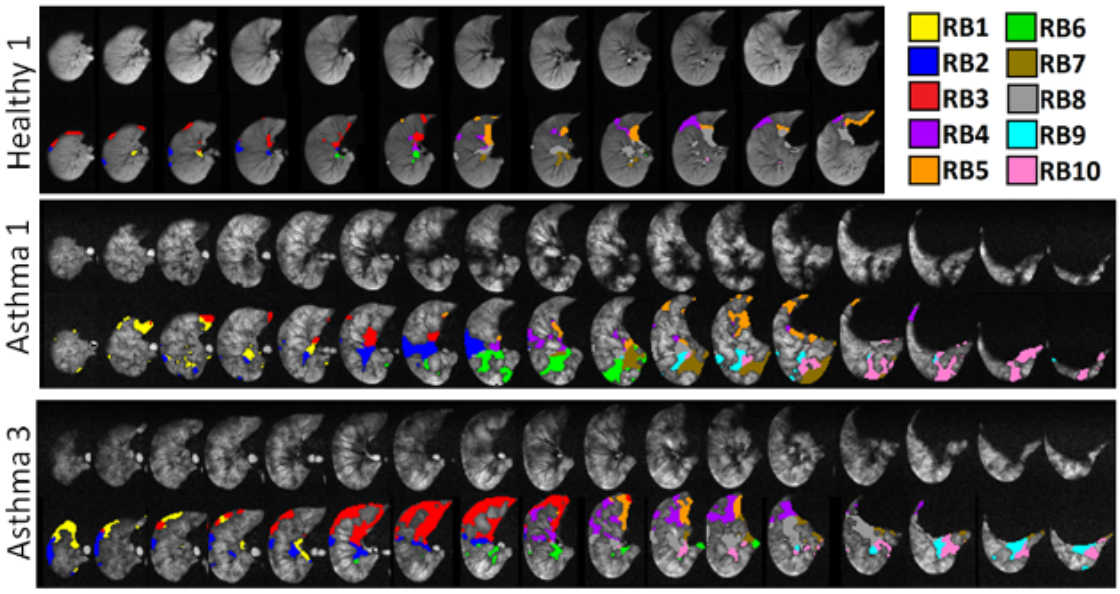

Figure 7.3: Sets of HP ^{3}He Images for a Healthy and 2 Severe Asthma Patients With and Without Defects Labeled. Figure published in Thomen *et al. Radiology* 2015 [41].

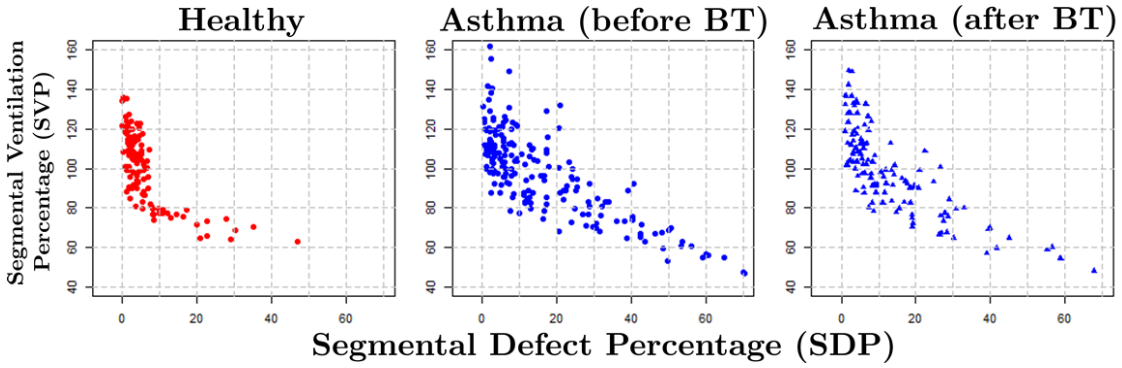

Figure 7.4: Plots of SVP vs SDP for all measured segments in healthy volunteers (n=114), severe asthma patients (n=190), and asthma patients following treatment by bronchial thermoplasty (n=133). Each datapoint represents a single segment in a single patient.

7.1.4 Discussion and Conclusions

Note in Figure 7.4 that healthy volunteers demonstrated low defect percentages, but a moderate dispersion of SVP's whereas asthma patients demonstrate a greater number of segments with large defects. Further, asthma subjects have segments of very high SVP

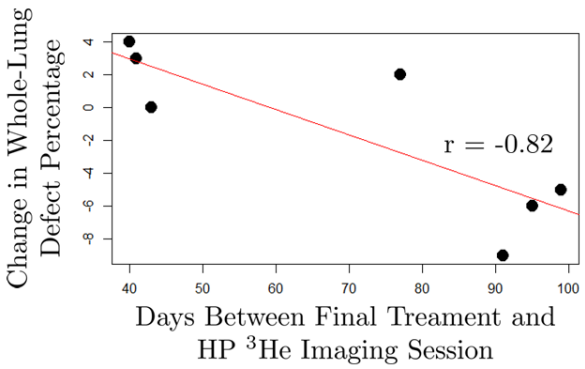

Figure 7.5: Plot of Change in Whole-Lung Defect Percentage vs Number of Days Between Final Therapy Session and HP Gas Imaging Session.

(hyperventilated) – information which cannot be revealed by the SDP[4]. We see as expected that segments with low SVP tend to have more defect, but this is not always the case and the information is not redundant since, unlike SDP's, SVP's are reflective of the particular airways supplying the entire segment.

At first glance, it seems that therapy by bronchial thermoplasty did little to mollify defective ventilation (Figure 7.4). Consider however that in the AIR2 trial [210, 214], patient followup was performed at 90 days following final treatment at which point patients had experienced dramatic improvement. However, in the 'post-treatment' period (< 6 weeks following final treatment), patients experienced worsened asthma and more hospitalizations. Those that received treatment by BT seemed to experience a brief refractory period of worsened symptoms. Figure 7.5 clearly shows a similar behavior even with a very small patient cohort. Unfortunately for this study, no clinical tests were administered prior to 100 days following final treatment so patient quality-of-life cannot be directly compared to measured defect percentages here. But these results indicate that the sensitivity of ^{3}He MRI to regional changes in ventilation may be useful in longitudinal studies investigating changes in airway geometry or clinical outcomes for asthma patients in clinical trials.

[4]Again, this is because our method of defect calculation by binary threshold was deliberately chosen to be as simple as possible. One could easily imagine more stratified defect identification (or hyperventilation identification) for more enhanced precision (in essence, what SVP's provide), but this would undermine the intended simplicity with which defects can be identified.

In this study we have shown that quantification of HP ^{3}He ventilation on the level of individual bronchopulmonary segments is feasible. Further, we have found that ventilation changes in severe asthma following treatment by bronchial thermoplasty reflect the results of similar studies and highlight the sensitivity of HP gas imaging in longitudinal research. We envision that HP gas imaging may aid in targeted treatments for BT in particular (perhaps in *rf* heating dosage, time between treatments, necessity of all treatment sessions, etc.). It is worth noting that HP ^{129}Xe may be worth exploring as well since ventilation defects are more pronounced in HP ^{129}Xe images compared to ^{3}He – likely due to xenon's much lower diffusion coefficient [183, 220].

7.2 Hyperpolarized Gas in Cystic Fibrosis

The section describes experiments performed by the author, Laura L Walkup, David Roach, Zackary I Cleveland, John Paul Clancy, and Jason C Woods. A manuscript for this work entitled 'Hyperpolarized ^{129}Xe for investigation of mild cystic fibrosis lung disease in pediatrics' has been submitted for publication in *Journal of Cystic Fibrosis*. The authors would like to gratefully acknowledge the Cincinnati Childrens Research Foundation and NIH funding via grant T32 HL007752.

7.2.1 Introduction

Cystic Fibrosis (CF) is a genetic disorder caused by mutations on the cystic fibrosis transmembrane conductance regulator (CFTR) which disrupts airway epithelial ion transport and mucus production, resulting in thick mucus accumulation, infection, inflammation and airway obstruction. CF affects over 70,000 people worldwide, carries a median survival slightly over 40 years, and requires lifelong management with pulmonary and nutrition-focused therapies. While several organs are impacted by CF, pulmonary morbidities are responsible for at least 80% of all CF-related deaths [221]. Because mucus retention, infection and inflammation are largely responsible for decline in lung function, disease management typically includes

therapies targeting these processes. CF airway obstruction is a regional process, supporting the use of imaging techniques (mostly CT) for diagnosis, investigation, and monitoring of regional structural pathology. What is lacking from current techniques is the ability to detect and monitor detailed functional information in the lungs a gap which hyperpolarized gas MRI is well-suited to fill.

As proven pulmonary treatments are being examined and extended into patients at early ages for disease prevention, it is vital to diagnose, understand and monitor pathologies in early CF lung disease to more effectively tailor individualized treatments and study efficacy of emerging therapies. Treatment goals have shifted towards early detection and limitation of more severe and irreversible abnormalities (e.g., bronchiectasis) but tools are lacking to detect and monitor regional lung function. There is a pressing need for sensitive measures of regional lung disease that can be employed for personalizing treatment regimens, for use in early phase clinical trials that serve as a robust biomarker of intervention efficacy, and for the conduct of studies with small cohorts of patients with rare CF-causing mutations (such as patients with gating mutations and other mutations responsive to the potentiator ivacaftor - approximately 6% of the total CF population) [222].

CT (computed tomography) is currently the gold standard in research for investigation of regional structural pathology in CF [176, 223], but because it involves exposure to ionizing radiation, its use is limited in pediatrics and in longitudinal research studies. Recent advances in ultra-short echo (UTE) MRI sequences have brought MRI into strong competition with CT for obtaining high-resolution structural images, but even the highest-quality CT or MR images provide only structural information [224] (sections 1.2.5 and 5.6). A multiple inert gas elimination technique (MIGET) involves precise measurement of partial pressures of various inert gases during inhalation and after exhalation to quantify ventilation and ventilation/perfusion ratios [225, 226]. One of these measures via multiple breath washout, lung clearance index (LCI), has been shown to have greater sensitivity than FEV_1 to detect ventilation inhomogeneity in mild CF lung disease, but is a global measure which cannot localize disease pathology [227, 228, 229, 230].

So far hyperpolarized gas studies performed in CF have only been performed with ^{3}He. Several groups have performed HP ^{3}He MRI in CF patients (mostly adults) in order to investigate regional defects in ventilation [231, 232, 233, 234], HP gas repeatability [38, 235], longitudinal ventilation changes [236], and treatment efficacy [180, 237, 238, 239]. Use of ^{129}Xe in pediatrics is more restricted than ^{3}He due to its slightly higher Ostwald solubility which raises concerns regarding its anesthetic effects, but a recent study has demonstrated that single-breath-hold ^{129}Xe MRI presents no safety concerns in adults [202, 240]. As discussed in section 6.4, the increasing cost and scarcity of ^{3}He, HP gas research has recently shifted focus toward ^{129}Xe, but CF research in pediatrics with HP ^{129}Xe MRI has not been reported.

In this study we hypothesized that ^{129}Xe MRI of lungs would provide a sensitive measure of regional ventilation defects in pediatric CF patients. Specifically, we sought to demonstrate that patients with mild CF lung disease exhibited ventilation defects compared to age-matched controls. Further, by comparing age-matched CF and control groups, we also sought to demonstrate that ^{129}Xe MRI is more sensitive than the clinical gold standard (FEV_1) to detect and quantify mild CF lung disease.

7.2.2 Methods

A total of 11 healthy volunteers and 11 cystic fibrosis patients ages 6-17 years old were recruited for this study; patient data are given in Table 7.1. Spirometry was performed on any subjects that did not have recent spirometric data (all healthy subjects, 2 CF patients) using a Koko (nSpire, Longmont, CO) handheld USB spirometer. Each subject was placed in the scanner and a proton survey, practice proton GRE scan, and HP xenon flip angle calibration scan were performed (section 5.4). The xenon ventilation gas dosage was catered to each subject to be $1/6^{\text{th}}$ of total lung capacity (TLC) and was delivered to the subject in the magnet bore to be inhaled for a breathold (<16 seconds) xenon ventilation scan.

Either the homebuilt xenon hyperpolarizer 'Alix' (section 4.2) or a commercial xenon hyperpolarizer (Polarean, Durham, NC) was used to produce the hyperpolarized xenon.

Subject		age [yr]	sex	height [cm]	weight [kg]	FEV_1 [%]	VDP [%]
Healthy	1	11	F	149	35.1	100	6.6
Controls	2	7	F	128	33.0	115	4.0
	3	14	M	150	40.6	108	5.8
	4	14	M	177	64.8	106	12.0
	5	12	M	141	34.8	103	7.7
	6	13	M	171	57.2	109	7.8
	7	13	M	160	45.8	89	7.9
	8	12	M	160	56.6	92	4.4
	9	8	M	136	35.2	91	7.2
	10	6	F	116	20.8	95	1.8
	11	16	F	169	49.6	95	4.7
	mean ± sd	11.5 ± 3.2	64% M	151 ± 19	43.0 ± 19.1	100.3 ± 8.5	6.4 ± 2.7
Cystic	1	14	M	167	54.4	97	19.3
Fibrosis	2	12	F	162	43.6	77	31.1
	3	13	F	161	48.9	96	9.6
	4	14	F	156	51.2	106	5.2
	5	16	M	179	65.5	120	14.5
	6	8	M	126	27.8	118	18.5
	7	11	M	142	34.5	102	27.5
	8	13	F	157	46.5	114	14.8
	9	15	F	159	43.7	72	32.2
	10	11	F	152	40.1	89	13.9
	11	11	F	147	34.3	86	15.4
	mean ± sd	12.5 ± 2.3	36% M	155 ± 14	44.5 ± 10.6	97.9 ± 16.0	18.3 ± 8.6
p values		0.37	0.23	0.52	0.78	0.672	0.0009

Table 7.1: Patient Information and Relevant Results for HP ^{129}Xe in CF. P values were calculated by Student's t-test between healthy and CF groups.

Isotopically enriched xenon (≈86% atom percentage of ^{129}Xe) was used in both polarizers. Gas produced with Alix was a 50/50 xenon/N_2 mixture at ≈25% xenon polarization; gas produced with the Polarean polarizer was a 100% xenon concentration at about ≈13% polarization[5]. The HP xenon was delivered from the polarizer lab to the magnet in a Tedlar bag for immediate administration to the patient and the xenon FLASH was performed upon inhalation (FA = 10-12°, TR/TE = 8/4 ms, voxel size ≈ 3×3×15 mm^3, 9-14 slices).

Images were analyzed by our standard protocol (section 6.2) where voxels whose signal was less than 60% of the whole-lung signal mean were considered defects (after *rf* sensitivity correction). A whole-lung ventilation defect percentage (VDP) was calculated for each subject to be compared with FEV_1 (percent predicted). One of the control subjects (control #5) was imaged twice in succession with two separate xenon doses (one from Alix, one from Polarean) to verify reproducibility between the two polarizers.

7.2.3 Results

The imaging session was well-tolerated by all subjects, and all images used in analysis were of satisfactory quality (SNR = 15.9 ± 5.8). The control patient that was imaged twice (#5) yielded a VDP of 7.7% for the Polarean dose ($P_{^{129}\mathrm{Xe}}$ = 32%, SNR = 22.9) and a VDP of 9.4% for the Alix dose ($P_{^{129}\mathrm{Xe}}$ = 12%, SNR = 22.9). Ventilation images for each xenon batch are given in Figure 7.6. The two VDP's calculated for each set of images is averaged in following analyses (VDP = 7.7%).

The mean FEV_1 (± standard deviation) was 100.3% ± 8.5% for control subjects and was 97.9% ± 16.0% (p = 0.672). The mean VDP (± standard deviation) was 6.4% ± 2.7% for control subjects and was 18.3% ± 8.6% (p = 0.0009). Individual patient data are given in Table 7.1 and are presented graphically in Figure 7.7. A Pearson correlation coefficient of r = -0.37 was calculated between VDP and FEV_1 for all subjects (p = 0.87).

Analyses have also been performed on the subgroup of patients with 'normal' FEV_1 > 85% (9 of the 11 CF subjects, CF#2 and #9 are excluded). Mean FEV_1 is then 103.1% ±

[5]Thus, either polarizer would yield approximately the same magnetic moment.

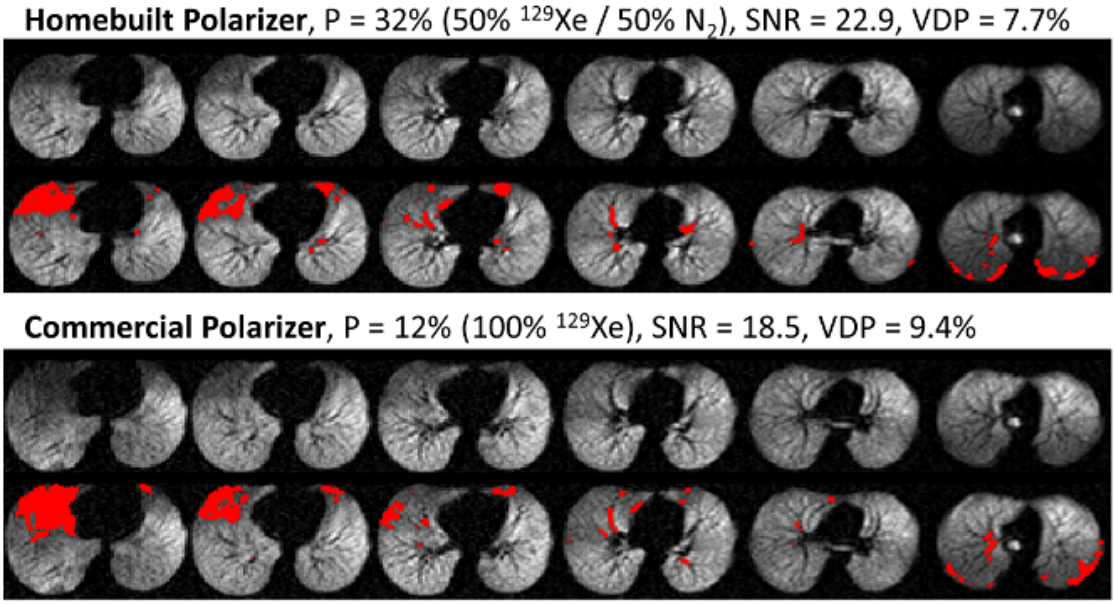

Figure 7.6: ^{129}Xe Ventilation Images in a Healthy Volunteer Comparing Polarean and Alix Polarizers.

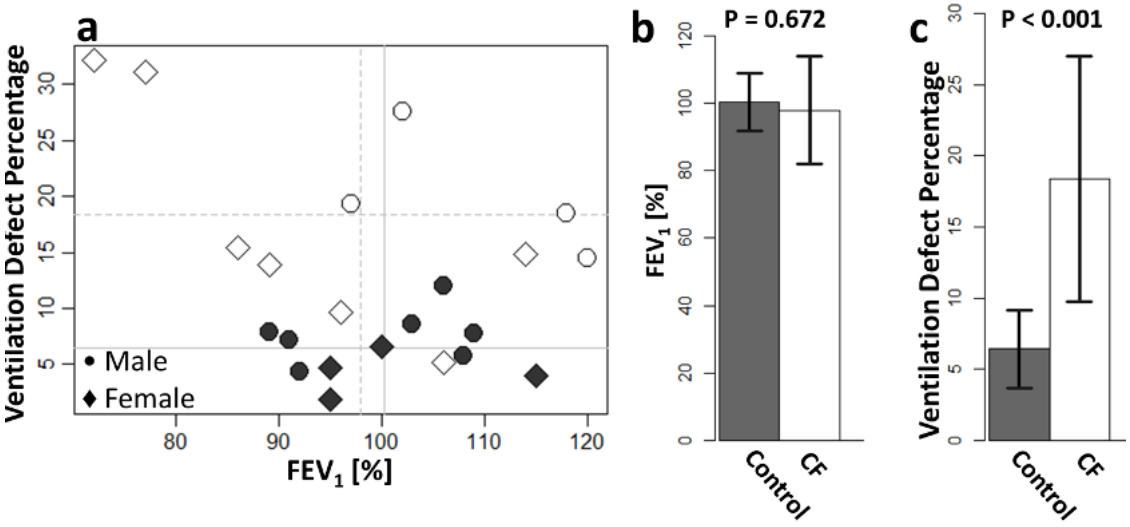

Figure 7.7: Scatter Plot of VDP vs FEV_1 for All Subjects (a). Bar plots of FEV_1 and VDP are shown for control and CF groups respectively showing clear group separation for VDP but not for FEV_1.

12.3% and VDP was 15.4% ± 6.3%, and the control / CF groups still demonstrate statistically significant group separation from VDP (p = 0.002), but not from FEV_1 (p = 0.57).

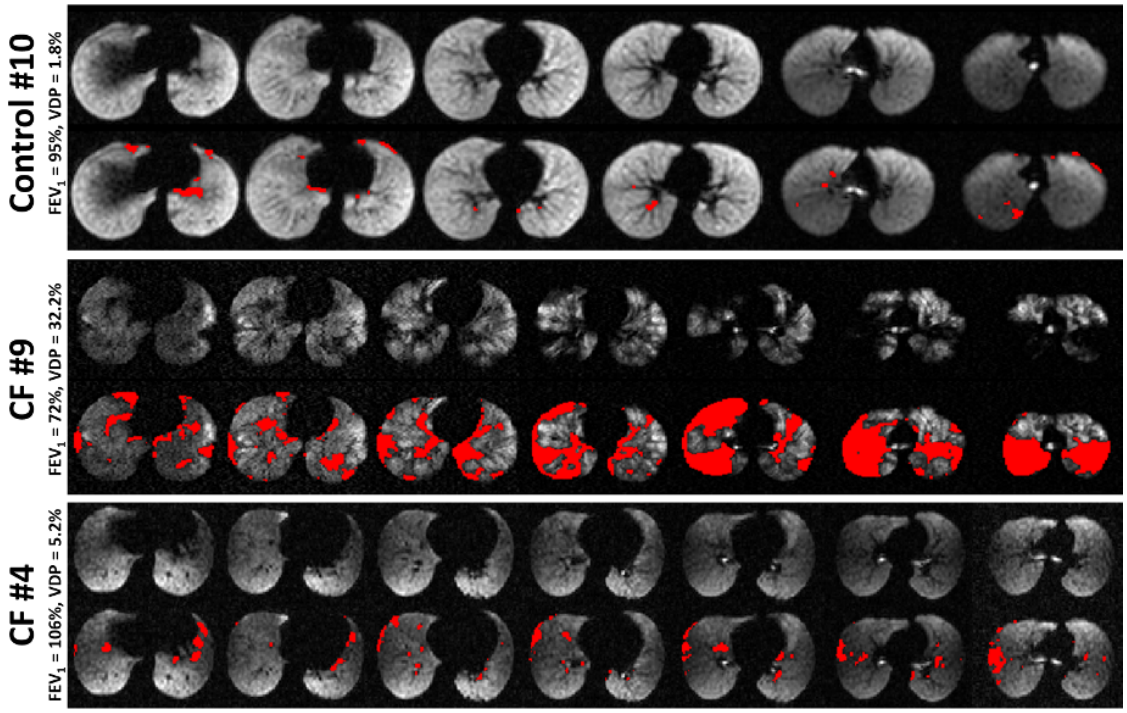

Figure 7.8: Images of HP Xenon in 1 Healthy Control and 2 Cystic Fibrosis Patients.

Only CF subject #4 showed a VDP less than the control mean VDP. Figure 7.8 shows example images of a healthy control, a CF patient with mild defects and high FEV_1 and a CF patient with significant defects and low FEV_1.

7.2.4 Discussion and Conclusions

Sensitive and functional biomarkers of regional lung disease are critical gaps in CF care and the development of new therapies, particularly in patients with mild disease manifestations. As new therapies improve outcomes, this need becomes more evident, as the capacity to detect the impact of new interventions becomes increasingly difficult with available tools. This study has presented the performance of ^{129}Xe HP MR imaging in pediatric controls and mild CF patients to detect and quantify regional ventilation abnormalities. We hypothesized that this imaging modality could be applied to this population, and that standardized quantification techniques would demonstrate differences between CF patients and healthy

controls that were not detectable by standard pulmonary function tests. ^{129}Xe HP MR imaging demonstrated the capacity to detect regional ventilation defects in the vast majority of CF patients despite only minimal lung disease as quantified by FEV_1 percent predicted, which is the current gold standard to monitor CF lung disease status and progression. These results demonstrate the power of HP ^{129}Xe MRI to regionally quantify functional ventilation defects in CF, and support further evaluation as a lung disease biomarker and monitoring tool.

In this study, results from HP ^{129}Xe were considerably more sensitive than FEV_1 in detecting CF lung disease and segregating CF patients from healthy controls. This capacity was sustained when our analysis was limited to CF patients without clear lung disease, and those with mild lung disease (FEV_1 <85%) were excluded. This is perhaps not surprising as FEV_1 is an effort-dependent measure of global lung function, whereas HP gas MRI reveals regional ventilation during a near-tidal breath hold. These differences have been described in past studies with ^{3}He in older patients [238]. Variability in FEV_1 for healthy control pediatric subjects may be expected to be increased relative to CF patients, as most control subjects have likely never performed pulmonary function tests, whereas CF patients routinely perform spirometry after 6 years of age. The impact of this training effect to provide meaningful spirometry data also becomes problematic in younger CF patients. Unlike FEV_1 however, the sensitivity and regional information obtained by HP gas imaging can be acquired in a single breath hold, and allows unique spatial precision to detect functional deficits that may relate to particular areas of structural abnormalities. The sensitivity of HP ^{129}Xe to detect ventilation abnormalities in this study compared to FEV_1 is particularly encouraging since the mean FEV_1 of the CF subjects did not differ from the controls. Detecting early changes in CF lung disease is critical, since emerging therapies are geared towards preventing or delaying permanent and/or irreversible lung pathologies such as bronchiectasis, and our results support HP ^{129}Xe VDP as a sensitive, functional biomarker to evaluate the efficacy of new therapies in individual CF patients.

While CT currently demonstrates the highest achievable structural resolution of all clin-

ical imaging techniques, its ionizing radiation limits its use in longitudinal studies. This is particularly important in the monitoring of pediatric patients [241]. Hyperpolarized ^{129}Xe MRI provides a robust method of investigating regional lung ventilatory function, and recent advancements in proton MRI (e.g., UTE techniques) have improved the visualization of the lung parenchymal structure; in concert, these techniques may provide complementary information to elucidate regional structure-function relationships of lung disease [205] which may be of use in determining the effect different pathologies may have on ventilation. The moderate negative correlation demonstrated between FEV_1 and VPD indicates that the two modalities capture related, but not necessarily the same, information. Importantly, our results demonstrate that subjects with normal FEV_1 can have regions of clearly defective ventilation. It is also notable that ^{129}Xe gas has the potential to detect and quantify other functional measures in the lung, including diffusion within parenchymal airspaces for airspace size measurement [188, 242], and gas exchange across the alveolar barrier [243]. These techniques may provide complementary information to conventional imaging or HP gas ventilation imaging relating to CF pathology.

There are also limitations of the work. First, the number of subjects enrolled was relatively small and was primarily limited to pediatric patients with normal or mild lung disease. Subsequent studies will be needed to determine the role of ^{129}Xe MR imaging in more advanced CF lung disease. Second, the studies were cross-sectional, and did not assess the longitudinal performance of HP ^{129}Xe VDP over time (during either periods of disease stability or instability). Studies of this nature will be critical to determine the future role of ^{129}Xe in disease monitoring or as a biomarker of intervention. In addition, subjects with lower SNR may arguably have artificially elevated VDP since a single threshold was used for defect identification. The subjects with the lowest SNR, however, were controls (control #3, SNR = 6.6, VDP=5.8%; control #4, SNR = 7.7, VDP = 12.0%). Because there was no significant difference in SNR between the control and CF groups ($p = 0.6$), this limitation does not likely affect its sensitivity to detect regional CF lung disease. Finally, hyperpolarized ^{129}Xe is currently classified by the FDA as an investigational new drug, and thus requires

FDA approval for use in clinical trials or disease management.

These results provide strong support to investigate the future role of ^{129}Xe MR imaging in clinical trials, particularly those focused on evaluating new therapies for CF patients with mild disease [244, 245, 246, 247]. This is a vital consideration, as patients who do not have established structural lung disease are likely to receive the greatest benefit from transformative therapies such as CFTR modulators [248, 249]. Here the efficacy of hyperpolarized ^{129}Xe to detect regional lung defects in pediatric patients with minimal CF lung disease as been demonstrated. The sensitivity of ^{129}Xe to quantitatively differentiate healthy subjects from mild CF was readily apparent utilizing our relatively simple defect identification threshold. These findings indicate that HP ^{129}Xe imaging may be a useful tool to detect and monitor disease progression, and to quantify individual responses to individualized treatments.

7.2.5 Future Directions

^{129}Xe MRI may also reveal relationships between various CF structural pathologies (bronchiectasis, mucus plugging, etc.) and regional ventilation. As more specialized clinical trials develop and CF phenotypic differences become more defined, knowledge of these structure-function relationships become more critical. UTE MRI has already shown promise as a structural imaging tool (section 6.1), and a combination of UTE and HP xenon MRI may be able to identify these pathologies regionally, thus quantitatively relating structural pathology to functional ventilation. Figure 7.9 shows example images from a CF patient with well resolved structural abnormalities (CF patient #9, $FEV_1 = 72\%$). Lobes have been visually identified here to illustrate that regional quantification is feasible. The author intends to move forward with this analysis as more subjects are enrolled in the study. Currently, only 6 subjects have been scored for pathological defects by radiologists, but preliminary results are promising and have been published in abstract form and presented at the North American Cystic Fibrosis Conference October 2015 [250].

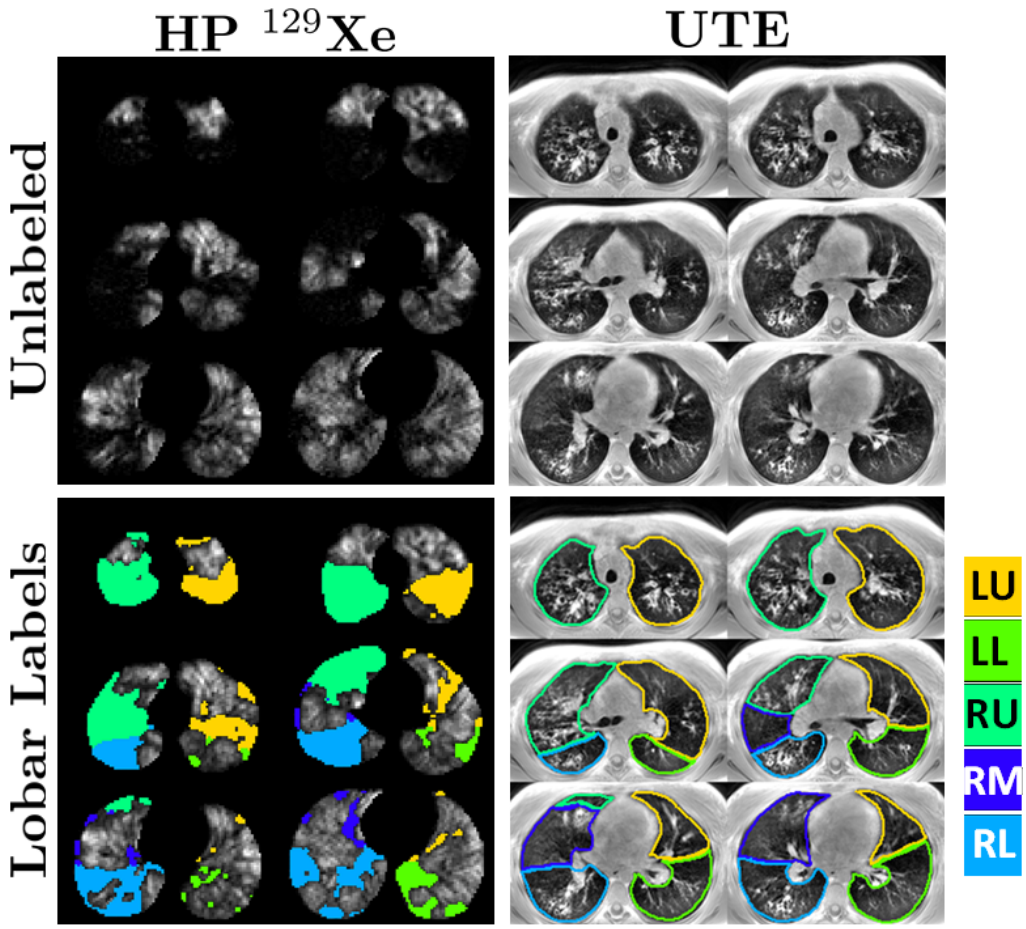

Figure 7.9: Images of HP ^{129}Xe and UTE for CF Patient #9 with and without Lobes Identified.

7.3 Hyperpolarized Gas in COPD

The section describes experiments performed by the author, James D Quirk, David Roach, Tiffany Egan-Rojas, Kai Ruppert, Roger D Yusen, Talissa A Altes, Dmitriy A Yablonskiy, and Jason C Woods. The results obtained in this work were published in *Magnetic Resonance in Medicine* in January 2016: 'Direct Comparison of ^{129}Xe Diffusion Measurements with Quantitative Histology in Human Lungs' [42]. This research was supported by funding provided by Cincinnati Children's Hospital Medical Center and to some investigators via 2R44HL087550.

7.3.1 Introduction

Chronic Obstructive Pulmonary Disease is an irreversible lung disease characterized by chronic bronchitis (small-airway obstruction) which is diagnosed clinically and emphysema (destruction of distal alveolar airspaces) which is diagnosed pathologically. It is currently the third most common cause of death in the United States [251] affecting nearly 15 million Americans [17] and is estimated to have cost the nation $49 billion in 2010 [6]. It is associated with several comorbidities including cardiovascular disease, stroke, and diabetes mellitus [252]. Symptoms of COPD include chronic cough, dyspnea, excessive sputum production, and decreased tolerance to exercise. Cigarette smoking has been definitively linked to more than 80% of all COPD diagnoses in America (the rest are often associated with a combination of tobacco smoke, dust, chemicals, pollutions, and other air-borne undesirables) [17]. Aside from lung transplant (only available for end-stage sufferers), there is no cure for COPD.

Spirometry, and sometimes x-ray or chest CT, can be used to diagnose COPD although it is generally insensitive and does not always correlate with symptoms or outcomes [19, 312]. As we have seen throughout this dissertation, the sensitivity of hyperpolarized gases is unparalleled and may spotlight the real nature of pathologic physiology in COPD. A number of studies have already shown definitive differences between healthy and COPD lungs using hyperpolarized gases [189, 253]. In particular, because emphysema is characterized by deterioration of alveolar airspaces, measurements of HP ^{3}He have already been shown to correlate with direct morphometric measures of histology in healthy and COPD lungs [187]. However, the same validation had not been performed for HP ^{129}Xe. In this study, we measured xenon diffusion in explanted human lungs from subjects with either COPD or idiopathic pulmonary fibrosis (IPF) and compared the regional xenon ADC to morphometric measures of histology from spatially matched regions of the same lungs. We hypothesized that, similar to helium studies, xenon ADC would reflect the severity of emphysema thus validating HP ^{129}Xe ADC as a biomarker for airspace size.

Importantly, IPF lungs are chosen to behave as controls here since healthy donor lungs

were unavailable for this study[6]. However, IPF is characterized by parenchymal scarring, reduced lung volume, and reduced compliance compared to healthy lungs, so we anticipate slightly elevated airspace sizes for IPF in accordance with results found in other research groups [254], though not near to the extent that it is expected in COPD [187].

7.3.2 Methods

Five COPD lungs (from patients with GOLD-4 COPD) and 2 IPF lungs were used in this study. Upon explantation, the lungs were delivered to our research group and a piece of Gore-Tex tubing was sewn into the inner perimeter of the major bronchus (Figure 7.10). The lung was moistened with saline and inflated to reveal any obvious leaks in the pleural

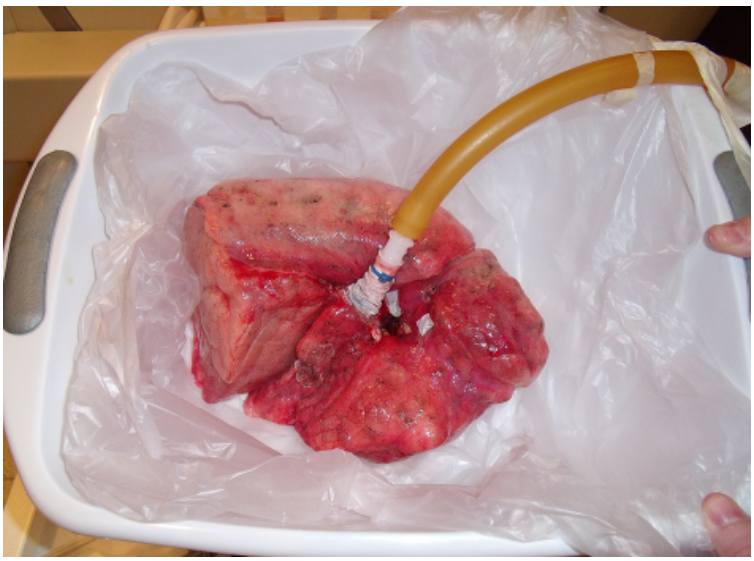

Figure 7.10: Photograph of an Explanted Lung Ready to be Imaged. Please note that this photograph contains graphic content; viewer discretion is advised.

surface which were repaired either using small sutures or small latex patches and tissue adhesive. Once the lungs could hold 10 in H_2O of air pressure, they were brought to the scanning facility in a plastic bin layered with ice for imaging with HP xenon. The lung

[6]Healthy lungs are a precious commodity, and we only receive such donor lungs if they are rejected for transplant.

was placed inside a flexible single-turn multi-loop solenoid coil tuned to $f_{^{129}\mathrm{Xe}} = 17.6$ MHz (at 1.5T) and inserted into the magnet bore such that the lung anterior-posterior axis was parallel to B_0 (bronchus facing upward). The lung was inflated to approximately 20 cm H_2O with nitrogen and a collection of proton images were performed to allow for anatomic matching of lung structure to diffusion images later. Then, the lung was allowed to passively deflate. A XeMed hyperpolarizer (Durham, NH, USA) was used to hyperpolarize ^{129}Xe to about 22% polarization, and a 50/50 xenon/nitrogen mixture was transported in a tedlar bag to the scanner for delivery to the lung. The lung was inflated with the mixture and axial image slices were acquired using a diffusion weighted 2D-multislice FLASH sequence (4-6° FA, TR/TE = 22/16, ≈6×6×6 mm^3 voxel size, pixel BW ≈130 Hz, b-values = 0,12.5 s/cm^2, $\Delta = \delta = 5$ ms, 6-12 slices, k-centric ordering). ADC was calculated for each voxel by $\mathrm{ADC} = \frac{1}{b} \ln \frac{S_0}{S}$.

After scanning, the lungs were inflated with ^{4}He to 10 cm H_2O and slowly frozen over liquid nitrogen (LN_2) in a Styrofoam container. The frozen/inflated lungs were cut into 2-cm-thick axial slices using a band saw. From these lung slices, a number of small tissue samples were harvested from well marked locations in each slice. The samples were chosen to effectively sample regions of varying tissue destruction. The samples were stained, processed, and fixed to microscope slides for morphometric analysis [255]. High-resolution pictomicrographs of each sample were obtained and the *mean linear intercept* (L_m) and *surface area to volume ratio* (SAV) were calculated for each using custom MatLab software (code given in Appendix A.8). Figure 7.11 illustrates the morphometry calculation process. SAV is calculated by summing the number of pixels which border tissue pixels and dividing by the total number of pixels in the scanned sample[7]. L_m is calculated by overlaying a bar grid on the sample bars (Figure 7.11.d) and counting the number of bars which intersect tissue; the total length of all bars divided by this value gives L_m. Measuring these two values separately provides internal validation since, for an isotropically distributed medium $L_m = 4/\mathrm{SAV}$ which is shown in Figure 7.12

[7]An individual pixel has an edge length of 1 pixel and has an area of 1 pixel^2. The appropriate units for SAV of cm^{-1} is preserved since 1 pixel edge equates to a finite measure of length.

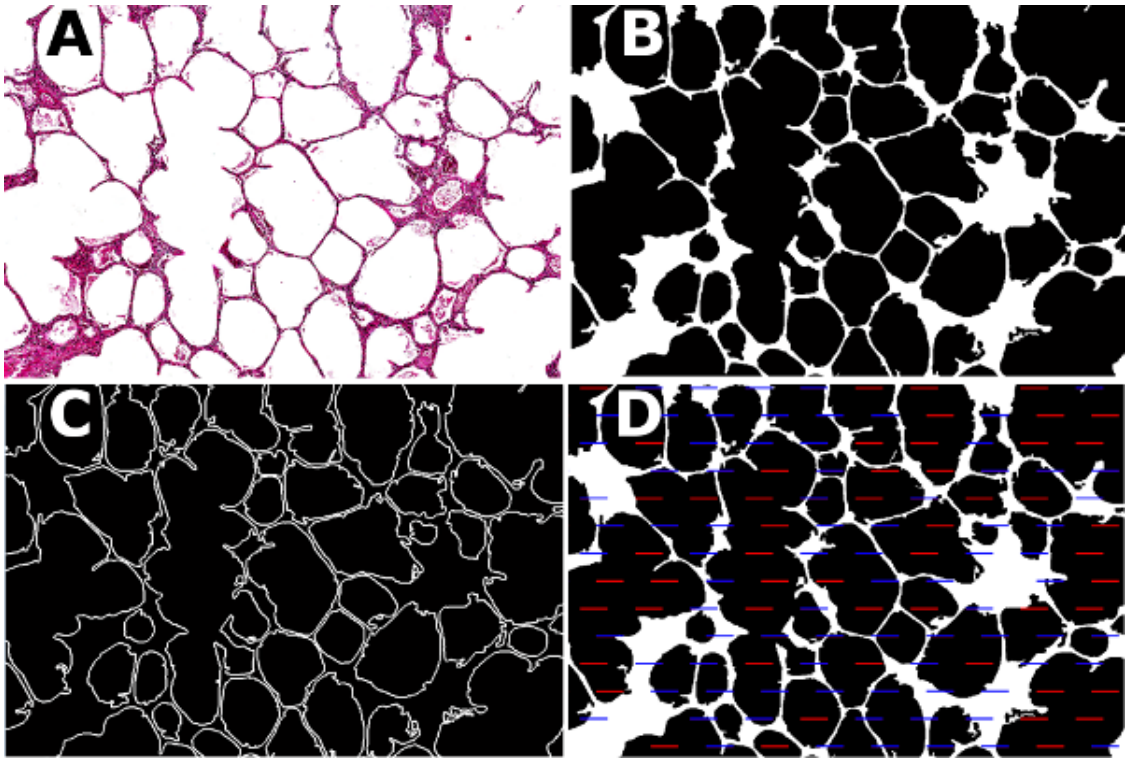

Figure 7.11: Illustration of Morphometry Calculations. A scanned histological slide (A), is binarized (B). SAV is calculated by binarizing a 2D gradient of (B), and L_m is calculated using a point-and-intercept method [255]. Blue bars intersect tissue, red bars do not (bar length is 141 μm in this image). Figure published in Thomen *et al. Magn Reson Med* 2016 [42].

For every histological sample harvested, corresponding ADC measurements were calculated from precisely matched locations within the ADC maps (approximately 4 voxels' ADC's were averaged) for accurate spatial comparison of the two airspace size measures. Figure 7.13 presents illustrates the methods of ADC-morphometry comparison in three samples – 1 from an IPF lung and 2 from a COPD lung. While this method of sample harvesting for quantitative comparison of morphometry to spatially-matched ADC measurements is a robust scientific approach to validating ^{129}Xe diffusion as a biomarker for airspace size, the author notes that for nearly every slab, even a simple visual comparison of tissue destruction in the lung slabs to ^{129}Xe ADC maps demonstrated overwhelming agreement (compare COPD ADC map and lung slab in Figure 7.13).

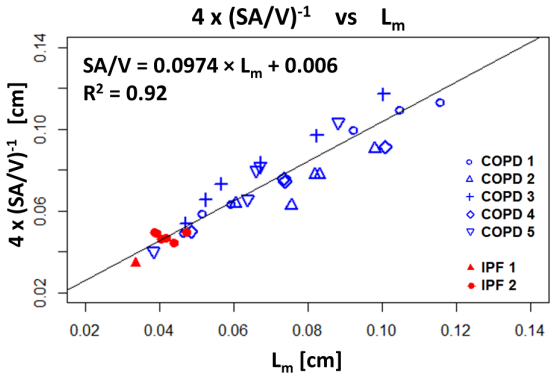

Figure 7.12: Plot of L_m vs 4/SAV. The linear relationship with slope = 1 indicates validates the morphometry calculations. Figure published in Thomen *et al. Magn Reson Med* 2016 [42].

7.3.3 Results

A total of 28 samples were processed from the COPD lungs and 7 samples from the IPF lungs (34 total histological samples). COPD samples demonstrated elevated ADC's (0.071 ± 0.011 cm^2/s) compared to IPF (0.033 ± 0.001 cm^2/s, P $< 10^{-15}$), and COPD histology revealed longer L_m (0.076 ± 0.027 cm) compared to IPF samples (0.041 ± 0.004 cm, P = 2.66×10^{-7}); values expressed as sample means ± standard deviations. Note in particular that the P value for group separation by ADC is smaller than for L_m indicated that note only does ADC provide greater precision than L_m but also better group separation. The ADC measures are in agreement with those obtained in *in vivo* HP ^{129}Xe diffusion studies (0.056 cm^2/s from Kaushik *et al.* [188], and 0.080 cm^2/s from Kirby *et al.* [181]). A Pearson correlation coefficient of r = 0.59 was found between ADC and L_m measures which is consistent with findings from previoius ^{3}He studies (r = 0.603 from Woods *et al.* [187]) and indicates moderate correlation between the two measures. Plots of measured ^{129}Xe ADC (individual samples, subject averages, and whole-lung averages) vs L_m are given in Figure 7.14.a-c; a histogram of all measured ADC's (all subjects, all voxels) for IPF and COPD is given in Figure 7.14.d.

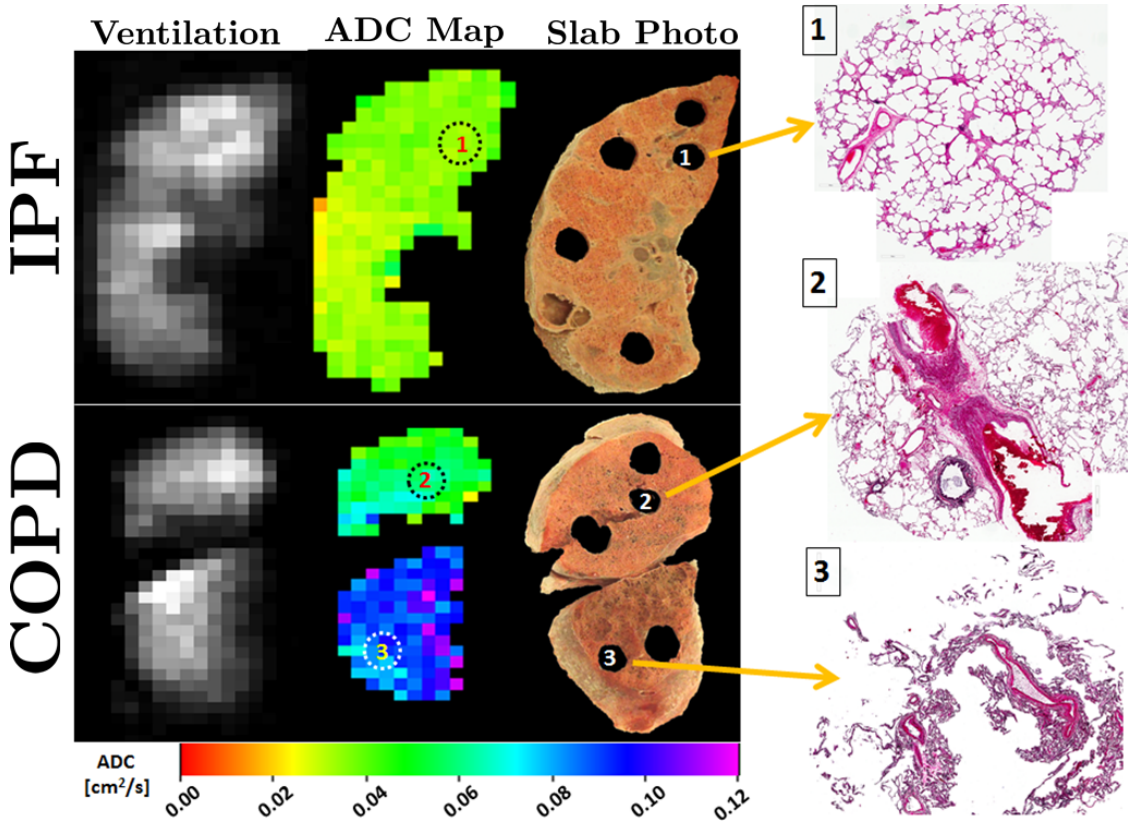

Figure 7.13: Illustration of ^{129}Xe Validation Methods. Samples taken from the frozen lung slabs were accurately spatially matched to regions within the xenon ADC maps. Samples were chosen to capitalize on the inherent spatial heterogeneity of emphysema in the COPD lungs as represented by the 3 presented samples' varying degrees of tissue destruction. ADC error as measured here is estimated at 0.002 cm^2/s using analysis described in section 6.3.1

7.3.4 Discussion and Conclusions

Generally, the results of this study speak for themselves: larger airspace size leads to an increase in both ^{129}Xe ADC and L_m as measured from histology. A major limitation of this study however is the small sample size (both in the number of control/COPD lungs and samples harvested from each), though the stark statistical significance seen between groups in so few samples could perhaps speak to the strength of the HP ^{129}Xe diffusion technique. Polarizer availability was another confounding factor which has since been mitigated with the construction of the new xenon polarizer described in section 4.2 [109, 160, 256]. While

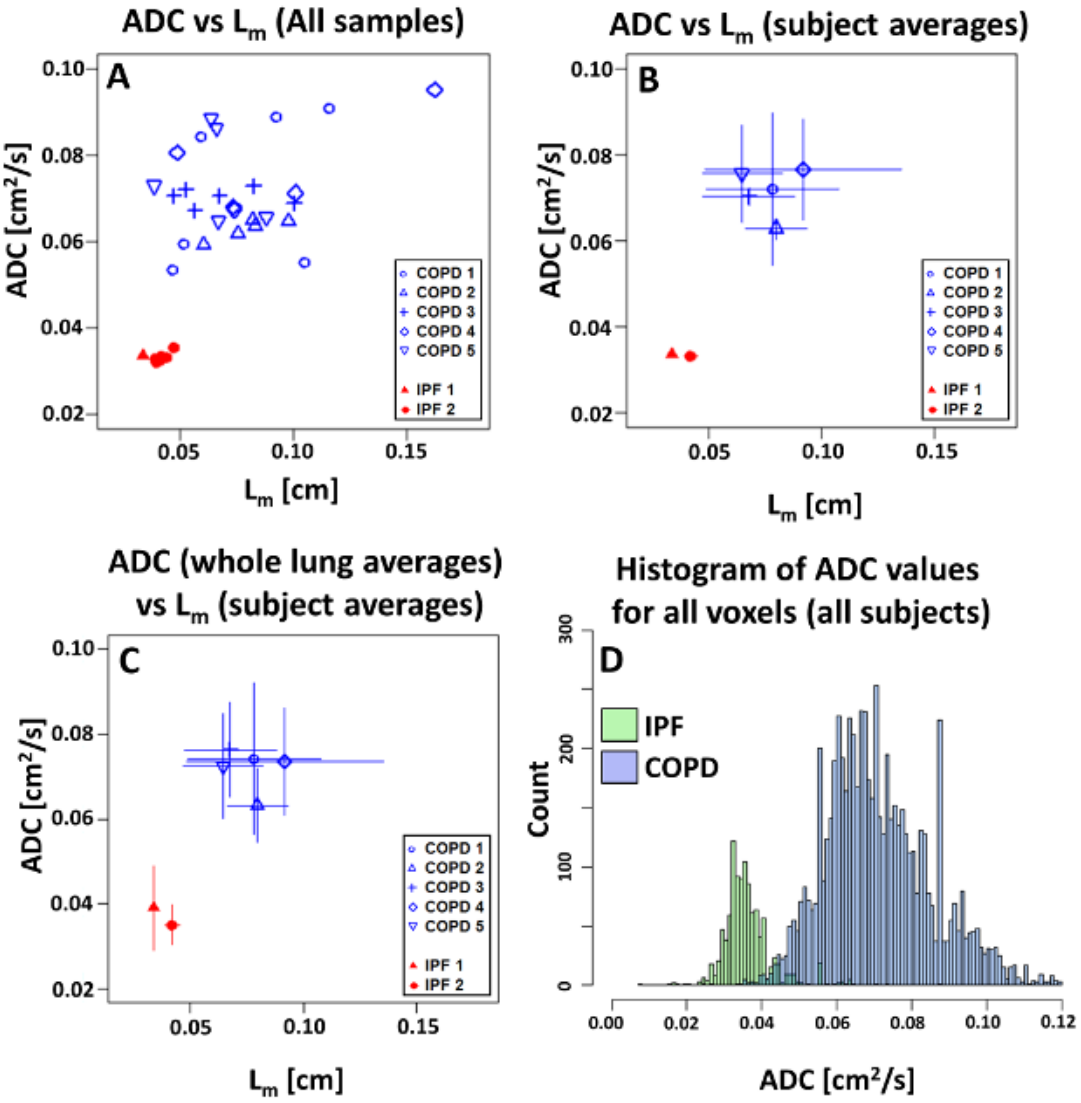

Figure 7.14: Plot of ADC for individual samples (a), sample averages for each subject (b) and all voxels of each subject (c) vs L_m. Panel d gives a histrogram of all voxels' ADC's for COPD and IPF. Figure published in Thomen *et al. Magn Reson Med* 2016 [42].

group separation by ADC was stronger than by L_m, it is important to note that histological processing involves delicate slicing of severely destroyed tissues in many cases, some of which became compressed in the process. All samples were harvested with an 11-mm core borer so this could easily be corrected by scaling the sample thickness in the direction of morphometric

measurement but indeed this would degrade precision in L_m.

The fact that airspace size measurement by ^{129}Xe diffusion is non-invasive is the most obvious strength of this method compared to histological sampling. ^{3}He diffusion has been widely recognized as an accurate measure of airspace size [178, 187, 189, 257], and several groups have developed elegant mathematical approaches to extracting more precise geometric measure of alveolar structure using HP gas diffusion [84, 85, 258, 259, 260]. As discussed in section 6.4, ^{3}He diffusion is much greater than that of ^{129}Xe [220] so the chosen b-values for the experiments have been chosen appropriately for adequate airspace sampling, $\Delta = \frac{L^2}{4D_0} = 6.4$ ms. Correct selection of b-value timing will provide the greatest contrast between control and COPD lungs, although the importance of precise b-timing selection for correct airways modeling has been extensively and hilariously debated in relevant literature [261].

Because xenon perfuses slightly across the blood-gas barrier and experiences chemical shift in the process, the spin-density of xenon in the gas phase decreases slightly in time [203]. However, the time constant for complete gas exchange to occur is approximately 100 ms [204, 262]; thus complete exchange occurs during the inflation time of 2-3 seconds and gas-phase spin density does not decrease between S_0 and S images[8]. These issues are believed to be even less of a concern for our *ex vivo* experiments here.

7.4 Summary

Here we have seen a few application of hyperpolarized gases to investigation lung structure-function relationships. In all gases, HP gases have been demonstrated excellent sensitivity in revealing useful physiological information in pulmonary disease. In particular, we have seen that HP ^{3}He MRI is sensitive to ventilation changes which occur following treatment for asthma by bronchial thermoplasty, that HP ^{129}Xe MRI is more sensitive than the accepted spirometric measure of FEV_1 for evaluation of disease severity in cystic fibrosis, and that HP ^{129}Xe diffusion is a more sensitive biomarker for airspace enlargement in COPD

[8]Even if this effect was a concern, the total loss of gas-phase signal is approximately 1-2% [205] so SNR would need to be quite high for this effect to be noticeable *in vivo*.

than even direct measurement of airspace size in histology[9]. These findings provide strong evidence that the structural abnormalities of these diseases correlate with functional deficits as revealed by hyperpolarized gas imaging. The hypotheses stated in section 1.3.2 have now been investigated, presented, and are now supported by scientific evidence. The next and final chapter will give a short summary of the strengths and weaknesses of hyperpolarized gas imaging and will conclude with future directions of the author and the research group.

[9]However, the sensitivity of HP gas imaging does suffer from lack of creative descriptors.

Chapter 8

Discussion, Conclusions, and Future of Hyperpolarized Gas and Functional Lung Imaging

"Let this be a lesson to you kids: kids never learn."

— Chief Wiggum, *The Simpsons*

While the results in this dissertation largely speak for themselves, the merit of hyperpolarized gases as an imaging research tool deserves a concise summary. This very brief chapter will present the strengths and weaknesses of HP gas as a viable imaging modality for lung function along with some comments concerning upcoming studies and clinical trials meant to push the technology forward in the clinic; future directions for the research described in the previous chapter will be given, and finally a brief summary of the dissertation and major conclusions will be presented.

8.1 Strengths and Limitations of Hyperpolarized Gas MRI of Lung

As the studies in this dissertation demonstrate (along with countless others), hyperpolarized gases are a sensitive measure of both lung function (ventilation, perfusion) *and* structure (airspace geometry). There is a clear potential for this technology to revolutionize pulmonary therapies and interventions. This is perhaps not surprising since the ability to image the actual gas contained within the lung would obviously reveal fantastically useful information regarding lung function regionally. Indeed HP gas imaging of lungs is a dynamic and growing field of research with continually emerging discoveries concerning lung mechanics and pathology.

Because MRI is non-invasive (no ionizing radiation), it is particularly attractive for longitudinal studies especially for pediatrics. If an adequate infrastructure for hyperpolarized gas imaging can be developed, then a single thoracic MRI session could yield invaluable information to clinicians and researchers. Because the patterns of pathologic development in lung disease are of critical importance to understanding disease progression, the ability to perform subsequent scans without adding risk to the patient may open the door to more rigorous analyses of milder cases of lung disease which often do not justify thoracic CT.

One might comment that because HP gas MRI is a non-equilibrium technique, the use of an expensive high-field MRI scanner is not only unnecessary but can actually introduce undesirable features in acquired images (increased SAR, shortened T_2^*, susceptibility artifacts) [263]. Why not build an inexpensive low-field scanner which wouldn't require cryogenic cooling. In fact this has been investigated by several groups with promising results [264, 265], although there currently exist no inexpensive low-field prototypes estimated to replace the ubiquitous MRI scanner which many clinics already have.

Throughout this dissertation, it has been made abundantly clear that the multifaceted utility of HP gas imaging for investigation of lung function obviates any other method for evaluation of respiratory health, but if hyperpolarized gas imaging is truly the panacea of

pulmonary investigation, why is it not yet the standard of care in the clinic? Indeed this is a major goal for the HP gas community [40, 266], but does HP gas really provide enough benefit/cost? If so, what remains to be done?

Those familiar with hyperpolarized gases generally recognize its diagnostic potential, and the conglomerate HP gas studies of the past 20 years are continually improving upon experimental design and data analysis in order to extract unique functional information from imaging. However there is generally a low population awareness of HP gas imaging, even among clinicians and researchers. Hyperpolarized gas imaging is not a money-saving technique; in fact the expense of a hyperpolarizer, necessary multinuclear imaging hardware, ^{3}He and/or ^{129}Xe gases, and MRI scanner imaging time can be prohibitive to a research institution let alone a clinic. Currently, both ^{3}He and ^{129}Xe are classified by the FDA as 'investigational new drugs' (IND) which requires special approval for admission to patients in our protocols. Since noble gases are chemically inert and thus harmless in imaging studies, there is currently a strong initiative within the community to remove these federal stipulations.

The natural abundance of ^{3}He is effectively zero, and the current supply of all ^{3}He comes from decay of tritium used in the manufacture of nuclear weapons. The dominant restriction on HP ^{3}He studies is its extremely low availability leading to hyperinflated prices. No matter what novel techniques and applications can be developed in HP ^{3}He MRI, it is a non-renewable resource, and supply will very likely become depleted within a matter of years (similar to the current ^{4}He supply crisis though much more certain), and many labs have employed recycling methods for their ^{3}He once it is exhaled and collected from subjects. Many researchers have shifted focus to the much more abundant ^{129}Xe specifically because of this purpose, and as a result, the hyperpolarization technology for ^{129}Xe has dramatically improved in recent years.

The medical benefits of diagnostic imaging are truly unsurpassed, but criticisms have emerged recently which suggest imaging is overutilized in medicine [267] relative to their expense. The procedures described in this work and data obtained may indeed be of great

benefit to society, but one must be cautious that confirmation bias does not cloud the usefulness of other techniques especially if they possess a greater benefit to cost ratio.

8.2 Future Directions

The utility of HP gas imaging as a diagnostic tool has been made apparent from the acquired images and results presented in the previous chapter, but to some extent each of the studies presented in this dissertation are driven by an interest in translation to the clinic. This is perhaps most apparent in the asthma/bronchial thermoplasty study where ^{3}He was shown to be feasible as an image-guidance technique for treatment and could be useful as a tool for therapists. Directed clinical trials could accelerate HP gas as a clinically relevant imaging modality for this purpose [268, 269, 270].

While the sensitivity of HP gas imaging to lung function in cystic fibrosis has been demonstrated, appropriate analysis comparing ventilatory information with regional structure may help identify the most problematic pathology for patients. This is especially important in treatment of children who may exhibit symptoms of dyspnea while having normal FEV_1 or CT. The non-invasive nature of MRI in particular is a powerful motivator for development of these techniques as well. A current clinical trial is underway at Cincinnati Children's hospital to identify correlations between lung ventilation volumes with HP ^{129}Xe and proton ^{1}H MRI [271].

Early onset of COPD often remains undiagnosed due to unclear association of symptoms and generally low population awareness [272, 273]. The sensitivity of HP gas diffusion MRI to subtle changes in alveolar airspace size could be invaluable as a diagnostic tool for COPD. All too often, COPD is left undiagnosed into late stages of disease development leaving a large financial burden on country. While the expense of an HP gas scan currently does not merit investigational medical imaging, the ability to recognize early disease development is attractive and could potentially counterbalance the expense of COPD management increasing overall quality of life in the process.

These are only a few of the many lung diseases from which HP gas imaging has the potential to reveal new insight. In general the hyperpolarized gas community has focused on obstructive lung diseases such as these, but there is potential for these techniques to be useful in investigations of infectious diseases as well (tuberculosis, pneumonia, mycoses, etc...) using combinations of HP gas ventilation and perfusion imaging[1]. One of the major goals of the research group is to implement techniques for chemical shift imaging of xenon's dissolved phase peaks [205]. Chemical Shift Saturation Recovery (CSSR) sequences have already shown that the rate of xenon uptake within the blood may be another useful measure of lung function, and development and implementation of these methods have already begun in our lab.

8.3 Dissertation Summary and Conclusion

In this work we have discovered that hyperpolarized gases are useful tools for investigation of regional lung structure-function relationships by addressing three major hypotheses. In particular we saw that (1) the ventilation defects revealed by hyperpolarized ^{3}He MRI in severe asthma can be identified on the level of bronchopulmonary segments (third-generation airway branches) and quantified to evaluate the efficacy of treatment by bronchial thermoplasty. [41], (2) Hyperpolarized ^{129}Xe is a sensitive measure of lung function in children with CF, and (3) Hyperpolarized ^{129}Xe is a sensitive biomarker for alveolar airspace size in COPD. [42]

[1]Because the root cause of infectious lung diseases are specific pathogens, they are most often diagnosed by a clinical microbiology lab [10], so imaging beyond projection x-ray is less necessary than for obstructive diseases.

Bibliography

"I happen to know that every word in your book was published years ago! Perhaps you've read...the dictionary!"

— Dick Solomon, *3rd Rock from the Sun*

[1] H. Goldstein, C. Poole, and J. Safko, *Classical Mechanics, 3e*. Addison-Wesley Longman, Incorporated, 2002.

[2] J. Jackson, *Classical Electrodynamics*. Wiley, 1998.

[3] K. Gottfried and T.-M. Yan, *Quantum Mechanics: Fundamentals*. New York: Springer, second ed., 2003.

[4] R. Pathria and P. Beale, *Statistical Mechanics*. Elsevier Science, 1996.

[5] J. West, *Respiratory Physiology: The Essentials*. Point (Lippincott Williams and Wilkins) Series, Wolters Kluwer Health/Lippincott Williams & Wilkins, 2008.

[6] S. L. Murphy, J. Xu, and K. D. Kochanek, "Deaths: final data for 2010," *Natl Vital Stat Rep*, vol. 61, no. 4, pp. 1–117, 2013.

[7] J. Guo, H. J. Huang, X. Wang, W. Wang, H. Ellison, R. P. Thomen, A. E. Gelman, and J. C. Woods, "Imaging mouse lung allograft rejection with 1h mri," *Magnetic Resonance in Medicine*, vol. 73, no. 5, pp. 1970–1978, 2015.

[8] W. Wang, N. M. Nguyen, D. A. Yablonskiy, A. L. Sukstanskii, E. Osmanagic, J. J. Atkinson, M. S. Conradi, and J. C. Woods, "Imaging lung microstructure in mice with hyperpolarized 3he diffusion mri," *Magnetic Resonance in Medicine*, vol. 65, no. 3, pp. 620–626, 2011.

[9] S. Freeman and H. Hamilton, *Biological Science: Evolution, Diversity, and Ecology*. Pearson Prentice Hall, 2005.

[10] R. Mason, V. Broaddus, T. Martin, T. King, D. Schraufnagel, J. Murray, and J. Nadel, *Murray and Nadel's Textbook of Respiratory Medicine: 2-Volume Set*. Expert consult title, Elsevier Health Sciences, 2010.

[11] F. Reif, *Fundamentals of Statistical and Thermal Physics:*. Waveland Press, 2009.

[12] E. R. Weibel, "What makes a good lung?: The morphometric basis of lung function," *Swiss Med Wkly*, vol. 139, no. 27-28, pp. 375–86, 2009.

[13] S. K. A-Ghazal, "The discovery of the pulmonary circulation who should get the credit: ibn al-nafis or william harvey'," 2002.

[14] R. Fraser and J. Paré, *Synopsis of diseases of the chest*. W.B. Saunders, 1994.

[15] J. West, *Pulmonary Pathophysiology: The Essentials*. M - Medicine Series, Wolters Kluwer Health, 2011.

[16] S. Fain, M. Schiebler, D. McCormack, and G. Parraga, "Imaging of lung function using hyperpolarized helium-3 magnetic resonance imaging: Review of current and emerging translational methods and applications," *J Magn Reson Imaging*, vol. 32, no. 6, pp. 1398–1408, 2010.

[17] M. Papadakis, S. McPhee, and M. Rabow, *CURRENT Medical Diagnosis and Treatment 2016*. LANGE CURRENT Series, McGraw-Hill Education, 2015.

[18] J. Hankinson, J. Odencrantz, and K. Fedan, "Spirometric reference values from a sample of the general u.s. population," *American Journal of Respiratory and Critical Care Medicine*, vol. 159, no. 1, pp. 179–187, 1999.

[19] P. A. de Jong, A. Lindblad, L. Rubin, W. C. Hop, J. C. de Jongste, M. Brink, and H. A. Tiddens, "Progression of lung disease on computed tomography and pulmonary function tests in children and adults with cystic fibrosis," *Thorax*, vol. 61, no. 1, pp. 80–5, 2006.

[20] E. Alpen, *Radiation Biophysics*. Academic Press, 1998.

[21] R. Munroe, "Radiation dose chart." `https://xkcd.com/radiation/`, 2011. Accessed: 2016-02-08.

[22] U. N. S. C. on the Effects of Atomic Radiation (UNSCEAR), "Unscear 2013 report: Sources, effects, and risks of ionizing radiation," *Volume 1: Report to the General Assembly*, vol. Scientific Annex A, 2013.

[23] L. Goldman and A. Schafer, *Goldman's Cecil Medicine*. Elsevier Health Sciences, 2011.

[24] R. Hill, B. Healy, L. Holloway, Z. Kuncic, D. Thwaites, and C. Baldock, "Advances in kilovoltage x-ray beam dosimetry," *Physics in Medicine and Biology*, vol. 59, no. 6, p. R183, 2014.

[25] S. K. Carlson, J. P. Felmlee, C. E. Bender, R. L. Ehman, K. L. Classic, T. L. Hoskin, W. S. Harmsen, and H. H. Hu, "Ct fluoroscopyguided biopsy of the lung or upper abdomen with a breath-hold monitoring and feedback system: A prospective randomized controlled clinical trial," *Radiology*, vol. 237, no. 2, pp. 701–708, 2005.

[26] P. A. Pellikka, P. S. Douglas, J. G. Miller, T. P. Abraham, R. Baumann, D. B. Buxton, B. F. Byrd III, P. Chen, N. L. Cook, J. M. Gardin, G. Hansen, H. C. Houle, S. Husson, S. Kaul, A. L. Klein, R. M. Lang, H. Leong-Poi, H. Lopez, T. M. Mahmoud, S. Maslak, M. L. McCulloch, S. Metz, S. F. Nagueh, A. S. Pearlman, P. Pibarot, M. H. Picard, T. R. Porter, D. Prater, R. Rodriguez, M. E. Sarano, M. Scherrer-Crosbie, G. S. Shirali, A. Sinusas, J. J. Slosky, L. Sugeng, A. Tatpati, F. S. Villanueva, O. T. Von Ramm, N. J. Weissman, and S. Zamani, "American society of echocardiography cardiovascular technology and research summit: A roadmap for 2020," *Journal of the American Society of Echocardiography*, vol. 26, no. 4, pp. 325–338, 2013.

[27] L. Gargani and G. Volpicelli, "How i do it: Lung ultrasound," *Cardiovascular Ultrasound*, vol. 12, no. 1, pp. 1–10, 2014.

[28] "International expert statement on training standards for critical care ultrasonography," *Intensive Care Medicine*, vol. 37, no. 7, pp. 1077–1083, 2011.

[29] J. Bushberg, *The Essential Physics of Medical Imaging*. Lippincott Williams & Wilkins, 2002.

[30] E. C. Lin, "Radiation risk from medical imaging," *Mayo Clinic Proceedings*, vol. 85, no. 12, pp. 1142 – 1146, 2010.

[31] M. T. Beinfeld and G. S. Gazelle, "Diagnostic imaging costs: Are they driving up the costs of hospital care?," *Radiology*, vol. 235, no. 3, pp. 934–939, 2005. PMID: 15833988.

[32] A. Baert and H. Kauczor, *MRI of the Lung*. Medical Radiology, Springer Berlin Heidelberg, 2008.

[33] L. Glover, "Why does an mri cost so darn much?." `http://time.com/money/2995166/why-does-mri-cost-so-much/`, 2014. Accessed: 2016-02-17.

[34] "Compare mri cost." `http://www.comparemricost.com/`. Accessed: 2016-02-17.

[35] M. S. Albert, G. D. Gates, B. Driehuys, W. Happer, B. Saam, C. S. Springer, and A. Wishnia, "Biological magnetic resonance imaging using laser-polarized 129xe," *Nature*, vol. 370, no. 6486, pp. 199–201, 1994.

[36] Z. I. Cleveland, G. E. Pavlovskaya, N. D. Elkins, K. F. Stupic, J. E. Repine, and T. Meersmann, "Hyperpolarized 83kr {MRI} of lungs," *Journal of Magnetic Resonance*, vol. 195, no. 2, pp. 232 – 237, 2008.

[37] S. Svenningsen, M. Kirby, D. Starr, H. O. Coxson, N. A. M. Paterson, D. G. McCormack, and G. Parraga, "What are ventilation defects in asthma?," *Thorax*, vol. 69, no. 1, pp. 63–71, 2014.

[38] B. O'Sullivan, M. Couch, J. P. Roche, R. Walvick, S. Zheng, D. Baker, M. Johnson, M. Botfield, and M. S. Albert, "Assessment of repeatability of hyperpolarized gas mr ventilation functional imaging in cystic fibrosis," *Acad Radiol*, vol. 21, no. 12, pp. 1524–9, 2014.

[39] "Hyperpolarized 129xe mri: A viable functional lung imaging modality?," *European Journal of Radiology*, vol. 64, no. 3, pp. 335 – 344, 2007. Pulmonary Functional Imaging.

[40] L. L. Walkup and J. C. Woods, "Translational applications of hyperpolarized 3he and 129xe," *NMR Biomed*, vol. 27, no. 12, pp. 1429–38, 2014.

[41] R. P. Thomen, A. Sheshadri, J. D. Quirk, J. Kozlowski, H. D. Ellison, R. D. Szczesniak, M. Castro, and J. C. Woods, "Regional ventilation changes in severe asthma after bronchial thermoplasty with (3)he mr imaging and ct," *Radiology*, vol. 274, no. 1, pp. 250–9, 2015.

[42] R. P. Thomen, J. D. Quirk, D. Roach, T. Egan-Rojas, K. Ruppert, R. D. Yusen, T. A. Altes, D. A. Yablonskiy, and J. C. Woods, "Direct comparison of 129xe diffusion measurements with quantitative histology in human lungs," *Magnetic Resonance in Medicine*, pp. n/a–n/a, 2016.

[43] A. Abragam, *The principles of nuclear magnetism*. International series of monographs on physics, Clarendon Press, 1983.

[44] C. Slichter, *Principles of Magnetic Resonance*. New York: Harper and Row, third springer ed., 1963.

[45] R. Ernst, G. Bodenhausen, and A. Wokaun, *Principles of Nuclear Magnetic Resonance in One and Two Dimensions*. International series of monographs on chemistry, Clarendon Press, 1990.

[46] M. Levitt, *Spin Dynamics: Basics of Nuclear Magnetic Resonance*. Wiley, 2001.

[47] E. Fukushima and S. Roeder, *Experimental Pulse NMR: A Nuts and Bolts Approach*. Advanced book program, Addison-Wesley, 1993.

[48] T. Farrar, *Introduction to Pulse Nmr Spectroscopy*. Farragut Press, 1989.

[49] E. Haacke, R. Brown, M. Thompson, and R. Venkatesan, *Magnetic Resonance Imaging: Physical Principles and Sequence Design*. Wiley, 1999.

[50] W. Happer, "Optical pumping," *Rev. Mod. Phys.*, vol. 44, no. 2, 1972.

[51] W. Happer, "Spin exchange, past, present, and future," *Ann. Phys. Fr.*, vol. 10, pp. 645–657, 1985.

[52] T. Walker and W. Happer, "Spin-exchange optical pumping of noble gas nuclei," *Rev. Mod. Phys.*, vol. 69, p. 629, 1997.

[53] R. Feynman, R. Leighton, M. Sands, and M. Gottlieb, *The Feynman lectures on physics*. The Feynman Lectures on Physics, Pearson/Addison-Wesley, 1963.

[54] R. Feynman, R. Leighton, and M. Sands, *The Feynman Lectures on Physics*. No. v. 3 in The Feynman Lectures on Physics, Pearson/Addison-Wesley, 1963.

[55] W. Gerlach and O. Stern, "Der experimentelle nachweis der richtungsquantelung im magnetfeld," *Zeitschrift fr Physik*, vol. 9, no. 1, pp. 349–352, 1922.

[56] S. Goudsmit and G. E. Uhlenbeck, "Spinning electrons and the structure of atoms," *Nature*, vol. 117, pp. 264–265, 1926.

[57] I. I. Rabi, "Space quantization in a gyrating magnetic field," *Phys. Rev.*, vol. 51, pp. 652–654, Apr 1937.

[58] I. I. Rabi, J. R. Zacharias, S. Millman, and P. Kusch, "A new method of measuring nuclear magnetic moment," *Phys. Rev.*, vol. 53, pp. 318–318, Feb 1938.

[59] E. M. Purcell, T. H. C., and R. V. Pound, "Resonance absorption by nuclear magnetic moments in a solid," *Phys Rev*, vol. 69, no. 37, 1946.

[60] F. Bloch, W. W. Hansen, and M. Packard, "Nuclear induction," *Phys Rev*, vol. 69, no. 127, 1946.

[61] M. Brown and R. Semelka, *MRI: Basic Principles and Applications*. Wiley, 2011.

[62] S. Codd and J. Seymour, *Magnetic Resonance Microscopy*. Wiley, 2008.

[63] G. E. Pavlovskaya, Z. I. Cleveland, K. F. Stupic, R. J. Basaraba, and T. Meersmann, "Hyperpolarized krypton-83 as a contrast agent for magnetic resonance imaging," *Proceedings of the National Academy of Sciences of the United States of America*, vol. 102, no. 51, pp. 18275–18279, 2005.

[64] K. F. Stupic, Z. I. Cleveland, G. E. Pavlovskaya, and T. Meersmann, "Hyperpolarized 131xe {NMR} spectroscopy," *Journal of Magnetic Resonance*, vol. 208, no. 1, pp. 58 – 69, 2011.

[65] R. K. Harris, E. D. Becker, S. M. Cabral de Menezes, R. Goodfellow, and P. Granger, "Nmr nomenclature: nuclear spin properties and conventions for chemical shifts. iupac recommendations 2001. international union of pure and applied chemistry. physical chemistry division. commission on molecular structure and spectroscopy," *Magnetic Resonance in Chemistry*, vol. 40, no. 7, pp. 489–505, 2002.

[66] J. Sakurai and J. Napolitano, *Modern Quantum Mechanics*. Addison-Wesley, 2011.

[67] D. Griffiths, *Introduction to Quantum Mechanics*. Pearson Custom Library, Pearson, 2013.

[68] D. Hoult and R. Richards, "The signal-to-noise ratio of the nuclear magnetic resonance experiment," *Journal of Magnetic Resonance*, vol. 213, no. 2, pp. 329 – 343, 2011. Magnetic MomentsGroundbreaking papers from the pages of the Journal Magnetic Resonance - and recollections from the scientists behind them.

[69] H. E. Moller, X. J. Chen, B. Saam, K. D. Hagspiel, G. A. Johnson, T. A. Altes, E. E. de Lange, and H. U. Kauczor, "Mri of the lungs using hyperpolarized noble gases," *Magn Reson Med*, vol. 47, no. 6, pp. 1029–51, 2002.

[70] H. Silver, *2015 ARRL Handbook*. Arrl Handbook for Radio Communications, American Radio Relay League, Incorporated, 2014.

[71] J. Emsley and J. Feeney, "Milestones in the first fifty years of {NMR}," *Progress in Nuclear Magnetic Resonance Spectroscopy*, vol. 28, no. 1, pp. 1 – 9, 1995. A collection of historical articles commissioned to celebrate 50 years of {NMR} and 30 years of Progress in {NMR} Spectroscopy.

[72] J. S. Rigden, "Quantum states and precession: The two discoveries of nmr," *Rev. Mod. Phys.*, vol. 58, pp. 433–448, Apr 1986.

[73] H. C. Torrey, "Transient nutations in nuclear magnetic resonance," *Phys. Rev.*, vol. 76, pp. 1059–1068, Oct 1949.

[74] E. L. Hahn, "Nuclear induction due to free larmor precession," *Phys. Rev.*, vol. 77, pp. 297–298, Jan 1950.

[75] P. C. Lauterbur, "Image formation by induced local interactions: Examples employing nuclear magnetic resonance," *Nature*, vol. 242, pp. 190–1, March 1973.

[76] A. N. Garroway, P. K. Grannell, and P. Mansfield, "Image formation in nmr by a selective irradiative process," *Journal of Physics C: Solid State Physics*, vol. 7, no. 24, p. L457, 1974.

[77] P. Mansfield and A. A. Maudsley, "Planar spin imaging by nmr," *Journal of Physics C: Solid State Physics*, vol. 9, no. 15, p. L409, 1976.

[78] R. R. Ernst and W. A. Anderson, "Application of fourier transform spectroscopy to magnetic resonance," *Review of Scientific Instruments*, vol. 37, no. 1, pp. 93–102, 1966.

[79] W. A. Edelstein, J. M. S. Hutchison, G. Johnson, and T. Redpath, "Spin warp nmr imaging and applications to human whole-body imaging," *Physics in Medicine and Biology*, vol. 25, no. 4, p. 751, 1980.

[80] P. A. Rinck, "Magnetic resonance: A peer-reviewed critical introduction." `http://www.magnetic-resonance.org/ch/21-01.html`, 2016. Accessed: 2016-02-12.

[81] M. Bernstein, K. King, and X. Zhou, *Handbook of MRI Pulse Sequences*. Elsevier Science, 2004.

[82] H. C. Torrey, "Bloch equations with diffusion terms," *Phys. Rev.*, vol. 104, pp. 563–565, Nov 1956.

[83] D. A. Yablonskiy, A. L. Sukstanskii, J. D. Quirk, J. C. Woods, and M. S. Conradi, "Probing lung microstructure with hyperpolarized noble gas diffusion mri: theoretical models and experimental results," *Magn Reson Med*, vol. 71, no. 2, pp. 486–505, 2014.

[84] A. L. Sukstanskii, J. D. Quirk, and D. A. Yablonskiy, "Probing lung microstructure with hyperpolarized 3he gradient echo mri," *NMR Biomed*, vol. 27, no. 12, pp. 1451–60, 2014.

[85] A. L. Sukstanskii and D. A. Yablonskiy, "Lung morphometry with hyperpolarized 129xe: theoretical background," *Magn Reson Med*, vol. 67, no. 3, pp. 856–66, 2012.

[86] P. L. Anthony, R. G. Arnold, H. R. Band, H. Borel, P. E. Bosted, V. Breton, G. D. Cates, T. E. Chupp, F. S. Dietrich, J. Dunne, R. Erbacher, J. Fellbaum, H. Fonvieille, R. Gearhart, R. Holmes, E. W. Hughes, J. R. Johnson, D. Kawall, C. Keppel, S. E. Kuhn, R. M. Lombard-Nelsen, J. Marroncle, T. Maruyama, W. Meyer, Z.-E. Meziani, H. Middleton, J. Morgenstern, N. R. Newbury, G. G. Petratos, R. Pitthan, R. Prepost, Y. Roblin, S. E. Rock, S. H. Rokni, G. Shapiro, T. Smith, P. A. Souder, M. Spengos, F. Staley, L. M. Stuart, Z. M. Szalata, Y. Terrien, A. K. Thompson, J. L. White, M. Woods, J. Xu, C. C. Young, and G. Zapalac, "Determination of the neutron spin structure function," *Phys. Rev. Lett.*, vol. 71, pp. 959–962, Aug 1993.

[87] F. P. Calaprice, W. Happer, D. F. Schreiber, M. M. Lowry, E. Miron, and X. Zeng, "Nuclear alignment and magnetic moments of ^{133}Xe, ^{133}Xe^m, and ^{131}Xe^m by spin exchange with optically pumped ^{87}Rb," *Phys. Rev. Lett.*, vol. 54, pp. 174–177, Jan 1985.

[88] T. G. Vold, F. J. Raab, B. Heckel, and E. N. Fortson, "Search for a permanent electric dipole moment on the ^{129}Xe atom," *Phys. Rev. Lett.*, vol. 52, pp. 2229–2232, Jun 1984.

[89] *Parity Nonconservation in Atomic Phenomena*. Taylor & Francis, 1991.

[90] J. A. Jones, "Quantum computing and nuclear magnetic resonance," *PhysChemComm*, vol. 4, pp. 49–56, 2001.

[91] P.-J. Nacher, *The Spin: Poincaré Seminar 2007*. Basel: Birkhäuser Basel, 2009.

[92] A. Kastler, "Quelques suggestions concernant la production optique et la dtection optique dune ingalit de population des niveaux de quantification spatiale des atomes. application lexprience de stern et gerlach et la rsonance magntique," *J. Phys. Radium*, vol. 11, no. 255.

[93] R. L. deZafra, "Optical Pumping," *Am J Phys*, vol. 28, p. 646, 1960.

[94] R. Benumof, "Optical Pumping Theory and Experiments," *American Journal of Physics*, vol. 33, pp. 151–160, Feb. 1965.

[95] M. E. Wagshul and T. E. Chupp, "Laser optical pumping of high-density rb in polarized he3 targets," *Phys. Rev. A*, vol. 49, p. 3854, 1994.

[96] S. Appelt, A. B.-A. Baranga, C. J. Erickson, M. V. Romalis, A. R. Young, and W. Happer, "Theory of spin-exchange optical pumping of 3He and 129Xe," *Phys. Rev A*, vol. 58, p. 1412, Aug. 1998.

[97] B. M. Goodson, "Nuclear magnetic resonance of laser-polarized noble gases in molecules, materials, and organisms," *Journal of Magnetic Resonance*, vol. 155, no. 2, pp. 157 – 216, 2002.

[98] E. Babcock, I. Nelson, S. Kadlecek, B. Driehuys, L. W. Anderson, F. W. Hersman, and T. G. Walker, "Hybrid spin-exchange optical pumping of ^{3}He," *Phys. Rev. Lett.*, vol. 91, p. 123003, Sep 2003.

[99] L. T. Aldrich, G. W. Wetherill, G. R. Tilton, and G. R. Davis, "Half-life of rb87," *Physical Review*, vol. 103, no. 4, pp. 1261–1270, 1956.

[100] D. A. Steck, "Alkali d line data: Rubidium 85 d line data." Oregon Center for Optics and Department of Physics, University of Oregon. revision 2.1.6, 20 September 2013 available from `http://steck.us/alkalidata/`, 2008. Accessed: 2016-02-19.

[101] D. A. Steck, "Alkali d line data: Rubidium 87 d line data." Oregon Center for Optics and Department of Physics, University of Oregon. revision 2.0.1, 2 May 2008 available from `http://steck.us/alkalidata/`, 2001. Accessed: 2016-02-19.

[102] I. Ruset, *Hyperpolarized 129Xe Production and Applications*. PhD thesis, University of New Hampshire, 2005.

[103] B. Larson, O. Häusser, P. P. J. Delheij, D. M. Whittal, and D. Thiessen, "Optical pumping of rb in the presence of high-pressure ^{3}He buffer gas," *Phys. Rev. A*, vol. 44, pp. 3108–3118, Sep 1991.

[104] W. Silfvast, *Laser Fundamentals*. Cambridge University Press, 2004.

[105] M. V. Romalis, E. Miron, and G. D. Cates, "Pressure broadening of rb D_1 and D_2 lines by ^{3}he, ^{4}he, n_2, and xe: Line cores and near wings," *Phys. Rev. A*, vol. 56, pp. 4569–4578, Dec 1997.

[106] B. Driehuys, G. D. Cates, E. Miron, K. Sauer, D. K. Walter, and W. Happer, "High-volume production of laser-polarized 129xe," *Applied Physics Letters*, vol. 69, no. 12, pp. 1668–1670, 1996.

[107] M. S. Rosen, T. E. Chupp, K. P. Coulter, R. C. Welsh, and S. D. Swanson, "Polarized 129xe optical pumping/spin exchange and delivery system for magnetic resonance spectroscopy and imaging studies," *Review of Scientific Instruments*, vol. 70, no. 2, 1999.

[108] I. C. Ruset, S. Ketel, and F. W. Hersman, "Optical pumping system design for large production of hyperpolarized ^{129}Xe," *Phys. Rev. Lett.*, vol. 96, p. 053002, Feb 2006.

[109] P. Nikolaou, A. M. Coffey, L. L. Walkup, B. M. Gust, N. Whiting, H. Newton, I. Muradyan, M. Dabaghyan, K. Ranta, G. D. Moroz, M. S. Rosen, S. Patz, M. J. Barlow, E. Y. Chekmenev, and B. M. Goodson, "Xena: An automated open-source 129xe hyperpolarizer for clinical use," *Magnetic Resonance Imaging*, vol. 32, no. 5, pp. 541 – 550, 2014.

[110] B. L. Volodin, S. V. Dolgy, E. D. Melnik, E. Downs, J. Shaw, and V. S. Ban, "Wavelength stabilization and spectrum narrowing of high-power multimode laser diodes and arrays by use of volume bragg gratings," *Opt. Lett.*, vol. 29, pp. 1891–1893, Aug 2004.

[111] T. J. Killian, "Thermionic phenomena caused by vapors of rubidium and potassium," *Phys. Rev.*, vol. 27, pp. 578–587, May 1926.

[112] T. Meersmann and E. Brunner, *Hyperpolarized Xenon-129 Magnetic Resonance: Concepts, Production, Techniques and Applications*. New developments in NMR, Royal Society of Chemistry, 2015.

[113] W. Happer, E. Miron, S. Schaefer, D. Schreiber, W. A. van Wijngaarden, and X. Zeng, "Polarization of the nuclear spins of noble-gas atoms by spin exchange with optically pumped alkali-metal atoms," *Phys. Rev. A*, vol. 29, pp. 3092–3110, Jun 1984.

[114] T. G. Walker, K. Bonin, and W. Happer, "Electron ˘ noble-gas spin-flip scattering at low energy," *Phys. Rev. A*, vol. 35, pp. 3749–3752, May 1987.

[115] F. Mackintosh, Z. Wu, and W. Happer, "A measurement of the spin-rotation coupling in naxe molecules," *Physics Letters A*, vol. 112, no. 9, pp. 435 – 439, 1985.

[116] J. C. Leawoods, D. A. Yablonskiy, B. Saam, D. S. Gierada, and M. S. Conradi, "Hyperpolarized 3he gas production and mr imaging of the lung," *Concepts in Magnetic Resonance*, vol. 13, no. 5, pp. 277–293, 2001.

[117] T. G. Walker, "Estimates of spin-exchange parameters for alkali-metal ˘ noble-gas pairs," *Phys. Rev. A*, vol. 40, pp. 4959–4964, Nov 1989.

[118] R. M. Herman, "Theory of spin exchange between optically pumped rubidium and foreign gas nuclei," *Phys. Rev.*, vol. 137, pp. A1062–A1065, Feb 1965.

[119] Z. Wu, T. G. Walker, and W. Happer, "Spin-rotation interaction of noble-gas alkali-metal atom pairs," *Phys. Rev. Lett.*, vol. 54, pp. 1921–1924, Apr 1985.

[120] C. H. Volk, T. M. Kwon, and J. G. Mark, "Measurement of the ^{87}Rb-^{129}Xe spin-exchange cross section," *Phys. Rev. A*, vol. 21, pp. 1549–1555, May 1980.

[121] N. D. Bhaskar, W. Happer, and T. McClelland, "Efficiency of spin exchange between rubidium spins and ^{129}Xe nuclei in a gas," *Phys. Rev. Lett.*, vol. 49, pp. 25–28, Jul 1982.

[122] J. C. Woods, L. L. Walkup, R. P. Thomen, N. Higano, and Z. I. Cleveland, "Initial experience in pediatric imaging with a homebuilt xenon-129 hyperpolarizer.." Euromar 2015, P129.

[123] G. Schrank, Z. Ma, A. Schoeck, and B. Saam, "Characterization of a low-pressure high-capacity ^{129}Xe flow-through polarizer," *Phys. Rev. A*, vol. 80, p. 063424, Dec 2009.

[124] G. D. Cates, R. J. Fitzgerald, A. S. Barton, P. Bogorad, M. Gatzke, N. R. Newbury, and B. Saam, "Rb$-^{129}$xe spin-exchange rates due to binary and three-body collisions at high xe pressures," *Phys. Rev. A*, vol. 45, pp. 4631–4639, Apr 1992.

[125] T. Hughes-Riley, J. S. Six, D. M. Lilburn, K. F. Stupic, A. C. Dorkes, D. E. Shaw, G. E. Pavlovskaya, and T. Meersmann, "Cryogenics free production of hyperpolarized 129xe and 83kr for biomedical {MRI} applications," *Journal of Magnetic Resonance*, vol. 237, pp. 23 – 33, 2013.

[126] N. R. Newbury, A. S. Barton, G. D. Cates, W. Happer, and H. Middleton, "Gaseous $^3-^3$he magnetic dipolar spin relaxation," *Phys. Rev. A*, vol. 48, pp. 4411–4420, Dec 1993.

[127] J. Ma, A. Kishinevski, Y.-Y. Jau, C. Reuter, and W. Happer, "Modification of glass cell walls by rubidium vapor," *Phys. Rev. A*, vol. 79, p. 042905, Apr 2009.

[128] B. Driehuys, G. D. Cates, and W. Happer, "Surface relaxation mechanisms of laser-polarized ^{129}Xe," *Phys. Rev. Lett.*, vol. 74, pp. 4943–4946, Jun 1995.

[129] S. R. Breeze, S. Lang, I. Moudrakovski, C. I. Ratcliffe, J. A. Ripmeester, G. Santyr, B. Simard, and I. Zuger, "Coatings for optical pumping cells and short-term storage of hyperpolarized xenon," *Journal of Applied Physics*, vol. 87, no. 11, 2000.

[130] W. Zheng, Z. I. Cleveland, H. E. Mller, and B. Driehuys, "Gradient-induced longitudinal relaxation of hyperpolarized noble gases in the fringe fields of superconducting magnets used for magnetic resonance," *Journal of Magnetic Resonance*, vol. 208, no. 2, pp. 284 – 290, 2011.

[131] B. Saam, W. Happer, and H. Middleton, "Nuclear relaxation of ^{3}He in the presence of o_2," *Phys. Rev. A*, vol. 52, pp. 862–865, Jul 1995.

[132] C. J. Jameson, A. K. Jameson, and J. K. Hwang, "Nuclear spin relaxation by intermolecular magnetic dipole coupling in the gas phase. 129xe in oxygen," *The Journal of Chemical Physics*, vol. 89, no. 7, 1988.

[133] H. E. Mller, X. Chen, M. S. Chawla, B. Driehuys, L. W. Hedlund, and G. Johnson, "Signal dynamics in magnetic resonance imaging of the lung with hyperpolarized noble gases," *Journal of Magnetic Resonance*, vol. 135, no. 1, pp. 133 – 143, 1998.

[134] F. D. Doty, *Probe Design and Construction*.

[135] D. G. Gadian, K. S. Panesar, A. J. Perez Linde, A. J. Horsewill, W. Kockenberger, and J. R. Owers-Bradley, "Preparation of highly polarized nuclear spin systems using brute-force and low-field thermal mixing," *Phys. Chem. Chem. Phys.*, vol. 14, pp. 5397–5402, 2012.

[136] E. V. Krjukov, J. D. O'Neill, and J. R. Owers-Bradley, "Brute force polarization of 129xe," *Journal of Low Temperature Physics*, vol. 140, no. 5, pp. 397–408.

[137] M. Chapellier, G. Frossati, and F. B. Rasmussen, "Spin polarization of liquid ^{3}He by rapid melting of polarized solid," *Phys. Rev. Lett.*, vol. 42, pp. 904–907, Apr 1979.

[138] F. D. Colegrove, L. D. Schearer, and G. K. Walters, "Polarization of he^3 gas by optical pumping," *Phys. Rev.*, vol. 132, pp. 2561–2572, Dec 1963.

[139] G. Eckert, W. Heil, M. Meyerhoff, E. Otten, R. Surkau, M. Werner, M. Leduc, P. Nacher, and L. Schearer, "A dense polarized 3he target based on compression of optically pumped gas," *Nuclear Instruments and Methods in Physics Research Section A: Accelerators, Spectrometers, Detectors and Associated Equipment*, vol. 320, no. 12, pp. 53 – 65, 1992.

[140] T. R. Gentile, M. E. Hayden, and M. J. Barlow, "Comparison of metastability-exchange optical pumping sources," *J. Opt. Soc. Am. B*, vol. 20, pp. 2068–2074, Oct 2003.

[141] J. Becker, W. Heil, B. Krug, M. Leduc, M. Meyerhoff, P. Nacher, E. Otten, T. Prokscha, L. Schearer, and R. Surkau, "Study of mechanical compression of spin-polarized 3he gas," *Nuclear Instruments and Methods in Physics Research Section A: Accelerators, Spectrometers, Detectors and Associated Equipment*, vol. 346, no. 1, pp. 45 – 51, 1994.

[142] J. Becker, J. Bermuth, M. Ebert, T. Grossmann, W. Heil, D. Hofmann, H. Humblot, M. Leduc, E. Otten, D. Rohe, and R. Surkau, "Interdisciplinary experiments with polarized 3he," *Nuclear Instruments and Methods in Physics Research Section A: Accelerators, Spectrometers, Detectors and Associated Equipment*, vol. 402, no. 23, pp. 327 – 336, 1998. Proceedings of the 7th {RCNP} International Workshop on Polarized He Beams and Gas Targets and Their Application.

[143] A. Comment, S. Jannin, J.-N. Hyacinthe, P. Miéville, R. Sarkar, P. Ahuja, P. R. Vasos, X. Montet, F. Lazeyras, J.-P. Vallée, P. Hautle, J. A. Konter, B. van den Brandt, J.-P. Ansermet, R. Gruetter, and G. Bodenhausen, "Hyperpolarizing gases via dynamic nuclear polarization and sublimation," *Phys. Rev. Lett.*, vol. 105, p. 018104, Jul 2010.

[144] A. W. Overhauser, "Polarization of nuclei in metals," *Phys. Rev.*, vol. 92, pp. 411–415, Oct 1953.

[145] A. Abragam and M. Goldman, "Principles of dynamic nuclear polarisation," *Reports on Progress in Physics*, vol. 41, no. 3, p. 395, 1978.

[146] P. Cheo, *Handbook of Solid-State Lasers*. Optical Science and Engineering, Taylor & Francis, 1988.

[147] B. Chann, E. Babcock, L. W. Anderson, and T. G. Walker, "Skew light propagation in optically thick optical pumping cells," *Phys. Rev. A*, vol. 66, p. 033406, Sep 2002.

[148] K. H. Ang, G. Chong, and Y. Li, "Pid control system analysis, design, and technology," *IEEE Transactions on Control Systems Technology*, vol. 13, pp. 559–576, July 2005.

[149] R. E. Jacob, S. W. Morgan, and B. Saam, "3he spin exchange cells for magnetic resonance imaging," *Journal of Applied Physics*, vol. 92, no. 3, 2002.

[150] R. Jacob, B. Driehuys, and B. Saam, "Fundamental mechanisms of 3he relaxation on glass," *Chemical Physics Letters*, vol. 370, no. 12, pp. 261 – 267, 2003.

[151] R. E. Jacob, J. Teter, B. Saam, W. C. Chen, and T. R. Gentile, "Low-field orientation dependence of ^{3}He relaxation in spin-exchange cells," *Phys. Rev. A*, vol. 69, p. 021401, Feb 2004.

[152] R. E. Jacob, S. W. Morgan, B. Saam, and J. C. Leawoods, "Wall relaxation of ^3he in spin-exchange cells," *Phys. Rev. Lett.*, vol. 87, p. 143004, Sep 2001.

[153] B. T. Saam and M. S. Conradi, "Low frequency {NMR} polarimeter for hyperpolarized gases," *Journal of Magnetic Resonance*, vol. 134, no. 1, pp. 67 – 71, 1998.

[154] J. Vaughan and J. Griffiths, *RF Coils for MRI*. eMagRes Books, Wiley, 2012.

[155] T. Hayes and P. Horowitz, *The Art of Electronics Student Manual*. Art of electronics / Paul Horowitz; Winfield Hill, Cambridge University Press, 1989.

[156] "'from arduino to a microcontroller on a breadboard'." https://www.arduino.cc/en/-Tutorial/ArduinoToBreadboard, retrieved April 25, 2016.

[157] P. Scherz and S. Monk, *Practical Electronics for Inventors, Third Edition*. McGraw-Hill Education, 2013.

[158] M. S. Conradi. personal communication, April 19, 2016.

[159] A. Compaan, A. Wagoner, and A. Aydinli, "Rotational raman scattering in the instructional laboratory," *American Journal of Physics*, vol. 62, no. 7, pp. 639–644, 1994.

[160] J. C. Woods, L. L. Walkup, R. P. , Thomen, N. Higano, and Z. I. Cleveland, "Initial experience in pediatric imaging with a homebuilt xenon-129 hyperpolarizer," July 8, 2015 2015.

[161] M. E. Hayden and P.-J. Nacher, "History and physical principles of MRI," in *Magnetic Resonance Imaging Handbook* (L. SABA, ed.), vol. 1, CRC press, 2016.

[162] S. Hidalgo-Tobon, "Theory of gradient coil design methods for magnetic resonance imaging," *Concepts in Magnetic Resonance Part A*, vol. 36, no. 4, pp. 223–242, 2010.

[163] P. M. Glover, "Interaction of mri field gradients with the human body," *Physics in Medicine and Biology*, vol. 54, no. 21, p. R99, 2009.

[164] C. E. Hayes, "The development of the birdcage resonator: a historical perspective," *NMR in Biomedicine*, vol. 22, no. 9, pp. 908–918, 2009.

[165] W. Loew, R. Thomen, R. Pratt, Z. I. Cleveland, C. Dumoulin, J. C. Woods, and R. Giaquinto, "A volume saddle coil for hyperpolarized 129xe lung imaging," *North American Cystic Fibrosis Conference*, 2015. Oral Presentation Presented at the NACFC, Oactober 2015.

[166] H. E. Mller, Z. I. Cleveland, and B. Driehuys, "Relaxation of hyperpolarized 129xe in a deflating polymer bag," *Journal of Magnetic Resonance*, vol. 212, no. 1, pp. 109 – 115, 2011.

[167] A. Haase, J. Frahm, D. Matthaei, W. Hnicke, and K.-D. Merboldt, "{FLASH} imaging: Rapid {NMR} imaging using low flip-angle pulses," *Journal of Magnetic Resonance*, vol. 213, no. 2, pp. 533 – 541, 2011. Magnetic MomentsGroundbreaking papers from the pages of the Journal Magnetic Resonance - and recollections from the scientists behind them.

[168] J. P. M. III, "Optimization of gradient-echo sequences for hyperpolarized noble gas mri," *Proceedings of the 6th annual meeting of ISMRM,Sydney, Australia*, p. 1904, 1998.

[169] W. G. Miller, A. T. Altes, R. J. Brookeman, E. E. de Lange, and P. J. Mugler III, "Hyperpolarized 3he lung ventilation imaging with b 1-inhomogeneity correction in a single breath-hold scan," *Magnetic Resonance Materials in Physics, Biology and Medicine*, vol. 16, no. 5, pp. 218–226, 2004.

[170] L. Zhao, R. Mulkern, C.-H. Tseng, D. Williamson, S. Patz, R. Kraft, R. L. Walsworth, F. A. Jolesz, and M. S. Albert, "Gradient-echo imaging considerations for hyperpolarized129xe {MR}," *Journal of Magnetic Resonance, Series B*, vol. 113, no. 2, pp. 179 – 183, 1996.

[171] D. Idiyatullin, C. Corum, J.-Y. Park, and M. Garwood, "Fast and quiet {MRI} using a swept radiofrequency," *Journal of Magnetic Resonance*, vol. 181, no. 2, pp. 342 – 349, 2006.

[172] N. C. Chuck, W. Jungraithmayr, G. D. Puippe, S. Pazahr, D. Nanz, and A. Boss, "Mri of the lung: comparison of ultrashort-echo-time (ute) to zero-echo-time (zte)," *Fortschr Rntgenstr*, vol. 183, no. 12, p. A7, 2011.

[173] M. Lederlin, G. Bauman, M. Eichinger, J. Dinkel, M. Brault, J. Biederer, and M. Puderbach, "Functional {MRI} using fourier decomposition of lung signal: Reproducibility of ventilation- and perfusion-weighted imaging in healthy volunteers," *European Journal of Radiology*, vol. 82, no. 6, pp. 1015 – 1022, 2013.

[174] O. Togao, R. Tsuji, Y. Ohno, I. Dimitrov, and M. Takahashi, "Ultrashort echo time (ute) mri of the lung: Assessment of tissue density in the lung parenchyma," *Magnetic Resonance in Medicine*, vol. 64, no. 5, pp. 1491–1498, 2010.

[175] W. Ma, K. Sheikh, S. Svenningsen, D. Pike, F. Guo, R. Etemad-Rezai, J. Leipsic, H. O. Coxson, D. G. McCormack, and G. Parraga, "Ultra-short echo-time pulmonary mri: Evaluation and reproducibility in copd subjects with and without bronchiectasis," *Journal of Magnetic Resonance Imaging*, vol. 41, no. 5, pp. 1465–1474, 2015.

[176] A. S. Brody, P. L. Molina, J. S. Klein, B. S. Rothman, M. Ramagopal, and D. R. Swartz, "High-resolution computed tomography of the chest in children with cystic fibrosis: support for use as an outcome surrogate," *Pediatr Radiol*, vol. 29, no. 10, pp. 731–5, 1999.

[177] A. S. Brody, "Scoring systems for ct in cystic fibrosis: Who cares?," *Radiology*, vol. 231, no. 2, pp. 296–298, 2004. PMID: 15128979.

[178] G. Parraga, A. Ouriadov, A. Evans, S. McKay, W. W. Lam, A. Fenster, R. Etemad-Rezai, D. McCormack, and G. Santyr, "Hyperpolarized 3he ventilation defects and apparent diffusion coefficients in chronic obstructive pulmonary disease: preliminary results at 3.0 tesla," *Invest Radiol*, vol. 42, no. 6, pp. 384–91, 2007.

[179] T. A. Altes, P. L. Powers, J. Knight-Scott, G. Rakes, T. A. Platts-Mills, E. E. de Lange, B. A. Alford, r. Mugler, J. P., and J. R. Brookeman, "Hyperpolarized 3he mr lung ventilation imaging in asthmatics: preliminary findings," *J Magn Reson Imaging*, vol. 13, no. 3, pp. 378–84, 2001.

[180] K. Mentore, D. K. Froh, E. E. de Lange, J. R. Brookeman, A. O. Paget-Brown, and T. A. Altes, "Hyperpolarized hhe 3 mri of the lung in cystic fibrosis: assessment at baseline and after bronchodilator and airway clearance treatment," *Acad Radiol*, vol. 12, no. 11, pp. 1423–9, 2005.

[181] M. Kirby, A. Ouriadov, S. Svenningsen, A. Owrangi, A. Wheatley, R. Etemad-Rezai, G. E. Santyr, D. G. McCormack, and G. Parraga, "Hyperpolarized 3he and 129xe magnetic resonance imaging apparent diffusion coefficients: physiological relevance in older never- and ex-smokers," *Physiol Rep*, vol. 2, no. 7, 2014.

[182] M. He, S. S. Kaushik, S. H. Robertson, M. S. Freeman, R. S. Virgincar, H. P. McAdams, and B. Driehuys, "Extending semiautomatic ventilation defect analysis for hyperpolarized (129)xe ventilation mri," *Acad Radiol*, vol. 21, no. 12, pp. 1530–41, 2014.

[183] M. Kirby, M. Heydarian, S. Svenningsen, A. Wheatley, D. G. McCormack, R. Etemad-Rezai, and G. Parraga, "Hyperpolarized 3he magnetic resonance functional imaging semiautomated segmentation," *Acad Radiol*, vol. 19, no. 2, pp. 141–52, 2012.

[184] N. J. Tustison, T. A. Altes, G. Song, E. E. de Lange, r. Mugler, J. P., and J. C. Gee, "Feature analysis of hyperpolarized helium-3 pulmonary mri: a study of asthmatics versus nonasthmatics," *Magn Reson Med*, vol. 63, no. 6, pp. 1448–55, 2010.

[185] H. U. Kauczor, K. Markstaller, M. Puderbach, J. Lill, B. Eberle, G. Hanisch, T. Grossmann, C. P. Heussel, W. Schreiber, and M. Thelen, "Volumetry of ventilated airspaces by 3he mri: preliminary results," *Invest Radiol*, vol. 36, no. 2, pp. 110–4, 2001.

[186] M. Kirby and G. Parraga, "Pulmonary functional imaging using hyperpolarized noble gas mri: six years of start-up experience at a single site," *Acad Radiol*, vol. 20, no. 11, pp. 1344–56, 2013.

[187] J. C. Woods, C. K. Choong, D. A. Yablonskiy, J. Bentley, J. Wong, J. A. Pierce, J. D. Cooper, P. T. Macklem, M. S. Conradi, and J. C. Hogg, "Hyperpolarized 3he diffusion mri and histology in pulmonary emphysema," *Magn Reson Med*, vol. 56, no. 6, pp. 1293–300, 2006.

[188] S. S. Kaushik, Z. I. Cleveland, G. P. Cofer, G. Metz, D. Beaver, J. Nouls, M. Kraft, W. Auffermann, J. Wolber, H. P. McAdams, and B. Driehuys, "Diffusion-weighted hyperpolarized xe-129 mri in healthy volunteers and subjects with chronic obstructive pulmonary disease," *Magnetic Resonance in Medicine*, vol. 65, no. 4, pp. 1155–1165, 2011.

[189] T. A. Altes, J. Mata, E. E. de Lange, J. R. Brookeman, and r. Mugler, J. P., "Assessment of lung development using hyperpolarized helium-3 diffusion mr imaging," *J Magn Reson Imaging*, vol. 24, no. 6, pp. 1277–83, 2006.

[190] M. S. Conradi, D. A. Yablonskiy, J. C. Woods, D. S. Gierada, S. E. T. Bartel, S. E. Haywood, and C. Menard, "The role of collateral paths in long-range diffusion of (3)he in lungs," *Acad Radiol*, vol. 15, no. 6, pp. 675–82, 2008.

[191] S.-E. T. Bartel, S. E. Haywood, J. C. Woods, Y. V. Chang, C. Menard, D. A. Yablonskiy, D. S. Gierada, and M. S. Conradi, "Role of collateral paths in long-range diffusion in lungs," *Journal of Applied Physiology*, vol. 104, no. 5, pp. 1495–1503, 2008.

[192] J. C. Woods, D. A. Yablonskiy, C. K. Choong, K. Chino, J. A. Pierce, J. C. Hogg, J. Bentley, J. D. Cooper, M. S. Conradi, and P. T. Macklem, "Long-range diffusion of hyperpolarized 3he in explanted normal and emphysematous human lungs via magnetization tagging," *Journal of Applied Physiology*, vol. 99, no. 5, pp. 1992–1997, 2005.

[193] D. S. Gierada, J. C. Woods, A. J. Bierhals, S. T. Bartel, J. H. Ritter, C. K. Choong, N. A. Das, C. Hong, T. K. Pilgram, Y. V. Chang, R. E. Jacob, J. C. Hogg, R. J. Battafarano, J. D. Cooper, B. F. Meyers, G. A. Patterson, D. A. Yablonskiy, and M. S. Conradi, "Effects of diffusion time on short-range hyperpolarized (3)he diffusivity measurements in emphysema," *J Magn Reson Imaging*, vol. 30, no. 4, pp. 801–8, 2009.

[194] P. Bevington and D. Robinson, *Data Reduction and Error Analysis for the Physical Sciences*. McGraw-Hill Higher Education, McGraw-Hill, 2003.

[195] D. F. Fairbanks and C. R. Wilke, "Diffusion coefficients in multicomponent gas mixtures," *Industrial & Engineering Chemistry*, vol. 42, no. 3, pp. 471–475, 1950.

[196] W. G. Pollard and R. D. Present, "On gaseous self-diffusion in long capillary tubes," *Phys. Rev.*, vol. 73, pp. 762–774, Apr 1948.

[197] E. Babcock, B. Chann, T. G. Walker, W. C. Chen, and T. R. Gentile, "Limits to the polarization for spin-exchange optical pumping of ^{3}He," *Phys. Rev. Lett.*, vol. 96, p. 083003, Mar 2006.

[198] J. C. Woods, "Mine the moon for 3he mri? not yet," *J Appl Physiol (1985)*, vol. 114, no. 6, pp. 705–6, 2013.

[199] "Its coming, but dont invest just yet in mining helium-3 on the moon," *The k2p Blog*, 2014.

[200] T. D. Telegraph, "China sets sights on mining the moon," *The Daily Telegraph*, 2016.

[201] L. J. Wittenberg, "Non-lunar ^{3}he sources," *Presented at the Second Wisconsin Symposium on Helium-3 and Fusion Power, 19-21 July, 1993, Madison WI*, 1994.

[202] L. L. Walkup, R. P. Thomen, T. Akinyi, E. Watters, K. Ruppert, J. P. Clancy, J. C. Woods, and Z. I. Cleveland, "Feasibility, tolerability, and safety of pediatric hyperpolarized xe magnetic resonance imaging in healthy volunteers and subjects with cystic fibrosis," *Pediatric Radiology*, 2016. Accepted 3-17-2016.

[203] I. Dregely, r. Mugler, J. P., I. C. Ruset, T. A. Altes, J. F. Mata, G. W. Miller, J. Ketel, S. Ketel, J. Distelbrink, F. W. Hersman, and K. Ruppert, "Hyperpolarized xenon-129 gas-exchange imaging of lung microstructure: first case studies in subjects with obstructive lung disease," *J Magn Reson Imaging*, vol. 33, no. 5, pp. 1052–62, 2011.

[204] Z. I. Cleveland, G. P. Cofer, G. Metz, D. Beaver, J. Nouls, S. S. Kaushik, M. Kraft, J. Wolber, K. T. Kelly, H. P. McAdams, and B. Driehuys, "Hyperpolarized xe mr imaging of alveolar gas uptake in humans," *PLoS One*, vol. 5, no. 8, p. e12192, 2010.

[205] K. Ruppert, J. F. Mata, J. R. Brookeman, K. D. Hagspiel, and r. Mugler, J. P., "Exploring lung function with hyperpolarized (129)xe nuclear magnetic resonance," *Magn Reson Med*, vol. 51, no. 4, pp. 676–87, 2004.

[206] N. A. Education, P. P. N. Heart, and B. I. S. E. P. on the Management of Asthma, *Expert panel report 3: guidelines for the diagnosis and management of asthma*. DIANE Publishing, 2007.

[207] F. L. Urbano, "Review of the naepp 2007 expert panel report (epr-3) on asthma diagnosis and treatment guidelines," *Journal of Managed Care Pharmacy*, vol. 14, no. 1, pp. 41–49, 2008. PMID: 18240881.

[208] U. F. (FDA) and D. Administration, "Approval of alair bronchial thermoplasty system: Alait catheter and alair rf controller," 2010.

[209] Y. Amrani and R. A. Panettieri, "Airway smooth muscle: contraction and beyond," *The International Journal of Biochemistry and Cell Biology*, vol. 35, no. 3, pp. 272 – 276, 2003.

[210] T. R. Gildea, S. B. Khatri, and M. Castro, "Bronchial thermoplasty: a new treatment for severe refractory asthma," *Cleve Clin J Med*, vol. 78, no. 7, pp. 477–85, 2011.

[211] J. D. Miller, G. Cox, L. Vincic, C. M. Lombard, B. E. Loomas, and C. J. Danek, "A prospective feasibility study of bronchial thermoplasty in the human airway," *Chest*, vol. 127, no. 6, pp. 1999–2006, 2005.

[212] G. Cox, N. C. Thomson, A. S. Rubin, R. M. Niven, P. A. Corris, H. C. Siersted, R. Olivenstein, I. D. Pavord, D. McCormack, R. Chaudhuri, J. D. Miller, M. Laviolette, and A. I. R. T. S. Group, "Asthma control during the year after bronchial thermoplasty," *N Engl J Med*, vol. 356, no. 13, pp. 1327–37, 2007.

[213] I. D. Pavord, G. Cox, N. C. Thomson, A. S. Rubin, P. A. Corris, R. M. Niven, K. F. Chung, M. Laviolette, and R. T. S. Group, "Safety and efficacy of bronchial thermoplasty in symptomatic, severe asthma," *Am J Respir Crit Care Med*, vol. 176, no. 12, pp. 1185–91, 2007.

[214] M. Castro, A. S. Rubin, M. Laviolette, J. Fiterman, M. De Andrade Lima, P. L. Shah, E. Fiss, R. Olivenstein, N. C. Thomson, R. M. Niven, I. D. Pavord, M. Simoff, D. R. Duhamel, C. McEvoy, R. Barbers, N. H. Ten Hacken, M. E. Wechsler, M. Holmes, M. J. Phillips, S. Erzurum, W. Lunn, E. Israel, N. Jarjour, M. Kraft, N. S. Shargill, J. Quiring, S. M. Berry, G. Cox, and A. I. R. T. S. Group, "Effectiveness and safety of bronchial thermoplasty in the treatment of severe asthma: a multicenter, randomized, double-blind, sham-controlled clinical trial," *Am J Respir Crit Care Med*, vol. 181, no. 2, pp. 116–24, 2010.

[215] G. Cox, J. D. Miller, A. McWilliams, J. M. Fitzgerald, and S. Lam, "Bronchial thermoplasty for asthma," *Am J Respir Crit Care Med*, vol. 173, no. 9, pp. 965–9, 2006.

[216] A. Busacker, J. Newell, J. D., T. Keefe, E. A. Hoffman, J. C. Granroth, M. Castro, S. Fain, and S. Wenzel, "A multivariate analysis of risk factors for the air-trapping asthmatic phenotype as measured by quantitative ct analysis," *Chest*, vol. 135, no. 1, pp. 48–56, 2009.

[217] F. Preparata and M. Shamos, *Computational Geometry: An Introduction*. Monographs in Computer Science, Springer New York, 2012.

[218] M. Salerno, J. Brookeman, E. de Lange, J. Knight-Scott, and J. P. r. Mugler, "Demonstration of an alveolar-size gradient in the healthy human lung: A study of the reproducibility of hyperpolarized 3he diffusion mri," 2000.

[219] S. Fichele, N. Woodhouse, A. J. Swift, Z. Said, M. N. J. Paley, L. Kasuboski, G. H. Mills, E. J. R. van Beek, and J. M. Wild, "Mri of helium-3 gas in healthy lungs: Posture related variations of alveolar size," *Journal of Magnetic Resonance Imaging*, vol. 20, no. 2, pp. 331–335, 2004.

[220] X. J. Chen, H. E. Moller, M. S. Chawla, G. P. Cofer, B. Driehuys, L. W. Hedlund, and G. A. Johnson, "Spatially resolved measurements of hyperpolarized gas properties in the lung in vivo. part i: diffusion coefficient," *Magn Reson Med*, vol. 42, no. 4, pp. 721–8, 1999.

[221] B. P. O'Sullivan and S. D. Freedman, "Cystic fibrosis," *Lancet*, vol. 373, no. 9678, pp. 1891–904, 2009.

[222] S. M. Rowe, S. L. Heltshe, T. Gonska, S. H. Donaldson, D. Borowitz, D. Gelfond, S. D. Sagel, U. Khan, N. Mayer-Hamblett, J. M. Van Dalfsen, E. Joseloff, B. W. Ramsey, and G. I. o. t. C. F. F. T. D. Network, "Clinical mechanism of the cystic fibrosis

transmembrane conductance regulator potentiator ivacaftor in g551d-mediated cystic fibrosis," *Am J Respir Crit Care Med*, vol. 190, no. 2, pp. 175–84, 2014.

[223] P. A. de Jong, M. D. Ottink, S. G. Robben, M. H. Lequin, W. C. Hop, J. J. Hendriks, P. D. Pare, and H. A. Tiddens, "Pulmonary disease assessment in cystic fibrosis: comparison of ct scoring systems and value of bronchial and arterial dimension measurements," *Radiology*, vol. 231, no. 2, pp. 434–9, 2004.

[224] N. D. Gai, A. Malayeri, H. Agarwal, R. Evers, and D. Bluemke, "Evaluation of optimized breath-hold and free-breathing 3d ultrashort echo time contrast agent-free mri of the human lung," *J Magn Reson Imaging*, 2015.

[225] R. Soni, C. J. Dobbin, M. A. Milross, I. H. Young, and P. P. Bye, "Gas exchange in stable patients with moderate-to-severe lung disease from cystic fibrosis," *J Cyst Fibros*, vol. 7, no. 4, pp. 285–91, 2008.

[226] P. D. Wagner, H. A. Saltzman, and J. B. West, "Measurement of continuous distributions of ventilation-perfusion ratios: theory," *J Appl Physiol*, vol. 36, no. 5, pp. 588–99, 1974.

[227] C. C. Aebischer and R. Kraemer, "The lung clearance index (lci) as an estimate of ventilation inequalities in patients with cystic fibrosis.," *Agents Actions Suppl*, vol. 40, pp. 73–83, 1993.

[228] J. Davies, H. Sheridan, N. Bell, S. Cunningham, S. D. Davis, J. S. Elborn, C. E. Milla, T. D. Starner, D. J. Weiner, P. S. Lee, and F. Ratjen, "Assessment of clinical response to ivacaftor with lung clearance index in cystic fibrosis patients with a g551d-cftr mutation and preserved spirometry: a randomised controlled trial.," *Lancet Respir. Med.*, vol. 1, no. 8, pp. 630–8, 2013.

[229] S. Stanojevic, R. Jensen, D. Sundaralingam, J. G. Salazar, S. Yammine, F. Singer, P. Latzin, R. S. Amin, P. Subbarao, P. Gustafsson, and F. Ratjen, "Alternative outcomes for the multiple breath washout in children with cf.," *J Cyst Fibrosis*, p. ePub ahead of print, 2015.

[230] P. Subbarao, S. Stanojevic, M. Brown, R. Jensen, M. Rosenfeld, S. Davis, L. Brumback, P. Gustafsson, and F. Ratjen, "Lung clearance index as an outcome measure for clinical trials in young children with cystic fibrosis. a pilot study using inhaled hypertonic saline," *American Journal of Respiratory and Critical Care Medicine*, vol. 188, no. 4, pp. 456–460, 2013.

[231] P. Koumellis, E. J. van Beek, N. Woodhouse, S. Fichele, A. J. Swift, M. N. Paley, C. Hill, C. J. Taylor, and J. M. Wild, "Quantitative analysis of regional airways obstruction using dynamic hyperpolarized 3he mri-preliminary results in children with cystic fibrosis," *J Magn Reson Imaging*, vol. 22, no. 3, pp. 420–6, 2005.

[232] E. J. van Beek, C. Hill, N. Woodhouse, S. Fichele, S. Fleming, B. Howe, S. Bott, J. M. Wild, and C. J. Taylor, "Assessment of lung disease in children with cystic fibrosis using hyperpolarized 3-helium mri: comparison with shwachman score, chrispin-norman score and spirometry," *Eur Radiol*, vol. 17, no. 4, pp. 1018–24, 2007.

[233] C. J. McMahon, J. D. Dodd, C. Hill, N. Woodhouse, J. M. Wild, S. Fichele, C. G. Gallagher, S. J. Skehan, E. J. van Beek, and J. B. Masterson, "Hyperpolarized 3helium magnetic resonance ventilation imaging of the lung in cystic fibrosis: comparison with high resolution ct and spirometry," *Eur Radiol*, vol. 16, no. 11, pp. 2483–90, 2006.

[234] L. F. Donnelly, J. R. MacFall, H. P. McAdams, J. M. Majure, J. Smith, D. P. Frush, P. Bogonad, H. C. Charles, and C. E. Ravin, "Cystic fibrosis: combined hyperpolarized 3he-enhanced and conventional proton mr imaging in the lung–preliminary observations," *Radiology*, vol. 212, no. 3, pp. 885–9, 1999.

[235] M. Kirby, S. Svenningsen, H. Ahmed, A. Wheatley, R. Etemad-Rezai, N. A. Paterson, and G. Parraga, "Quantitative evaluation of hyperpolarized helium-3 magnetic resonance imaging of lung function variability in cystic fibrosis," *Acad Radiol*, vol. 18, no. 8, pp. 1006–13, 2011.

[236] G. A. Paulin, S. Svenningsen, B. N. Jobse, S. Mohan, M. Kirby, J. F. Lewis, and G. Parraga, "Differences in hyperpolarized (3) he ventilation imaging after 4 years in adults with cystic fibrosis," *J Magn Reson Imaging*, vol. 41, no. 6, pp. 1701–7, 2015.

[237] N. Woodhouse, J. M. Wild, E. J. van Beek, N. Hoggard, N. Barker, and C. J. Taylor, "Assessment of hyperpolarized 3he lung mri for regional evaluation of interventional therapy: a pilot study in pediatric cystic fibrosis," *J Magn Reson Imaging*, vol. 30, no. 5, pp. 981–8, 2009.

[238] E. Bannier, K. Cieslar, K. Mosbah, F. Aubert, F. Duboeuf, Z. Salhi, S. Gaillard, Y. Berthezene, Y. Cremillieux, and P. Reix, "Hyperpolarized 3he mr for sensitive imaging of ventilation function and treatment efficiency in young cystic fibrosis patients with normal lung function," *Radiology*, vol. 255, no. 1, pp. 225–32, 2010.

[239] Y. Sun, B. P. O'Sullivan, J. P. Roche, R. Walvick, A. Reno, D. Baker, J. K. Mansour, and M. S. Albert, "Using hyperpolarized 3he mri to evaluate treatment efficacy in cystic fibrosis patients," *J Magn Reson Imaging*, vol. 34, no. 5, pp. 1206–11, 2011.

[240] B. Driehuys, S. Martinez-Jimenez, Z. I. Cleveland, G. M. Metz, D. M. Beaver, J. C. Nouls, S. S. Kaushik, R. Firszt, C. Willis, K. T. Kelly, J. Wolber, M. Kraft, and H. P. McAdams, "Chronic obstructive pulmonary disease: safety and tolerability of hyperpolarized 129xe mr imaging in healthy volunteers and patients," *Radiology*, vol. 262, no. 1, pp. 279–89, 2012.

[241] P. A. de Jong, Y. Nakano, M. H. Lequin, J. R. Mayo, R. Woods, P. D. Pare, and H. A. Tiddens, "Progressive damage on high resolution computed tomography despite stable lung function in cystic fibrosis," *Eur Respir J*, vol. 23, no. 1, pp. 93–7, 2004.

[242] r. Mugler, J. P., T. A. Altes, I. C. Ruset, I. M. Dregely, J. F. Mata, G. W. Miller, S. Ketel, J. Ketel, F. W. Hersman, and K. Ruppert, "Simultaneous magnetic resonance imaging of ventilation distribution and gas uptake in the human lung using hyperpolarized xenon-129," *Proc Natl Acad Sci U S A*, vol. 107, no. 50, pp. 21707–12, 2010.

[243] M. S. Freeman, Z. I. Cleveland, Y. Qi, and B. Driehuys, "Enabling hyperpolarized (129) xe mr spectroscopy and imaging of pulmonary gas transfer to the red blood cells in transgenic mice expressing human hemoglobin," *Magn Reson Med*, vol. 70, no. 5, pp. 1192–9, 2013.

[244] ClinicalTrials.gov, "Study of lumacaftor in combination with ivacaftor in cystic fibrosis subjects 6 to 11 years of age with f508del-cftr mutation," 2013.

[245] ClinicalTrials.gov, "A study of lumacaftor in combination with ivacaftor in cystic fibrosis subjects aged 12 years and older who are homozygous for the f508del-cftr mutation (traffic)," 2014.

[246] ClinicalTrials.gov, "A study of lumacaftor in combination with ivacaftor in cystic fibrosis subjects aged 12 years and older who are homozygous for the f508del-cftr mutation (transport)," 2014.

[247] ClinicalTrials.gov, "The effect of hypertonic saline on the lung clearance index in patients with cystic fibrosis," 2015.

[248] T. Ong and B. W. Ramsey, "Modifying disease in cystic fibrosis: current and future therapies on the horizon," *Current Opinion in Pulmonary Medicine*, vol. 19, no. 6, pp. 645–651, 2013.

[249] K. De Boeck, L. Kent, J. Davies, N. Derichs, M. Amaral, S. Rowe, P. Middleton, H. de Jonge, I. Bronsveld, M. Wilschanski, P. Melotti, I. Danner-Boucher, S. Boerner, I. Fajac, K. Southern, R. de Nooijer, A. Bot, Y. de Rijke, E. de Wachter, T. Leal, F. Vermeulen, M. Hug, G. Rault, T. Nguyen-Khoa, C. Barreto, M. Proesmans, and I. Sermet-Gaudelus, "Cftr biomarkers: time for promotion to surrogate end-point," *European Respiratory Journal*, vol. 41, no. 1, pp. 203–216, 2013.

[250] R. P. Thomen, L. L. Walkup, D. Roach, Z. I. Cleveland, J. P. Clancy, and J. C. Woods, "Emerging regional structure-function relationships in cf lungs in adolescents using ct, ute mri, and hyperpolarized xenon mri," *Proc. Intl. Soc. Mag. Reson. Med*, vol. 23, p. 1507, 2015.

[251] E. S. Ford, L. B. Murphy, O. Khavjou, W. H. Giles, J. B. Holt, and J. B. Croft, "Total and state-specific medical and absenteeism costs of copd among adults aged ¿/= 18 years in the united states for 2010 and projections through 2020," *Chest*, vol. 147, no. 1, pp. 31–45, 2015.

[252] J. R. Feary, L. C. Rodrigues, C. J. Smith, R. B. Hubbard, and J. E. Gibson, "Prevalence of major comorbidities in subjects with copd and incidence of myocardial infarction and stroke: a comprehensive analysis using data from primary care," *Thorax*, vol. 65, no. 11, pp. 956–962, 2010.

[253] J. F. Mata, T. A. Altes, J. Cai, K. Ruppert, W. Mitzner, K. D. Hagspiel, B. Patel, M. Salerno, J. R. Brookeman, E. E. de Lange, W. A. Tobias, H. T. Wang, G. D. Cates, and r. Mugler, J. P., "Evaluation of emphysema severity and progression in a rabbit model: comparison of hyperpolarized 3he and 129xe diffusion mri with lung morphometry," *J Appl Physiol (1985)*, vol. 102, no. 3, pp. 1273–80, 2007.

[254] M. Rabeyrin, F. Thivolet, G. R. Ferretti, L. Chalabreysse, A. Jankowski, V. Cottin, C. Pison, J. F. Cordier, and S. Lantuejoul, "Usual interstitial pneumonia end-stage features from explants with radiologic and pathological correlations," *Ann Diagn Pathol*, vol. 19, no. 4, pp. 269–76, 2015.

[255] C. C. Hsia, D. M. Hyde, M. Ochs, E. R. Weibel, and A. E. J. T. F. o. Q. A. o. L. Structure, "An official research policy statement of the american thoracic society/european respiratory society: standards for quantitative assessment of lung structure," *Am J Respir Crit Care Med*, vol. 181, no. 4, pp. 394–418, 2010.

[256] P. Nikolaou, A. M. Coffey, L. L. Walkup, B. M. Gust, N. Whiting, H. Newton, S. Barcus, I. Muradyan, M. Dabaghyan, G. D. Moroz, M. S. Rosen, S. Patz, M. J. Barlow, E. Y. Chekmenev, and B. M. Goodson, "Near-unity nuclear polarization with an open-source 129xe hyperpolarizer for nmr and mri," *Proc Natl Acad Sci U S A*, vol. 110, no. 35, pp. 14150–5, 2013.

[257] R. L. O'Halloran, J. H. Holmes, T. A. Altes, M. Salerno, and S. B. Fain, "The effects of snr on adc measurements in diffusion-weighted hyperpolarized he-3 mri," *J Magn Reson*, vol. 185, no. 1, pp. 42–9, 2007.

[258] J. Parra-Robles and J. M. Wild, "The influence of lung airways branching structure and diffusion time on measurements and models of short-range 3he gas mr diffusion," *J Magn Reson*, vol. 225, pp. 102–13, 2012.

[259] A. J. Hajari, D. A. Yablonskiy, A. L. Sukstanskii, J. D. Quirk, M. S. Conradi, and J. C. Woods, "Morphometric changes in the human pulmonary acinus during inflation," *J Appl Physiol (1985)*, vol. 112, no. 6, pp. 937–43, 2012.

[260] D. A. Yablonskiy, A. L. Sukstanskii, J. C. Woods, D. S. Gierada, J. D. Quirk, J. C. Hogg, J. D. Cooper, and M. S. Conradi, "Quantification of lung microstructure with hyperpolarized 3he diffusion mri," *J Appl Physiol (1985)*, vol. 107, no. 4, pp. 1258–65, 2009.

[261] D. A. Yablonskiy, A. L. Sukstanskii, and M. S. Conradi, "Commentary on "the influence of lung airways branching structure and diffusion time on measurements and models of short-range 3he gas mr diffusion"," *J Magn Reson*, vol. 239, pp. 139–42, 2014.

[262] Y. V. Chang, "Moxe: a model of gas exchange for hyperpolarized 129xe magnetic resonance of the lung," *Magn Reson Med*, vol. 69, no. 3, pp. 884–90, 2013.

[263] A. M. Coffey, M. L. Truong, and E. Y. Chekmenev, "Low-field {MRI} can be more sensitive than high-field {MRI}," *Journal of Magnetic Resonance*, vol. 237, pp. 169 – 174, 2013.

[264] R. W. Mair, M. I. Hrovat, S. Patz, M. S. Rosen, I. C. Ruset, G. P. Topulos, L. L. Tsai, J. P. Butler, F. W. Hersman, and R. L. Walsworth, "3he lung imaging in an open access, very-low-field human magnetic resonance imaging system," *Magnetic Resonance in Medicine*, vol. 53, no. 4, pp. 745–749, 2005.

[265] C. H. Tseng, G. P. Wong, V. R. Pomeroy, R. W. Mair, D. P. Hinton, D. Hoffmann, R. E. Stoner, F. W. Hersman, D. G. Cory, and R. L. Walsworth, "Low-field mri of laser polarized noble gas," *Phys. Rev. Lett.*, vol. 81, pp. 3785–3788, Oct 1998.

[266] Z. Liu, T. Araki, Y. Okajima, M. Albert, and H. Hatabu, "Pulmonary hyperpolarized noble gas mri: Recent advances and perspectives in clinical application," *European Journal of Radiology*, vol. 83, no. 7, pp. 1282 – 1291, 2014.

[267] W. R. Hendee, G. J. Becker, J. P. Borgstede, J. Bosma, W. J. Casarella, B. A. Erickson, C. D. Maynard, J. H. Thrall, and P. E. Wallner, "Addressing overutilization in medical imaging," *Radiology*, vol. 257, no. 1, pp. 240–245, 2010. PMID: 20736333.

[268] ClinicalTrials.gov, "University of wisconsin severe asthma research program iii," 2015. *Sponsor:* University of Wisconsin Madison, Washington University School of Medicine, *Status:* RECRUITING, *Identifier*: NCT01760915.

[269] ClinicalTrials.gov, "Hyperpolarized magnetic resonance imaging in asthma pre- and post-bronchial thermoplasty," 2015. *Sponsor:* Grace Parraga, Western University, Canada *Status:* ENROLLING BY INVITATION ONLY, *Identifier*: NCT02263794.

[270] ClinicalTrials.gov, "Bronchial thermoplasty for severe asthmatics guided by hxe mri (hxe-bt)," 2015. *Sponsor:* Xemed LLC *Status:* RECRUITING, *Identifier*: NCT01832363.

[271] ClinicalTrials.gov, "Use of hyperpolarized xenon gas for lung imaging in children and adults (hpxemr)," 2015. *Sponsor:* Jason C Woods, Cincinnati Children's Hospital Medical Center, *Status:* RECRUITING, *Identifier*: NCT02272049.

[272] J. A. Dirven, H. J. Tange, J. W. Muris, K. M. van Haaren, G. Vink, and O. C. van Schayck, "Early detection of copd in general practice: implementation, workload and socioeconomic status. a mixed methods observational study," *Prim Care Respir J*, vol. 22, no. 3, pp. 338–43, 2013.

[273] N. Sverzellati, F. Molinari, T. Pirronti, L. Bonomo, P. Spagnolo, and M. Zompatori, "New insights on copd imaging via ct and mri," *Int J Chron Obstruct Pulmon Dis*, vol. 2, no. 3, pp. 301–12, 2007.

[274] F. Bloch, "Nuclear induction," *Phys. Rev.*, vol. 70, pp. 460–474, Oct 1946.

[275] "Mri facts and figures."

[276] R. Benumof, "Optical Pumping Theory and Experiments," *American Journal of Physics*, vol. 33, pp. 151–160, Feb. 1965.

[277] M. E. Wagshul and T. E. Chupp, "Optical pumping of high-density rb with a broad-band dye laser and gaalas diode laser arrays: Application to ^{3}He polarization," *Phys. Rev. A*, vol. 40, pp. 4447–4454, Oct 1989.

[278] B. Saam, A. K. Petukhov, J. Chastagnier, T. R. Gentile, R. Golub, and C. M. Swank, "Comment on "pressure dependence of wall relaxation in polarized ^{3}he gaseous cells"," *Phys. Rev. A*, vol. 85, p. 047401, Apr 2012.

[279] W. H. Organization, "Chronic respiratory diseases," 2015.

[280] A. Aliverti, F. Pennati, C. Salito, and J. C. Woods, "Regional lung function and heterogeneity of specific gas volume in healthy and emphysematous subjects," *Eur Respir J*, vol. 41, no. 5, pp. 1179–88, 2013.

[281] T. A. Altes, P. K. Rehm, F. Harrell, M. Salerno, T. M. Daniel, and E. E. De Lange, "Ventilation imaging of the lung: comparison of hyperpolarized helium-3 mr imaging with xe-133 scintigraphy," *Acad Radiol*, vol. 11, no. 7, pp. 729–34, 2004.

[282] J. Biederer, M. Both, J. Graessner, C. Liess, P. Jakob, M. Reuter, and M. Heller, "Lung morphology: fast mr imaging assessment with a volumetric interpolated breath-hold technique: initial experience with patients," *Radiology*, vol. 226, no. 1, pp. 242–9, 2003.

[283] R. V. Cadman, J. Lemanske, R. F., M. D. Evans, D. J. Jackson, J. E. Gern, R. L. Sorkness, and S. B. Fain, "Pulmonary 3he magnetic resonance imaging of childhood asthma," *J Allergy Clin Immunol*, vol. 131, no. 2, pp. 369–76 e1–5, 2013.

[284] M. Castro, S. Fain, E. Hoffman, D. Gierada, S. Erzurum, and S. Wenzel, "Lung imaging in asthmatic patients: the picture is clearer," *J Allergy Clin Immunol*, vol. 128, no. 3, pp. 467–478, 2011.

[285] C. J. Danek, C. M. Lombard, D. L. Dungworth, P. G. Cox, J. D. Miller, M. J. Biggs, T. M. Keast, B. E. Loomas, W. J. Wizeman, J. C. Hogg, and A. R. Leff, "Reduction in airway hyperresponsiveness to methacholine by the application of rf energy in dogs," *J Appl Physiol (1985)*, vol. 97, no. 5, pp. 1946–53, 2004.

[286] E. E. de Lange, T. A. Altes, J. T. Patrie, J. J. Battiston, A. P. Juersivich, r. Mugler, J. P., and T. A. Platts-Mills, "Changes in regional airflow obstruction over time in the lungs of patients with asthma: evaluation with 3he mr imaging," *Radiology*, vol. 250, no. 2, pp. 567–75, 2009.

[287] E. E. de Lange, T. A. Altes, J. T. Patrie, J. D. Gaare, J. J. Knake, r. Mugler, J. P., and T. A. Platts-Mills, "Evaluation of asthma with hyperpolarized helium-3 mri: correlation with clinical severity and spirometry," *Chest*, vol. 130, no. 4, pp. 1055–62, 2006.

[288] S. B. Fain, G. Gonzalez-Fernandez, E. T. Peterson, M. D. Evans, R. L. Sorkness, N. N. Jarjour, W. W. Busse, and J. E. Kuhlman, "Evaluation of structure-function relationships in asthma using multidetector ct and hyperpolarized he-3 mri," *Acad Radiol*, vol. 15, no. 6, pp. 753–62, 2008.

[289] G. Galluccio and G. Lucantoni, "Bronchoscopic lung volume reduction for pulmonary emphysema: preliminary experience with a new novatech endobronchial silicone one-way valve," *Interact Cardiovasc Thorac Surg*, vol. 11, no. 2, pp. 213–5, 2010.

[290] H. Goo, "Free-breathing cine ct for the diagnosis of tracheomalacia in young children," *Pediatric Radiology*, vol. 43, no. 8, pp. 922–928, 2013.

[291] R. H. Ireland, N. Woodhouse, N. Hoggard, J. A. Swinscoe, B. H. Foran, M. Q. Hatton, and J. M. Wild, "An image acquisition and registration strategy for the fusion of hyperpolarized helium-3 mri and x-ray ct images of the lung," *Phys Med Biol*, vol. 53, no. 21, pp. 6055–63, 2008.

[292] R. E. Jacob and W. J. Lamm, "Stable small animal ventilation for dynamic lung imaging to support computational fluid dynamics models," *PLoS One*, vol. 6, no. 11, p. e27577, 2011.

[293] M. Khadadah, B. Jayakrishnan, A. Muquim, O. Roberts, T. Sinan, N. Maradny, and I. Lasheen, "High resolution computed tomography in asthma," *Oman Med J*, vol. 27, no. 2, pp. 145–50, 2012.

[294] D. O. Kuethe, N. L. Adolphi, and E. Fukushima, "Short data-acquisition times improve projection images of lung tissue," *Magn Reson Med*, vol. 57, no. 6, pp. 1058–64, 2007.

[295] H. F. Lausberg, K. Chino, G. A. Patterson, B. F. Meyers, P. D. Toeniskoetter, and J. D. Cooper, "Bronchial fenestration improves expiratory flow in emphysematous human lungs," *Ann Thorac Surg*, vol. 75, no. 2, pp. 393–7; discussion 398, 2003.

[296] E. Y. Lee, Y. Sun, D. Zurakowski, H. Hatabu, U. Khatwa, and M. S. Albert, "Hyperpolarized 3he mr imaging of the lung: normal range of ventilation defects and pft correlation in young adults," *J Thorac Imaging*, vol. 24, no. 2, pp. 110–4, 2009.

[297] D. J. Niles, S. J. Kruger, B. J. Dardzinski, A. Harman, N. N. Jarjour, M. Ruddy, S. K. Nagle, C. J. Francois, and S. B. Fain, "Exercise-induced bronchoconstriction: reproducibility of hyperpolarized 3he mr imaging," *Radiology*, vol. 266, no. 2, pp. 618–25, 2013.

[298] J. D. Quirk, B. A. Lutey, D. S. Gierada, J. C. Woods, R. M. Senior, S. S. Lefrak, A. L. Sukstanskii, M. S. Conradi, and D. A. Yablonskiy, "In vivo detection of acinar microstructural changes in early emphysema with (3)he lung morphometry," *Radiology*, vol. 260, no. 3, pp. 866–74, 2011.

[299] S. Sethi and J. Cicenia, "Treatment of pcp-related pneumothorax using one-way endobronchial valves," *CHEST Journal*, vol. 134, no. 4, pp. 9002–9002, 2008.

[300] T. Suzuki, T. Sakagami, L. R. Young, B. C. Carey, R. E. Wood, M. Luisetti, S. E. Wert, B. K. Rubin, K. Kevill, C. Chalk, J. A. Whitsett, C. Stevens, L. M. Nogee, I. Campo, and B. C. Trapnell, "Hereditary pulmonary alveolar proteinosis: pathogenesis, presentation, diagnosis, and therapy," *Am J Respir Crit Care Med*, vol. 182, no. 10, pp. 1292–304, 2010.

[301] B. C. Trapnell, B. C. Carey, K. Uchida, and T. Suzuki, "Pulmonary alveolar proteinosis, a primary immunodeficiency of impaired gm-csf stimulation of macrophages," *Curr Opin Immunol*, vol. 21, no. 5, pp. 514–21, 2009.

[302] J. Tschirren, E. A. Hoffman, G. McLennan, and M. Sonka, "Intrathoracic airway trees: segmentation and airway morphology analysis from low-dose ct scans," *IEEE Trans Med Imaging*, vol. 24, no. 12, pp. 1529–39, 2005.

[303] J. Tschirren, G. McLennan, K. Palagyi, E. A. Hoffman, and M. Sonka, "Matching and anatomical labeling of human airway tree," *IEEE Trans Med Imaging*, vol. 24, no. 12, pp. 1540–7, 2005.

[304] N. J. Tustison, B. B. Avants, L. Flors, T. A. Altes, E. E. de Lange, r. Mugler, J. P., and J. C. Gee, "Ventilation-based segmentation of the lungs using hyperpolarized (3)he mri," *J Magn Reson Imaging*, vol. 34, no. 4, pp. 831–41, 2011.

[305] N. Woodhouse, J. M. Wild, M. N. Paley, S. Fichele, Z. Said, A. J. Swift, and E. J. van Beek, "Combined helium-3/proton magnetic resonance imaging measurement of ventilated lung volumes in smokers compared to never-smokers," *J Magn Reson Imaging*, vol. 21, no. 4, pp. 365–9, 2005.

[306] I. Zahid, S. Sharif, T. Routledge, and M. Scarci, "Is lung volume reduction surgery effective in the treatment of advanced emphysema?," *Interact Cardiovasc Thorac Surg*, vol. 12, no. 3, pp. 480–6, 2011.

[307] M. S. Albert, D. Balamore, D. F. Kacher, A. K. Venkatesh, and F. A. Jolesz, "Hyperpolarized (129)xe t (1) in oxygenated and deoxygenated blood," *NMR Biomed*, vol. 13, no. 7, pp. 407–14, 2000.

[308] M. J. Couch, B. Blasiak, B. Tomanek, A. V. Ouriadov, M. S. Fox, K. M. Dowhos, and M. S. Albert, "Hyperpolarized and inert gas mri: The future," *Mol Imaging Biol*, vol. 17, no. 2, pp. 149–62, 2015.

[309] O. J. Dempsey, "Clinical review: idiopathic pulmonary fibrosis–past, present and future," *Respir Med*, vol. 100, no. 11, pp. 1871–85, 2006.

[310] O. J. Dempsey, K. M. Kerr, L. Gomersall, H. Remmen, and G. P. Currie, "Idiopathic pulmonary fibrosis: an update," *QJM*, vol. 99, no. 10, pp. 643–54, 2006.

[311] S. Diaz, I. Casselbrant, E. Piitulainen, G. Pettersson, P. Magnusson, B. Peterson, P. Wollmer, P. Leander, O. Ekberg, and P. Akeson, "Hyperpolarized 3he apparent diffusion coefficient mri of the lung: reproducibility and volume dependency in healthy volunteers and patients with emphysema," *J Magn Reson Imaging*, vol. 27, no. 4, pp. 763–70, 2008.

[312] T. Eaton, S. Withy, J. E. Garrett, J. Mercer, R. M. Whitlock, and H. H. Rea, "Spirometry in primary care practice: the importance of quality assurance and the impact of spirometry workshops," *Chest*, vol. 116, no. 2, pp. 416–23, 1999.

[313] S. B. Fain, F. R. Korosec, J. H. Holmes, R. O'Halloran, R. L. Sorkness, and T. M. Grist, "Functional lung imaging using hyperpolarized gas mri," *J Magn Reson Imaging*, vol. 25, no. 5, pp. 910–23, 2007.

[314] L. Flors, T. A. Altes, J. P. Mugler, E. E. de Lange, G. W. Miller, J. F. Mata, I. C. Ruset, and F. W. Hersman, "New insights into lung diseases using hyperpolarized gas mri," *Radiologia*, 2015.

[315] G. C. Grimes, J. L. Manning, P. Patel, and R. M. Via, "Medications for copd: a review of effectiveness," *Am Fam Physician*, vol. 76, no. 8, pp. 1141–8, 2007.

[316] F. W. Hersman, I. C. Ruset, S. Ketel, I. Muradian, S. D. Covrig, J. Distelbrink, W. Porter, D. Watt, J. Ketel, J. Brackett, A. Hope, and S. Patz, "Large production system for hyperpolarized xe-129 for human lung imaging studies," *Academic Radiology*, vol. 15, no. 6, pp. 683–692, 2008.

[317] K. M. Johnson, S. B. Fain, M. L. Schiebler, and S. Nagle, "Optimized 3d ultrashort echo time pulmonary mri," *Magn Reson Med*, vol. 70, no. 5, pp. 1241–50, 2013.

[318] M. Kirby, S. Svenningsen, N. Kanhere, A. Owrangi, A. Wheatley, H. O. Coxson, G. E. Santyr, N. A. Paterson, D. G. McCormack, and G. Parraga, "Pulmonary ventilation visualized using hyperpolarized helium-3 and xenon-129 magnetic resonance imaging: differences in copd and relationship to emphysema," *J Appl Physiol (1985)*, vol. 114, no. 6, pp. 707–15, 2013.

[319] M. Lederlin and Y. Cremillieux, "Three-dimensional assessment of lung tissue density using a clinical ultrashort echo time at 3 tesla: a feasibility study in healthy subjects," *J Magn Reson Imaging*, vol. 40, no. 4, pp. 839–47, 2014.

[320] K. O. Leslie, "Pathology of interstitial lung disease," *Clin Chest Med*, vol. 25, no. 4, pp. 657–703, vi, 2004.

[321] r. Mugler, J. P. and T. A. Altes, "Hyperpolarized 129xe mri of the human lung," *J Magn Reson Imaging*, vol. 37, no. 2, pp. 313–31, 2013.

[322] I. A. Schettino, A. M. Ab'Saber, R. Vollmer, P. H. Saldiva, C. R. Carvalho, R. A. Kairalla, and V. L. Capelozzi, "Accuracy of high resolution ct in assessing idiopathic pulmonary fibrosis histology by objective morphometric index," *Pathol Res Pract*, vol. 198, no. 5, pp. 347–54, 2002.

[323] R. S. Amin, P. Subbarao, A. Jabar, S. Balkovec, R. Jensen, S. Kerrigan, P. Gustafsson, and F. Ratjen, "Hypertonic saline improves the lci in paediatric patients with cf with normal lung function.," *Thorax*, vol. 65, no. 5, pp. 379–83, 2010.

[324] ClinicalTrials.gov, "Hyperpolarized noble gas mr imaging for pulmonary disorders," 2016. *Sponsor:* Mitch Albert, University of Massachusetts, *Status:* COMPLETED, *Identifier*: NCT00846573.

[325] M. Eichinger, D. E. Optazaite, A. Kopp-Schneider, C. Hintze, J. Biederer, A. Niemann, M. A. Mall, M. O. Wielputz, H. U. Kauczor, and M. Puderbach, "Morphologic and functional scoring of cystic fibrosis lung disease using mri," *Eur J Radiol*, vol. 81, no. 6, pp. 1321–9, 2012.

[326] P. A. Flume, T. G. Liou, D. S. Borowitz, H. Li, K. Yen, C. L. Ordonez, D. E. Geller, and V. X. S. Group, "Ivacaftor in subjects with cystic fibrosis who are homozygous for the f508del-cftr mutation," *Chest*, vol. 142, no. 3, pp. 718–24, 2012.

[327] D. Hannon, J. M. Bradley, I. Bradbury, N. Bell, J. S. Elborn, and K. O'Neill, "Shortened lung clearance index is a repeatable and sensitive test in children and adults with cystic fibrosis.," *BMJ Open Respir Res*, p. eCollection, 2014.

[328] J. D. Quirk, Y. V. Chang, and D. A. Yablonskiy, "In vivo lung morphometry with hyperpolarized (3) he diffusion mri: reproducibility and the role of diffusion-sensitizing gradient direction," *Magn Reson Med*, vol. 73, no. 3, pp. 1252–7, 2015.

[329] J. E. Roos, H. P. McAdams, S. S. Kaushik, and B. Driehuys, "Hyperpolarized gas mr imaging: Technique and applications," *Magn Reson Imaging Clin N Am*, vol. 23, no. 2, pp. 217–29, 2015.

[330] M. Rosenfeld, F. Ratjen, L. Brumback, S. Daniel, R. Rowbotham, S. McNamara, R. Johnson, R. Kronmal, S. D. Davis, and I. S. Group, "Inhaled hypertonic saline in infants and children younger than 6 years with cystic fibrosis: the isis randomized controlled trial.," *JAMA*, vol. 307, no. 21, pp. 2269–77, 2012.

[331] L. Saiman, M. Anstead, N. Mayer-Hamblett, L. C. Lands, M. Kloster, J. Hocevar-Trnka, C. H. Goss, L. M. Rose, J. L. Burns, B. C. Marshall, F. Ratjen, and A. A. S. Group., "Effect of azithromycin on pulmonary function in patients with cystic fibrosis uninfected with pseudomonas aeruginosa: a randomized controlled trial.," *JAMA*, vol. 303, no. 17, pp. 1707–15, 2010.

[332] L. Saiman, B. C. Marshall, N. Mayer-Hamblett, J. L. Burns, A. L. Quittner, D. A. Cibene, S. Coquillette, A. Y. Fieberg, F. J. Accurso, P. W. r. Campbell, and M. S. Group, "Azithromycin in patients with cystic fibrosis chronically infected with pseudomonas aeruginosa: a randomized controlled trial.," *JAMA*, vol. 290, no. 3, pp. 1749–56, 2003.

[333] R. D. VanDyke, G. L. McPhail, B. Huang, M. C. Fenchel, R. S. Amin, A. C. Carle, B. A. Chini, and M. Seid, "Inhaled tobramycin effectively reduces fev1 decline in cystic fibrosis. an instrumental variables analysis.," *Ann Am Thorac Soc*, vol. 10, no. 3, pp. 205–12, 2013.

[334] I. Marco-Rius, S. E. Bohndiek, M. I. Kettunen, T. J. Larkin, M. Basharat, C. Seeley, and K. M. Brindle, "Quantitation of a spin polarization-induced nuclear overhauser effect (spinoe) between a hyperpolarized 13c-labeled cell metabolite and water protons," *Contrast Media and Molecular Imaging*, vol. 9, no. 2, pp. 182–186, 2014.

[335] J. P. Simmons, L. D. Nelson, and U. Simonsohn, "False-positive psychology: Undisclosed flexibility in data collection and analysis allows presenting anything as significant," *Psychological Science*, vol. 22, no. 11, pp. 1359–1366, 2011.

[336] J. Vestbo, S. S. Hurd, A. G. Agust, P. W. Jones, C. Vogelmeier, A. Anzueto, P. J. Barnes, L. M. Fabbri, F. J. Martinez, M. Nishimura, R. A. Stockley, D. D. Sin, and R. Rodriguez-Roisin, "Global strategy for the diagnosis, management, and prevention of chronic obstructive pulmonary disease," *American Journal of Respiratory and Critical Care Medicine*, vol. 187, no. 4, pp. 347–365, 2013.

Appendix A

Code

"I am Error."

— Error, *Zelda II: Adventure of Link*

Following are selections of computer code used for the various analyses described throughout the text. Languages presented here include R, MATLAB, and others, and are indicated accordingly. The author is fluent in over six million forms of communication and the vast majority are not represented here.

A.1 NMR Microcontroller Pulse Timer Code [C++]

The following C++ code is programmed into the Atmel ATTiny85 microcontroller for automatic pulse timing of the HP gas NMR circuit.

```
1  //ATtiny85 pulse generation code, Robert Thomen 10-5-2014
2  int i=0;
3  void setup() {
4  pinMode(1, OUTPUT); //Pulse out
5  attachInterrupt(0,intRoutine, RISING);
6  pinMode(4,INPUT); // Rep Gen State
7  pinMode(3,INPUT); // Rep Gen State
8  pinMode(0,INPUT); // Rep Gen State
9  }
10 void loop(){
11 boolean pin4 = digitalRead(4);
```

```
boolean pin3 = digitalRead(3);
boolean pin0 = digitalRead(0);
if(!pin0 && !pin3 && !pin4){while(1){if(i>0){break;}};} //infinity
else if(pin0 && !pin3 && !pin4){delay(3600000);} //1 hr
else if(!pin0 && !pin3 && pin4){delay(1800000);} // 30 min
else if(pin0 && !pin3 && !pin4){delay(600000);} //10 min
else if(!pin0 && pin3 && !pin4){delay(180000);} // 3 min
else if(pin0 && pin3 && !pin4){delay(5000);} //5 sec
pulse();
}
void pulse(){
digitalWrite(1,HIGH);
delay(1);
digitalWrite(1,LOW);
delay(1);
}
void intRoutine(){
if(i==0){
i=i+1;
digitalWrite(1,HIGH);
delay(1);
digitalWrite(1,LOW);
delay(5000);
}
deyal(1000);
i=0;
}
```

A.2 Verify Flip Angle θ and T_1 calculation [R]

The following code was used to verify the NMR calibration equations derived in section 4.1.5.

```
##'Verify FA and T1 calculations from NMR', Robert Thomen
##Code will produce theoretical HP NMR experiment data verify that entered T1 and theta
    match

ns = 84 #number of excitations (s)
nf = 2500 #number of excitations (f)
Ds = 600 #Delta s in seconds
Df = 5 #Delta f in seconds
```

```
theta = 1.11 #theta in degrees (specified to 1.11 degrees here)
T1 = 40*60*60 #T1 in seconds (specified to 40hrs here)

#calculate theoretical S and F curves
S = 1:84
for(i in 1:ns){S[i] = exp(-Ds*i/T1)*cos(theta*pi/180)^i}
F = 1:2500
for(i in 1:nf){F[i] = exp(-Df*i/T1)*cos(theta*pi/180)^i}

#plot S and F curves
plot((1:84)*Ds,S,ylim=c(0,1))
points((1:2500)*Df,F)

Pf = F[length(F)]
Ps = S[length(S)]

(1/log((Ps*Pf^(-ns/nf))^(1/(Df*ns-Ds*ns))))/3600 # T1 in hours
acos(Pf^(1/nf)*(  (Ps*Pf^(-ns/nf))^(Df/(Df*ns-Ds*ns))))*180/pi #FA in degrees
```

A.3 Calculate T_1 [R]

The following code can be used to calculate the T_1 for a collection of NMR measurements s in time t [hr].

```
#Spin Down Plotting Code, Robby Thomen, 8-5-2014, 1-5-2014
#Given vectors of t (time in hours) and s (signal), this produces plots of
#s vs t and ln(s) vs t and calculates T1 in units of hrs

par(mfrow=c(1,2))
plot(t,s,pch=19,cex=1.8,xlab='time [hr]',ylab = 'Signal [mV]')
abline(v=24*0:7,col='gray',lty=2)
points(t,s,pch=19,cex=1.8)
pt = seq(min(t),max(t),length=1000)
Y0 = lm(log(s)~t)$coefficients[1]
Tone = -1/lm(log(s)~t)$coefficients[2]
points(pt,exp(Y0)*exp(-pt/Tone),cex=.3,col='red')

plot(t,log(s),pch=19,cex=1.8,xlab='time [hr]',ylab='ln(Signal)')
abline(v=24*0:7,col='gray',lty=2)
points(t,log(s),pch=19,cex=1.8)
```

```
abline(lm(log(s)~t),col='red')
text(mean(c(min(t),min(t),max(t))),mean(c(rep(min(log(s)),10),max(log(s)))),paste('T1 = ',
    round(Tone,2),'hr',sep=''),cex=1.6)
Tone
```

A.4 Flip Angle Calibration [R]

The following R code requests a **.data** file (raw data output from the Philips scanner) containing the 64-phase-encode flip angle calibration data. It returns the actual flip angle and, if desired, the recommended flip angles to prescribe for ventilation and/or diffusion scans.

```
#FAcal, flip angle calibration, Robert Thomen
#Flip angle calibration function will display flip cal plots and save them in parte folder
#optional varibles are FA(default 10), points (default 1:64),ventPE (default 54),diffPE (
    default 41),NOI (default 147456),bVals (default 5)

FAcal = function(...){

flip_angle_used_in_calibration = 10
PE = 54
number_of_phase_encodes_in_diffusion_sequence = 41
number_of_b_values = 5
points = 1:64
NOI = 147456

z = list(...)
if(!is.null(z$FA)){flip_angle_used_in_calibration = z$FA}
if(!is.null(z$points)){points = z$points}
if(!is.null(z$ventPE)){PE = z$ventPE}
if(!is.null(z$bVals)){number_of_b_values = z$bVals}
if(!is.null(z$diffPE)){number_of_phase_encodes_in_diffusion_sequence = z$diffPE}
if(!is.null(z$NOI)){NOI = z$NOI}

install.packages('png', repos='http://cran.us.r-project.org')
require(png)
shiftfft = function(v){newv = c(v[(round(length(v)/2)+1):length(v)],v[1:round(length(v)/2)])
    }
fileName = file.choose('C:/')
```

```
parentFolder = paste(dirname(fileName),'/',sep='')
#con <- file(paste(parentFolder,substring(fileName,nchar(fileName)-11,nchar(fileName)-5),'.list',sep=''), "rt")
#A = readLines(con,n=-1L)
#PE = as.numeric(substring(fileName,nchar(fileName)-7,nchar(fileName)-5))
fileSize <- file.info(fileName)$size
raw <- readBin(fileName, what="raw", n=fileSize)
nbrOfRecords <- length(raw) %/% 8;
dim(raw) <- c(8, nbrOfRecords);
floatsReal <- readBin(con=raw[1:4,], what="double", size=4, n=nbrOfRecords, endian="little");
floatsImg <- readBin(con=raw[5:8,], what="double", size=4, n=nbrOfRecords, endian="little");
floats=complex(real = floatsReal,imaginary=floatsImg)

floats=floats[(NOI/8):length(floats)]
kspace=matrix(0,256,2048)
decay = 1:256
for(i in 1:256){
fid = floats[2048*(i-1)+1:2048]
kspace[i,] = fid
#decay[i] = max(Mod(fft(fid[1:2048])))
decay[i] = sum(Mod(fft(kspace[i,])))
#decay[i] = sum(Mod(kspace[i,]))
}

#print to file
png(paste(parentFolder,'FAcal.png',sep=''),width=900,height=700)
par(mar=c(2.5,2.5,2.5,2.5),mfrow=c(2,2))

#plot first FID
plot(Mod(kspace[1,]),cex=.5,ylim=c(min(c(Mod(kspace[1,]),Re(kspace[1,]),Im(kspace[1,]))),max(c(Mod(kspace[1,]),Re(kspace[1,]),Im(kspace[1,])))))
abline(h=0,lty=2,col='gray')
points(Re(kspace[points[1],]),col=rgb(0,.8,0),cex=.5)
points(Im(kspace[points[1],]),col='purple',cex=.5)
text(1400,max(Mod(kspace[points[1],]))*3/4,substring(fileName,4,20),cex=1.5)
text(1400,max(Mod(kspace[points[1],]))*2/3,'First FID',cex=1.5)

#plot FFT of first FID
plot(1000:1050,shiftfft(Mod(fft(kspace[points[1],])))[1000:1050],cex=.8,ylim=c(min(c(Mod(fft(kspace[1,])),Re(fft(kspace[1,])),Im(fft(kspace[1,])))),max(c(Mod(fft(kspace[1,])),Re(fft(kspace[1,])),Im(fft(kspace[1,]))))))
points(1000:1050,shiftfft(Re(fft(kspace[points[1],])))[1000:1050],cex=.5,col='white')
```

```
lines(1000:1050,shiftfft(Re(fft(kspace[points[1],])))[1000:1050],cex=.5,col='green')
points(1000:1050,shiftfft(Im(fft(kspace[points[1],])))[1000:1050],cex=.5,col='white')
lines(1000:1050,shiftfft(Im(fft(kspace[points[1],])))[1000:1050],cex=.5,col='purple')
lines(1000:1050,shiftfft(Mod(fft(kspace[points[1],])))[1000:1050],lwd=2)
abline(v=1025,lty=2,col='gray')
SNR1 = round(max(Mod(fft(kspace[points[1],])))/mean(Mod(fft(kspace[1,10:2000]))),0)
SNR64 = round(max(Mod(fft(kspace[points[length(points)],])))/mean(Mod(fft(kspace[length(
    points),10:2000]))),0)
text(1010,max(Mod(fft(kspace[points[1],])))*2/3,'FFT of First FID',cex=1.5)
text(1040,max(Mod(fft(kspace[points[1],])))*2/3,paste('SNR 1 - ', SNR1,sep=''),cex=1.5)
text(1040,max(Mod(fft(kspace[points[1],])))/2,paste('SNR N - ', SNR64,sep=''),cex=1.5)
t = points
s = decay[points]

#plot S v n
plot(t,s,pch=19,cex=1.3,xlab='Excitation Number',ylab = 'Maximum of FID Fourier Transform')
points(t,s,pch=19,cex=1.3)
lines(t,s,pch=19)
pt = seq(min(t),max(t),length=1000)
Y0 = lm(log(s)~t)$coefficients[1]
theta = acos(lm(log(s)~t)$coefficients[2]+1)*180/pi
A = lm(1:length(s)~log(s))
B = summary(A)
er = B$coefficients[2,2]
er = sqrt(er^2*(-A$coefficients[2]^(-2)*180/pi)^2)
points(pt,exp(Y0)*exp((cos(theta*pi/180)-1)*pt),cex=.3,col='red')
text(floor(length(points)*40/64),decay[floor(length(points)*10/64)],'Signal Decay',cex=1.5)
text(floor(length(points)*40/64),decay[floor(length(points)*15/64)],'(sums of FFTs of FIDs)'
    ,cex=1.5)
text(floor(length(points)*10/64),max(decay),paste('<----',round(max(decay),0)))
text(floor(length(points)*45/64),min(decay),paste(round(min(decay),0),  '--->'))

#plot ln(s) v n
plot(t,log(s),pch=19,cex=1.3,xlab='Excitation Number',ylab='ln(Maximum of FID Fourier
    Transform)')
points(t,log(s),pch=19,cex=1.3)
abline(lm(log(s)~t),col='red')
text(floor(length(points)*45/64),log(decay[floor(length(points)*10/64)]),'ln(Signal Decay)')

#calculate and print calculated flip angle and corrected flip angles to prescribe
text(floor(length(points)*20/64),log(decay[floor(length(points)*40/64)]),paste('Flip Angle
    is ', round(theta,2) ,'    ', round(er,2),' ',  sep=''),cex=1.2,col='red')
text(floor(length(points)*25/64),log(decay[floor(length(points)*48/64)]),paste(PE, ' PE vent
```

```
     requires a ', round(atan(sqrt(2/PE))*180/pi,1), '  flip',  sep=''),cex=1.2,col='blue')
text(floor(length(points)*25/64),log(decay[floor(length(points)*52/64)]),paste('Please
    prescribe a ', round((flip_angle_used_in_calibration/theta)*atan(sqrt(2/PE))*180/pi,1),
    '  flip',  sep=''),cex=1.2,col='blue')
newFA = (flip_angle_used_in_calibration/theta)*atan(sqrt(2/PE))*180/pi
exponent = number_of_phase_encodes_in_diffusion_sequence*number_of_b_values
FA = 180*acos((.2)^(1/exponent))/pi
text(floor(length(points)*25/64),log(decay[floor(length(points)*58/64)]),paste(number_of_
    phase_encodes_in_diffusion_sequence, ' PE diffusion: ', round(FA,1), '  flip',  sep=''),
    cex=1.2,col='purple')
text(floor(length(points)*25/64),log(decay[floor(length(points)*64/64)]),paste('Please
    prescribe a ', round(FA*flip_angle_used_in_calibration/theta,1), '  flip',  sep=''),cex
    =1.2,col='purple')
dev.off()
par(mar=c(3,3,3,3),mfrow=c(1,1))
}
```

A.5 Optimum Flip Angle [R]

This code is used to computationally evaluate the optimum flip angle to prescribe for a HP-gas ventilation scan as a function of the number of phase encode steps. The flip angle which maximizes the total recieved signal across all k-space is considered optimum.

```
for(PEs in 1:128){
M = 1;S = M
for(theta in (1:900)/10){
for(i in 1:PEs){
S[i] = sin(theta*pi/180)*M[i]
M[i+1] = cos(theta*pi/180)*M[i]
}
totS[theta*10] = sum(S)
}
bestT[PEs] = sum((max(totS)==totS)*(1:900))
}

par(mar=c(4,4,4,4))
plot(bestT/10,ylim=c(0,40),pch=)
lines(180*atan(sqrt(2/(1:128)))/pi)
abline(h=10*(1:10),lty=2,col='gray')
abline(v=20*(1:10),lty=2,col='gray')
```

A.6 Analyze Ventilation Data for Defects [R]

Following is R code to evaluate the segmental ventilation percentage (SVP) and ventilation defect percentage (VDP) of ventilation images. The input is a 3D array of ventilation images (NormMR) and array of identical geometry where each bronchopulmonary segment is labeled with an integer (maskarray). The defectThreshold is the percentage of the lung signal mean below which ventilation is considered defective.

```
analysis = function(NormMR, maskarray, defectThreshold){
totalSignal = sum(NormMR*(maskarray!=0))
totalVolume = sum(maskarray!=0)
results = array(dim=c(21,5))
MRmean = mean((NormMR*(maskarray!=0))[NormMR*(maskarray!=0)!=0])
defectArray = (NormMR<MRmean*defectThreshold)*maskarray
for(k in 1:dim(defectArray)[3]){defectArray[,,k] = medFilter(defectArray[,,k])}
defectPercent = sum(defectArray!=0)/totalVolume
for(segment in 1:21){
results[segment,1] = sum(NormMR*(maskarray==segment))/totalSignal
results[segment,2] = sum(maskarray==segment)/totalVolume
results[segment,4] = sd((NormMR*(maskarray==segment))[NormMR*(maskarray==segment)!=0])/
    totalSignal
results[segment,5] = sum(defectArray==segment)/sum(maskarray==segment)
}
results[,3] = results[,1]/results[,2]
results[6:19,] = results[8:21,]
results = results[1:19,]
rtr = list(defectPercent=defectPercent,defectArray=defectArray,results=results,MRmean=MRmean
    ,totalSignal=totalSignal,totalVolume=totalVolume)
return(rtr)
}
```

A.7 Image Registration Algorithm [MatLab]

The following MatLab code will register a CT-generated mask image to an HP gas MRI for regional quantification. Subroutines are not included here.

```
%Image Registration Code - Robert Thomen, adapted from Open Source code by Ethan Meyers -
    10-13-2012
```

```
clearvars -except lung frame;
clc;
global lung;
%~~~~~~~~~~~~~~~~~~~~~~~~~~~~~~~~~~~~~~~~~~~~~~~~~~~~~~~~~~~~~~~~~~~~~~~~~~~~
%~~~~~~~~~~~~~~~~~~~~~~~~~~~~~~Set Parameters~~~~~~~~~~~~~~~~~~~~~~~~~~~~~~~~
MagicSheet = [0;393;313;300;273;232;218;181;163;116];
folder = ['C:\076\warps\'];
mrfolder = 'C:\Data\IRC186H\IRC186H-12\20150223\801_Image_TEST_XE_AP_015022311454375263\';
mrext = '*.dcm';
ctfolder = 'E:\Thomen\ThomenBTR\6174\6174\';
ctext = '*.IMA';
maskfolder = 'C:\gMasks\';
[MR,magicCT,magicmask] = buildMagicArrays(folder,mrfolder,mrext,ctfolder,ctext,maskfolder,
    uint16(MagicSheet));
%~~~~~~~~~~~~~~~~~~~~~~PARAMETER SETUP~~~~~~~~~~~~~~~~~~~~~~~~~~~~~~~~~~~~~~
%~~~~~~~~~~~~~~~~~~~~~~~~~~~~~~~~~~~~~~~~~~~~~~~~~~~~~~~~~~~~~~~~~~~~~~~~~~~~
    magicMR = MR;
frame = 10;%MR frame
lung = 1;%1 for left lung, 2 for right lung
MRscale = 5.7;%enlarge MR by this scale factor
BTR = 1;%I don't use this anymore, but I keep it to remind me of better times
warp=1;%If you don't want to warp again, set equal to 0
trim=1;%Allows you to trim the mask
%~~~~~Everything above this line should be manually set before running~~~~
%~~~~~~~~~~~~~~~~~~~~~~~~~~~~~~~~~~~~~~~~~~~~~~~~~~~~~~~~~~~~~~~~~~~~~~~~~~~~
%~~~~~~~~~~~~~~~~~~~~~~~~~~~~~~~~~~~~~~~~~~~~~~~~~~~~~~~~~~~~~~~~~~~~~~~~~~~
MRimage = MR(:,:,frame);
CT = magicCT(:,:,frame);
mask = magicmask(:,:,frame);
MR = imresize(MRimage,MRscale);
mask = maskShift(mask);
%PointShift centers the mask on the MR according to user clicks
[firsty firstx mask CT] = PointShift(mask, MR, CT, lung);
%Arrow keys for further centering
imshow(maskMRcombineImage(double(mask),double(MR)),[]);
disp('Use Arrow Keys to Position Mask onto MR image. Then Mouseclick to Proceed...');
[~,~,b] = ginput(1);
while b ~= 1
    if b == 28
        mask(1:size(mask,1),1:(size(mask,2)-1)) = mask(1:size(mask,1),2:(size(mask,2)));
        CT(1:size(CT,1),1:(size(CT,2)-1)) = CT(1:size(CT,1),2:(size(CT,2)));
    elseif b == 29
        mask(1:size(mask,1),2:(size(mask,2))) = mask(1:size(mask,1),1:(size(mask,2)-1));
```

```
        CT(1:size(CT,1),2:(size(CT,2))) = CT(1:size(CT,1),1:(size(CT,2)-1));
    elseif b == 30
        mask(1:(size(mask,1)-1),1:(size(mask,2))) = mask(2:size(mask,1),1:(size(mask,2)));
        CT(1:(size(CT,1)-1),1:(size(CT,2))) = CT(2:size(CT,1),1:(size(CT,2)));
    elseif b == 31
        mask(2:(size(mask,1)),1:(size(mask,2))) = mask(1:(size(mask,1)-1),1:(size(mask,2)));
        CT(2:(size(CT,1)),1:(size(CT,2))) = CT(1:(size(CT,1)-1),1:(size(CT,2)));
    elseif b == 115
        smask = imresize(mask,[(size(mask,1)-1) size(mask,2)],'nearest');
        mask(1:(size(mask,1)-1),size(mask,2)) = smask;
    end
    imshow(maskMRcombineImage(double(mask),double(MR)),[]);
    [~,~,b] = ginput(1);
end
if warp
%This becomes the first registration point
    refPoints{1} = [uint16(firsty) uint16(firstx)];
    warpPoints{1} = [uint16(firsty) uint16(firstx)];
disp('Click some warping landmarks (as many as youd like). Then Spacebar to proceed');
    %click points around the CT as reference points
    CTdots=CT/max(CT(:));CTdots(:,:,2) = CT/max(CT(:)); CTdots(:,:,3) = CT/max(CT(:));
    CTdots((firstx-1):(firstx+1),(firsty-1):(firsty+1),1) = max(CT(:));
    i=1;
    while 1
    imshow(CTdots);
    [y,x,b] = ginput(1);
    if (b~=1) break; end;
    CTdots((x-1):(x+1),(y-1):(y+1),1) = max(CT(:));
    refPoints{i} = [double(y) double(x)];
    i=i+1;
    end
    close();
    %click same points around MR at warping landmarks
    MRdots=MR/max(MR(:));MRdots(:,:,2) = MR/max(MR(:));MRdots(:,:,3) = MR/max(MR(:));
    MRdots((firstx-1):(firstx+1),(firsty-1):(firsty+1),1) = max(MR(:));
    for i=1:length(refPoints)
    y = uint16(refPoints{i}(1));
    x = uint16(refPoints{i}(2));
    CTdots=CT/max(CT(:));CTdots(:,:,2) = CT/max(CT(:)); CTdots(:,:,3) = CT/max(CT(:));
    CTdots((x-1):(x+1),(y-1):(y+1),1) = max(CT(:));
    imshow(CTdots);
    figure(1);
    set(1, 'Position', [100,100,size(CT,1),size(CT,2)]);
```

```
    imshow(CTdots)
    figure(2);
    set(2, 'Position', [700,600,size(MR,1),size(MR,2)]);
    imshow(double(MRdots),[]);
    [wy, wx] = ginput(1);
    wx=uint16(wx);wy=uint16(wy);
    MRdots((wx-1):(wx+1),(wy-1):(wy+1),1) = max(MR(:));
    warpPoints{i} = [double(wy) double(wx)];
    close();
    end
for i=1:length(refPoints)
     disp(refPoints{i}(1)>size(mask,1));
     disp(refPoints{i}(2)>size(mask,2));
     %refPoints{i} = [x y];
     disp(warpPoints{i}(1)>size(mask,1));
     disp(warpPoints{i}(2)>size(mask,2));
     %warpPoints{i} = [x y];
end
for i=1:length(refPoints)
    disp(refPoints{i});
    disp(warpPoints{i});
end
 end
mask = warpImage(double(mask), refPoints, warpPoints);
if trim;
    mask = uint8(trimTheMask(mask,MR));
end
mask = imresize(mask,1/MRscale,'nearest');
size(mask)
size(imresize(MR,1/MRscale,'nearest'))
if exist([folder 'warped\'])==0 mkdir([folder 'warped\']); end
imwrite(mask,[folder 'warped\' num2str(frame) '_' num2str(lung) '.bmp'],'bmp');
%warpedMasks(:,:,frame) = warpedMasks(:,:,frame) + mask;
%save([folder 'WarpedMasks.Mat'],'warpedMasks');

%frame = frame+(lung==2)*1;
%lung = (lung==1)+1;

close();
disp('SUCCESS!');
```

A.8 Morphometry Calculating Code [MatLab]

The following code was used to calculate the mean linear intercept L_m and surface area to volume ratio of the lung sample histology.

```
clear lm;
%kk = [3,5,7,9,11,15,19,59,61,67];
load('C:\076\mmPerPx.Mat');load('C:\076\thiz.mat');load('C:\076\namez.mat');load('C:\076\
    shrinkage2.mat');

files = dir('C:\076\Histology\full');
for kk = 31 %which slide

barlength = double(uint8(.1*mean(shrinkage(kk,:))*.175/mmPerPx(kk,1))); %50um bar
clearvars -except files results barlength lm mmPerPx kk namez thiz shrinkage
A = imread(['C:\076\Histology\full\' namez{kk}]);
doof=A;
this = imread(['C:\076\Histology\full\' thiz{kk}]);
this = (this(:,:,1)==0).*(this(:,:,2)==0).*(this(:,:,3)==0);

this = medfilt2(this,[5 5]);
A = double(A);
img = sqrt(A(:,:,2).^2+A(:,:,3).^2);
C = img;
C = medfilt2(C,[3 3]);
C = C<(mean(C(:))-4);
C = imdilate(C,ones(5,5));C=imerode(C,ones(5,5));
C = ~bwareaopen(~C,1000);
C = bwareaopen(C,1000);

img = C;
A = img;
%Surface area map
%Lmh = 0; count = 0; k=1;
for i = 1:(size(C,1)-1)
    for j = 1:(size(C,2)-1)
       % if this(i,j)==1
            %Lmh(k) = count;
            %count = (~C(i,j)+count)*~C(i,j);
            %k = k+(count==0)*1;
            D(i,j) = double((abs(C(i,j+1)-C(i,j))+abs(C(i+1,j)-C(i,j))))*double((this(i,j)
                ==1));
            %imshow(D,[]); pause(.001);
```

```
37        % end
38      end
39  end
40  %create bar grid
41  clear B;
42  count=1;
43  for i=1:barlength:size(A,1)
44      for j=1:size(A,2)
45          B(i,j) = (count>barlength);
46          count = uint8(count*uint8(count~=2*barlength));
47          count = count+1;
48          %disp(B(i,j));
49          %pause(.1)
50      end
51      if mod(i,2)
52          B(i,:) = ~B(i,:);
53          count=1;
54      end
55  end
56  B(:,size(A,2))=0;
57  B(size(A,1),:)=0;
58  %imshow(B,[])
59  B = B.*this;
60  B = bwareaopen(B,barlength-1);
61  B = bwlabel(B);
62  C = uint16(B~=B);
63  inters=uint16(0);
64  for k = 1:max(max(bwlabel(B)))
65      inters = inters + uint16((sum(sum(~A.*(B==k)))>0)*(sum(sum(~A.*(B==k)))<barlength));
66      C = C+uint16(B==k)*uint16((sum(sum(~A.*(B==k)))>0)*(sum(sum(~A.*(B==k)))<barlength));
67  end
68  imshow(double(C)*2+double(A)+double(B>1),[]) % A = binary, B = lines, C = intercepts
69  BB = B;BB(2:size(BB,1),:)=BB(2:size(BB,1),:)+B(1:(size(BB,1)-1),:);BB(3:size(BB,1),:)=BB(3:
        size(BB,1),:)+B(1:(size(BB,1)-2),:);
70  CC = C;CC(2:size(CC,1),:)=CC(2:size(CC,1),:)+C(1:(size(CC,1)-1),:);CC(3:size(CC,1),:)=CC(3:
        size(CC,1),:)+C(1:(size(CC,1)-2),:);
71   [y,x] = ginput(1);
72   [yy,xx] = ginput(1);
73   imshow(cat(3,doof(x:xx,y:yy,1),doof(x:xx,y:yy,2),doof(x:xx,y:yy,3)),[]) %image
74   imshow(cat(3,double(A(x:xx,y:yy,1))+BB(x:xx,y:yy),double(A(x:xx,y:yy,1)),double(A(x:xx,y:yy
         ,1))),[])% binary w bars
75   imshow(cat(3,zeros(uint16(xx-x+1),uint16(1+yy-y)),zeros(uint16(xx-x+1),uint16(1+yy-y)),
         double(CC(x:xx,y:yy))),[])% intercept bars
```

```
 imshow(double(A(x:xx,y:yy)),[])
 imshow(imdilate(double(D(x:xx,y:yy)),[0,1,0;1,1,1;0,1,0])>0,[])%surface area (dilated)
imwrite((double(C)*2+double(A)+double(B>1))/4,['C:\076\Histology\analyzed\' namez{kk}]);
files(kk).name
lm(kk,1) = mmPerPx(kk,1); %pixel size in mm
lm(kk,2) = barlength; % length of lm bar in pixels
lm(kk,3) = inters; % number of bars intersecting tissue/airspace
lm(kk,4) = .1*mmPerPx(kk,1)*sum(double(B(:)>0))/double(inters) % Lm in cm
lm(kk,5) = sum(sum(D>0))/(sum(sum(this>0))*mmPerPx(kk,1)*.1) % SA/V in cm-1
for i=1:(size(this,1)-1)
llmm(i,1) = .1*mmPerPx(kk,1)*size(this,2)/sum(this(i,:).*[D(i,:),0]>0);
end
llmm(isinf(llmm)) = NaN
lm(kk,6) = nanmean(llmm)
end
```

Appendix B

Copyright Clearance Permissions

"You wouldn't download a car..."

— Anti-Piracy Avert

Appropriate copyright permissions have been obtained for any images used in this dissertation which have been published in peer-reviewed journals. Below are statements of copyright permission from journals *Magnetic Resonance in Medicine* for [42] and *Radiology* for [41].

JOHN WILEY AND SONS LICENSE TERMS AND CONDITIONS

Mar 18, 2016

This Agreement between Robert P Thomen ("You") and John Wiley and Sons ("John Wiley and Sons") consists of your license details and the terms and conditions provided by John Wiley and Sons and Copyright Clearance Center.

License Number	3806090040058
License date	Feb 11, 2016
Licensed Content Publisher	John Wiley and Sons
Licensed Content Publication	Magnetic Resonance in Medicine
Licensed Content Title	Direct comparison of 129Xe diffusion measurements with quantitative histology in human lungs
Licensed Content Author	Robert P. Thomen,James D. Quirk,David Roach,Tiffany Egan-Rojas,Kai Ruppert,Roger D. Yusen,Talissa A. Altes,Dmitriy A. Yablonskiy,Jason C. Woods
Licensed Content Date	Jan 17, 2016
Pages	1
Type of use	Dissertation/Thesis
Requestor type	Author of this Wiley article
Format	Electronic
Portion	Figure/table
Number of figures/tables	4
Original Wiley figure/table number(s)	Figure 1, Figure 2, Figure 3, Figure 4
Will you be translating?	No
Order reference number	160211
Title of your thesis / dissertation	Investigation of Lung Structure-Function Relationships Using Hyperpolarized Noble Gases
Expected completion date	Apr 2016
Expected size (number of pages)	120
Requestor Location	Robert P Thomen 3287 Morrison Ave, Apt 10 CINCINNATI, OH 45220 United States Attn: Robert P Thomen
Billing Type	Invoice
Billing Address	Robert P Thomen 3287 Morrison Ave, Apt 10 CINCINNATI, OH 45220 United States Attn: Robert P Thomen
Total	0.00 USD

RADIOLOGICAL SOCIETY OF NORTH AMERICA
820 JORIE BLVD. OAK BROOK, IL 60523
TEL 1-630-571-2670 FAX 1-630-571-7837
RSNA.ORG

February 15, 2016

Robert Thomen
3287 Morrison Ave., Apt. 10
Cincinnati, OH 45220

Dear Robert Thomen:

The Radiological Society of North America (RSNA®) is pleased to grant you permission to reproduce the following figures in electronic format for educational, non-profit use in your dissertation, provided you give full credit to the authors of the original publication.

> Figures 1, 3, 4
> Thomen R P, Sheshadri A, Quirk J D, et al. Regional ventilation changes in severe asthma after bronchial thermoplasty with ^{3}He MR imaging and CT. *Radiology* 2015;274:250-259.

This permission is a one-time, non-exclusive grant for English-language use and is exclusively limited to the usage stated and underlined above. The requestor guarantees to reproduce the material as originally published. Permission is granted under the condition that a full credit line is prominently placed (i.e. author name(s), journal name, copyright year, volume #, inclusive pages and copyright holder).

This permission becomes effective upon receipt of this signed contract. Please sign a copy of this agreement, return a signed copy to me and retain a copy for your files. Thank you for your interest in our publication.

[Print Name]: Robert Thomen

SIGNATURE: [signature] Date: 3-18-2016

Sincerely,

Ashley E. Daly

Ashley E. Daly
Senior Manager, Journal Rights & Communications
Publications

Phone: 630-590-7771
Fax: 630-571-7837
E-mail: *permissions@rsna.org*